UNIVERSITY OF ALBERTA

BIAXIAL MONOTONIC AND FATIGUE BEHAVIOUR OF A MULTIDIRECTIONAL GLASS FIBRE REINFORCED EPOXY PIPE

By

MICHAEL G. MARTENS ©

A thesis submitted to the Faculty of Graduate Studies in partial fulfillment of the requirements for the degree Masters of Science

Department of Mechanical Engineering

Edmonton, Alberta

Spring, 1999

National Library of Canada
Acquisitions and Bibliographic Services
395 Wellington Street
Ottawa ON K1A 0N4
Canada

Bibliothèque nationale du Canada
Acquisitions et services bibliographiques
395, rue Wellington
Ottawa ON K1A 0N4
Canada

Your file Votre référence

Our file Notre référence

The author has granted a non-exclusive licence allowing the National Library of Canada to reproduce, loan, distribute or sell copies of this thesis in microform, paper or electronic formats.

L'auteur a accordé une licence non exclusive permettant à la Bibliothèque nationale du Canada de reproduire, prêter, distribuer ou vendre des copies de cette thèse sous la forme de microfiche/film, de reproduction sur papier ou sur format électronique.

The author retains ownership of the copyright in this thesis. Neither the thesis nor substantial extracts from it may be printed or otherwise reproduced without the author's permission.

L'auteur conserve la propriété du droit d'auteur qui protège cette thèse. Ni la thèse ni des extraits substantiels de celle-ci ne doivent être imprimés ou autrement reproduits sans son autorisation.

0-612-40086-7

Canada

UNIVERSITY OF ALBERTA

LIBRARY RELEASE FORM

Name of Author: Michael Gordon Martens

Title of Thesis: Biaxial Monotonic and Fatigue Behaviour of a Multidirectional Glass Fibre Reinforced Epoxy Pipe

Degree: Masters of Science

Year this Degree Granted: 1999

Permission is hereby granted to the University of Alberta Library to reproduce single copies of this thesis and to lend or sell such copies for private, scholarly, or scientific research purposes only.

The author reserves all other publication and other rights in association with the copy in the thesis, and except as hereinbefore provided, neither the thesis nor any substantial portion thereof may be printed or otherwise reproduced in any material from what ever without the author's prior written permission.

Michael G. Martens
R.R.# 1, Site #6, Box 35
Grande Prairie, Alberta
CANADA, T8V 2Z8

April 14, 99

UNIVERSITY OF ALBERTA

Faculty of Graduate Studies and Research

The undersigned certify that they have read, and recommended to the Faculty of Graduate Studies and Research for acceptance, a thesis entitled Biaxial Monotonic and Fatigue Behaviour of a Multidirectional Glass Fibre Reinforced Epoxy Pipe submitted by Michael Gordon Martens in partial fulfillment of the requirements for the degree of Masters of Science.

Dr. F. Ellyin (Superisor)

aw Lipsett

Dr. A. W. Lipsett

Dr. J. Szymanski

April 12, 1999

TO MY PARTENS

Dr. Victor and Mary Martens

ABSTRACT

One advantage of filament-wound, fiber-reinforced polymer-matrix composite pipe is the ability to optimize the fiber direction, in order to provide a higher strength and stiffness for a specified biaxial load. The development of a multidirectional lay-up can allow for strengthening and stiffening for more than one biaxial loading ratio. The composite pipe under investigation has a significant number of glass fibers wound predominantly in the hoop direction to account for high internal pressures and fibers in the axial direction, to account for axial loading. However, such a configuration does cause large stiffness changes in neighboring plies, which may result in delamination.

The objective of this investigation was to study the effect of the applied biaxial loading conditions, for both short-term and long-term loadings. Monotonic leakage failure envelope and fatigue leakage life envelope for various biaxial loading ratios were determined. The influence of imperfections, inherent to the large-scale filament winding process was also investigated.

ACKNOWLEDGEMENTS

This work was completed under the direction of Dr. F. Ellyin. I would like to thank him for his guidance and patience throughout this project.

I also would like to take this opportunity to thank John Wolodko, Bernie Faulkner and Ian Buttar for their helpful support, encouragement, and patience, which made this work possible. In addition my thanks goes out to Vern Whiteman of Western Fiberglass Pipe Sales LTD. of Estevan Saskatchewan and Fiber Glass System, Inc. STAR® of San Antonio, Texas for supplying and manufacturing the multidirectional fiberglass reinforced pipe

I would also like to thank all other members of the technical and academic staff of the Department of Mechanical Engineering at the University of Alberta who have assisted with various aspects of the work. I also recognize and appreciate the lifelong influence of my parents as well as my friends and colleagues who have offered encouragement and fruitful discussions throughout this study. I would like to record my thanks to Cassie Genoe and Garret Meijer for editing this thesis.

Finally, I would like to thank NOVA Research for providing the financial and technical assistance, which made this study possible.

Table of Contents

Page

Chapter 1: Introduction to Polymeric Composite Pipe 1

1.1 INTRODUCTION 1
1.2 COMPOSITE PIPELINES IN CANADA 3
1.3 FIBERGLASS PIPELINE IN SERVICE 3
1.4 PIPELINE LOADING 4
  1.4.1 PIPELINE CONSTRUCTION LOADS 4
  1.4.2 PIPELINE OPERATION LOADS 5
1.5 EXPERIMENTAL APPROACH 5
  1.5.1 MONOTONIC TESTING OF FIBERGLASS PIPE 6
  1.5.2 FATIGUE TESTING OF FIBERGLASS PIPE 6
1.6 EXPERIMENTAL BACKGROUND 8
  1.6.1 BI-DIRECTIONAL LAY-UP OF FIBERGLASS PIPE 9
  1.6.2 MULTI-DIRECTIONAL LAY-UPS OF FIBERGLASS PIPE 10
1.7 SCOPE OF THE CURRENT INVESTIGATION 11

Chapter 2: Multidirectional Composite Pipe 18

2.1 INTRODUCTION 18
2.2 MANUFACTURING VARIABLES 19
2.3 PRESENT FILAMENT WOUND PIPE 20
2.4 MATRIX BURN OFF 21
  2.4.1 PROCEDURE FOR MATRIX BURN OFF 21
  2.4.2 VOLUME FRACTION 22
  2.4.3 FIBER LAY-UP 22
2.5 IMPERFECTIONS 22
  2.5.1 FIBER MISALIGNMENT 23
  2.5.2 FIBER WAVINESS 23

Table of Contents

Page

2.5.3 RESIN RICH REGIONS 24
2.5.4 PARTIAL LAYERS 24
2.5.5 VOIDS (POROSITY) 24
2.6 DIMENSIONS 25
2.7 GLOBALLY APPLIED STRESSES 26
2.8 SUMMARY 27

Chapter 3: Testing Apparatus 44

3.1 INTRODUCTION 44
3.2 THE MTS BIAXIAL TESTING MACHINE 45
3.2.1 CRITICAL EVALUATION 47
3.2.1.1 DATA ACQUISITION 47
3.2.1.2 AXIAL LOAD 48
3.2.1.3 INTERNAL PRESSURE 49
3.2.1.4 STRAIN 49
3.2.1.5 OIL VOLUME 51
3.2.1.6 STROKE 51
3.3 GRIPPING SYSTEM 52
3.3.1 CRITICAL EVALUATION 54
3.3.1.1 FLUID CONTAINMENT 54
3.3.1.2 RADIAL LOADING 55
3.3.2 CONTINUING EVOLUTION 56
3.3.2.1 FLUID CONTAINMENT 56
3.3.2.2 RADIAL LOADING 57
3.3.2.3 SPECIMEN PREPARATION 58
3.4 SUMMARY 59

Table of Contents

Page

Chapter 4: Leakage Failure Point 74

4.1 INTRODUCTION 74
4.2 LEAKAGE FAILURE 75
4.3 LEAKAGE CURVES 76
  4.3.1 THE SPECIMEN EXPANSION VOLUME 76
  4.3.2 COMPRESSIBILITY 78
    4.3.2.1 HYDRAULIC FLUID COMPRESSION 79
    4.3.2.2 AERATION 80
  4.3.3 TUBE EXPANSION 83
4.4 LEAKAGE 84
4.5 CORRECTION CONSIDERATIONS 85
4.6 FAILURE POINT 86
4.7 SUMMARY 87

Chapter 5: Monotonic Testing 95

5.1 INTRODUCTION 95
5.2 TESTING PROCEDURE 95
5.3 TEST RESULTS 97
  5.3.1 STRESS-STRAIN OBSERVATIONS 97
  5.3.2 STRAIN-STRAIN / OIL VOLUME OBSERVATIONS 99
  5.3.3 MONOTONIC BIAXIAL FAILURE ENVELOPES 101
  5.3.4 MACRO FAILURE OBSERVATIONS 102
  5.2.5 MICRO DAMAGE OBSERVATIONS 103
5.4 INTERPRETATION OF DATA 104
  5.4.1 LINEAR ELASTIC BEHAVIOR 104
  5.4.2 POISSON'S RATIO BEHAVIOR 105

Table of Contents

Page

5.4.3 LEAKAGE BEHAVIOR 106
5.4.4 DISCUSSION OF THE FAILURE ENVELOPES 107
5.4.5 MACRO AND MICRO BEHAVIOR 107
5.5 CONCLUDING REMARKS 108

Chapter 6: Fatigue Testing 142

6.1 INTRODUCTION 142
6.2 TESTING PROCEDURE 142
6.3 PROCEDURES FOR TEST RESULTS 144
6.3.1 STRESS-STRAIN RESPONSE 144
6.3.2 LEAKAGE CURVES 145
6.4 TEST RESULTS 145
6.4.1 STRESS-STRAIN RESPONSE 146
6.4.2 LEAKAGE CURVES 147
6.4.3 FATIGUE LIFE CURVES 149
6.4.4 FATIGUE BIAXIAL FAILURE ENVELOPES 150
6.4.5 OBSERVATIONS OF MACRO DAMAGE 151
6.4.6 OBSERVATIONS OF MICRO DAMAGE PART I 153
6.4.7 OBSERVATIONS OF MICRO DAMAGE PART II 155
6.5 INTERPRETATION OF DATA 157
6.5.1 STRESS-STRAIN BEHAVIOR 157
6.5.2 LEAKAGE BEHAVIOR 159
6.5.3 FATIGUE LEAKAGE LIFE 160
6.5.4 FATIGUE LEAKAGE LIFE ENVELOPE 161
6.5.5 MACRO AND MICRO BEHAVIOR 161
6.5.6 TEMPERATURE BEHAVIOR 164
6.6 FATIGUE AND MONOTONIC RESULTS 165
6.7 CONCLUDING REMARKS 165

Table of Contents

Page

Chapter 7: Conclusions 217

7.1 INTRODUCTION 217
7.2 MONOTONIC LOADING 218
7.3 FATIGUE LOADING 220

Bibliography 224

Appendix A: Netting Analysis 233

A.0 NOMENCLATURE 233
A.1 INTRODUCTION 233
A.2 NETTING ANALYSIS 234
A.3 FIBER STRENGTH 236
A.4 FIBER FAILURE ENVELOPE 237
A.5 BIBLIOGRAPHY 240

Appendix B: Stress and Load Calculations 244

B.0 NOMENCLATURE 244
B.1 INTRODUCTION 245
B.2 CALCULATING GLOBALLY APPLIED STRESSES 245
B.3 EQUATION FOR TUBULAR TESTING 246
B.4 CASE SCENARIOS FOR APPLYING STRESS RATIO 249
B.5 BIBLIOGRAPHY 250

Table of Contents

Page

Appendix C: Specimen Expansion Volume 251

C.0 NOMENCLATURE 251
C.1 INTRODUCTION 251
C.2 MAXIMUM EXPANDED VOLUME 252
C.3 EXPANDED VOLUME 253
C.4 ASSUMPTIONS 257
C.5 VALIDITY 258
C.5 BIBLIOGRAPHY 258

Appendix D: Pressure Vessel Loading Stress Ratio 264

D.0 NOMENCLATURE 264
D.1 INTRODUCTION 264
D.2 DERIVATION OF STRESS RATIO 265
D.5 BIBLIOGRAPHY 268

Appendix E: Fatigue Conversion Source Code 269

E1 INTRODUCTION 269
E.2 C SOURCE CODE 269

List of Tables

Page

Table 3-1: Summary of Data Acquisition System 61

Table 5-1: Loading Rate with Corresponding Reference Figures and Failure Modes. 110

Table 5-2: End of Linearly on the Hoop Stress/Strain Curve 111

Table 5-3: End of Linearly on the Axial Stress/Strain Curve 112

Table 5-4: End of Linearly on the Hoop Strain/Axial Strain Curve 113

Table 5-5: Initiation Point of Leakage 114

Table 5-6: Initiation Point of Intense Leakage 115

Table 5-7: Final Test Point 116

Table 6-1: Fatigue Tests with Corresponding Reference Figures. 167

Table 6-2: Summary of Tests Results for the Applied 0H:1A Stress Ratio 168

Table 6-3: Summary of Tests Results for the Applied 2.5H:1A Stress Ratio 169

Table 6-4: Summary of Tests Results for the Applied 1H:0A Stress Ratio 170

List of Figures

Page

Figure 1-1: Illustration of critically combined loading conditions applied to a composite pipe from the surroundings during construction and operation. Where σ_a is the axial stress and σ_h is the hoop stress. 14

Figure 1-2: Graphical illustration of the S-N curve based on steel. Shows the characteristic fatigue life performance of a material. 15

Figure 1-3: Graphical illustration of the ASTM Strandard D2143 / D2992 Procedure A Test for determining the long-term strength of filament wound composite pipe. 16

Figure 1-4: Illustration of a multidirectional lay-up for a composite pipe to with stand the high internal pressures and axial loading due to bending. This lay-up considers having a number of layers of glass fiber wrapped in the hoop direction to accounting for the internal pressure. In addition, layers in the axial direction account for axial loading. 17

Figure 2-1: The principle stages of the filament winding process, figure adapted form Tarnopol'ski & Beil' (1983). 29

Figure 2-2: The resulting lay-up sequence determined when the matrix was burnt off. 30

Figure 2-3: Plot of the angle measured for each ply after the matrix was burnt off. 31

List of Figures

Page

Figure 2-4: Photo of the cross-section of the fiberglass pipe under investigation. Illustrates fiber distortion and resin rich areas. This cross-section will be further observed in Figures 2-5, 2-6, 2-8a, 2-8b, 2-9a, and 2-9b. 32

Figure 2-5: A magnified view showing half of the cross-section of the fiberglass pipe under investigation. Illustrates fiber waviness and resin richness. 33

Figure 2-6: A magnified view showing a section of the fiberglass pipe under investigation. Illustrates fiber waviness and resin richness. 34

Figure 2-7: Resulting lay-up sequence developed from the burning off the matrix. Illustrates partial layers of fiberglass and added partial layers. 35

Figure 2-8a: A segment of the cross-section of the pipe, seen in Figure 2-4, magnified 40x. Illustrated are the voids (dark areas) and resin rich areas (white areas). 36

Figure 2-8b: A segment of the cross-section of the pipe, seen in Figure 2-4, magnified 440x, note the excess resin (white areas) between the layers. 37

Figure 2-9a: A segment of the cross-section of the pipe, seen in Figure 2-4, magnified 40x. Illustrate are the voids (dark areas), resin rich areas (white areas) and fiber distortion in the 0° layer. 38

Figure 2-9b: A segment of the cross-section of the pipe, seen in Figure 2-4, magnified 440x, note the excess resin (white areas) between the layers. 39

List of Figures

Page

Figure 2-10: Polar plot of the inner pipe surface, illustrates the small variation in roundness. Note the scale on the left. 40

Figure 2-11: Polar plot of the outer pipe surface, illustrates a large variation in roundness. Note the scale on the left. 41

Figure 2-12: Polar plot of both the inner and outer pipe surface, illustrates the change in thickness. 42

Figure 2-13: Geometry of the composite pipe used in determining the applied stresses. Where t_i is one of eight points used to calculated t_{mean} and r_{mean}. 43

Figure 3-1: Schematic of the testing apparatus setup for both monotonic and fatigue testing of fiberglass epoxy pipe, figure adapted form Carroll (1994). 62

Figure 3-2: A photograph of the biaxial testing machine. On the right the pressurization system developed in-house. On the left a specimen placed in the redeveloped gripping system. 63

Figure 3-3: A photograph of the MTS axial load and the pressurization controllers, along with the data acquisition system. 64

Figure 3-4: A photograph of the pressurization system developed in-house. 65

Figure 3-5: A photograph of the hoop extensometer developed in-house. 66

List of Figures

Page

Figure 3-6: A photograph of the axial extensometer developed in-house. 67

Figure 3-7: A photograph of the disassembled mandrel used to centering the specimen for indexing and machining. 68

Figure 3-8: A photograph of a specimen mounted in the centering mandrel, places in an indexing dividing head. This device is used to mark surface lines parallel to the centerline for aligning the hoop and axial extensometer and strain gauges. 69

Figure 3-9: Schematic illustration of the grip assembly developed by Carroll (1994), figure adapted from Carroll (1994). 70

Figure 3-10: Schematic illustration of the redesigned grip assembly. 71

Figure 3-11: A photograph of the partially disassembled and assembled grip assembly. 72

Figure 3-12: A photograph of two specimens with end reinforcement after being potted in ColdCure Epoxy, showing before (left) and after (right) of machining. 73

Figure 4-1: A plot of the change in fluid volume measured from the pressure intensifier verses the internal pressure, a monotonic test. 89

Figure 4-2: Plot of the decreasing fluid volume with increasing pressure. Determined from pressurization of the intensifier used to calculate the compressibility coefficient. 90

List of Figures

Page

Figure 4-3: A plot of the change in fluid volume measured from the pressure intensifier verses the internal pressure compared with the change in volume for air calculated from the Ideal Gas Law. 91

Figure 4-4: Plot of the correcting change in volume verses pressure for the added volume of air, oil compression, and specimen expansion. 92

Figure 4-5: Plot of the change in volume corrected for the added volume of air, oil compression, and specimen expansion, for a monotonic test. 93

Figure 4-6: A plot of the change in fluid volume corrected verses the internal pressure. Note the initiation point of leakage and the initiation point for intense leakage (knee point). 94

Figure 5-1: The applied axial stress with the corresponding surface strains for the 0H:1A stress ratio. The measured axial stiffness is 21.6 GPa. 117

Figure 5-2a: The applied axial stress with the corresponding surface strains for the 1H:1A stress ratio. 118

Figure 5-2b: The applied hoop stress with the corresponding surface strains for the 1H:1A stress ratio. 119

Figure 5-3a: The applied axial stress with the corresponding surface strain for the 2H:1A stress ratio. 120

List of Figures

Page

Figure 5-3b: The applied hoop stress with the corresponding surface strain for the 2H:1A stress ratio. 121

Figure 5-4: The applied axial stress with the corresponding surface strain for the 1H:0A stress ratio. The measured axial stiffness is 37.7 GPa. 122

Figure 5-5a: The applied axial stress with the corresponding surface strains for the 1H:-1A stress ratio. 123

Figure 5-5b: The applied hoop stress with the corresponding surface strains for the 1H:-1A stress ratio. 124

Figure 5-6: The applied axial stress with the corresponding surface strains for the 0H:-1A stress ratio. 125

Figure 5-7: The axial surface strain with the corresponding hoop surface strain and corrected leakage curve for 0H:1A stress ratio. The measured axial to hoop Poisson's ratio is 0.244. 126

Figure 5-8: The axial surface strain with the corresponding hoop surface strain and corrected leakage curve for 1H:1A stress ratio. 127

Figure 5-9: The axial surface strain with the corresponding hoop surface strain and corrected leakage curve for 2H:1A stress ratio. 128

Figure 5-10: The axial surface strain with the corresponding hoop surface strain and corrected leakage curve for 1H:0A stress ratio. The measured hoop to axial Poisson's ratio is 0.326. 129

List of Figures

Page

Figure 5-11: The axial surface strain with the corresponding hoop surface strain and corrected leakage curve for 1H:-1A 130

Figure 5-12: The axial surface strain with the corresponding hoop surface strain and corrected leakage curve for 0H:-1A 131

Figure 5-13: The monotonic biaxial failure envelopes illustrated in stress space. Observe the position of the linear limit points in comparison to the leakage. 132

Figure 5-14: The monotonic biaxial failure envelopes illustrated in strain space. Observe the position of the linear limit points in comparison to the leakage. 133

Figure 5-15: Structural failure observed for the 0H:1A applied stress ratio. Once structural failure occurred, the 0^0 plies fractured, the specimen twisted fracturing the ± 66^0 plies. 134

Figure 5-16: Uniform matrix cracking observed parallel to the $\pm 66^0$ plies for the 1H:1A applied stress ratio. 135

Figure 5-17: Matrix cracking and delamination observed for the 2H:1A stress ratio. The matrix cracking was not uniform. 136

Figure 5-18: Structural crushing failure observed for the 0H:-1A stress ratio. 137

Figure 5-19: A photograph taken of the cross section of the observed structural failure for the 0H:1A stress ratio. Due to the visibility of the damage area a photograph was taken near the end of the damage zone. 138

List of Figures

Page

Figure 5-20: A micrograph taken of the observed uniform matrix cracking for the 1H:1A stress ratio magnified 40x. Observe the cracks, which extend through the 0^0 ply into the $\pm 66^0$ plies. 139

Figure 5-21: A micrograph taken of the observed matrix cracking and delamination for the 2H:1A stress ratio magnified 40x. Observe the inter-ply cracks, which extend through the 0^0 ply. 140

Figure 5-22: A photograph taken of the cross section of the observed structural failure for the 0H:-1A stress ratio. Due to the visibility of the damage area a photograph was taken near the end of the damage zone. 141

Figure 6-1: Illustration of the secant stress-strain behavior during a single fatigue cyclic. The secant stiffness was determined by linear regression fit through the stress-strain data. 171

Figure 6-2: Recorded applied axial stress verses axial surface strain response of the composite pipe under investigation with a 0H:1A stress ratio, note the change in slope with loading cycle. 172

Figure 6-3: Secant modulus and stress intercept curves for the 0H:1A stress ratio the corresponding applied stress-strain response was presented in Figure 6-2. This test had a maximum axial stress level of 117.4 MPa (17000 psi). 173

Figure 6-4: Secant modulus and stress intercept curves with a 0H:1A stress ratio. The corresponding maximum axial stress level is 78.01 MPa (11310 psi). Note the waviness in the axial secant modulus and stress intercept is due to temperature interference. 174

List of Figures

Page

Figure 6-5: Secant modulus and stress intercept curves with a 2.5H:1A stress ratio. The corresponding maximum hoop stress level is 127.4 MPa (18481 psi) and the maximum axial stress level is 49.8 MPa (7227 psi). Note the debonding and slipping of the transverse extensometer occurred at approximately 2700 cycles. 175

Figure 6-6: Secant modulus and stress intercept curves with a 2.5H:1A stress ratio. The corresponding maximum hoop stress level is 103.3 MPa (14978 psi) and maximum axial stress is 41.3 MPa (5991 psi). Note the debonding and slipping of the transverse extensometer occurred at approximately 58000 cycles. 176

Figure 6-7: Secant modulus and stress intercept curves with a 1H:0A stress ratio. The corresponding maximum hoop stress level of 142.2 MPa (120637 psi). Note the debonding and slipping of the transverse extensometer occurred at approximately 32000 cycles. 177

Figure 6-8: Secant modulus and stress intercept curves with a 1H:0A stress ratio. The corresponding maximum hoop stress level is 118.9 MPa (17248 psi). Note the debonding and slipping of the transverse extensometer occurred at approximately 70000 cycles. 178

Figure 6-9 (a-e): Leakage verses the number of cycles for the 0H:1A stress ratio in descending order from the highest axial stress to the lowest. 179

Figure 6-9 (a-e)(con't): Leakage verses the number of cycles for the 0H:1A stress ratio in descending order from the highest axial stress to the lowest. 180

List of Figures

Page

Figure 6-10 (a-g): Leakage verses the number of cycles for the 2.5H:1A stress ratio in descending order from the highest equivalent stress to the lowest. 181

Figure 6-10 (a-g)(con't): Leakage verses the number of cycles for the 2.5H:1A stress ratio in descending order from the highest equivalent stress to the lowest. 182

Figure 6-10 (a-g) (con't): Leakage verses the number of cycles for the 2.5H:1A stress ratio in descending order from the highest equivalent stress to the lowest. 183

Figure 6-11 (a-e): Leakage verses the number of cycles for the 1H:0A stress ratio in descending order from the highest hoop stress to the lowest. Note intensifier leakage is suspected in Figure 6.11 (d-e) 184

Figure 6-11 (a-e)(con't): Leakage verses the number of cycles for the 1H:0A stress ratio in descending order from the highest hoop stress to the lowest. Note intensifier leakage is suspected in Figure 6.11 (d-e) 185

Figure 6-12: Applied maximum axial stress verses cycles to leakage in Log scale for the 0H:1A stress ratio 186

Figure 6-13: Applied maximum equivalent stress verses cycles to leakage in Log scale for the 2.5H:1A stress ratio 187

Figure 6-14: Applied maximum hoop stress verses cycles to leakage in Log scale for the 1H:0A stress ratio. 188

List of Figures

Page

Figure 6-15: The biaxial fatigue leakage envelope illustrating the characteristic cyclic behavior of this multidirectional lay-up composite pipe for very short-term (10^3) to long-term (10^6) leakage. The monotonic leakage envelop is also included for comparison. 189

Figure 6-16: Photograph of the observed macro damage for the 0H:1A stress ratio with the corresponding maximum cyclic axial stress of 91.38 MPa (13250 psi). Note the uniform matrix cracking. 190

Figure 6-17: Photograph of the observed macro damage for the 0H:1A stress ratio with the corresponding maximum cyclic axial stress of 79.04 MPa (11460 psi). Note the uniform matrix cracking. 191

Figure 6-18: Photograph of the observed macro damage for the 2.5H:1A stress ratio with the corresponding maximum cyclic hoop stress of 127.42 MPa (18480 psi). Note the combined matrix cracking and delamination of the pipe. 192

Figure 6-19: Photograph of the observed macro damage for the 2.5H:1A stress ratio with the corresponding maximum cyclic hoop stress of 103.27 MPa (14980 psi). Note the matrix cracking parallel to the ± 66° fibers. 193

Figure 6-20: Photograph of the observed macro damage for the 2.5H:1A stress ratio with the corresponding maximum cyclic hoop stress of 103.27 MPa (14980 psi). This is a different specimen then the one presented in figure 6.19. Note the change in the failure mode to delamination leading to pin hole bursting. 194

List of Figures

Page

Figure 6-21: Photograph of the observed macro damage for the 1H:0A stress ratio with the corresponding maximum cyclic hoop stress of 219.11 MPa (31780 psi). Note uniform type of matrix cracking parallel to the ± 66^0 fibers, similar to the failure mode initially seen in the 0H:1A stress ratio. 195

Figure 6-22: Photograph of the observed macro damage for the 1H:0A stress ratio with the corresponding maximum cyclic hoop stress of 166.7 MPa (24180 psi). Note delamination giving way to pin hole bursting. 196

Figure 6-23: Photograph of the observed macro damage for the 1H:0A stress ratio with the corresponding maximum cyclic hoop stress of 142.28 MPa (20640 psi). Note delamination and matrix cracking can be seen giving way to pin hole bursting. As well a small amount of matrix cracking can also be seen in the 0^{0}fiber layer. 197

Figure 6-24: Photograph of the observed macro damage for the 1H:0A stress ratio with the corresponding maximum cyclic hoop stress of 118.92 MPa (17250 psi). Note only a spot of delamination giving way to pin hole bursting. 198

Figure 6-25: Photograph of the observed macro damage for the 1H:0A stress ratio with the corresponding maximum cyclic hoop stress of 118.92 MPa (17250 psi). This is the same specimen presented in figure 6.24, with a different orientation. Note the matrix cracking in, both the 0^0 and the ± 66^0 fiber layer as well as delamination occurring in the 0^{0}fiber layer. 199

List of Figures

Page

Figure 6-26: A micrograph taken of the observed uniform matrix cracking of the 0H:1A stress ratio magnified 40x. Observe the cracks in the ±66° plies. 200

Figure 6-27: A micrograph taken of the observed matrix cracking and delamination section seen in Figure 6.18 of the 2.5H:1A stress ratio magnified 40x. Observe the cracks in the 0° ply. 201

Figure 6-28: A micrograph taken of the observed matrix cracking and delamination section seen in Figure 6.20 of the 2.5H:1A stress ratio magnified 40x. Observe the cracks in the 0° ply extending into the ± 66° plies. 202

Figure 6-29: A micrograph taken of the observed matrix cracking and delamination section seen in Figure 6.20 of the 2.5H:1A stress ratio magnified 40x. Observe the cracks in the 0° ply extending into the ± 66° plies. 203

Figure 6-30: A micrograph taken of the observed uniform matrix cracking section seen in Figure 6.21 of the 1H:0A stress ratio magnified 40x. Observe the extensive cracking in both the 0° ply and the ± 66° plies. 204

Figure 6-31: A micrograph taken of the observed matrix cracking and delamination section seen in Figure 6.23 of the 1H:0A stress ratio magnified 40x. Observe the extensive cracking in both the 0° ply and the ± 66° plies. 205

List of Figures

Page

Figure 6-32: A micrograph taken of the observed matrix cracking and delamination section seen in Figure 6.25 of the 1H:0A stress ratio magnified 40x. Observe the extensive cracking in both the 0^0 ply and the $\pm 66^0$ plies. 206

Figure 6-33: A micrograph taken of the observed cracking in a large resin rich area in the 0^0 ply, magnified 40x, note how the inter-ply and interface cracking seams to be confined to this one area. 207

Figure 6-34: A micrograph, magnified 40x, taken of the observed cracking through two large voids in the 0^0 ply, note the over sized voids compared to the rest of the void population. 208

Figure 6-35: A photograph of the observed matrix cracking for the 0H:1A stress ratio, corresponding to Figure 6-17. The top photograph is taken under ultra violate light to observe cracking, the bottom is to compare damaged zones with imperfections. 209

Figure 6-36: A photograph of the observed matrix cracking for the 2.5H:1A stress ratio, corresponding to Figure 6-18. The top photograph is taken under ultra violate light to observe cracking, the bottom is to compare damaged zones with imperfections. 210

Figure 6-37: A photograph of the observed matrix cracking for the 2.5H:1A stress ratio, corresponding to Figure 6-20. The top photograph taken under ultra violate light to observe cracking, the bottom is to compare damaged zones with imperfections. 211

List of Figures

Page

Figure 6-38: A photograph of the observed matrix cracking for the 1H:0A stress ratio, corresponding to Figure 6-21. The top photograph is taken under ultra violate light to observe cracking, the bottom is to compare damaged zones with imperfections. 212

Figure 6-39: A photograph of the observed matrix cracking for the 1H:0A stress ratio, corresponding to Figure 6-23. The top photograph is taken under ultra violate light to observe cracking, the bottom is to compare damaged zones with imperfections. 213

Figure 6-40: A photograph of the observed matrix cracking for the 1H:0A stress ratio, corresponding to Figure 6-25. The top photograph is taken under ultra violate light to observe cracking, the bottom is to compare damaged zones with imperfections. 214

Figure 6-41: The key monotonic data points superimposed on the biaxial fatigue life envelope. 215

Figure 6-42: The linear limit strain-strain and the leakage failure points found from monotonic testing are superimposed on to biaxial fatigue life envelope. Note the relative position of the linear limit for strain-strain and the shot term fatigue leakage life (10^4 cycles). 216

Figure A-1: Orientation of the membrane loads, N_θ and N_ϕ, for the composite pipe, figure adapted form Tew (1995). 241

Figure A-2: Free-body diagrams of the fibers oriented in circumferential (θ) and longitudinal (ϕ) directions, figure adapted form Tew (1995). 242

List of Figures

Page

Figure A-3: The fiber failure envelope based on netting analysis for the pipe lay-up under investigation in this thesis. Note complete structural failure with an axial applied load occurred at an axial stress of 184.049 MPa. Failure in the hoop direction was not attainable under internal pressure loading. 243

Figure C-1: Layout of the expanded specimen assuming a uniform radial expansion through the specimen length. 259

Figure C-2: Layout of the expanded specimen accounting for radial expansion through the specimen length. 260

Figure C-3: An illustration of the loaded pipe specimen with fix end conditions. 261

Figure C-4: A plot of the expanded shape, of the loaded pipe specimen with fix end conditions, approximated from Thin Wall Theory. 262

Figure C-5: A plot of the fluid volume for a fatigue cyclic. Shows the corrections applied to the volume change of the intensifier by specimen expansion and oil compression to obtain the overall volume expansion. 263

CHAPTER 1

INTRODUCTION TO POLYMERIC COMPOSITE PIPE

1.1 INTRODUCTION

The corrosion resistance and the high strength-to-weight ratio benefits of polymeric composites over steels have been discussed extensively in literature [15, 17, 19, 22, 37, 39, 40, 46, 51, 56, 70, 81, 83, 86, 101]. The greatest benefit of polymeric composites to the chemical, petroleum and processing industries is the reduction in the capital cost of projects and operating expenses [37].

The cost of corrosion can be as high as 4.9% of the gross national product of an industrialized nation, such as Canada [6]. This corrosion cost is a significant driving force for industries to use polymeric composites as a cost-effective alternative to specialty steels, in terms of capital and maintenance costs. Therefore, it is compelling to obtain a comprehensive understanding of the limitations of polymeric composites.

Polymeric composites offer many cost advantages over steel due to a considerably higher strength-to-weight ratio. For example, an increase in the ease of handling decreases the amount of manpower and size of equipment needed for construction and installation on projects. The cost saving in transportation must also be emphasized. Down-hole steel tubing, which is a requirement in the recovery of oil in Alberta, has an estimated weight 62% greater then that of a polymeric composite down-hole tubing of similar function. The above is based on a 60.3 mm (2-3/8 in) diameter down-hole tubing manufactured by Fiber Glass Systems Inc. under the trade name STAR®. Therefore, use of polymeric composite down-hole tubing would have a considerable effect on reducing the shipping costs. Thus, the limiting factor in transporting pipes shifts from weight for steel to volume for composites, thereby decreasing the transportation cost. This cost saving also occurs in accessing remote locations as well as offshore applications [37].

Polymeric composites offer another cost advantage over steels because of its excellent hydraulic characteristic (i.e. smoothness of the internal surface of the pipe). For example, the increased smoothness of composite pipe at 0.762 μm (30 μin) from that of a type commercial steel pipe at 8.89 μm (350 μin) translates approximately into a 20% reduction in the friction factor [102]. The percent reduction in the friction factor is approximately the same percent reduction in compressor power (i.e. fuel consumption). With 22000 km (13,670 miles) of installed pipe in Alberta for gas transmission by NOVA with an associated 887 MW (1,189,486 HP) of installed compressor power, the above translates into a $10 million savings annually [102]. (The assumed cost of natural gas was $1.75/GJ ($0.18/TBTU))

There is some reluctance in certain industries to convert to polymeric composites as a partial or complete replacement material of metals in their high load operations, mainly because of the lack of infrastructure and unproven record of accomplishment. An infrastructure, which consists of designers and contractors for polymeric composite material, is necessary to develop a proven record of accomplishment to take full advantage of the added benefits. The lack of infrastructure is partly due to an insufficient understanding of the fundamental knowledge of design, working life, and failures (i.e. a generally accepted comfort level). In contrast, steels have many years of an accomplished track record, solid design principals, and the full infrastructure.

The one added advantage of polymeric composites over steel is the lack of required hot work (i.e. welding). This increases safety by decreasing the chances of accidents and incidences due to hot work. However, this added advantage, which is beneficial in offshore applications where hot work can be dangerous, is in conflict with the mandate of and therefore opposed by some unions (i.e. the weld's unions)[45].

1.2 COMPOSITE PIPELINES IN CANADA

The polymeric composite piping industry grew from U.S. Government Research Grants issued during World War II to search for viable alternatives to exotic metals, which were in short supply [52]. Research conducted by the U.S. Navy during the 1950's revealed the ability of a composite pipe to resist erosion, fouling of marine organisms, and chemical attack. During the late 50's and early 60's oil companies in North America seriously considered implementing fiberglass pipelines, to take advantage of its corrosion capabilities [52].

The first fiberglass pipeline in Canada was installed by Dowell of Canada as a low-pressure line and implemented in 1961[103]. Initially fiberglass pipelines were not well accepted because of the low comfort level with the new material and the skeptical public and oil industry. Potential customers were hesitant, at this point to implement any fiberglass pipelines because of the high overhead costs required for experimental testing. Nevertheless, as knowledge and comfort levels improved, general acceptance of fiberglass pipelines increased in the oil industry. It was not until the 1980's that the western Canadian fiberglass pipeline market proceeded into high-pressure pipeline applications [103]. This market was initially limited to small diameter injection lines. Today, there are countless miles of fiberglass feeder lines in service throughout Western Canada, with some lines dating back 25 years [103].

1.3 FIBERGLASS PIPELINE IN SERVICE

Currently there is little published material on the long-term effects of functional and environmental conditions on composite pipelines. A literature review revealed only one paper researching the effects of oil field flow line in low-pressure service on an unlined epoxy fiberglass pipeline over a 25-year period [70].

Oswall (1996) presented the results of research conducted by a composite pipeline manufacturer and the end user of the pipeline to determine the overall long-term corrosion effects on an oil flow line in service [70]. An unlined 2-inch diameter epoxy fiberglass pipeline, with a 300-psi cyclic pressure rating, had been in continuous service since 1962 handling sour crude oil, saltwater and natural gas at 40 to 60 psi. Specimens were removed from the line every five years to conduct strength and fatigue tests. After 15 years there was a small loss of strength as seen from fatigue and monotonic testing [70]. After 25 years of service, Oswall (1996) concluded that resin degradation was evident as seen by a change in the resin properties as well as the mode of failure, from matrix cracking causing weepage failure to catastrophic matrix fracturing [70]. However, it was concluded that the pipeline could have seen many more years of service before being taken out of commission [70].

1.4 PIPELINE LOADS

The loading on a pipeline is a combined function of the applied load from the surroundings and from operating, as observed in Figure 1-1. These loads have been further divided into two sections: (1) the loads applied during construction and (2) those applied during operations.

1.4.1 PIPELINE CONSTRUCTION LOADS

During construction it is difficult to determine all types of field loading conditions. However, it is possible to design the pipeline to withstand a predetermined maximum loading condition. Construction loading is typically a once in a lifetime occurrence for the pipeline [67]. Therefore, monotonic testing can be used to determine the maximum installation loads the line can endure. Typically these loads are not of one type but a combination of different loading types [67]. Some types of loading that should be accounted for during construction and combinations thereof are as follows:

- Self-Weight: the weight of the pipeline with contents and added attachments.
- Internal and External Pressures: internal test pressures and soil loads.

- Point Forces: the added stresses of lowering the pipeline into the ditch, impact loading and point loading due to back filling onto the line.

1.4.2 PIPELINE OPERATIONAL LOADS

Operational loading of a pipeline typically consists of cyclic internal pressure involving a high frequency of small pressure fluctuations about a high mean pressure developed from the compressor or pump with the occasional large change in pressure, with line shut down for servicing [67]. The pipeline also can receive axial loading caused by an applied bending moment, which may be a function of the internal pressure loading, ground movement and thermal expansion [67]. Some of the types of loading that should be accounted for during operation of the pipeline are as follows:

- Self-Weight: the weight of the pipeline with contents and added attachments spanning unsupported sections of pipe.
- Pressures: the maximum internal cyclic pressure, external hydrostatic pressures and soil loads.
- Temperature: thermal effects causing expansion and contraction.
- Point and Distributed Forces: the added stress from anchoring

1.5 EXPERIMENTAL APPROACH

The important mechanical properties of a composite pipe are strength, stiffness, and service life, which are imperative to determine the leakage integrity and reliability of the pipeline. Experimental development of the biaxial monotonic leakage envelope and the biaxial fatigue leakage life envelope is required to characterize the integrity and the reliability of the composite pipe under installation and operational loads. The failure envelopes give a comprehensive understanding of the limitations in terms of leakage, ultimate failure and the maximum design loads. At least three main stress ratios (ratio of applied hoop stress to applied axial stress) are required to outline the failure envelopes:

e.g. (1) pure axial stress (0H:1A), (2) pure hoop stress (1H:0A) and (3) a pressure vessel stress ratio (the hoop stress being twice the axial stress, 2H:1A).

1.5.1 MONOTONIC TESTING OF FIBERGLASS PIPE

To determine the ultimate load that the composite pipe could endure under possible service condition, biaxial monotonic envelopes are developed under stress control (i.e. load control). This conventional approach, described by Carroll (1994), is used to determine structural strength and stiffness at specific hoop to axial stress ratios, maintaining an equivalent stress loading rate [8].

Carroll (1994) focused an experimental investigation into the biaxial monotonic characteristics under varying rates of loading for a commercially manufactured multidirectional composite pipe (with a $[+55^0/-55^0]_3$ lay-up and a $[\pm 45_5, 0, -70, \pm 45_2, \pm 70]$ lay-up) [8]. Tests were conducted at two loading rates, one a 100 times greater than the other, over the positive quadrant of the biaxial stress ratio. Carroll (1994) discovered that there was approximately a 10 % increase in the ultimate failure stresses. This was apparent in both hoop and axial directions for all the tested stress ratios [8]. The axial linear elastic modulus seemed to be slightly affected by the stress rate, but no apparent affect was noted in the hoop modulus. Thus, pointing out that loading rate has little effect on determining the mechanical properties of the multidirectional composite pipe, and suggesting that the effect of equivalent stress loading rate within the bounds of test values were not significant.

1.5.2 FATIGUE TESTING OF FIBERGLASS PIPE

To determine the leakage life that the composite pipe could attain, the fatigue leakage life envelope has to be developed under stress control at specific hoop to axial stress ratios. The biaxial fatigue leakage life envelope is required to characterize the reliability of the composite pipe under operational cyclic loads.

The conventional approach for determining the fatigue life involves determining the S-N curves at specific hoop to axial stress ratios, where S is the stress amplitude and N_f is the number of cycles to failure [16]. An illustration of an S-N curve is depicted in Figure 1-2. The general characteristic of fatigue resistance is in terms of cycles to failure, which decreases with increasing stress amplitude. The important aspect attainable from the characteristic S-N curve is the fatigue limit σ_{fl} (the stress level of infinite life), the fatigue strength coefficient σ'_f (the extrapolated point of failure after one cycle) and the slope of the S-N curve α. These parameters determine the fatigue performance under applied stress amplitudes. The monotonic failure strength σ_f is the static strength of the material. For steel the extrapolated fatigue strength coefficient σ'_f, is greater or equal to the monotonic tension failure strength σ_f, thus: $\sigma'_f \geq \sigma_f$, the same appears to be true for fibre-reinforced polymeric composites [16].

The procedure for determining the long-term strength of filament wound composite pipe is based on ASTM Standard D2992 [89]. The ASTM standard stipulates cycling the internal hydrostatic pressure at a rate of 25 cycles per minute (frequency of 0.42 Hz) over the full pressure range (i.e. applied pressure ratio $R= P_{min}/P_{max}=0$) [89]. There are two loading conditions: a restrained-end condition (pure hoop stress) and a free-end condition in which the hoop stress is twice the axial stress. A graphical illustration of the loading cycles is shown in Figure 1-3.

However, there is some concern in using the ASTM Standard for experimentally determining the fatigue life of composite pipes [50]. Kujawski et al. (1996) proposed that a composite pipe used in the oil field is subjected to a constant peak pressures at varying R-ratios (i.e. applied pressure ratio $R = P_{min}/P_{max}$) at a higher-cyclic frequency, than the loading conditions defined by the ASTM Standard D2992 [89]. The argument is that the maximum pressure remains relatively constant, but the R-ratio and the cyclic frequency vary depending on the type of pump or compressor used. For example the R-ratio and frequency would be lower for a single action simplex pump than that of a multiplex pump [48]. The present ASTM Standard D2992 required R-ratio (R=0) outlines a worst-case scenario for a pipeline [89]. The internal hydrostatic pressure applied at a rate of 25 cycles per minute (0.42 Hz) is an operational pump jack frequency [48]. This is not intended to be the operating pump or compressor frequency, but is equivalent to restarting the pipeline 25 times a minute [67].

The effect of frequency on glass fibre composite pipe with a $[+55^0/-55^0]_3$ lay-up was studied by Joseph and Perreux (1997) at frequencies of 0.01Hz, 1.0 HZ and 5 Hz [46]. Joseph and Perreux (1997) concluded that frequency plays a complex role that acts on two levels: (1) The material life may not be intrinsic to the specimen as the frequency increases, but the geometrical shape and size are [46]. (2) The interaction between fatigue and creep is dominant. At lower frequencies the loading time was greater, thus the specimen creeped to a greater extent [46].

The inhomogeneity and anisotropy aspect of this material plays an important part in the ability to resist the effects of cyclic loading (i.e. creep, internal damage etc.). A study conducted by Lockett (1980) concluded that the combined anisotropy and wall thickness resulted in inner surface strains 50% greater than that found on the outer surface, with the wall thickness having more of an effect, than the material being anisotropic. Lockett (1980) also found that inhomogeneities caused from manufacturing led to variations in local stiffness, which cause associated bending strains with magnitudes equivalent to the primary strains, thus reducing fatigue life [56].

1.6 EXPERIMENTAL BACKGROUND

Filament wound composite pipe has been the focus of numerous experimental investigations found throughout the literature [18, 19, 22, 23, 39, 40, 46, 50, 52, 56, 70, 81, 83, 84, 86, 101]. The investigations under review have been divided into bi-directional lay-up and multidirectional lay-up. The bi-directional lay-up involves fibre layers being placed into two discrete directions in the same plane. The sequence of stacking is described as $[+\theta/-\theta]_n$ where θ is the orientation of the fibre placements with respect to the pipe axis and n is the number of sequenced layers present. The multidirectional lay-up involves the placement of fibre layers into multiple discrete directions in the same plane. The majority of the experimental investigations found in the literature have focused on the development of mechanical properties of bi-directional thin wall asymmetric and symmetric shells.

1.6.1 BI-DIRECTIONAL LAY-UPS OF FIBERGLASS PIPE

The influence of the winding angle on the biaxial and uniaxial monotonic characteristic of the filament wound composite pipe were the focus of several experimental investigations [39, 40, 67, 81, 83, 84].

Hull et al. (1978, 1979) studied the effect of the wind angle and concluded that the wind angle had a pronounced effect on the associated deformation, weepage and fracture strength. Weepage was governed by transverse cracking which was also associated with areas with a high fibre content [39, 40].

Soden et al. (1978) developed the failure envelopes for $[+35^{0}/-35^{0}]_{n}$ and $[+55^{0}/-55^{0}]_{n}$ glass fibre filament wound composite pipes and was able to predict the predominant load carrying component for the winding angles using netting analysis [81]. (The netting analysis is described in Appendix A.) This method assumes that the fibres will carry the entire load and the maximum strength then occurs at an optimum stress ratio. Soden et al. (1978) concluded that the netting analysis would enable the designer to select the appropriate winding angle based on the applied axial and circumferential stress [81]. However, a fully developed failure envelope is needed to determine the strength under a variety of load conditions.

The failure envelope for the $[+75^{0}/-75^{0}]_{n}$ winding angle was also determined by Soden et al. (1985) and they further investigated the failure envelope for the $[+55^{0}/-55^{0}]_{n}$ winding angle [81, 83]. The above two failure envelopes were reviewed and a failure envelope for the $[+45^{0}/-45^{0}]_{n}$ winding angle was determined in Soden et al. (1993) [86]. A comparison of the failure envelopes indicated, that decreasing the winding angle increases the uniaxial strength in tension. However, the compression strength appeared only to improve slightly. The failures were determined by leakage at stresses which were significantly lower than that of the fracture stresses, the biggest difference between the two was at the stress ratio calculated by the netting analysis and the smallest difference was at pure pressure (pure hoop stress).

Frost (1995) studied the long-term fatigue behavior of a $[+55^0/-55^0]_n$ glass-fibre/epoxy filament wound pipe and concluded that the failure mechanisms for both short and long-term fatigue were weepage from matrix-cracking [22]. The damage found after long-term cyclic tests was notably less than that of the short-term.

This review of the experimental investigation of the bi-directional lay-ups, revealed that a bi-directional lay-up is strong for an intended stress ratio, which can be determined by netting analysis (see Appendix A.). However, outside of the intended stress ratio the lay-up is prone to transverse cracking, thus revealing a weakness. To eliminate the weakness a multidirectional lay-up maybe implemented to reinforce the pipe in other stress ratios, allowing the pipe to be less dependent on the stress ratio.

1.6.2 MULTI-DIRECTIONAL LAY-UPS OF FIBERGLASS PIPE

A multidirectional lay-up is intended to produce a more damage tolerant composite pipe under a range of stress ratios, occurring in a structural loading (i.e. axial bending, etc.). However, there is a lack of experimental investigations focusing on multidirectional lay-ups in the literature [8, 18, 101].

The long-term fatigue behavior of multidirectional fiberglass epoxy pipe was investigated by Ellyin et al. (1995) [18]. The commercially wound lay-up $[\pm 70, \pm 45_2, -70, 0, +45, \pm 45_4]$ was tested at two pressure ratios R = 0.05 and R = 0.3. It was noted that the fatigue life was about four times smaller for R = 0.3 for the same pressure range. Also noted was the fact that there was extensive delamination through the 0^0 layer and transverse cracking of the $[+45^0/-45^0]$ layers.

Wang et al. (1997) investigated the long-term leakage failure of $[\pm 66_2, 0_3, \pm 66_3, 0]$, wound pipe [101]. This lay-up is very similar to the one investigated here, but very few results were presented in the paper. Wang et al. (1997) reported that this lay-up showed a better resistance to leakage under uniaxial loading than in biaxial loading (i.e. pressure vessel type of loading), which leaves a concave surface in the positive quadrant of the leakage envelope. This can be attributed to the high fiber content in the axial and hoop directions.

1.7 SCOPE OF THE CURRENT INVESTIGATION

This research project is focused on an experimental investigation into a multidirectional lay-up to address some of the concerns not yet reported in the published literature.

To meet demands set out by industry for high internal pressures and axial loads with reassured long-term performance, insight is imperative to better understand the behaviour of a multidirectional composite pipe, which can meet these requirements. The multidirectional lay-up of interest in this investigation has a dominant number of plies in the hoop direction to resist the high internal pressure and added layers in the axial direction to account for axial tension or bending (as illustrated in Figure 1-4). This makes it especially strong in both the hoop and axial directions. This particular lay-up was of interest because of its design concept, which causes a large change in the stiffness between plies. There is some concern about producing detrimental shear stresses between plies, which can greatly reduce the fatigue leakage life of a composite pipe. There is some interest, with the addition of fibres in the axial direction, to determine whether it inhibits transverse cracking in the hoop dominated plies under high axial loads or aides in the development of damage with the added imperfections within the axial plies.

In this investigation a commercially wound fiberglass pipe was chosen, because of the added advantages gained from the manufacturer, which include experienced operators, dedicated winding equipment developing a true working product and expected imperfections. The issue of imperfections produced during manufacturing will give an insight into their complexities and their effect on the performance of the pipe with respect to dominant factors controlling failure of this type of lay-up. As well, the imperfections, seen in commercially wound fiberglass pipe, can be used to determine the overall effect of simple design tools used for calculating the fiber failure envelope and the stiffness properties of the multidirectional lay-up (i.e. netting analysis and classical laminate theory).

The underlining function of the composite pipe is to contain a pressurized fluid. However, there is a lack of published information pertaining to leakage failures of composite pipes. Most of the experimental investigations, reported in literature, use the initiation of surface wetting as a failure point determined by either visual inspection or a conductive metal mesh [101]. Since a visual inspection to determine a point of fatigue leakage was not possible because of the duration of the test and a non-conductive fluid was used in this experimental investigation, the leakage could only be determined from a change in the intensifier volume. To obtain a leakage failure point some added considerations were required, specifically the factors that influence changes in the fluid volume had to be considered. However, determining leakage failure in this manner enabled the characteristic leakage curves to be determined based on the applied stress and the applied stress ratio.

The commercially wound fiberglass pipe chosen for this investigation is discussed in Chapter 2, along with the imperfections produced during manufacturing. In order to run both biaxial monotonic and biaxial fatigue tests on the composite pipe, modifications were required to the MTS uniaxial resonant fatigue testing machine, as discussed in Chapter 3. To implement a leakage failure point determined from the pressure intensifier, factors that influence changes in the fluid volume had to be considered, such as the expanded volume of specimen under load and the volume of fluid compressed as discussed in Chapter 4. Chapter 5 focuses on the development of the biaxial monotonic failure envelope for the multidirectional composite pipe and investigates the mechanical properties, such as strength, stiffness and the damage response of the composite pipe under biaxial monotonic loading. Chapter 6 is concerned with the development of a biaxial fatigue leakage life envelope to characterize the leakage integrity of the multidirectional composite pipe under cyclic loading and observed the location of the imperfections to the damaged areas. Finally, conclusions of this study are reported in Chapter 7.

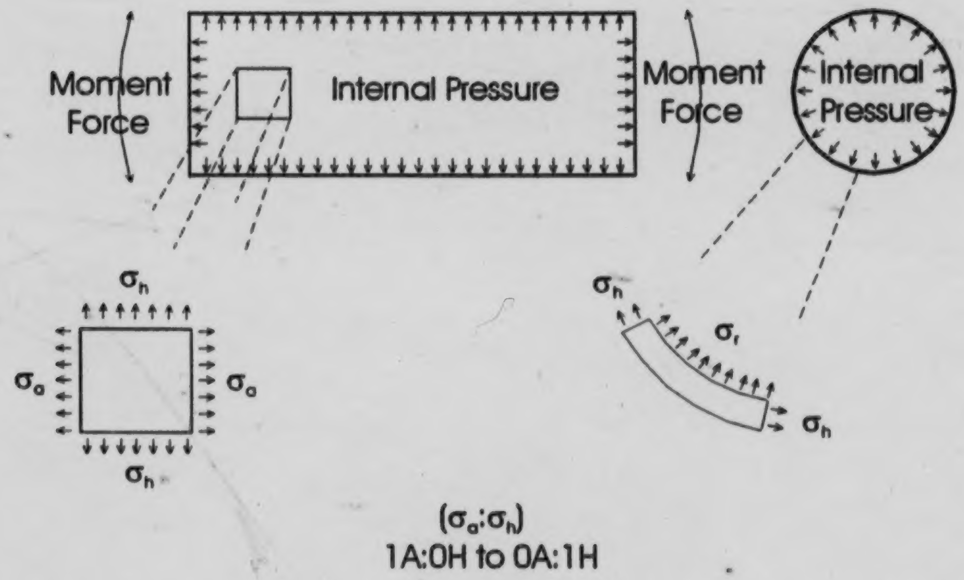

Figure 1-1: Illustration of critically combined loading conditions applied to a composite pipe from the surroundings during construction and operation. Where σ_a is the axial stress and σ_h is the hoop stress.

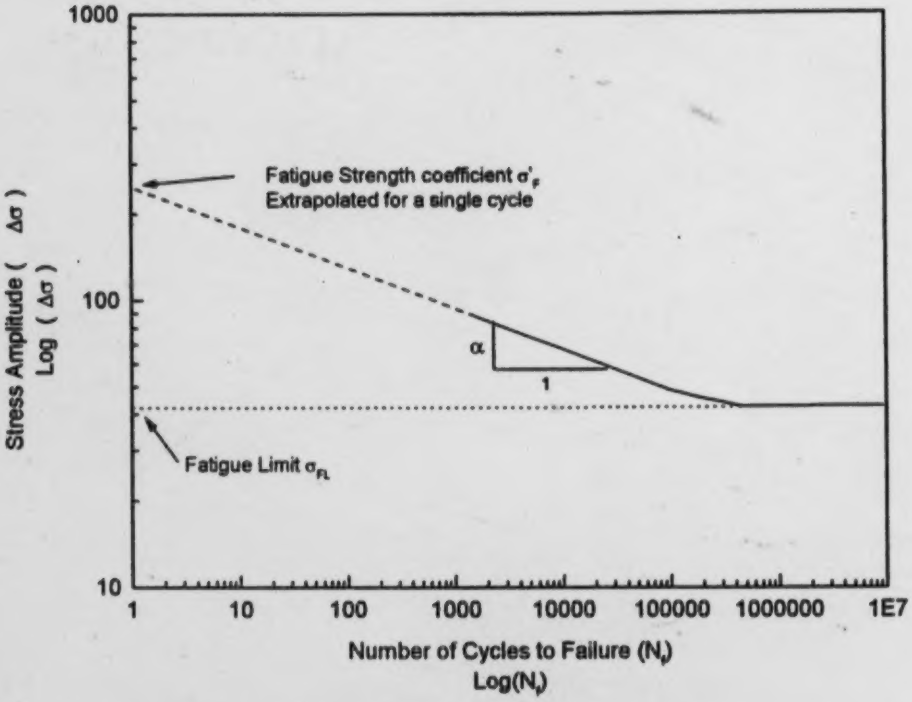

Figure 1-2: Graphical illustration of the S-N curve based on steel. Shows the characteristic fatigue life performance of a material.

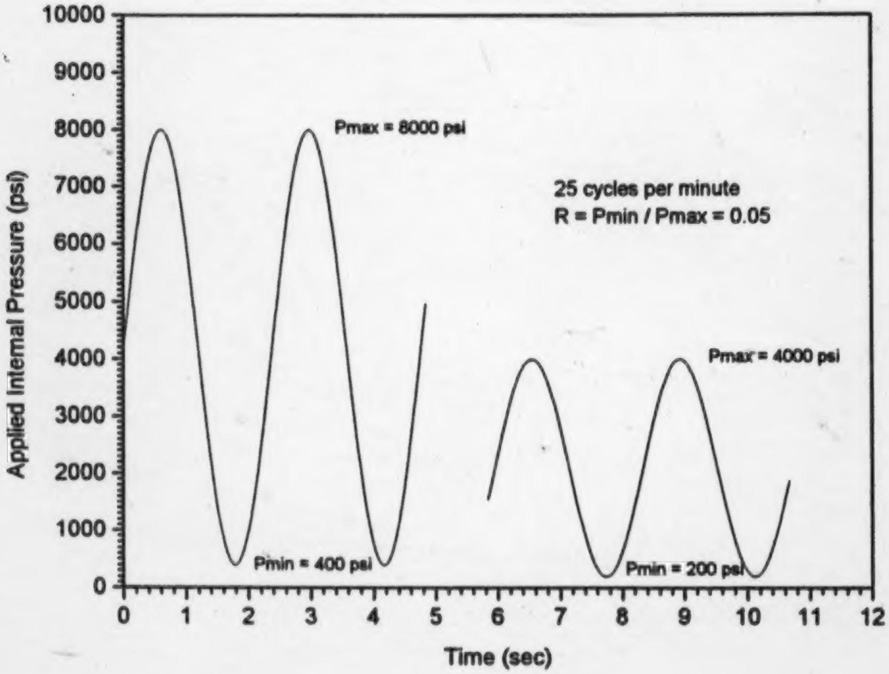

Figure 1-3: Graphical illustration of the ASTM Strandard D2143 / D2992 Procedure A Test for determining the long-term strength of filament wound composite pipe.

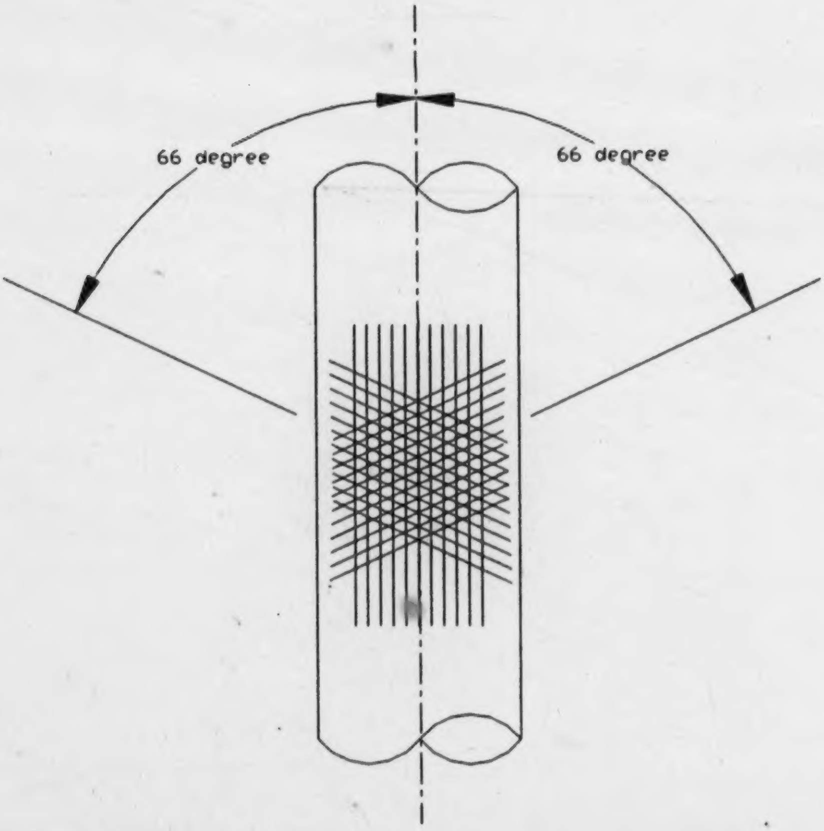

Figure 1-4: Illustration of a multidirectional lay-up for a composite pipe to with stand the high internal pressures and axial loading due to bending. This lay-up considers having a number of layers of glass fiber wrapped in the hoop direction to accounting for the internal pressure. In addition, layers in the axial direction account for axial loading.

CHAPTER 2

MULTIDIRECTIONAL COMPOSITE PIPE

2.1 INTRODUCTION

The process of filament winding is very complex. It requires experienced operators and dedicated specialized winding equipment to obtain the best results. However, the filament winding process is the most efficient way of manufacturing composite pipe. The principal stages of the filament winding process consist of (1) fiber winding, (2) curing of the epoxy resin and (3) mandrel removal. A schematic of these stages is presented in Figure 2-1.

Basically there are two common types of winding processes: (1) prepreg winding and (2) wet winding. In prepreg winding, fibres are supplied pre-impregnated with a partially cured epoxy resin and wound onto a mandrel. In the wet winding process, dry fibres are passed through a resin bath impregnating fibres with resin and are then wound onto a mandrel. After winding, the pipe is cured in an autoclave, according to the specification laid out by the epoxy resin manufacturer. After curing the pipe is removed from the mandrel.

Commercially wound products contain inherent defects. These defects are very difficult, if not impossible, to detect after the filament winding process, and if present in sufficient numbers could have serious effects on mechanical properties [11]. Commercially produced pipes, as opposed to laboratory manufactured specimens, were tested to observe the influence of defects as produced by the commercial process (large scale production) on the composite properties.

Chapter 2: Multidirectional Composite Pipe

This chapter is focused on the commercially filament wound multidirectional pipe studied in this investigation. Some of the process variables in manufacturing that contribute to the inherent defects seen in this multidirectional lay-up are discussed as well as the effects on dimensions.

2.2 MANUFACTURING VARIABLES

The filament winding process is very complex with over fifty different variables affecting the performance of the filament wound part and has been referred to as a " Black Art " [11, 45]. All the variables have different degrees of influence on the performance of the composite pipe. The more critical variables, according to Cohen (1997), include: fiber tension, variability of the fiber strength, fiber damage, fiber wet-out, winding time and control over the winding pattern [11]. Care must be taken not to confuse the design variables (i.e. fiber selection, resin selection and lay-up sequence) with the variables associated with the manufacturing process.

A review of the literature suggested that the most important variable to control is fiber tension (the tension of the fiber during winding). Besides decreasing the resin build-up and fiber bunching which results in fiber waviness fiber tension also reduces the void content, which has been linked to transverse tensile strength [7, 9, 11, 94].

Some of the mechanical interactions which make a significant contribution to the residual state of stress, are: (1) Relaxation of fiber tension due to the mandrel deflecting. An external pressure due to winding tension causes the mandrel to deflect thus reducing the tensile strain in the fiber [49A]. (2) Relaxation of fiber tension due to resin squeeze. After several fiber layer have been added to the mandrel, external pressure from the fiber winding tension causes resin to squeeze out from the underlying layers, further reducing the fiber strain in the inner layers [49A]. Other process variables which have an influence on the residual stress are resin shrinkage, resin viscosity as well as thermal curing.

Fiber damage (damage caused by manufacturing of the fiber and the composite pipe) causes a variability in the fiber strength. To maintain quality, care must be taken to ensure that fibers are not handled excessively and over tensioned. Variability in the fiber strength and damage sustained due to excessive handling, contribute to decreasing the overall strength [11].

Fiber wet-out (the resin content on the fiber during winding) is also a very important aspect. Too little fiber wet-out will cause dry areas and air pockets. Too much fiber wet-out will cause excess resin on the composite pipe leading to resin rich areas and waviness. The fiber resin ratio is dependent on fiber, the resin, winding speed and fiber tension [11].

The winding time (the overall time to wind the composite pipe) is dependent on the resin, geometry of the winding, and wall thickness required. On thicker walled sections of pipe with extended winding time a hot curing resin is preferred to avoid polymerization before the winding is completed [11]. Polymerization maybe initiated by uncontrolled self-heating prior to completion of the winding process, leading to resin rich areas and waviness.

Control over the winding pattern (the intended designed winding angle and lay-up) is another important aspect of the filament winding process. There is some allowable difference between the intended winding angle and the actual winding angle, but the amount of allowable difference has yet to be investigated. Variation from the intended design angle will change the intended stiffness and directional strength.

2.3 PRESENT FILAMENT WOUND PIPE

Five, 9 meter (30 foot) sections of a commercially wound, fiberglass epoxy, multidirectional pipe were used in this investigation. This pipe was manufactured by Fiber Glass Systems Inc. under the trade name STAR®

Using a commercially produced pipe has some disadvantages, as opposed to the advantages already discussed. These include not knowing the intricacies of the manufacturing process (i.e. fiber tension, curing process, resin characteristics, unable to control manufacturing variables, and the distribution of the imperfections). To explore some of underlying imperfections, the matrix was burnt off to determine the lay-up. In addition, the pipe was sectioned to observe the cross-section.

2.4 MATRIX BURN OFF

Matrix burn off was carried out to obtain the fiber volume fraction and the lay-up sequence. This procedure also shows any imperfections seen in the winding process (i.e. missing and/or partial layers). Burning off the matrix is only applicable to glass fiber, unlike carbon and kevlar fibers, a glass fiber does not burn.

2.4.1 PROCEDURE FOR MATRIX BURN OFF

(1) A small sample was removed from the composite pipe. To ensure that the sample was square, the walls of the sample were sanded flat and smooth.

(2) The total volume of the sample was measured by placing the sample into a beaker of water and measuring the displaced water.

(3) The sample was placed in an oven at 1000^0 F for one hour and 30 minutes, to burn off the matrix.

(4) The sample was allowed to cool and then weighed, to attain the fiber weight.

(5) The fiber volume fraction was calculated from the following equation.

$$\text{Percent Fiber Volume} = \frac{W_f}{\rho \cdot V_t} \times 100\% \qquad 2\text{-}1$$

where V_t is the total volume of the sample, W_f is the mass of the fibers after matrix burn off, and ρ is the fiber density taken as 2.62 g/cm^3 [75].

(6) The fiber layers were separated to attain the lay-up sequence and probe for lay-up flaws.

2.4.2 VOLUME FRACTION

Using the matrix burn off procedure, four samples taken from the pipe sections were used to calculate the volume fraction. One of the four samples revealed an unflawed sample with a fiber volume fraction of approximately 58%. The other samples showed imperfections incurred during manufacturing and deemed unsuitable for the volume fraction determination.

2.4.3 FIBER LAY-UP

The resulting lay-up sequence developed from the matrix burn off is illustrated in Figure 2-2. The initial lay-up measured was $\pm 66^{\circ}$ for the angle-plies and 0° for the axial plies. The angles measured from the burn out test, based on the vertical edge, are plotted in Figure 2-3. The manufactured lay-up is determined to be:

$$\text{Inside } [\pm66^{\circ}_{4},0^{\circ},\pm66^{\circ}_{3},0^{\circ},\pm66^{\circ}_{3},0^{\circ},\pm66^{\circ}_{5}] \text{ Outside}$$

2.5 IMPERFECTIONS

The process of filament winding may develop and/or introduce undesirable imperfections in the pipe. These defects are very difficult, if not impossible, to detect after the filament winding process, and if present in sufficient numbers, can have serious effects on mechanical properties [9]. For this reason it is important to obtain an idea of the imperfections that exist, to better understand their effects on the mechanical behavior. The following are the imperfections noted in the composite pipe specimens.

2.5.1 FIBER MISALIGNMENT

Fiber misalignment essentially is the failure to align the fibers as intended, this was noted in two forms: (1) A micro-scale type of inter-ply misalignment of the fibers, where the fibers were seen crossing over each other. (2) A macro-scale type of misalignment between the plies, where the fibers failed to line up to the intended wind angle, as illustrated in Figure 2-3. The misalignment between the plies is affect by the wind diameter of the pipe size [4]. In measuring the fiber angle from the burn-off test there is some question as to the effect of temperature on the fiber angle.

2.5.2 FIBER WAVINESS

Fiber waviness is the geometry of the fiber in not following the circumference of the pipe as illustrated in Figure 2-4. The cause of which can be attributed to wrapped-over underlying imperfections (i.e. resin rich areas). The waviness seen from the cross-section is in the $\pm 66^0$ angle-plies after passing over resin rich areas in the 0^0 plies. The resin rich areas can be caused by a variation in the winding tension between the $\pm 66^0$ angle-plies and the 0^0 plies, thus not squeezing the resin through the 0^0 plies.

The wavy geometry (illustrated in Figure 2-4) has a more detrimental effect under external hydrostatic loading than internal pressure loading [7]. Under external hydrostatic loading the fiber is under a compression load which produces a tensile and compression region on the surrounding matrix. This leads to fiber debonding from the matrix and delamination [7]. With internal pressure loading the fibers remain under pure tension, no buckling occurs, but a decrease in strength has been noted [98].

2.5.3 RESIN RICH REGIONS

Both Figures 2-5 and 2-6 are photographs of the cross-section illustrated in Figure 2-4, enlarged to observe fiber waviness and provide an in depth view of the resin build-up in the 0^0 ply. This indicates that there could have been a variation in tension and/or a difference between the winding time of the $\pm 66^0$ angle-plies and the 0^0 plies causing the resin build up [7, 11].

The imperfections of the resin rich regions cause a variation in the thickness around the circumference and uneven fiber volume distribution, these have been linked to a reduction in the mechanical performance [9]. When subjected to fatigue loading cracking was found to initiate in these regions, thus leading to a formation of local planes of delamination [9]. The variation in thickness will also cause variation in the surface strains and the deformed shape under an applied pressure.

2.5.4 PARTIAL LAYERS

Figure 2-7 illustrates the results from a burnout test in which partial layers are present. Note that partial layers only exist in layers 8 and 9. As well, partial layers have been added between layers 17 and 18 and 24 and 25. These partial layers contribute to fiber waviness and cause a variation in the stiffness. The strength around the circumference of the pipe will also vary.

2.5.5 VOIDS (POROSITY)

The most common micro-scale imperfection that was found in the composite pipe was voids (porosity), which is the entrapping of air in the resin. The content of voids entrapped in the resin is dependent on the resin viscosity at the time of winding as well as the winding tension, if the tension is too light there will be less likelihood for air to escape [97]. Tang et al. (1987) has also emphasized these points by studying the effect of fiber compaction on void content [94]. It was concluded that no apparent movement was seen from the voids, indicating that voids do not migrate but have to be squeezed through the wound filaments [94]. Voids (porosity) were considered to have a marginal influence the mechanical properties; if the level remained below 1 % per volume [9, 94].

Micrographs were taken of a representative cross-section, shown in Figure 2-4, of the multidirectional pipe at 40 times magnification, as illustrated in Figures 2-8a and 2-9a, with the corresponding micrographs taken at 440 times magnification, as illustrated in Figures 2-8b and 2-9b. The specimens were prepared for micrographs according to Hull (1979) [40]. These micrographs illustrate the persistence of voids (porosity) within the layers with an increased void density in the 0^0 plies and at the ply interface. Also note the resin-rich areas and fiber packing in the 0^0 plies, illustrated in Figure 2-9b. Note these micrographs do not give a representative sample of the void content found in the pipe, as these micrographs are solicited cases to show the resin rich areas and fiber packing. Only an idea of the void content can be obtained from these cross-sections.
The possibility of using the ASTM Standard D2734-85 to find the void content was considered, however the density of the matrix free of voids was unattainable [90].
(The matrix density must be obtained at the time of winding because the resin density changes from batch to batch and the appropriate resin to hardener ratio will change slightly, varying the density.)

2.6 DIMENSIONS

The choice of this particular size of the multidirectional glass fiber reinforced epoxy pipe for this investigation was based on the structural loading capacity of the MTS testing machine. (Further details are given in Chapter 3)

The pipe had an inside diameter of 50 mm (1.950 inch) that varied ± 0.5 mm (± 0.020 inch) from section to section. The variation in roundness in the internal diameter was less than ± 0.025 mm (± 0.001 inch). The consistently round internal surface with a surface roughness of Hazen Williams C=150, can be contributed to the ground mandrel the pipe was wound on [21].

The outer surface had a nominal diameter of 62 mm (2.440 inch) and a large variation from section to section of ± 5.0 mm (± 0.200 inch). The outer surface was non-circular and often resembled an elliptical shape. The large variation in roundness of the outer diameter of the pipe of ± 1.2 mm (± 0.050 inch) can be attributed to the resin rich areas built-up through the wall thickness. The outer surface shape and variation in roundness was dependent on the placement and resin-rich imperfections between the $\pm 66^{\circ}$ and the 0^{0} layers. However, small variations in the surface were also attributed to the protective resin coating.

The inner and outer surfaces were probed with a Brown and Sharpe coordinate measurement machine. The coordinate measurement machine allows for detailed mapping of the pipe surface. The resulting surfaces are illustrated in polar plots in Figure 2-10 to 2-12. Figure 2-10 illustrates the small variation in roundness in the inner-surface. Figure 2-11 illustrates the large variation in roundness in the outer-surface. The spikes seen in Figure 2-11 are from small bundles of fiber wrapped around the outer surface and small variations in the protective coating. To help visualize the comparison between the larger variation in roundness for the outer surface to the inner surface, both the surfaces are plotted in Figure 2-12.

2.7 GLOBALLY APPLIED STRESSES

The irregular geometric features of the multidirectional pipe discussed in Section 2.6 complicate the calculation of the globally applied stresses. The applied average stresses were calculated from the internal pressure and axial load according to the ASTM Standard D2992-91 (thin cylinder theory) [89]. Noted that the stresses determined in thin cylinder theory are an indication of the applied average stresses.

The hoop stress was calculated for the pipe specimen loaded by internal pressure ($P_{internal}$) with fixed end conditions according to Equation 2-2, and the axial stress from the internal pressure and the axial load (L_{axial}) according to Equation 2-3.

$$\sigma_{hoop} = \frac{p_{internal} \cdot r_{mean}}{t_{mean}} \qquad 2\text{-}2$$

$$\sigma_{axial} = \frac{L_{axial}}{\pi \cdot (r_{inside} + t_{mean})^2 - \pi \cdot r_{inside}^2} + \frac{p_{internal} \cdot r_{mean}}{2 \cdot t_{mean}} \qquad 2\text{-}3$$

where the mean thickness t_{mean} of the tubular wall and the mean radius r_{mean} were calculated according to Equation 2-4 and Equation 2-5, respectively. The geometry of the composite pipe used in determining the applied stresses is illustrated in Figure 2-13.

$$t_{mean} = \frac{\sum_{i=1}^{m} t_i}{m} \qquad 2\text{-}4$$

$$r_{mean} = r_{inside} + \frac{t_{mean}}{2} \qquad 2\text{-}5$$

where m is the total number of measured points, eight in total, and r_{inside} is the inside radius.

(The globally applied stress and load calculation under required loading conditions are further discussed in Appendix B.)

2.8 SUMMARY

A commercially wound fiberglass pipe was chosen for this investigation. The pipe was manufactured by experienced operators with dedicated winding equipment, which resulted in a product with inherent imperfections to be expected in a commercial operation. Imperfections are very difficult, if not impossible, to detect after the filament winding process, and if present in sufficient numbers could have serious effects on mechanical properties [11]. These pipes were tested to observe the influence of imperfections, inhere in a commercial process (large-scale production) on the composite properties. It was deemed important to obtain a measure of the existing imperfections. A destructive investigation was conducted to observe the underlying imperfections found by exposing the cross-section and exploring the lay-up by burning off the matrix. The imperfections noted were:

The misalignment of the fiber was seen on two scales. A macro-scale type of misalignment between the plies, where the fibers failed to line up to the intended wind angle, as illustrated in Figure 2-3, and a micro-scale type of inter-ply misalignment of the fibers, where the fibers were seen crossing over each other.

The waviness of the fiber around the circumference of the pipe, as illustrated in Figure 2-4. The observed waviness was seen in the $\pm 66^0$ angle-plies after passing over resin rich areas in the 0^0 plies. The resin rich regions caused a variation in the thickness around the circumference, as observed in Figures 2-5 and 2-6. This indicates that there could have been a variation in tension and/or a difference between the winding time of the $\pm 66^0$ angle-plies and the 0^0 plies causing the resin build up [7, 11]. In addition, partial plies were also observed, as illustrated in Figure 2-7, from the burnout test conducted on the specimen. This also contributes to fiber waviness.

The most common micro-scale imperfections that were observed in the composite pipe were voids (porosity), which are the entrapment of air in the resin. Micrographs were taken of a representative cross-section of the multidirectional pipe at 40 times magnification, as illustrated in Figures 2-8a and 2-9a, with the corresponding micrographs taken at 440 times magnification, as illustrated in Figures 2-8b and 2-9b. These micrographs illustrate the persistence of voids (porosity) within the layers with an increased void density in the 0^0 plies and at the ply interface. Also note the resin-rich areas and fiber packing in the 0^0 plies, illustrated in Figure 2-9b.

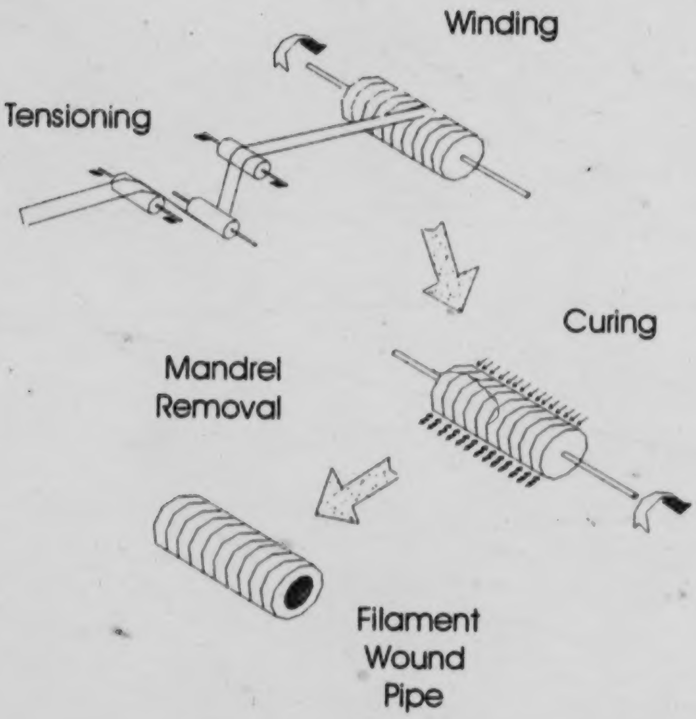

Figure 2-1: The principle stages of the filament winding process, figure adapted form Tarnopol'ski & Beil' (1983).

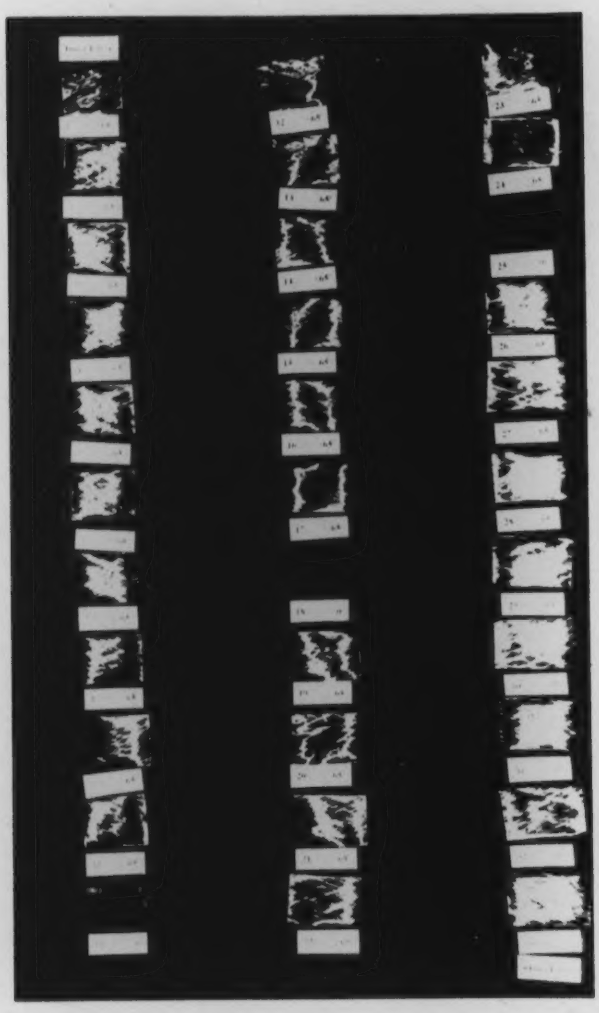

Figure 2-2: The resulting lay-up sequence determined when the matrix was burnt off.

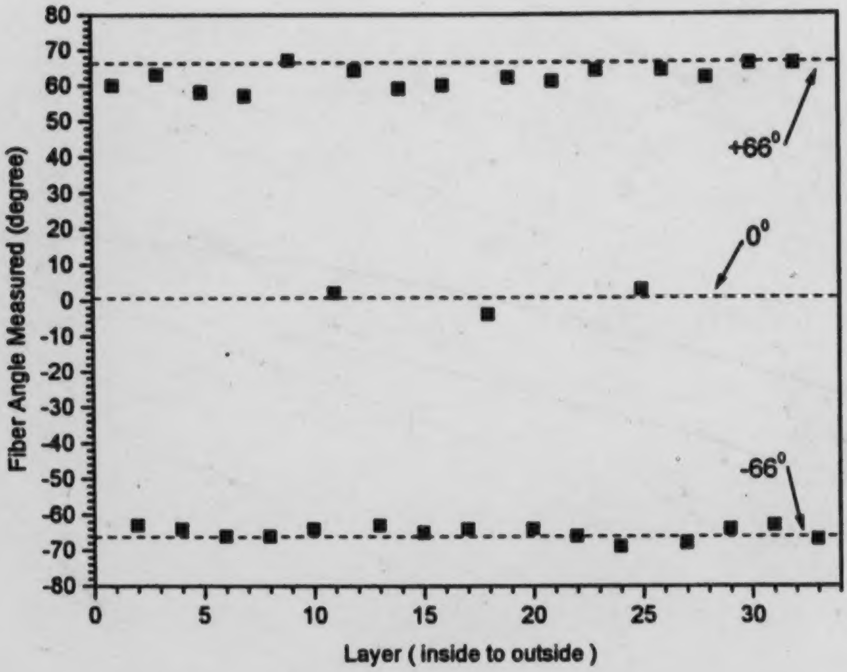

Figure 2-3: Plot of the angle measured for each ply after the matrix was burnt off.

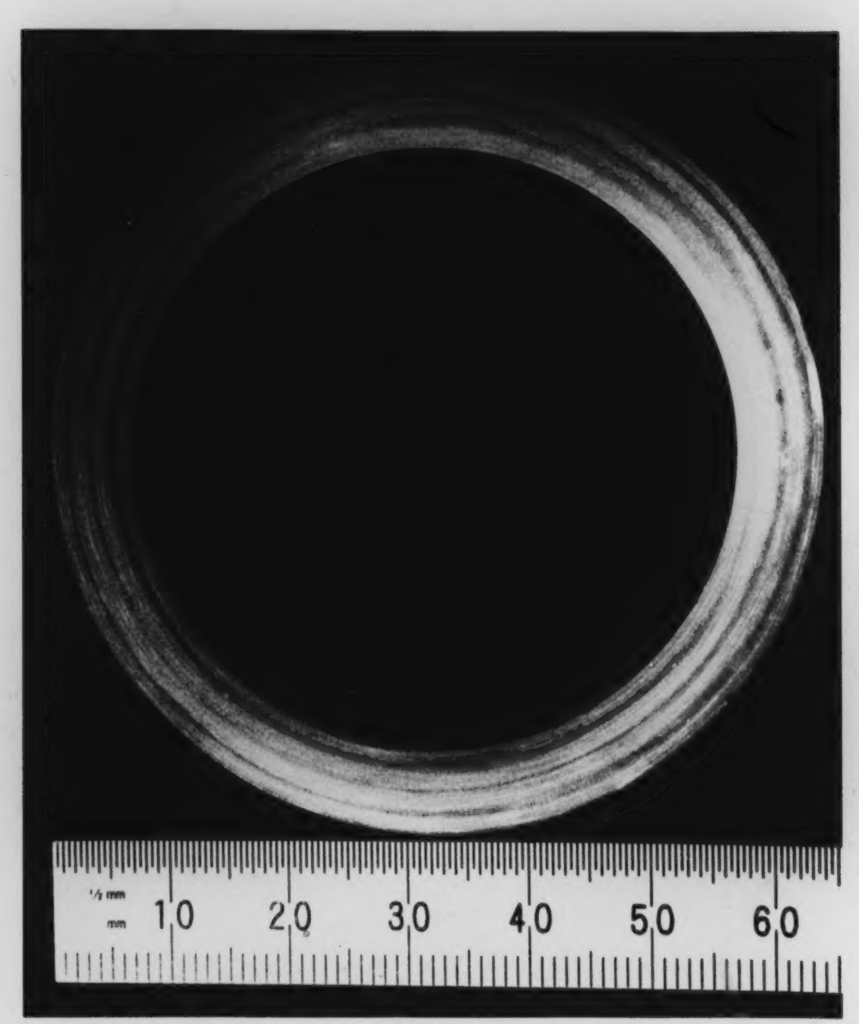

Figure 2-4: Photo of the cross-section of the fiberglass pipe under investigation. Illustrates fiber distortion and resin rich areas. This cross-section will be further observed in Figures 2-5, 2-6, 2-8a, 2-8b, 2-9a, and 2-9b.

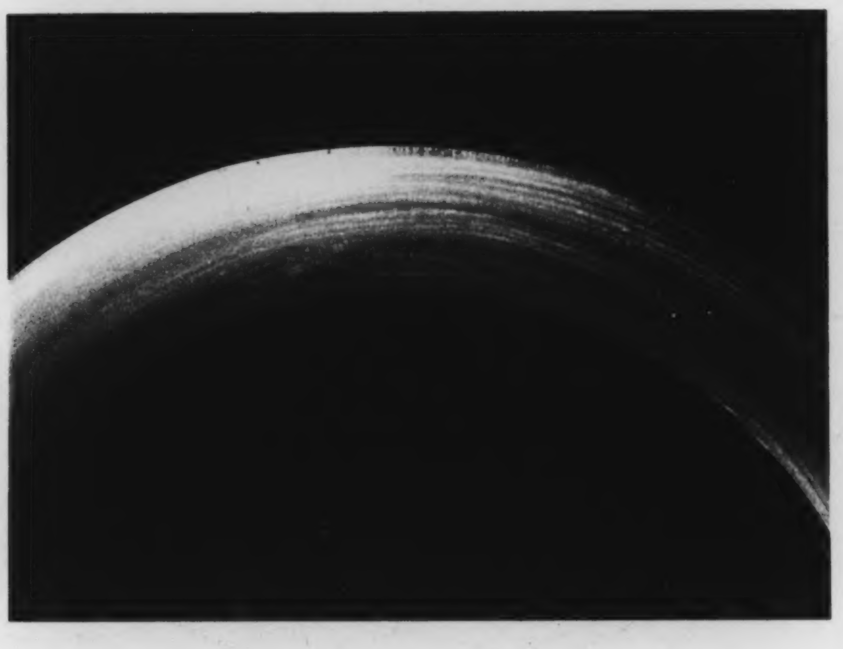

Figure 2-5: A magnified view showing half of the cross-section of the fiberglass pipe under investigation. Illustrates fiber waviness and resin richness.

Figure 2-6: A magnified view showing a section of the fiberglass pipe under investigation. Illustrates fiber waviness and resin richness.

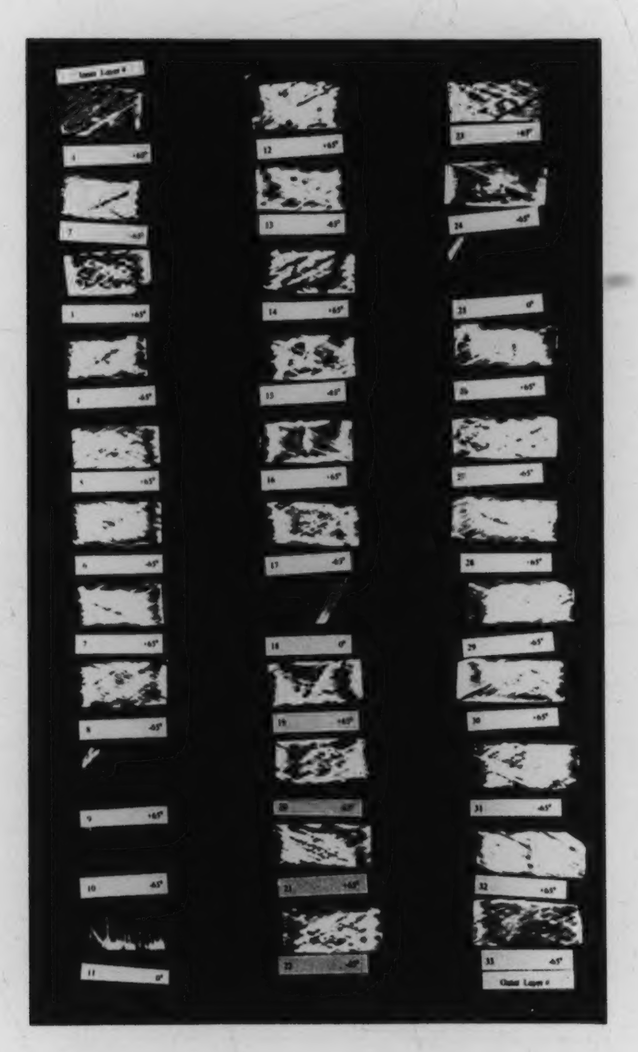

Figure 2-7: Resulting lay-up sequence developed from the burning off the matrix. Illustrates partial layers of fiberglass and added partial layers.

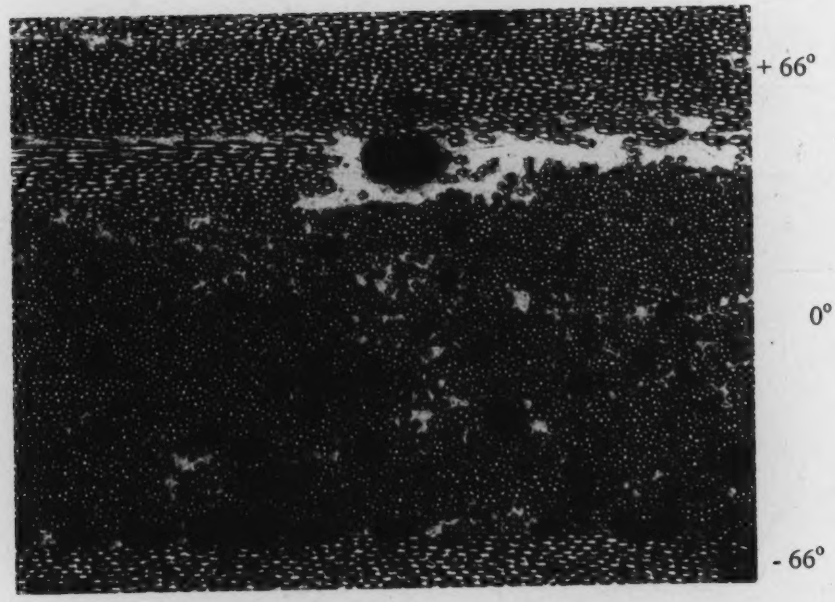

Figure 2-8a: A segment of the cross-section of the pipe, seen in Figure 2-4, magnified 40x. Illustrated are the voids (dark areas) and resin rich areas (white areas).

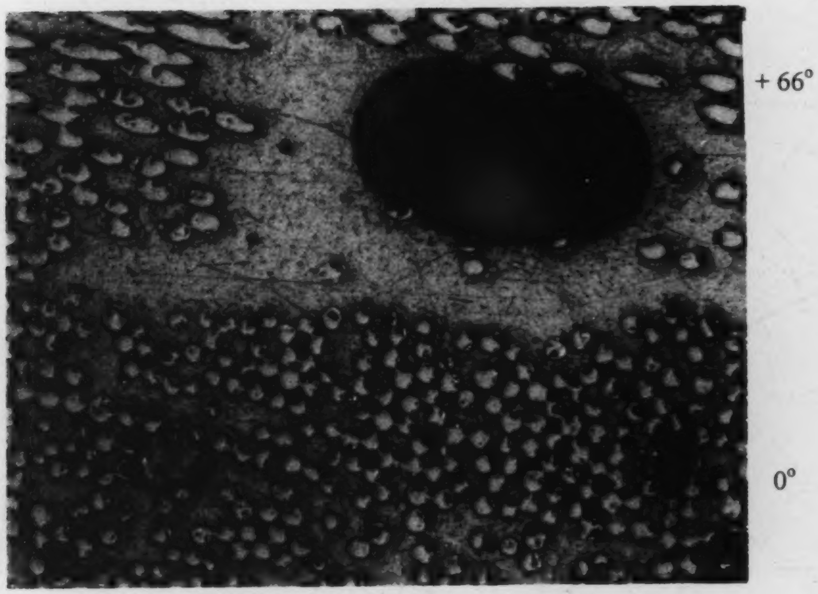

Figure 2-8b: A segment of the cross-section of the pipe, seen in Figure 2-4, magnified 440x, note the excess resin (white areas) between the layers.

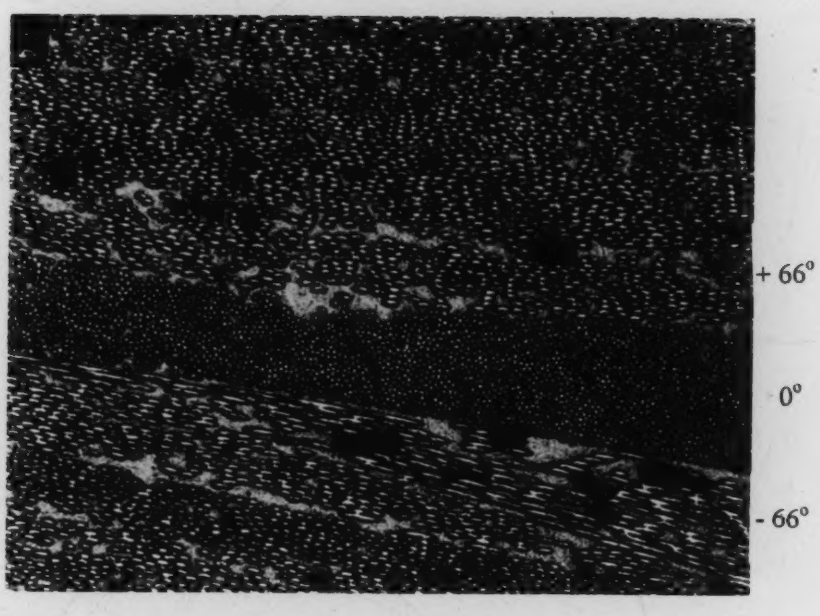

Figure 2-9a: A segment of the cross-section of the pipe, seen in Figure 2-4, magnified 40x. Illustrate are the voids (dark areas), resin rich areas (white areas) and fiber distortion in the 0° layer.

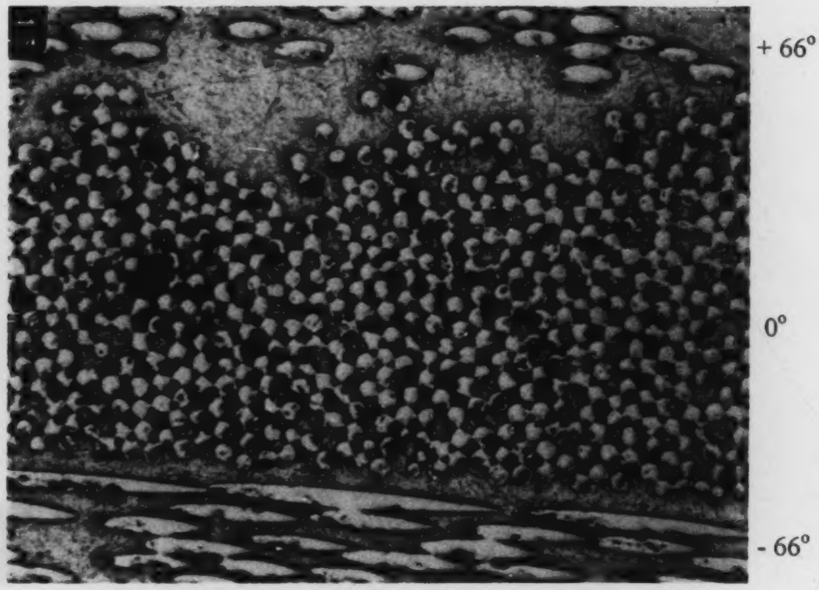

Figure 2-9b: A segment of the cross-section of the pipe, seen in Figure 2-4, magnified 440x, note the excess resin (white areas) between the layers.

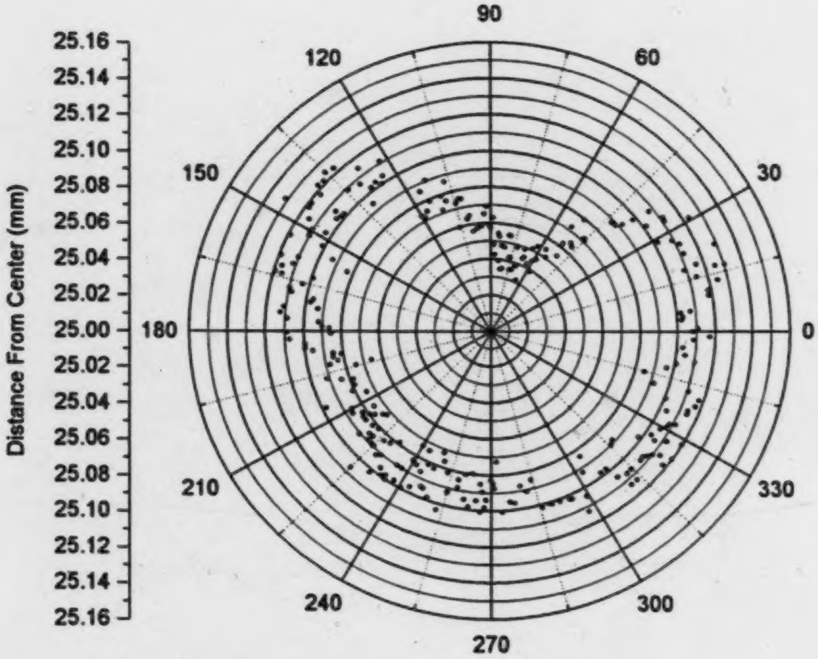

Figure 2-10: Polar plot of the inner pipe surface, illustrates the small variation in roundness. Note the scale on the left.

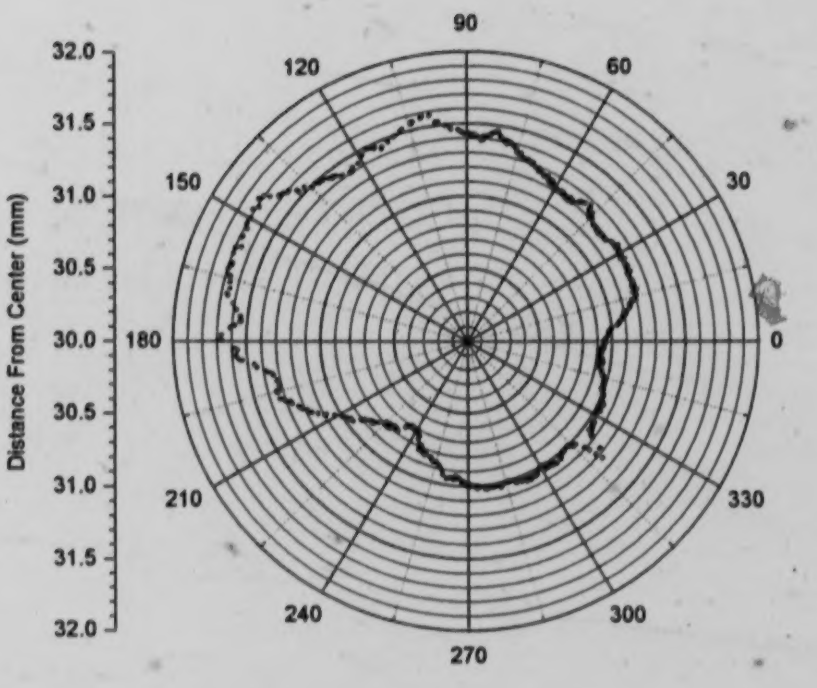

Figure 2-11: Polar plot of the outer pipe surface, illustrates a large variation in roundness. Note the scale on the left.

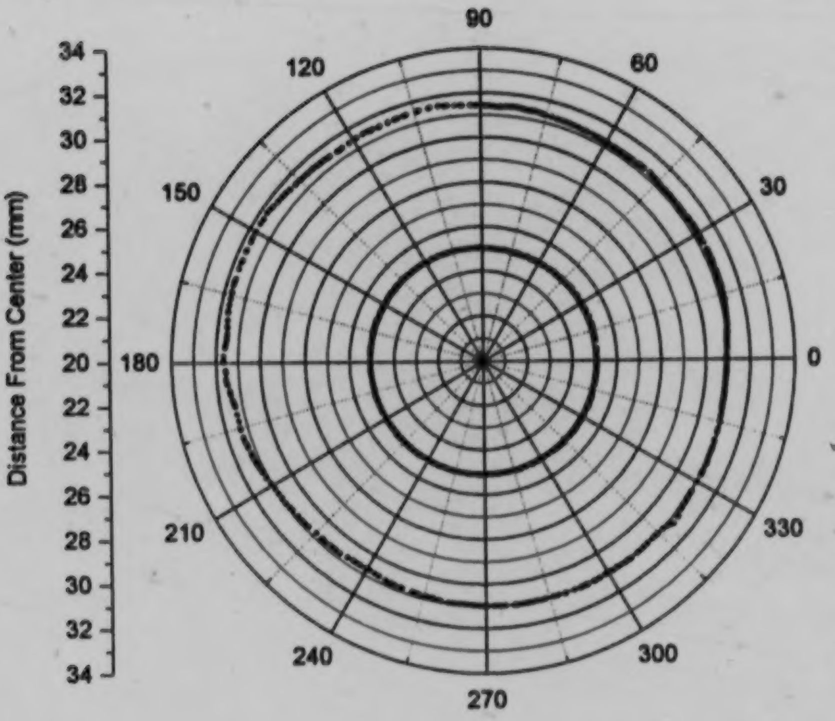

Figure 2-12: Polar plot of both the inner and outer pipe surface, illustrates the change in thickness.

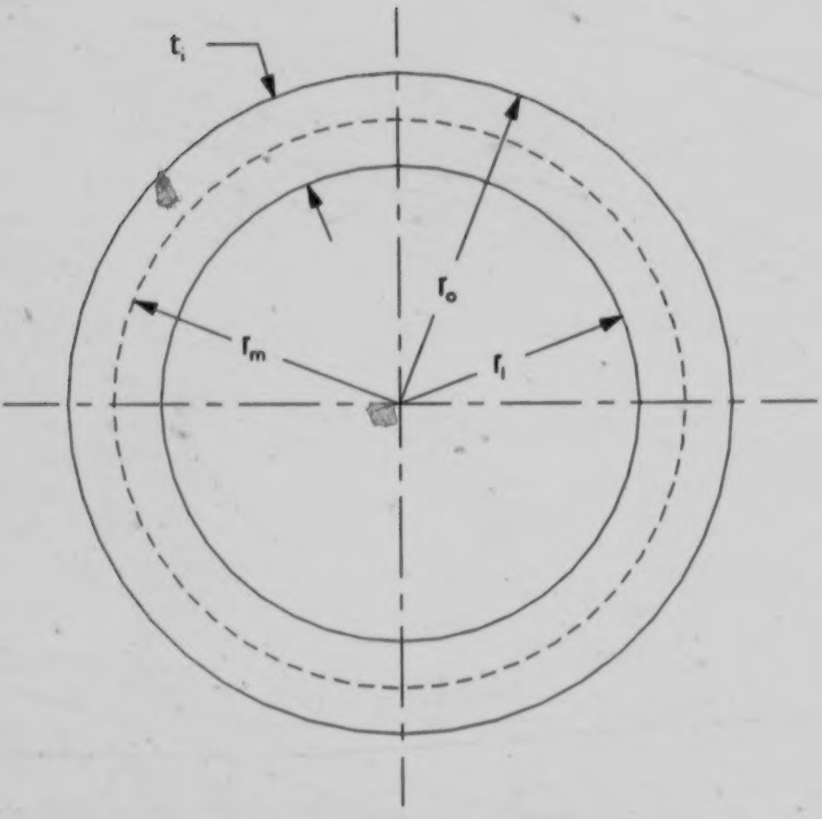

Figure 2-13: Geometry of the composite pipe used in determining the applied stresses. Where t_i is one of eight points used to calculated t_{mean} and r_{mean}.

CHAPTER 3

TESTING APPARATUS

3.1 INTRODUCTION

An MTS uniaxial resonant fatigue testing machine was modified to perform biaxial monotonic tests on composite pipe specimens, as described in Carroll (1994) [8]. These modifications included the addition of an MTS digital function generator and an internal pressurization system. The function generator was placed in the control system in order to supply a smooth monotonic loading ramp to full load, by feeding an appropriate command signal to the servo controllers.

Internal pressure and axial loading were required in order to achieve the biaxial state of stress in the fiberglass tubes. The servo controlled pressure system that was developed included: a pressure intensifier, a servo control valve, a control unit, and a pressure transducer. The servo valve controlled the flow of oil from the main hydraulic pump into the 3.8:1 pressure intensifier that was connected directly to the tubular specimen through stainless steel tubing.

Several cyclic tests were performed on the testing apparatus modified for monotonic testing. The results suggested that more modifications were required in order to adjust the testing apparatus from a biaxial monotonic function to performing a biaxial fatigue function. The following is a discussion of the modifications made to the existing apparatus.

3.2 THE MTS BIAXIAL TESTING MACHINE

A schematic of the testing apparatus after modification is illustrated in Figure 3-1. Observe the layout of the MTS and the pressurization controllers, along with the data acquisition systems in Figure 3-2. The data acquisition computer initiates the test by signaling the function generator, which supplies a control signal for both monotonic ramping and fatigue cycling. The function generator feeds an analog command signal to both the axial and pressure controllers. The load applied to the specimen is based on the load set point and span. For fatigue testing the set point is the applied mean load and the span is the load amplitude. In monotonic testing the set point is set to zero and the span is set to the maximum attainable load for full ramp time from the function generator.

The pressure controller supplies an analog command signal to the servo control valve, applying the appropriate hydraulic pressure to the pressure intensifier. A pressure transducer supplies feedback to the pressure controller. The signal sent to the servo control valve is based on an incoming command signal from the function generator and the pressure transducer feedback. A pressure error detect was setup to note the difference between the incoming command signal and the feedback from the pressure transducer. Once the difference between the two is greater then the error limit set by the operator, the pressure controller will signal the data acquisition computer to halt the function generator, stopping the test. The test can only be halted if the required pressure can not be maintained.

The servo valve controls the flow of oil from the main hydraulic pump into the 3.8:1 pressure intensifier connected directly to the pipe specimen through stainless steel tubing, as illustrated in Figure 3-2. The oil volume in the intensifier is measured in terms of intensifier piston displacement by a pulley rotary potentiometer system as seen in Figure 3-4 as a volume transducer.

The load controller supplies an analog command signal to the MTS servo control valve, which applies the appropriate hydraulic pressure to the axial actuator. The axial load cell and the cross-head position supply feedback to the axial controller. The axial controller sends a signal to the servo control valve based on the incoming command signal from the function generator and the feedback. An axial error detect was set up based on the cross-head position of the axial actuator. Once the cross-head displacement passes a preset limit set by the operator, the axial controller sets an interlock, which stops the hydraulic pump. Once the displacement preset limit is passed a signal is sent to the data acquisition computer, halting the test. The only time an interlock will be set off is when the axial movement is greater then the set limit, which is seen in structural types of failures and slippage in the gripping system.

Hoop and axial strains were measured by extensometers (observed in Figures 3-5 and 3-6) for both monotonic and fatigue testing. The axial and transverse extensometers have gauge lengths of 50.80 mm (2.0 in) and 62.23mm (2.45 inches), respectively. Both extensometers were calibrated for a maximum output of 5% strain.

An analog filtering system was added to condition the incoming instrument signals to reduce the 60 Hz noise inherent to the testing apparatus. Also an analog filtering system was added to the input power of the control system. Power spikes cause system shut down and other related problems during long term fatigue testing.

The data acquisition computer system consisted of a 386 Personal Computer and a Keithley MetraByte DAS-16 data acquisition card with 12-bit resolution with a total range of ± 10 volts. The DAS-16 has an added burst mode, which allowed for channel scanning at 5000 Hz. During the fatigue and monotonic tests, the following data was recorded: the axial load, the internal pressure, the axial strain, the transverse strain, the cross-head position and the intensifier stroke.

For monotonic testing strain gauges were added because of the concern about damaging the extensometers. This was only found to be of a concern under pure axial loading.

The data was collected in 10 seconds intervals during testing, which was found to be sufficient.

The temperature of the specimen was monitored during fatigue testing, by a type J thermo-couple placed on the surface with Devcon 5-Minute Epoxy. The purpose of monitoring temperature, was to obtain an over all idea of the surrounding effects during the lengthy fatigue tests. Thirty data samples per cycle were collected at every 10th cycle for the first 100 cycles and every 100th cycle for the remainder of the test.

3.2.1 CRITICAL EVALUATION

The MTS uniaxial resonant fatigue testing machine was initially modified by Carroll (1994) for biaxial monotonic testing of fiberglass tubular specimens [8]. Results from several cyclic tests revealed some concerns about the level of confidence of the collected data. In order to proceed with an adequate level of confidence, the fatigue-testing machine was examined for any faults, and instrumentation calibration was checked, the results are summarize in Table 3-1.

3.2.1.1 DATA ACQUISITION

The data acquisition was set-up to take data fast and reliably. In order to do this the original Keithley MetraByte DAS-8 was replaced with a Keithley MetraByte DAS-16 [47]. The DAS-16 data acquisition card offered a burst mode so the channels could be scanned at 5000 Hz as well as a high speed DMA transfer, which implements fast data storage [47]. The Keithley MetraByte DAS-16 has a 12-bit resolution and accuracy of +/- 1 bit, with a ± 10 volts total range the resolution is 0.00488 volts [47].

The resolution in an analog to digital system is one half of the maximum fluctions of the digital output [44, 54]. With incoming data having as much as 0.150 volts peak to peak 60 Hz noise, the resolution was decreased to 0.075 volts. To reduce the effects of noise in the system, 5th order Butterworth lowpass filters were added to all the incoming channels, increasing the resolution to 0.010 volts.

Data sampling was given ample consideration. It was important to gather the data at a sufficient rate to retrieve all the relevant data from the incoming signals. A data-sampling rate that is too large may lead to unnecessary increase in data processing time without the corresponding benefit. An optimum-sampling rate gives a sufficient amount of data, but minimizes the time between last recorded point or cycle and the final failure point or cycle.

Monotonic testing was sampled at 10 second intervals due to the loading rate (loading rate is discussed in Chapter 5), therefore the file size was kept small but still gave an ample number of data points. During fatigue testing, thirty data samples were collected at every 100th cycle. Thirty samples per cycle causes an offset error in the measured maximum and minimum and a true maximum and minimum of only 1.093 % of the intended amplitude [104]. This is critical to determine the secant modulus (dynamic stiffness), which will be discussed in Chapter 6. Sampling at every 100th cycle minimizes the time between last recorded cycle and the final cycle.

3.2.1.2 AXIAL LOAD

The axial load on the fiber glass specimen was monitored by an MTS 373,650 N (84000 lbs.) reversible load cell with a published accuracy of ±0.15% at reading or ±560 N (±126 lbs.) at full scale [66]. The resolution with the analog filtering system in place, was 373 N (84 lbs.). The calibration of the load cell was checked with a More House Roving ring S/N 495 which has a maximum capacity of 889,644 N (200,000 lbs.) compression. The proving ring has an accuracy of ±0.05% at reading or ±444 N (±100 lbs.) at full scale. The proving ring was calibrated by the National Research Council of Canada at the National Aeronautical Establishment [64, 65].

3.2.1.3 INTERNAL PRESSURE

The pressure transducer, which measures the internal pressure of the specimen, is an Omega PX613 with a published accuracy of ± 0.4% at full scale [69]. Full scale being 103 MPa (15000 psi) the accuracy is then ± 0.4 MPa (± 60 psi) and the corresponding resolution after filtering is 0.096 MPa (14 psi). The calibration was checked with an Omega type DWT 1305 D dead weight tester, with a published accuracy within ± 0.1% of the measured pressure, at varying pressures between 0.69 MPa (100 psi) and 69 MPa (10000 psi).

Some of the results seen from several of the cyclic tests performed on the modified uniaxial testing apparatus indicated that the intensifier was 'bottoming out'. This is when the intensifier cannot reach the intended minimum pressure. This phenomenon occurs when the intensifier is filled and the pressure from the external hydraulic system is not bled. This leaves a greater than minimum pressure inside the specimen at the start of the test. Therefore, the intensifier is not allowed to reach its intended minimum pressure. Care was taken to ensure that the intensifier pressure was zero before the test were initiated.

3.2.1.4 STRAIN

Hoop and axial strains were measured using extensometers for both fatigue and monotonic testing. (Observe Figures 3-5 and 3-6) The extensometers were developed in-house and were calibrated to 5.0 % strain on a MTS model 650.03 extensometer calibrator with an accuracy of ± 0.00254 mm (± 0.0001 in) or ± 0.005 % strain. The axial and transverse extensometers had gauge lengths of 50.8 mm (2.0 in) and 62.2 mm (2.45 in) respectively. The calibrated extensometer was determined to have an accuracy of ± 0.05% strain and resolution after filtering of 0.01% strain. Other possible concerns with extensometer include errors caused by slippage and positioning.

The axial and transverse extensometers are held to the surface of the specimen by the contact force applied by the knife-edges through the use of springs. The results from the initial cyclic tests indicated that there was some type of axial extensometer movement. Since the dynamic cyclic frequency was only 0.42 Hz and the contact force was 3.0 N (0.66 lbs.), the zero shift was not considered to be caused by the frequency but rather by surface conditions [2, 3]. The external surface of the specimen is uneven but smooth as noted in Section 2.5. Once the surface was covered in hydraulic fluid it became slippery.

To reduce the chances of slippage, the contact force was increased to 7 N (1.6 lbs.), between the extensometer and the specimen. This increase in the contact force was not considered to cause any detrimental effects (i.e. damage to the specimen) because of the epoxy coating on the outer surface and the thickness of the specimen. Epoxy was also added to the knife-edges of the axial extensometer and the pins of the transverse extensometer, to further reduce the chances of slippage.

The placement of the extensometers is critical to determining the strain with the least amount of error. In order to ensure that measuring points of the hoop extensometer pass through the centerline of the specimen and the axial extensometer is lined up parallel to the internal centerline of the specimen. The specimen was mounted in a specially designed mandrel Figure 3-7, which was placed in an indexing dividing head as illustrated in Figure 3-8, to maintain centricity with the inner surface of the specimen. This was required because of the non-circular outer surface. The dividing head was placed on a lay-up table in order to mark the specimen in one hundred and eighty-degree intervals. The surface with the greatest wall thickness was determined as the base line and placement of the axial extensometer and the hoop extensometer. The hoop extensometer was placed in the center of the composite specimen determined with a digital caliper. The same procedure was followed for strain gauge placement for monotonic testing.

3.2.1.5 OIL VOLUME

The pressure intensifier is an integral part of biaxial testing of composite pipe. It is used to create the second required axis for biaxial testing and to determine leakage from the specimen. The amount of leakage from the specimen is determined by monitoring the displacement of the intensifier piston rod. The rod position is converted into voltage through the use of a rotary potentiometer and pulley combination.

The rotary potentiometer was an Omega RP100 Series with a published accuracy of ± 20 minutes of arc or ± 0.3333 degrees in combination with the pulley, which has a contact radius of 73.61 mm (2.898 in) [69]. The piston on the high-pressure side of the intensifier has a bore of 22.20 mm (0.874 in) and a stroke of 184.22mm (7.253 in) leaving a total volume of 71.31 ml (4.35 in^3). Thus, the high-pressure system has an overall accuracy of ± 0.43 mm (± 0.0168 in) or 0.165 ml (0.010 in^3) and a corresponding resolution after filtering of 0.177 ml (0.011 in^3).

The direct relationship between the rotating pulley and the vertically moving rod is maintained by friction. Slippage between the rotary potentiometer pulley and the intensifier piston rod was of some concern. The intensifier was refilled after every test to check the zero or full position to ensure no slippage. None was found.

For monotonic testing the oil volume lost was determined by the difference of the initial oil volume measured and the oil volume measured at the n^{th} point. For fatigue testing, the oil volume lost was determined by difference between the mean oil volume of the first recorded cycle and the mean oil volume of the n^{th} cycle. (The topic of oil volume is further discussed in Chapter 4.)

3.2.1.6 STROKE

The axial actuator stroke producing axial load on the fiberglass specimen was monitor by an XS-D series linear variable differential transformer (LVDT) made by Lucas Schaevitz, installed by MTS. The linear variable differential transformer (LVDT) had a nominal linear range of ± 125 mm (± 5.000 in) with a non-linearity of ± 2.0 % of full range or ± 2.5 mm (0.1 in.) [3.29]. The resolution with the analog filtering system in place, is 0.125 mm (0.00492 in.). The calibration of the stroke measurement was checked with a Starrett series 656, 6-inch long-range dial indicator with 0.001-inch graduations [91].

3.3 GRIPPING SYSTEM

The specially designed double collet gripping system used in this investigation was initially developed by Carroll (1994) for biaxial monotonic testing of fiberglass tubular specimens without end reinforcement [8]. The major difficulty found was gripping the brittle specimens in order to maintain the high axial loads and the internal pressures without developing damaging transitional stresses. The existence of abnormally high concentrations of stress in filament wound tubes could lead to erroneous results, which would not reflect the true characteristics of the material. Carroll (1994) reported, after spending considerable time on the problem, that the solution had not been a complete success [8]. Damage was seen in the gripped section of pipe, slippage was reported as well.

A double collet end gripping system is the suggested holding device by ASTM Standard D-2105, which was comparable to the design developed by Carroll (1994), but the subject of end reinforcement is not addressed in this standard [8, 87].

Most investigators approach the problem of transitional stresses by modifying the specimen with the addition of end reinforcement. However, the subject of end reinforcement is a complex issue. Soden (1989) has investigated this through step reinforcement wound over the composite tubular specimen [85]. Soden (1989) concluded that, although, the composite structure, was able to accommodate high stress concentrations near the step, it sustained local resin cracking and a small amount of local damage at relatively low loads[85].

The approach of using a tapered hub made from fiber over-wrapping, was also investigated by Soden & Highton (1982) [82]. The simple method of assuming that the reinforced end is a series of laminated shells which behave like a series of semi-infinite beams on elastic foundations was used to design the composite taped hub on the specimen ends. Soden & Highton (1982) reported great success with this type of end reinforcement designed, by observing no failures outside the test section [82]. The drawback to fiber over-wrapping as end reinforcement is the requirement of a fiber winding device. To obtain the best results it should be applied during the manufacturing process.

Other approaches to reinforcing the specimen ends were developed Sullivan & Chamis (1973) and Groves et al. (1992) [92, 25]. Sullivan & Chamis (1973) and Groves et al. (1992) found that using potted epoxy, instead of fiber wrapped ends was sufficient to keep the transitional stresses low. Sullivan & Chamis (1973) supported the inside of the tubular specimen with a compression plug, while epoxy collets were potted into tapered metal grips on the external surface. As the tapered grips placed additional radial compressive loading on the ends of specimen, there was some concern about the bonded strength at the interface between the composite tube and the epoxy during tension loading.

Groves et al. (1992), who had a similar setup to Sullivan & Chamis (1973), was interested in evaluating the shear joints of composite cylinders in order to reduce transitional stresses [25, 92]. The most interesting designs that Groves et al. (1992) proposed were bonded epoxy wedge cones and integral wedge cones wound from graphite epoxy [25]. Groves et al. (1992) concluded that the strongest candidate was the integral wedge design, which showed potential to reach higher shear strengths than those it was tested too [25]. However, valuable insight was given on how hydrostatic compression affected the epoxy wedge cones.

The pre-load on the epoxy wedge cones was set by the clearance between the internal plug and the internal wall of the tube and the amount by which the wedge was tightened.

The hydrostatic compression from radial loading increased the shear strength of the epoxy adhesive exponentially [25]. But this hydrostatic compression can only be achieved with the internal compression plug in place. Without it the tube would be crushed. Groves et al. (1992) also reported that the through-thickness compressive stress component suppressed any fracture dominated interface failure at the joint [25].

3.3.1 CRITICAL EVALUATION

The double collet gripping system, illustrated in Figure 3-9, developed by Carroll (1994) initially revealed two difficulties [8]. First, some concern was expressed about not having any end reinforcement. The direct contact of the metal collets with the brittle specimen could lead to unnecessarily high transitional stresses. This could be one of the reasons Carroll (1994) did not have complete success with the proposed solution [8]. Second, due to the existing design of the gripping system, the specimen had to be sectioned before removal. This made it difficult to get an idea of the extent of the damage and reveal any other problems, as well as time consuming. A more in depth evaluation was conducted to determine if any other abnormalities could cause premature failure or give erroneous results under cyclic loading conditions.

The gripping system was tested cyclically under various loading conditions for any indicating problems that could produce abnormal leakage and/or grip slippage. This evaluation revealed two inter-linked problems: (1) fluid containment and (2) inconsistent radial loading from the gripping system.

3.3.1.1 FLUID CONTAINMENT

The hydraulic fluid was contained with a single O-ring in a brass plug that was placed above the mandrel. The plug was above the outside collet and did not receive the radial compressive loading needed to allow tightening of the plug to the internal wall. With sufficient cracking on the internal wall of the specimen, the hydraulic fluid could leak past the O-ring through the first few internal plies. Contributing to the problem was the variation in the internal diameter from specimen to specimen, which was as much as ±0.025 mm (±0.001 inch). This results in an inconsistent gap between the plug containing the O-ring and the internal diameter. With no radial compressive loading the contact pressure between of the O-ring on the internal wall of the specimen would vary.

3.3.1.2 RADIAL LOADING

Initially the problem of slippage was interpreted to be the inability of the gripping system to grasp the specimen. An abrasive surface such as sandpaper was placed between the collets and the specimen to alleviate slippage. An analysis revealed that success depended on the applied radial load and not the abrasive surface. Ultimately many factors contributed to inconsistent radial loading on the ends of the specimen.

The outer collets were loaded into the collar (i.e. grip), with a restraining ring, which held the collet and was tightened by hand. Tightness was measured by the gap between the restraining ring and the collar (i.e. grip). The changing outer diameter, from specimen to specimen, made it impossible to obtain the same radial load for each specimen. The changing outer diameter of the specimen also influenced the seating of the specimen on the bottom of the collar. The bottom of the collar was considered to be the most preferred seating, in order to maintain a constant testable section on the specimen and a maximum area to apply the collet loads on the ends.

The main problem was the configuration of the outer collet. The outer collet was placed in the collar in such away that it did not allow for self-tightening after the axial load exceeded the bolt pre-load. This can be observed in Figure 3-9. In addition, the collets were under sized and could not transfer a sufficient radial load to avoid slippage. The collets were also being plastically deformed and cracked under normal loading conditions. The most detrimental aspect to the performance of the specimen was the loading sequence. The outer collet was hand loaded before the inside collet. Using this sequence of loading the specimen would not be supported on the interior wall during the initial stages of loading. Thus allowed the inside wall to move freely and fiber buckling to take place [1]. Acoustic emissions were also detected when the specimen was loaded in this manner. Acoustic emissions are a good indication of matrix cracking. Examination of the ends of the specimen after testing revealed that the outer surface, contacted by the collet was no longer uneven and out of round, but was smooth and conformed to the indentations of the collets. The contacted outer surface was also 'whitened'. The phenomenon of 'whitening' has been investigated and is attributed to interface debonding and matrix cracking [63].

3.3.2 CONTINUING EVOLUTION

To overcome the fluid containment and inconsistent radial loading problems, major redesigning of the gripping system was required. In order to overcome these problems the topic of end reinforcement had to be addressed to reduce the transitional stresses (i.e. to develop a more consistent radial load). The ASTM Standard D2105 does not address the topic other than stating that the gripping system is required to be self-aligning and that no crushing loads could be applied to the ends of the specimen [87].

Since the existing gripping system met the ASTM Standard D2105 requirement of being self-aligning and the gripping system was in good shape, it was used as the basis for a new design, illustrated in Figures 3-10 and 3-11. Redesigning of the gripping system was separated into the two related problems of fluid containment and inconsistent radial loading from the gripping system.

3.3.2.1 FLUID CONTAINMENT

To resolve the fluid containment problem, the amount of internal radial deflection was decreased, and a larger O-ring was added to increase the sealing surface area. The brass plug from the design developed by Carroll (1994) was replaced with a high strength steel plug (ASTM 4340) to minimize the internal radial deflection [8]. The position of the brass plug above the internal collets, observed in Figure 3-9, was also in question because it was unclear if the brass plug was receiving radial loading from the external collets to ensure a proper seal. The steel plug was placed below the internal collets, as shown in Figure 3-10, in the new design to ensure a proper seal. Since an internal displacement is detrimental to the specimen, several high strength steel plugs were made of varying sizes to ensure a tighter fit on the internal diameter of the pipe. Anti-extrusion rings were also added to ensure that the O-ring did not extrude through the gap between the plug and the internal wall of the pipe at pressures above 10.3 MPa (1500 psi) [59]

3.3.2.2 RADIAL LOADING

Sufficient radial loading must be applied to the brittle composite specimens with the metal collets to prevent any slippage without causing any other detrimental effects. This is somewhat complicated by the uneven and non-circular outer surface caused by the manufacturing process. In order to resolve this problem, modifications were required for both the specimen and the grips.

To reduce the transitional stresses and prevent any detrimental effects, the ends of the specimen were potted in epoxy to reduce the effects from the collets. The insight to this idea resulted from Groves et al. (1992), who showed that hydrostatic compression caused by the collet increased the shear strength of the epoxy adhesive exponentially [25]. Valuable insight was also gained from Xia & Ellyin (1998), who studied the epoxy resin used in this investigation [105].

The epoxy material used is generally known as 'coldcure epoxy'. This resin, EPON 828, is a reaction product of epichlorohydrin and bisphenol A with a corresponding hardener of methylenebiscyclohexylamine [43].

The epoxy potted ends were then machined to give a constant diameter, circular outer surface to the specimens. This soft epoxy layer suppressed any fractures at the collet and specimen interface, as well as, reduced the transitional stresses.

To ensure that the collets did not plastically deform and crack under normal loading conditions, a new set of thicker and longer, outer collets were made from a high strength steel (ASTM 4340). These collets were made longer to decrease the radial loading on the specimen and reduce any detrimental effects. To eliminate the dependence of the outer collets on the pre-loaded bolts, the collets were redesigned to be self-tightening after the axial load exceeded the total pre-load, see Figures 3-9 and 3-10. In order to accommodate the new design and the new external collets, the grips had to be parted and expanded. The original taper was maintained because of space restrictions.

The most detrimental aspect to the performance of the specimen was the sequence in which the specimen was loaded into the grips and the amount of control over the radial load. An INSTRON hydraulic screw driven testing machine was used to perform all loading functions on the gripping system. This allowed for fine and repeatable control over the radial load, applied to the specimen. To ensure that the specimen was supported on the interior, the inside collets were loaded first, to 88,964 N (20,000 lbs.). Applying an internal load (i.e. loading the internal collets first) places the fibers in the ± 66^0 plies in tension, not allowing fiber micro-buckling to take place [1]. This also does not allow the inside wall to deform when the external collets were loaded to 177,928 N (40,000 lbs.). To ensure even loading of the collets and to lower the amount of stress concentration, radial washers were added to the base plate. (Observe Figures 3-10 and 3-11) With radial washers the diameter of the boltholes were increased to ensure trouble free loading of the external collets.

3.3.2.3 SPECIMEN PREPARATION

Tubular specimens, 355.6 mm (14 in) in length, were cut from five of the 5 m (30 foot) sections of the commercially wound 60mm (2.375 in) fiberglass pipe. The specimens were mounted on a mandrel, which was specially designed to maintain the inside center. This was required due to the non-circular shape of the outer surface. The specimens were then machined to a finished length of 348.0 mm (13.7 in) and 82 mm (3.25 in) from both ends were lightly sanded with 120 grit emery cloth to allow proper bonding of the

Cold-Cure epoxy to the composite surface. The machined end faces were coated with a wax to protect them from the epoxy.

An acrylic mold was used to pot the ends of the specimens into 'coldcure epoxy' [43]. The specimens were cured in an autoclave at 40° C (104° F) for one-hour and thirty minutes, and then at room temperature for one day. They were placed in a 4-jaw chuck to center them to the outside diameter, so as not to cut the fiber glass when machining. The epoxy was machined to a constant outer diameter of 64.26 mm (2.53 in), as illustrated in Figure 3-12.

3.4 SUMMARY

The biaxial testing apparatus was developed in-house to take advantage of an MTS uniaxial resonant fatigue testing machine. The original modifications to the system were made for monotonic biaxial testing by Carroll (1994) [8]. The results of several cyclic tests conducted with the apparatus revealed several problems with regard to the testing apparatus and the gripping system. These problems included: slow data gathering affected by signal noise, uncertainty in reading from the instrumentation, and unexplained control system shut downs. To overcome these problems a faster data acquisition system was added along with an analog filtering system. To ensure a level of certainty in the data, the instrumentation was calibrated. The source of the control system shut down was determined to be power fluctuation caused within the building. These changes ensured a certain level of confidence in the testing apparatus.

The gripping system implemented in this investigation was initially developed for a thinner walled tube, which caused a few problems, when testing thicker tubular specimens [8]. These problems included: the specimen slipping from the grips, inconsistent loads on the collets holding the specimen, maintaining a seal on the specimen, and damage to the grips during loading.

To over come the above problems, the gripping system was totally redesigned. The new design focused on fluid containment, radial loading through the pipe wall, and end reinforcement. The objective was to apply a sufficient amount of radial load to hold the specimen, without damaging it and/or allowing it to slip. Insight was gained from Groves & Chamis (1992), who showed that epoxy resin would reduce the effect of the outer metal collets on the outer metal collets on the specimen. The hydrostatic compression applied to the epoxy from the outer collets, increase the bonding and shear strength of the epoxy adhesive exponentially [25].

The addition of a non-deflecting inner plug with a larger O-ring and an anti-extrusion ring solved the problem of maintaining a seal. This was noted by the fact that no leakage was seen in the grips, which could only have been caused by damage introduced during the loading of the grips.

To ensure consistent loading in the collets (i.e. consistent radial loading in the specimen), the grips were loaded on an INSTRON hydraulic screw driven testing machine. The problem of the inconsistent radial loading due to the slight changes in the geometric features between specimens was improved by the epoxy added the ends of the specimens.

Table 3-1 Summary of Data Acquisition System

PRESSURE	
Accuracy	± 0.4 MPa (± 60psi)
Resolution	0.096 MPa (14 psi)
A/D Convesion	10.342 MPa/V (1500 psi / V)
LOAD	
Accuracy	± 560 N (± 126 lbs.)
Resolution	373 N (84 lbs.)
A/D Convesion	37365 N/V (8400 lbs./V)
STRAIN	
Accuracy	± 0.05 % strain
Resolution	0.01% strain
A/D Convesion	0.5% strain/Volt
OIL VOLUME	
Accuracy	± 0.165 mL (± 0.010 in^3)
Resolution	0.177 mL (0.011 in^3)
A/D Convesion	17.69 mL/V (1.079 in^3/V)
STROKE	
Non-Linearity	± 2.5 mm (± 0.1 in) over full range
Resolution	0.125 mm (0.00492 in)
A/D Convesion	6.25 mm/V (0.5 in/V)

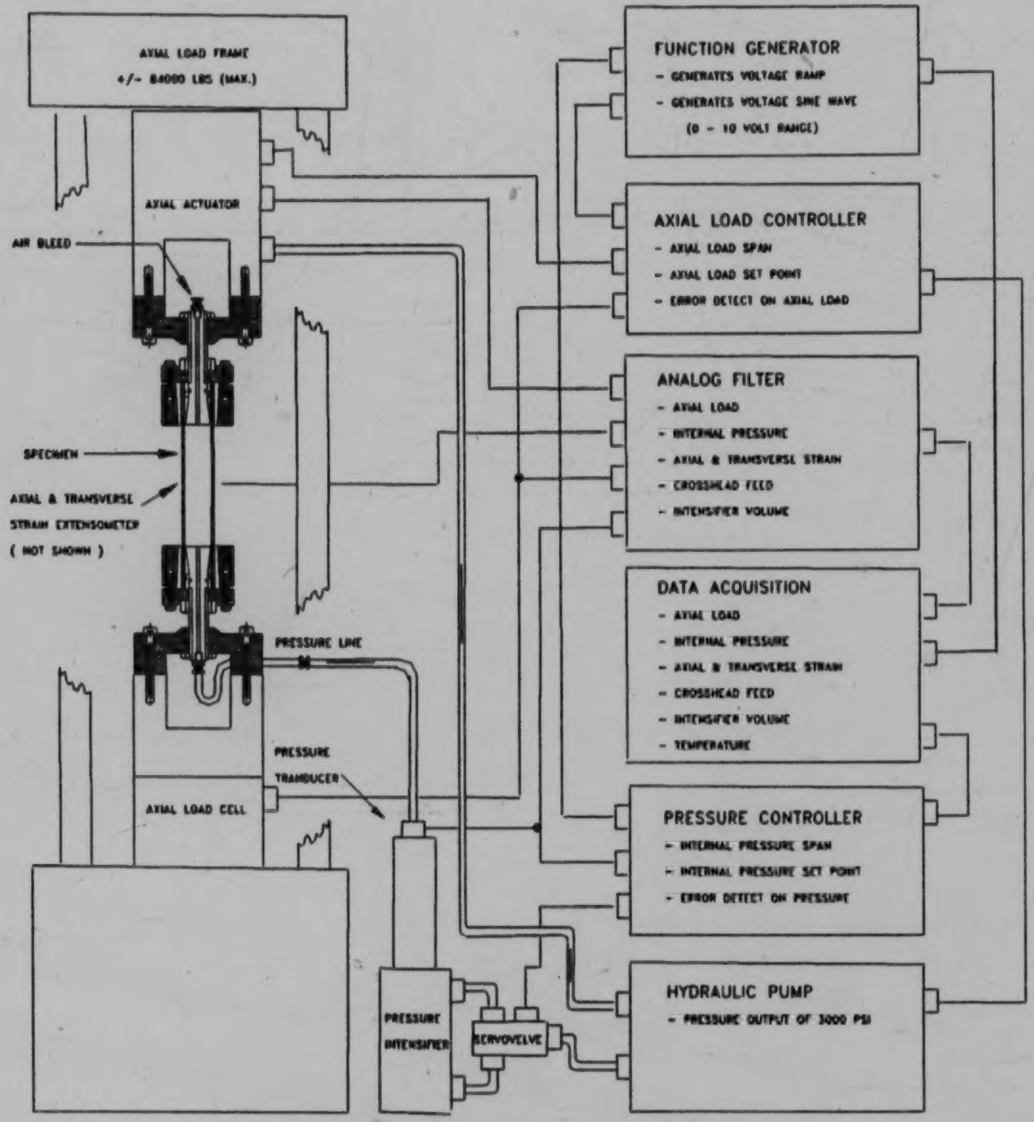

Figure 3-1: Schematic of the testing apparatus setup for both monotonic and fatigue testing of fiberglass epoxy pipe, figure adapted form Carroll (1994).

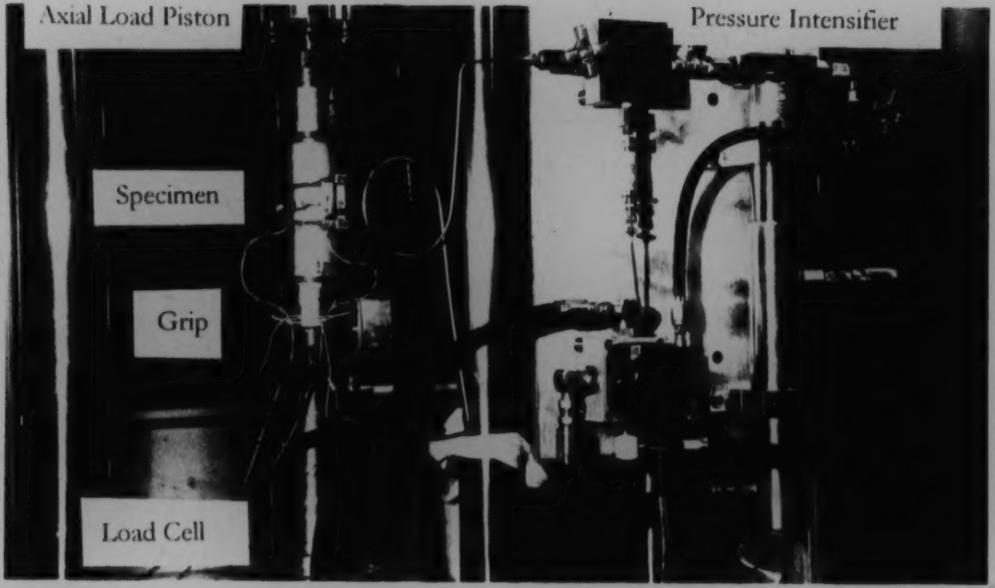

Figure 3-2: A photograph of the biaxial testing machine. On the right the pressurization system developed in-house. On the left a specimen placed in the redeveloped gripping system.

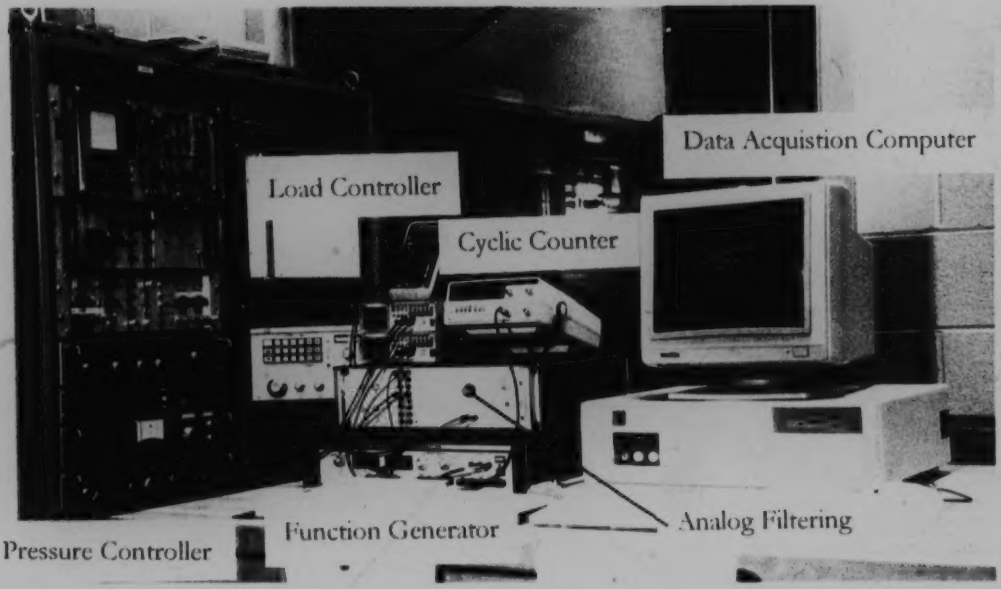

Figure 3-3: A photograph of the MTS axial load and the pressurization controllers, along with the data acquisition system.

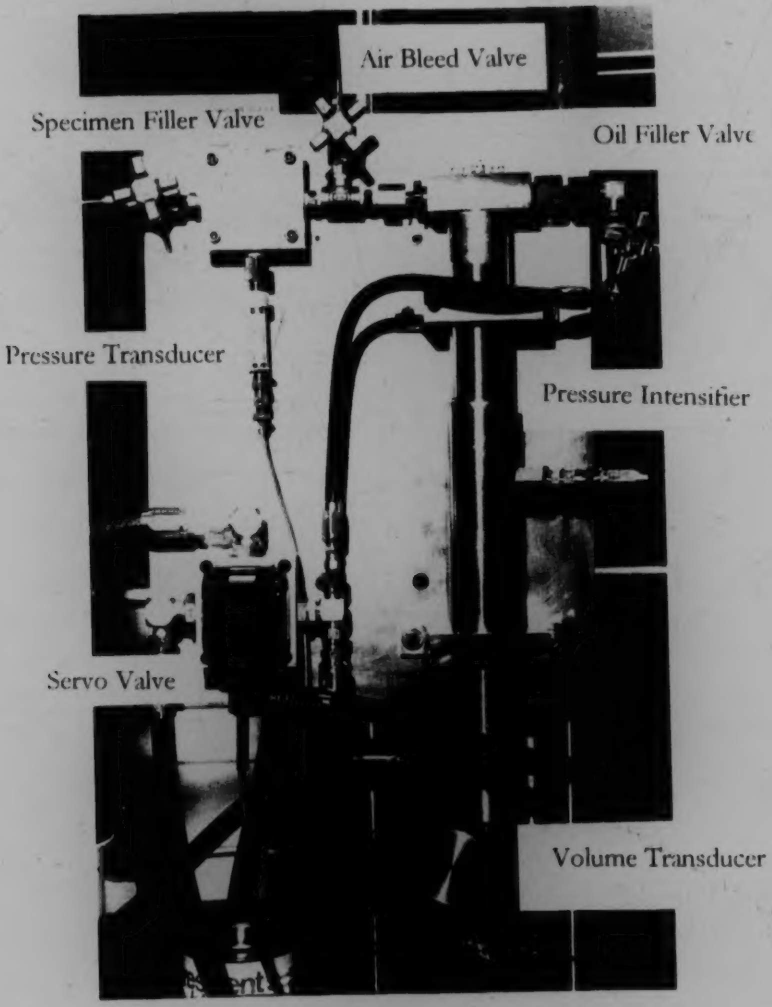

Figure 3-4: A photograph of the pressurization system developed in-house.

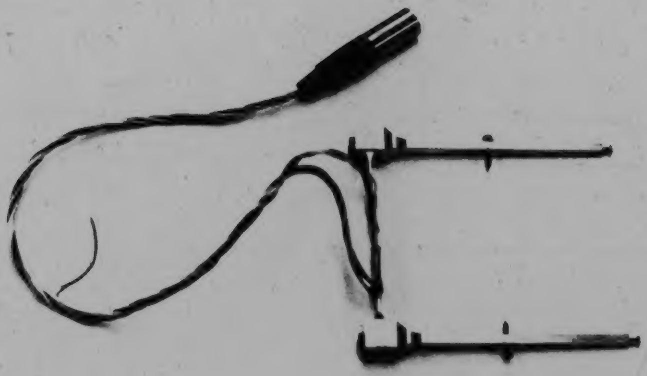

Figure 3-5: A photograph of the hoop extensometer developed in-house.

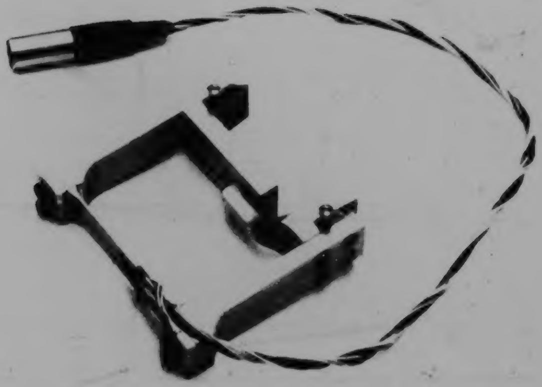

Figure 3-6: A photograph of the axial extensometer developed in-house.

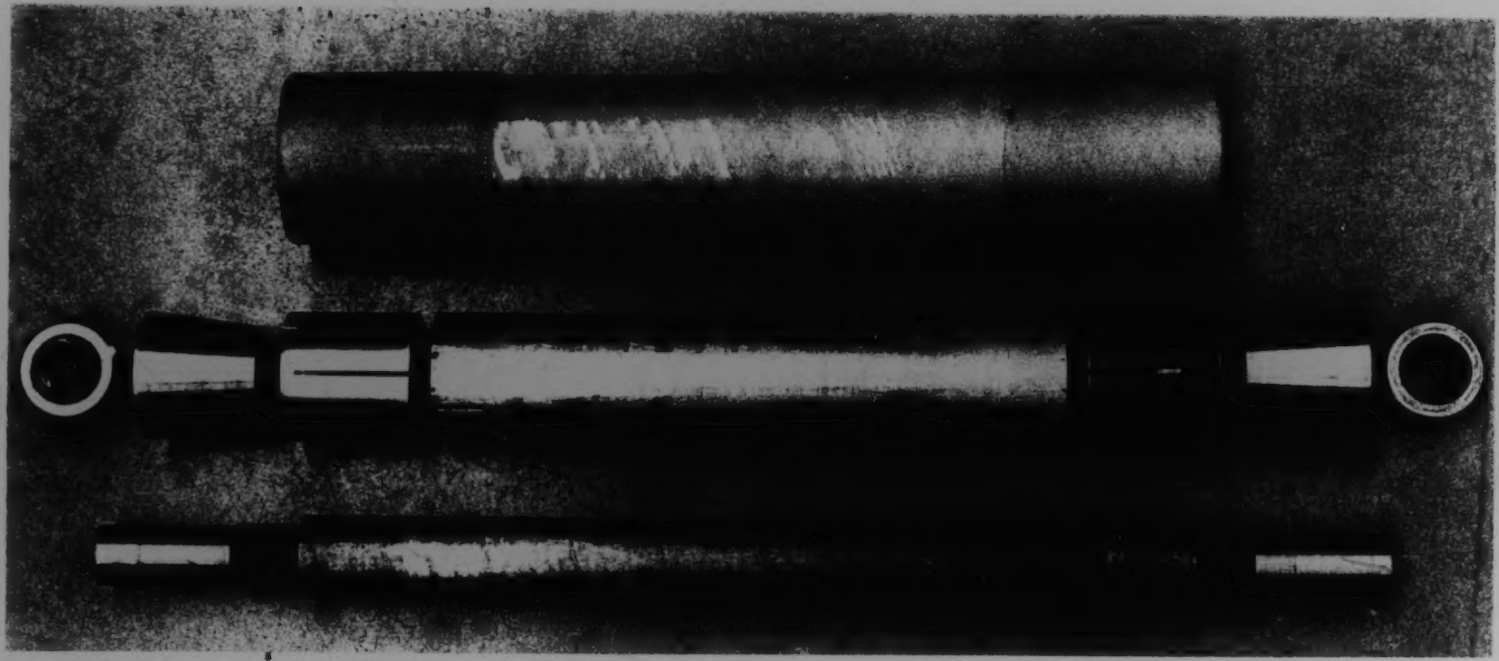

Figure 3-7: A photograph of the disassembled mandrel used to centering the specimen for indexing and machining.

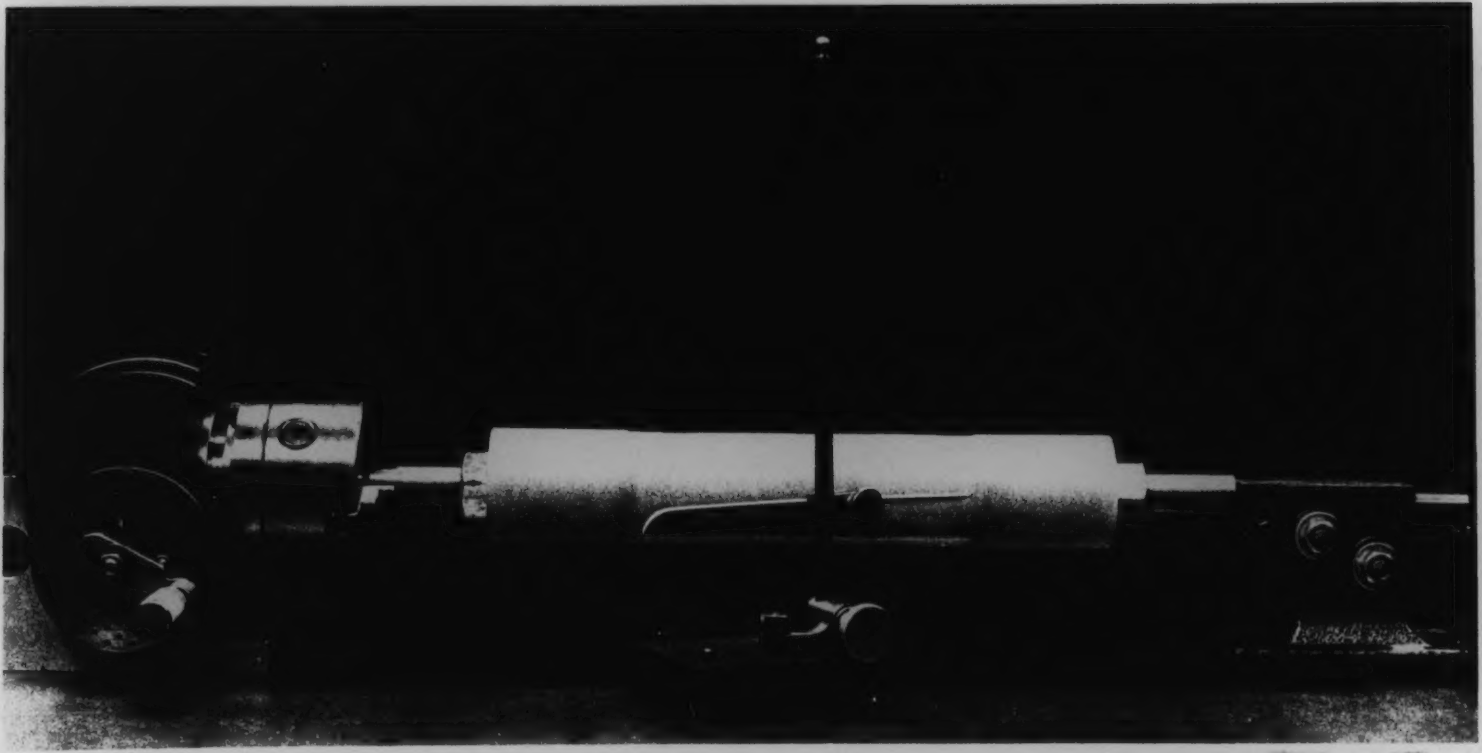

Figure 3-8: A photograph of a specimen mounted in the centering mandrel, places in an indexing dividing head. This device is used to mark surface lines parallel to the centerline for aligning the hoop and axial extensometer and strain gauges.

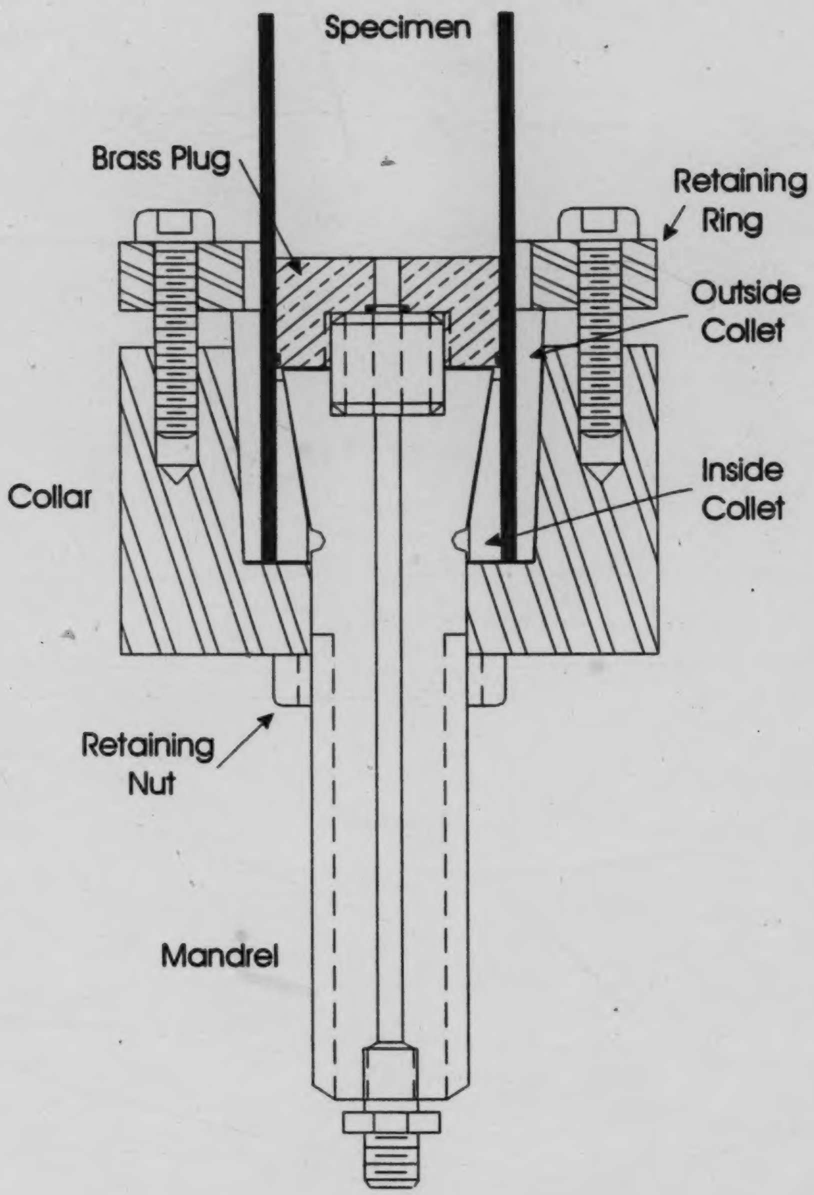

Figure 3-9: Schematic illustration of the grip assembly developed by Carroll (1994), figure adapted from Carroll (1994).

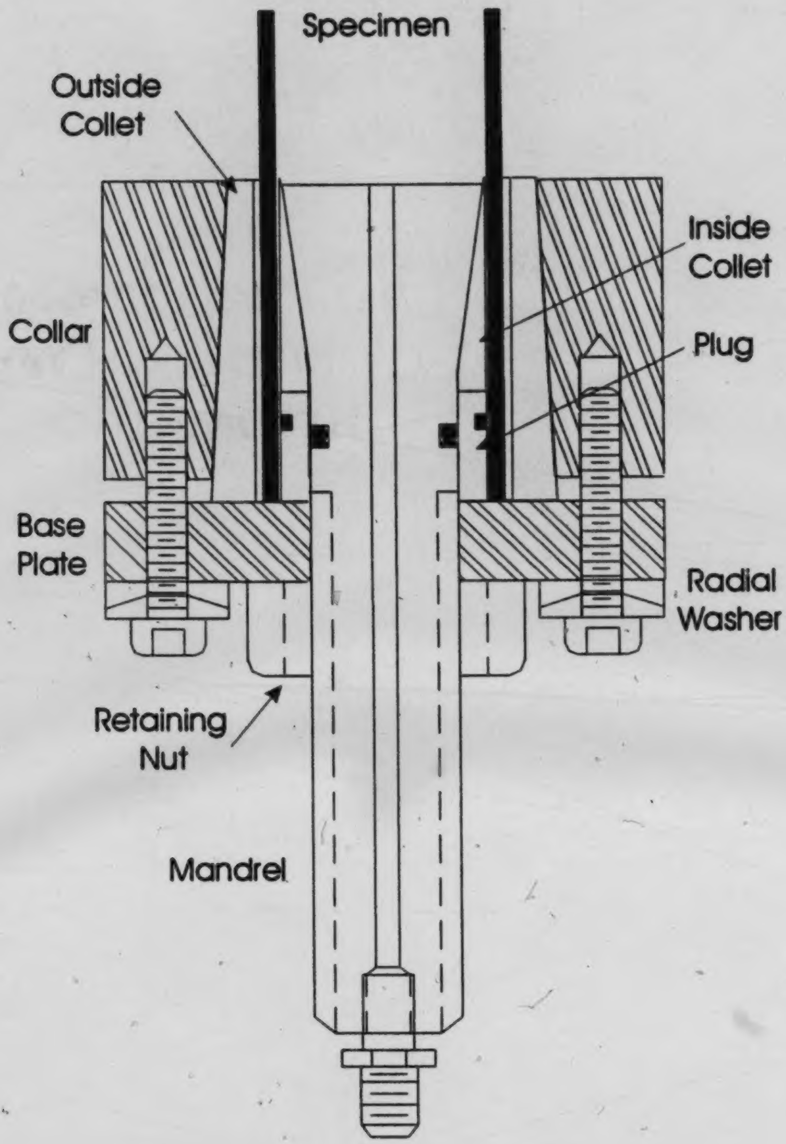

Figure 3-10: Schematic illustration of the redesigned grip assembly.

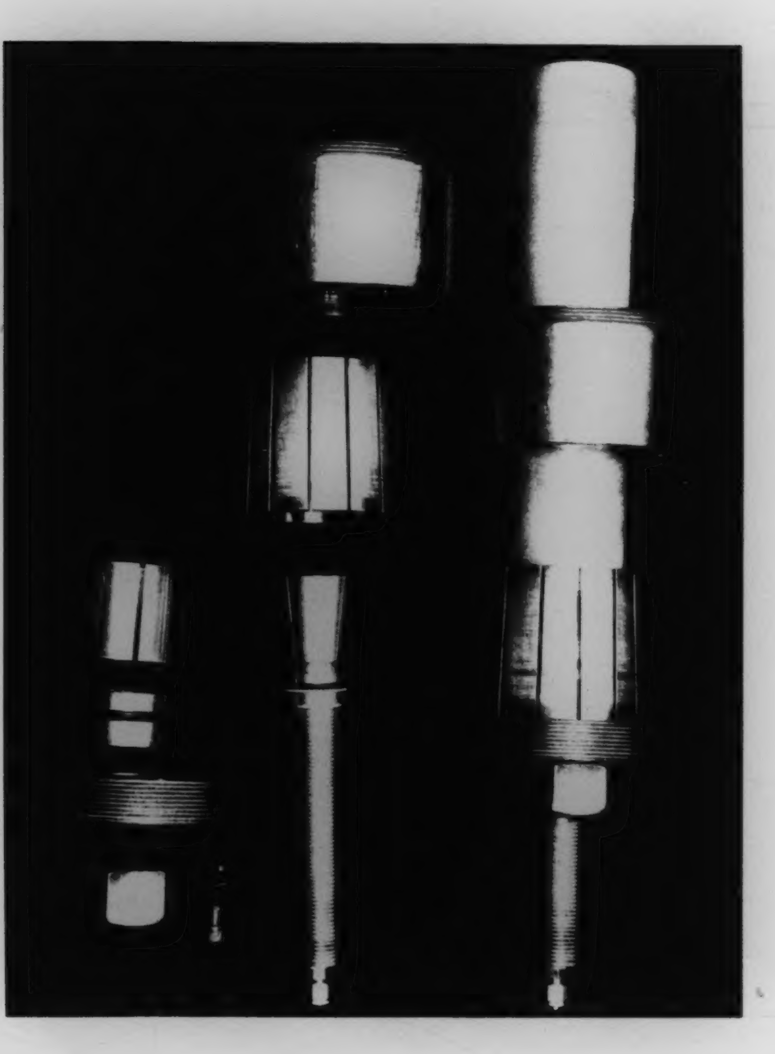

Figure 3-11: A photograph of the partially disassembled and assembled grip assembly.

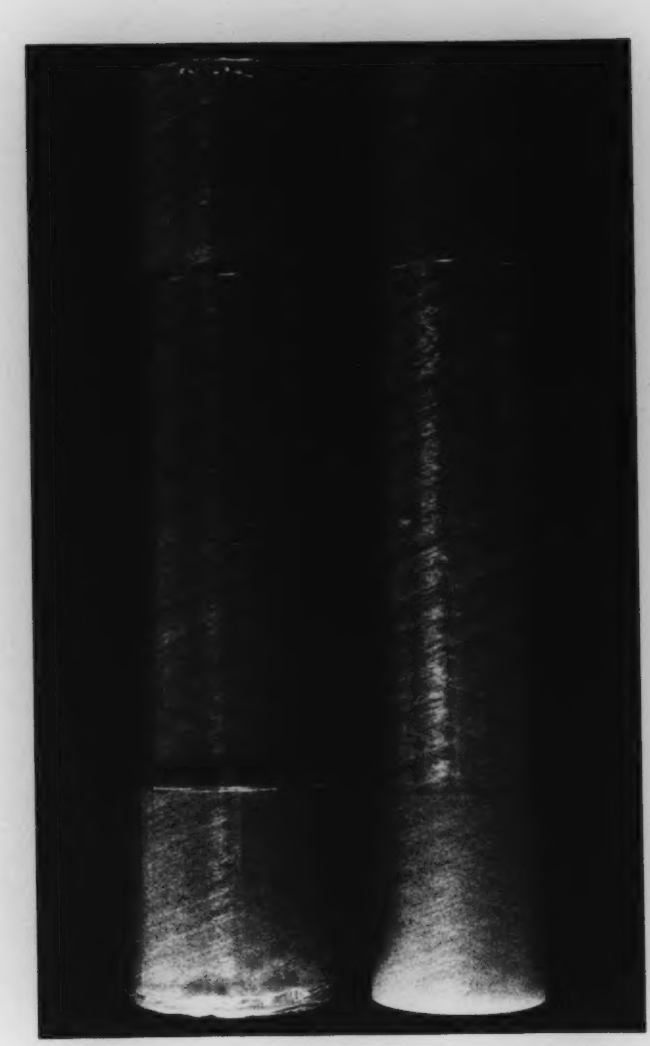

Figure 3-12: A photograph of two specimens with end reinforcement after being potted in ColdCure Epoxy, showing before (left) and after (right) of machining.

CHAPTER 4

LEAKAGE FAILURE POINT

4.1 INTRODUCTION

The preferred design condition of all pressure containment devices is to have a leakage failure prior to a catastrophic structural failure. Polymeric composite pipes are no exception. The leakage from a polymeric matrix composite pipe is dependent on the damage accumulation, which is dependent on load, loading history and conditions under which it is applied [33].

The critical aspect of experimental testing of a composite material is the consideration of a failure point. With load bearing structures the failure point can be set at which the structure can no longer support load; thus, specifying the ultimate failure envelope [31, 32]. The underlined function for a composite pipe without an internal liner is to contain a pressurized fluid. When leakage occurs due to the development of matrix damage, the composite pipe no longer can carryout the intended function. Functional failure, which occurs prior to the complete loss of the structural load carrying capacity of multidirectional fiber-wound pipe, can also be used to describe the state of damage in which micro-cracks coalesce to form cracks through the wall thickness, forming a path for the fluid flow.

The point of failure in terms of leakage is dependent on the amount of damage that is allowed to occur. For example, the failure point could be the initiation of leakage, or after a certain volume of leakage, or when there is a change in the leakage rate. The added benefit to leakage as a failure criteria, is that it is independent of the test type, be it monotonic or fatigue, as well as the mode of failure, structural or functional. As for structural type of failures, the characteristic leakage curve is seen as the sudden loss of fluid. In addition, defining a failure point independent of the failure mode allows for mapping of the complete biaxial leakage envelope. Ultimately, the main goal is to develop a leakage envelope, based on matrix dependent failure criterion, as leakage is dependent on progression of micro-cracks in the matrix to coalesce and form cracks through the wall thickness allowing for the fluid flow.

4.2 LEAKAGE FAILURE

The ability of a composite pipe to resist internal damage and arrest cracking under operating conditions is very important to the designer. The fundamental knowledge of damage initiation and progression on a micro and macro scale can aid in the development of a realistic design for long life. However, most of the experimental investigations, found in the literature, have focused on the structural aspect of pipe and pressure vessel testing, without addressing the effectiveness of composite pipe to resist internal damage and arrest cracking or noting the amount of internal damage accumulated prior to structural failure.

A literature review revealed a lack of published laboratory test data as well as information pertaining to leakage failures of composite pipe. However, there is one published article in which the experimental system contained a conductive mesh to indicate the point at which the fluid penetrated through the wall [101]. The point of functional failure was described as the initiation of surface wetting by Wang et al. (1997),[101].

The implementation of a conductive metal mesh to indicate the point surface wetting was considered for the present apparatus. However, implementation requires a conductive test fluid such as water. Hydraulic fluid, which was used as the working fluid
7 in this investigation, is nonconductive, therefore, this investigation was depended on measurements of the fluid volume of the intensifier to determine the leakage curves.

4.3 LEAKAGE CURVE

An uncorrected graph of leakage, measured from the intensifier, verses pressure for a monotonic test is illustrated in Figure 4-1. From the leakage curve it appears that the specimen started off by leaking at a very fast rate, which then leveled off, and subsequently increased once again towards the end of the test. There is a problem here, it appears to indicate that the specimen began to leak with little to no applied internal pressure. This then requires further examination.

To determine the failure point from leakage, it is important to understand and account for the complexities of the system and the condition of the specimen. This information is pertinent to extracting a ' true ' leakage curve. A leakage curve, which is determined by the change in volume of the intensifier, is directly affected by three main factors: specimen expansion, compression and leakage.

4.3.1 THE SPECIMEN EXPANDED VOLUME

The application of the internal pressure and/or axial load causes the specimen to deform, increasing the amount of fluid volume in the specimen. If the expansion volume is not accounted for, it may be erroneously interpreted as leakage, therefore, it is imperative to account for this fluid volume in determining the leakage curve.

To account for the expansion volume, the expanded shape of the deformed specimen under loading was first estimated. The grips introduce a non-deforming boundary condition causing a barreling shape [20,92]. Determining the expanded shape of the deformed specimen, which accounts for all the geometric imperfections, (described in Chapter 2) is a very complex task. One method considered was to determine the barrel shape experimentally. Thus requiring the placement of strain gauges on the interior wall as well as subjecting the specimens to many combinations of load ratios to obtain a realistic picture of the expansion shape. This method was considered to be impractical because of the geometric differences for each specimen, and the changing deformed shape.

Another method to determining the expanded shape was to estimate it from the general pipe deflection solution developed by Timoshenko & Woinowsky-Krieger (1959) [96]. This general pipe deflection solution takes into account the material properties of the pipe as well as the measured deflections. The solution for the expanded volume to the general pipe deflection given in Timoshenko & Woinowsky-Krieger (1959) is described in Appendix C.

The material properties used to approximate the expanded shape were determined from the pure internal pressure and axial tension monotonic testing. The deflections were measured from the hoop extensometer at the mid-length of the specimen and an axial extensometer centered at the mid-length.

In order to approximate the expanded volume using the deflections measured from the hoop and axial extensometer, the following assumptions were made: (1) The hoop deflection measured by the hoop extensometer at the mid-length on the exterior surface is the same as if it were measured on the interior surface. (2) The thickness around the circumference of the specimen is constant, leading to a constant radial expansion around the circumference. (3) The axial extensometer does not see any effects of radial and hoop expansion causing a barreling shape [20].

Sullivan & Chamis (1973) showed that there is a variation in strain between the inner and outer surfaces of a composite pipe under pressure and axial loading [92]. The small radial component, which makes up a portion of the mid-length hoop strain, might be able to account for the variation in the strain between the inner and outer surfaces of the pipe [76]. Without the knowledge of the geometric features including the defects (discussed in Chapter 2), it is difficult to determine the radial strain component with a stress analysis, which will vary around the circumference of the pipe. As well, to measure the radial component of the strain, one must be able to measure strain on the inner surface of the pipe also.

The radial and hoop expansion combined with the non-deforming boundary condition at the grips, cause a barreling shape which in turn off-sets the axial extensometer and/or axial strain gauge. This is further complicated by the variation in the wall thickness around the circumference, which can cause a slight twisting in the axial extensometer and/or the axial strain gauge offsetting the measured axial strain even further from the true axial strain. Using the axial stroke to measure the axial expansion instead of the axial strain might alleviate these problems. But the axial stroke will be affected by the flexing in the grips.

4.3.2 COMPRESSIBILITY

This investigation focuses on the mechanical properties of the composite pipe developed for a petroleum application. Hydraulic fluid is considered to have the least detrimental effects on the composite pipe and the pressure intensifier as well. The test fluid used in this application was an industrial grade hydraulic fluid, Esso Nuto H-46. A good understanding of the behavior of the hydraulic fluid exposed to the extreme test pressures and how the fluid volume is influenced, is of importance.

Compressibility ($\partial V / \partial P$) is essentially a decrease in fluid volume with an increase in pressure. Compressibility of the hydraulic fluid can easily be overlooked. Since most hydraulic systems operate at low-pressure conditions, most references consider the fluid incompressible (example see Michener (1980) and Vickers (1992)). Compressibility can be mistaken as weepage due to the decreasing fluid volume.

The bulk modulus ($\partial P / \partial V$), which is the reciprocal of the compressibility property of the fluid, is also often used in many references to illustrate the volume change [28, 34, 60, 79]. However, compressibility will be illustrated through out this study.

The compressibility of hydraulic fluid is only part of the volume change during pressurization. The overall volume change, which is the total compressibility of the pressure system, is depended on three main components: the compressibility of hydraulic fluid, the amount of aeration, and the amount of flexing in the pipe linking the intensifier to the specimen.

4.3.2.1 HYDRAULIC FLUID COMPRESSION

Determining the compressibility of hydraulic fluid, Esso Nuto H-46, is necessary to correct leakage curves. The compressibility can be determined in two ways: (1) measure the compressibility from pressure tests, or (2) determine the compressibility from compressibility tables [14]. For hydraulic fluid, Esso Nuto H-46, measuring the compressibility is highly preferred because it leaves fewer chances for error by assuming the properties of a dissimilar fluid.

The compressibility for hydraulic fluid was determined from the compressibility coefficient calculated from Equation 4-1. The compressibility coefficient describes the fluid compression characteristics.

$$\beta_f = \frac{1}{V_1} \cdot \frac{(V_1 - V_2)}{(P_2 - P_1)} \qquad 4\text{-}1$$

where V_1 and V_2 are the initial and final volume, respectively, after the fluid compression from the initial pressure P_1 to the final pressure P_2

The intensifier, with a total volume of 71.31 ml (4.35 in^3) was ramped up to the maximum pressure 68.95 MPa (10000 psi). The results from the compressibility test are plotted in Figure 4-2. Note the linear relation between the change in fluid volume and pressure. The hydraulic fluid was compressed 3.27 ml (0.199 in^3) at a maximum pressure, which corresponds to a change in volume to a change in pressure of

0.04619 ml/MPa (1.99E-5 in^3/psi). This translates into a compressibility coefficient of 6.477E10-4/MPa (4.465E-6/psi).

The changes in fluid volume, due to pressure based on the entire volume of the intensifier and the specimen, was determined from Equation 4-2.

$$\Delta V_f = V_{total} \cdot \beta_f \left(P_2 - P_1\right) \tag{4-2}$$

where V_{total} is the total volume of hydraulic fluid being pressurized, which is between 400 ml (24.4 in^3) and 450 ml (27.5 in^3), depending on the specimen volume.

The volume of the compressed fluid is affected by many factors and an explanation for this variation in compression requires an understanding of the oil at the molecular level. This type of understanding is beyond the scope of this study, however, an understanding of the overall effects on the compressibility of hydraulic fluid is noted [36]:

- The compressibility coefficient increases with the increasing temperature.
- The compressibility coefficient decreases with the increasing pressure.
- The compressibility coefficient decreases with the increasing viscosity.
- The compressibility coefficient decreases with the increasing density.

These effects are not a steadfast rule for hydraulic fluid and are dependent on the additives. Emphasized here is the importance of determining the compressibility of the fluid.

4.3.2.2 AERATION

The amount of air in the system has a considerable effect on compressibility at low pressures. Air being a thousand times more compressible than hydraulic fluid, can easily consume a large portion of the intensifier volume [34]. It is important to minimize the amount of aeration in order to ascertain the maximum attainable fluid volume of the intensifier. However, it is impossible to evacuate all the air from the system. To lessen the effect, a bleed valve was added to ensure that most of the air could be bled off before a test was initiated.

Air can be present in the system in two basic forms: dissolved air and entrained air. It is possible for air to change from one form to the other depending on the pressure conditions.

Dissolved air in the system, besides expanding the fluid slightly, has minimal effects on the compressibility of the fluid [34]. According to Henry's law, the solubility of a gas is directly proportional to the absolute air pressure and is fluid dependent [34]. Hayward (1961) suggests that the solubility of air in a mineral oil is between 12 and 6 percent per atmosphere (1 atm = 0.101 MPa). So when the fluid pressure reaches somewhere between 0.84 MPa (122 psi) and 1.7 MPa (246 psi) the solubility of air should be close to 100 %; thus, theoretically, dissolving all of the entrained air.

Undoubtedly, both forms of air in the system make it particularly hard to maximize the attainable fluid volume in the intensifier. But entrained air, which occurs as bubbles, has drastic effects on the system at lower pressures and occupies valuable intensifier volume.

Since air is very compressible, the effects of entrained air are very critical at lower pressures. At higher pressures, the volume, which is taken up by the air, can be subtracted from the system because the air present is either compressed to a minute amount or dissolved into the fluid. Nevertheless it still important to understand when to account for the effects of air, even though aeration in the system is negligible when compared to the total size of the system.

The compressibility of the entrained air can be found by two methods: (1) find the change in volume with pressure through the ideal gas law or (2) measure the change in volume with pressure in a two-phase solution of air and the test fluid.

Since the compressibility coefficient calculated form Equation 4-1 assumes a linear relation, the compressibility coefficient of air can not be obtained for the domain at hand, 0 to 68.95 MPa (0 to 10000 psi), because compression is exponential over this range. The best way to determine the change in volume with pressure is to assume that the ideal-gas model is valid, Equation 4-3 [99].

$$PV = mRT \tag{4-3}$$

where P is the air pressure, V is the volume of air, m is the molecular weight and R is the universal gas constant (8.3145 KJ/Kmol K), and T the temperature ($^{\circ}$K) .

Assuming a polytropic compression process Equation 4-4 is obtained [99].

$$P_1V_1 = P_2V_2 \tag{4-4}$$

From Equation 4-4 and Equation 4-1 the air compressed can be expressed as a percent change in volume as in Equation 4-5.

$$\text{Percent Change in Volume} = (1-\frac{P_1}{P_2})\times 100\ \% \tag{4-5}$$

Figure 4-3 illustrates Equation 4-5, which is plotted to show the compressibility of air at relatively low pressures. Note the comparison between the Ideal Gas Law and the test data re-plotted from Figure 4-1. It is apparent from Figure 4-3 the importance to bleed as much air as possible from the system. It is thus necessary to determine the amount of air present in the pressurized fluid and subtract it from the total, or bleed it off. The majority of the tests conducted will require an internal pressure of about 1.72 MPa (250 psi), thus the presents of air will be subtracted from the total volume of fluid.

4.3.3. TUBE EXPANSION

The tube, which connects the intensifier to the specimen, will also expand during pressurization. Since the tube has a small diameter, and the total length is small, the expanding volume will be small compared to the specimen expansion and fluid compression. This makes it difficult to measure the tubes expanding volume. However, the compressibility coefficient for the stainless steel tubing can be calculated from thin cylinder theory as in Equation 4-6 from McCloy et al. (1980) [60].

$$\beta_p = \frac{D}{tE} \qquad 4\text{-}6$$

where D is the pipe diameter, t is the wall thickness and E is the modulus of elasticity.

The stainless steel tube that was used to connect the intensifier to the specimen, had an inside diameter of 2.95 mm (0.116 in), a thickness of 0.95 mm (0.0375 in) and an elastic modulus of 196.5 GPa (28.5E6 psi). This translates to a compressibility coefficient of 1.574E-5/MPa (1.085E-7/psi) determined from Equation 4-6. Using Equation 4-7 the compressed volume can be found.

$$\Delta V_p = V_{tube} \cdot \beta_p (P_2 - P_1) \qquad 4\text{-}7$$

where V_{tube} is the fluid volume in the tube being pressurized, P_1 is the initial pressure, and P_2 is the final pressure.

For the stainless steel tubing with a total length of 1.371 m (54 in), the fluid volume is 9.35 ml (0.57 in^3). At a maximum pressure 68.95 MPa (10000 psi) the change in volume due to expansion is 0.0102 ml (6.19E-4 in^3). Note how negligible the change in volume for the stainless steel tube is compared to specimen expansion volume (14.25 ml) and fluid compression volume (20.47 ml), based on typical test fluid volumes. Greater expansion volume would be expected if hydraulic hose was used instead of stainless steel tubing.

4.4 LEAKAGE

The amount of allowable fluid leakage has been predetermined from the intensifier volume, 71.31 ml (4.35 in^3), which is shared with the expanded volume of specimen, the compression fluid volume and a fixed volume of air (illustrated in Figure 4-4). To determine the minimum leakage volume, the maximum measurements of the specimen under the applied load conditions have been approximated. Using a specimen similar to one found in this investigation, with an internal diameter of 49.53 mm (1.95 in), thickness of 6.35 mm (0.25 in), and a wetted length of 190.5 mm (7.5 in), the specimen will have a fluid volume of 367 ml (22.4 in^3). The total volume of the fluid being pressurized will be 458 ml (27.95 in^3). This includes the fluid volume of the intensifier 71.31 ml (4.35 in^3) and of the tubing plus fittings 19.7 ml (1.20 in^3), assuming a maximum strain limit of 2.0% strain in both the axial and hoop directions. The expanded volume of the specimen for the maximum shape is 22.46 ml (1.37 in^3) and for the Timoshenko & Woinowsky-Krieger (1959) shape is 14.25 ml (0.87 in^3) (Expanded volume determine from Appendix C) [96]. Assuming the Timoshenko & Woinowsky-Krieger (1959) shape is the correct shape for this exercise, and failure does not occur until after the maximum operating pressure of 68.95 MPa (10000 psi), with a compressed volume of 20.47 ml (1.25 in^3) [4.7]. The compiled assumptions then give a minimum leakage volume of 34.58 ml (2.23 in^3) which is 48.5 % of the maximum intensifier volume.

It is important therefore, to correct for changes in compression due to leakage. Using the above example, the minimum leakage volume is 34.58 ml (2.23 in^3). Subtracting this leakage volume from the total pressurized fluid volume will decrease the compressed volume by 1.637 ml (0.01 in^3). The total volume must be recalculated after leakage is initiated.

4.5 CORRECTION CONSIDERATIONS

The leakage corrections for monotonic testing are quite different from those required for fatigue testing. In order to implement these corrections, a good understanding of the test conditions is required.

In monotonic testing, a biaxial load is increased until the specimen fails. The fluid volume will start decreasing at a very fast rate and then level off. Toward the end of the test the rate of change of fluid volume will increase once again (illustrated in Figure 4-1). As the internal pressure is applied to the specimen the air trapped in the system will start compressing to the point where it is 94% compressed at 1.72 MPa (250 psi). This volume taken up by air can be subtracted from the total volume. The specimen will also start expanding and the hydraulic oil will start compressing as soon as the test is initiated, decreasing the fluid volume in the intensifier. This can be observed in Figure 4-4. As leakage occurs, the total fluid volume will decrease, requiring a correction to the hydraulic fluid compression. The corrected leakage can be served in Figure 4-5.

In fatigue testing, the loading signature is much different. A biaxial load is increased to a mean load condition, compressing the hydraulic fluid and expanding the specimen. Cyclic loading is then initiated, increasing and decreasing the compressed fluid volume and increasing and decreasing the expanded specimen volume. The maximum and minimum expanded volume will stay relatively constant until creep occurs. The maximum and minimum compressed fluid volume will also remain relatively constant until the specimen starts weeping. With time there will be a small amount of movement in the grips, due to settling. This produces an offset in the leakage volume, which can be corrected by monitoring the movement. To ensure a stable volume reading, which is independent of the variances in the system, the average of the total oil volume is sought.

Since the leakage correction is dependent on all of the measured variables, problems will be encountered. Figure 4-4, illustrates the effect of strain gauge failure. Since strain is used to compensate for specimen expansion, an error will be seen in the specimen expansion curve. Note Figure 4-5, where the effect of the strain gauge failure is compounded into the leakage curve. A robust failure point is required to overcome anomalies seen in the test data.

4.6 FAILURE POINT

Detecting matrix cracking inside a composite tube while *in-situ* is important. Cracks can be observed by sectioning after testing but this does not allow for *in-situ* determination of the damage-state. In order to determine the state of damage, in which micro-cracks coalesce to form larger cracks through the wall thickness, the leakage is monitored. Using the corrected leakage curve, leakage can be visually correlated to the level of damage.

Determining a point of failure, which describes the same level of damage independent of the biaxial loading conditions, is difficult, as well as having immunity to any errors. Two stages of leakage can be envisaged: (1) the initiation of leakage, and (2) a drastic change in the leakage rate as illustrated in Figure 4-6.

The initiation point on the corrected leakage curve indicates that the amount of micro cracking has become sufficient to develop fluid loss. This is similar to Wang et al. (1997) where the failure point was indicated as the initiation of any external weepage [101]. The indicated point of leakage on the corrected leakage curve is a good indication of functional failure, and it is also sensitive to factors such as changes in the specimen shape and intensifier leakage.

The point of intense leakage, also known as the knee on the corrected leakage curve, is found from the slope of the curve before and after the change in the leakage rate. This change in the leakage rate is a good indicator of the state of macro-cracks through the wall thickness. As well, the point of intense leakage describes a state of damage independent of failure mode (i.e. delamination causing pinholes, sudden bursting, and uniform matrix cracking).

4.7 SUMMARY

Leakage was used to find the load at which the composite pipe could no longer fulfill its defined function. (i.e. hold and transport fluid efficiently) This is defined as the functional failure point, which in most cases occurs prior to the complete loss of structural load carrying capacity of multidirectional fiber-wound tubes. In some cases where there are high axial loads and small internal pressures, an abrupt structural failure is observed. Leakage seems to be a good way to describe the state of damage and also trace the rate of damage. Essentially leakage develops from the coalescence of micro-cracks that eventually form cracks through the wall thickness.

Examining the uncorrected leakage curve (illustrated in Figure 4.1) demonstrates the importance of understanding and accounting for the complexities of the system and the conditions of the specimen, in order to extract the leakage curve and determine the leakage failure load. Factors affecting the change in oil volume of the intensifier are: the expansion of the specimen compression of the oil and leakage.

The application of the internal pressure and/or axial load cause the specimen to deform, thus increasing the fluid volume in the specimen. The expanded volume was determined by estimating the expansion shape from the general pipe deflection solution developed by Timoshenko & Woinowsky-Krieger (1959) [96]. Even though, it does not predict the exact expansion volume, it does aid in correcting the change in intensifier volume.

Oil compression is the largest factor affecting the intensifier volume, a change in total volume of almost 5% at 68.95 MPa (10000 psi) as seen in Figure 4-2. However, the change in volume, due to fluid compression is very distinguishable, note the characteristic compression curve in Figure 4-1. The compressibility coefficient is expectable to fluctuation with temperature as well as increased pressure. (Temperature effects are discussed in Chapter 6) For the pressure range required in this investigation, the compressibility coefficient was considered constant.

Any type of aeration in the pressurization system is considered to be detrimental. Air being a thousand times more compressible then hydraulic fluid can easily consume a large portion of the intensifier volume as seen in Figure 4-3 [34]. Plotting the change in volume of air as predicted by the ideal gas law with the test data shows a good correlation. Note that the ideal gas approximates the air as well as the pressurization system under the effects of specimen expansion and oil compression.

Once the negative effect of aeration in the pressurization system was noted, a considerable amount of effort was directed to evacuating it. This included allowing the fluid to settle several times so that the maximum amount of air could be bled off before the testing was initiated.

With all the above mentioned corrections, the minimum volume that is devoted to leakage is only 48.5% of the total volume at maximum conditions, 34.58 ml (2.23 in^3). This still leaves ample volume to determine the initiation point of leakage and the initiation point of intense leakage.

These two leakage failure points were considered to be a good representation of the damage state, due to the fact that these points are based on a change in the rate of leakage. Since leakage correction is strongly dependent on all of the measured factors. It may have considerable uncertainly associated with it. This can be noted in Figure 4-4, which illustrates the effect of strain gauge failure on the correcting specimen expansion curve. Figure 4-5 shows were the effect of the strain gauge failure is compounded in to the leakage curve. As well, even with testing anomalies (strain gauge failure) these failure points can be approximated.

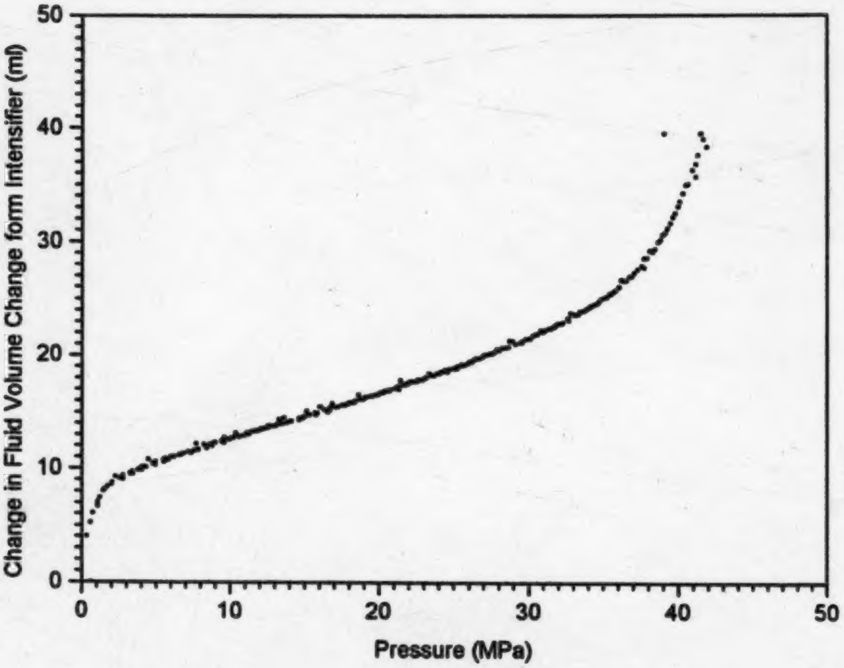

Figure 4-1: A plot of the change in fluid volume measured from the pressure intensifier verses the internal pressure, a monotonic test.

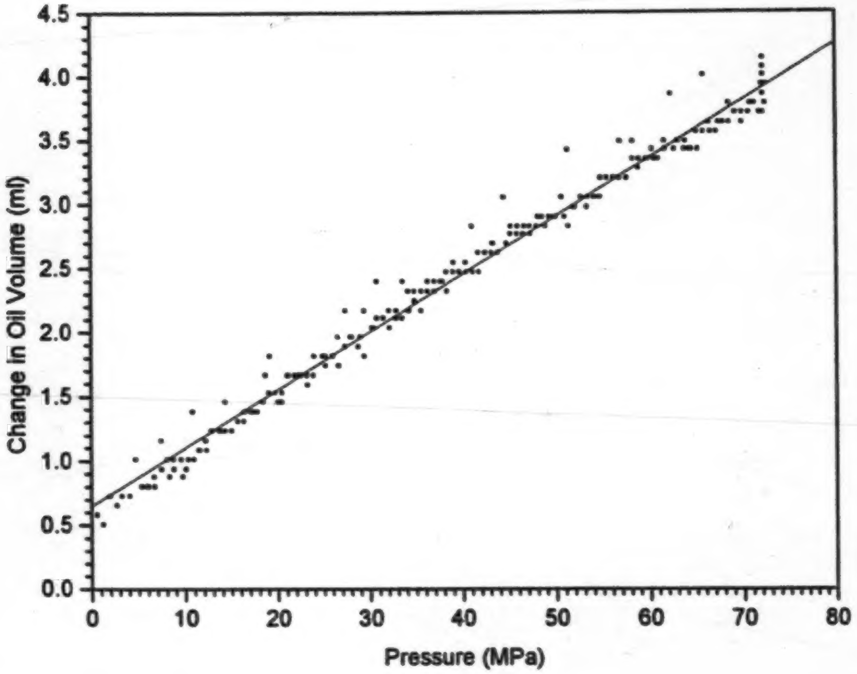

Figure 4-2: Plot of the decreasing fluid volume with increasing pressure. Determined from pressurization of the intensifier used to calculate the compressibility coefficient.

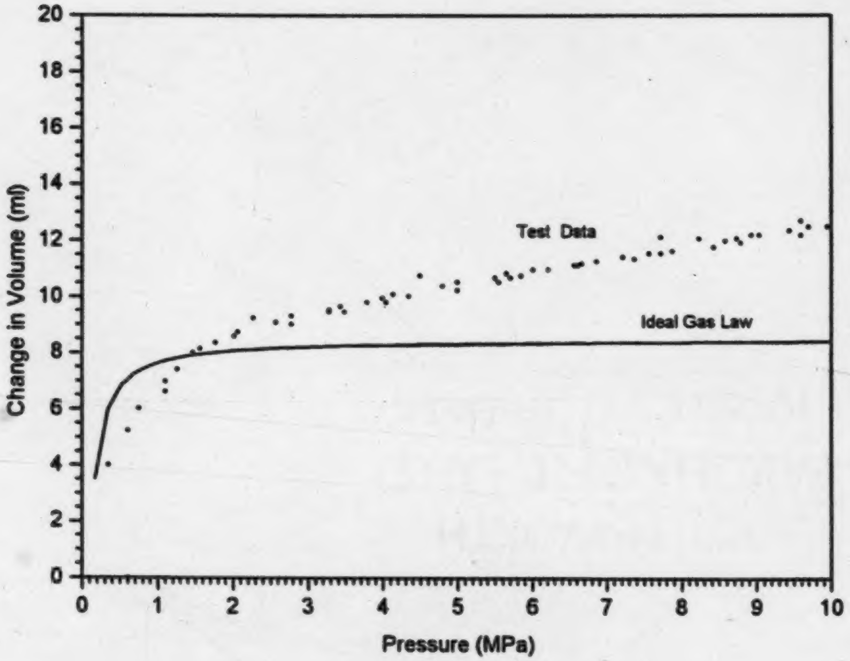

Figure 4-3: A plot of the change in fluid volume measured from the pressure intensifier verses the internal pressure compared with the change in volume for air calculated from the Ideal Gas Law.

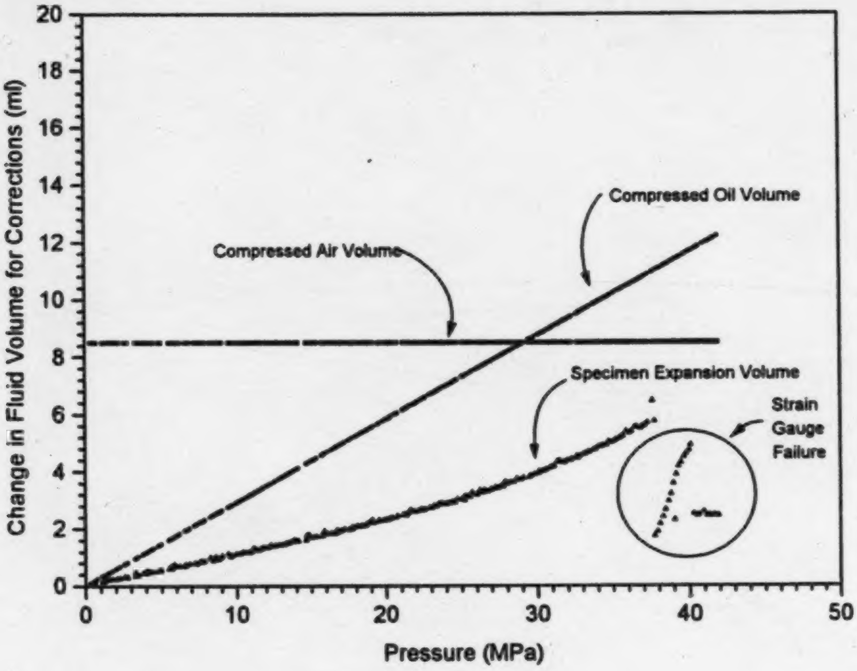

Figure 4-4: Plot of the correcting change in volume verses pressure for the added volume of air, oil compression, and specimne expansion.

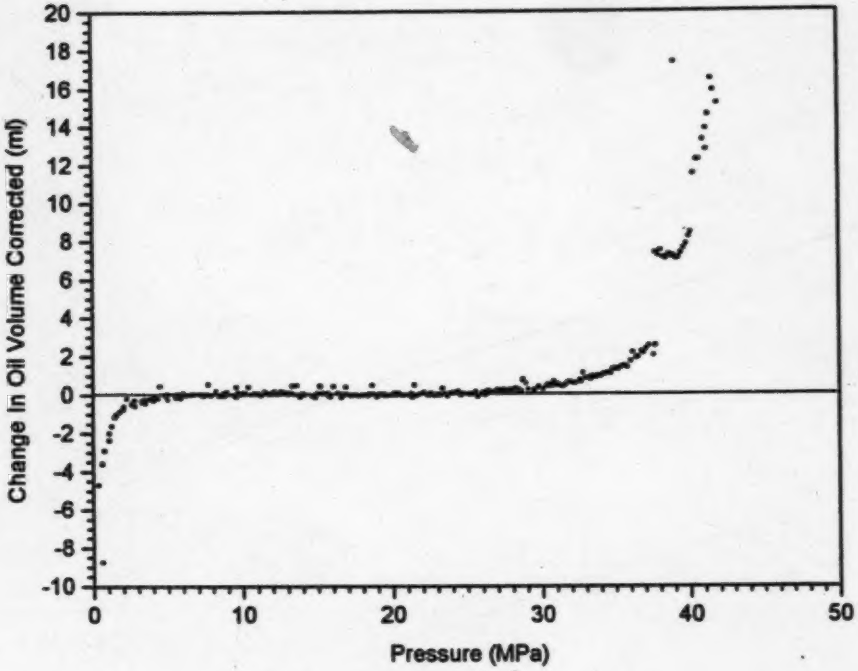

Figure 4-5: Plot of the change in volume corrected for the added volume of air, oil compression, and specimen expansion, for a monotonic test. Similar fatigue leakage curves can be observed in Chapter 6.

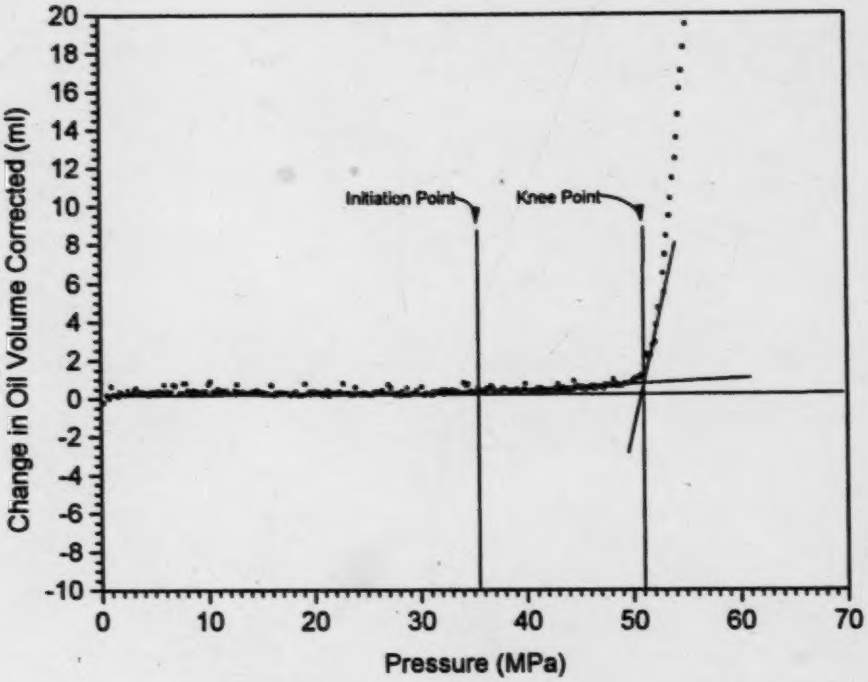

Figure 4-6: A plot of the change in fluid volume corrected verses the internal pressure. Note the initiation point of leakage and the initiation point for intense leakage (knee point).

CHAPTER 5

MONOTONIC TESTING

5.1 INTRODUCTION

This chapter focuses on the development of the biaxial monotonic failure envelope for the commercially wound multidirectional composite pipe described in Chapter 2. This investigation into the mechanical properties, such as strength, stiffness and the damage response of the composite pipe under biaxial monotonic loading, gives an essential understanding of the leakage mechanisms of this filament wound lay-up.

The stress-strain relationship along with the observed initiation and accumulation of damage, determined from leakage, provide insight into the functional behavior and characteristics of this composite lay-up. As well, the response to monotonic loading is an essential guide for the cyclic investigation.

5.2 TESTING PROCEDURE

To determine the load that the composite pipe could endure, a biaxial monotonic envelope was developed under stress control (load control). This envelope is an indication of the maximum functional overload conditions. The specified hoop to axial stress ratios applied to the specimen to define the envelope are listed below:

0H:1A The zero hoop to one axial stress ratio simulates a pipeline with a small amount of internal pressure and an increasing axial tension. Axial tension is used to determine the maximum load carrying structural capability of the pipe in the axial direction.

1H:1A The one hoop to one axial stress ratio is an equibiaxial load used to determine the failure envelope.

2H:1A The two hoop to one axial stress ratio simulates a 'pressure vessel' type of loading. The ends of the pipe are capped with an increasing internal pressure being applied.

1H:0A The one hoop to zero axial stress ratio simulates a long pipeline load with an increasing internal pressure. Pressure loading is used to determine the maximum functional capability of the pipe.

1H:-1A The one hoop to a negative one axial stress ratio was added to determine the failure envelope in the compressive axial quadrant. It is also an indication of the response to an applied 'pure shear' loading

0H:-1A The zero hoop to a negative one axial stress ratio simulates a pipeline with a small amount of internal pressure and an increasing axial compressive load. This is also used to portray the compressive stress in an increasing moment load. Axial compression is used to determine the maximum structural load capacity of the pipe.

The loading rates were determined from the specific stress ratio and the constant 'von Mises' equivalent stress loading rate of 68.25 kPa/sec (9.89 psi/sec). The equivalent stress loading rate was based on Carroll (1994) definition:

$$d\sigma_{\text{equivalent}}/dt = 68.251\text{kPa/sec} \qquad \sigma_{\text{equivalent}} = \sqrt{\sigma_A^2 - \sigma_A\sigma_H + \sigma_H^2} \qquad 5\text{-}1$$

where the indices A and H refer to the axial and hoop directions, respectively.

The applied average stresses were calculated from the internal pressure and axial load according to the ASTM Standard D2992-91, thin cylinder theory [89]. Thin cylinder theory was assumed in order to simplify calculations. (For a further discussion refer to Chapter 2)

For monotonic testing the data acquisition computer recorded the hoop (transverse) and axial strains, axial load, internal pressure, oil volume and axial stroke in 10-second intervals. The pressure and axial loads are applied at a specified constant stress rate until the test was halted. Halting of the test occurred after the high-pressure reservoir in the intensifier was exhausted or a significant amount of movement in the axial stroke was recorded, both indicating failure.

5.3 TEST RESULTS

The hoop and axial stress rate for the corresponding stress ratios were obtained from the constant 'von Mises' equivalent biaxial stress loading rate. A summary of the test conditions for each tested stress ratio and reference figures are listed in Table 5-1.

5.3.1 STRESS-STRAIN OBSERVATIONS

The stress values used in this investigation are averaged through thickness values and the surface strains are obtained from the surface mounted extensometers and strain gauges. This approach for determining the stresses may seem simplistic compared to the complex lay-up with all the defects noted (see Chapter 2) indicating a very complex field of stresses and strains within the pipe. However, this approach gives an estimate of the globally applied stresses.

The 0H:1A stress ratio had an axial stress loading rate of 68.25 kPa/sec (9.89 psi/sec) and a constant internal pressure of 2.58 MPa (375psi). The corresponding applied stress to surface strain curve is illustrated in Figure 5-1. Note the necking effect as seen by the negative hoop strain under the applied axial tension. The linear elastic range is 39 % of the axial failure stress, with a corresponding strain of -0.06 % and 0.31 % for the hoop and axial direction, respectively. A complete structural failure (fiber failure) occurred at an axial stress of 184.05 MPa (26,694 psi) with an axial strain of 1.57% and a hoop strain of -0.32%.

The 1H:1A stress ratio was loaded with an axial stress loading rate of 68.25 kPa/sec (9.89 psi/sec) and a hoop stress rate 68.25 kPa/sec (9.89 psi/sec). The corresponding applied stress to surface strain curves are illustrated in Figures 5-2a and 5-2b. The axial stress at the end of linear elastic range is 59.30 MPa (8,600 psi) on the axial stress-strain curve with a hoop strain of 0.06% and an axial strain of 0.23%. This axial linear elastic range is comparable to the axial linear elastic range found under pure axial tension. On the hoop stress-strain curve the end of the linear elastic range is 115.47 MPa (16,750 psi) with a hoop strain of 0.22% and an axial strain of 0.72%. Note the effect of the increased stiffness in the hoop direction due to the 15 layers of $\pm 66^0$ angle-plies.

The 2H:1A stress ratio had an hoop stress loading rate of 78.81 kPa/sec (11.43 psi/sec) and an axial stress rate 39.41 kPa/sec (5.71 psi/sec). The corresponding applied stress to surface strain curves are illustrated in Figures 5-3a and 5-3b. The axial stress at the end of linear elastic range is 52.38 MPa (7600 psi) on the axial stress-strain curve with a hoop strain of 0.21% and an axial strain of 0.19%. Again this is comparable to the axial linear elastic range for both the 1H:1A and the 0H:1A stress ratios. The hoop stress at the end of linear elastic range is 159.36 MPa (23,110 psi) on the hoop stress-strain curve with a hoop strain of 0.34% and an axial strain of 0.33%.

The 1H:0A stress ratio was investigated with a hoop stress rate of 68.25 kPa/sec (9.89 psi/sec). The corresponding applied stress to surface strain curve is illustrated in Figure 5-4. The hoop stress at the end of linear elastic range is 154.79 MPa (22,450 psi) on the hoop stress-strain curve with a hoop strain of 0.42% and an axial strain -0.14%. The negative axial strain is due to the small amount of over correcting in the axial load. The end of the hoop linear elastic range is comparable to the 2H:1A stress ratio.

For the pure shear loading, 1H:-1A stress ratio, was loaded with an axial stress rate of -39.41 kPa/sec (5.71 psi/sec) and hoop stress rate 39.41 kPa/sec (5.71psi/sec). The corresponding applied stress to surface strain curves are illustrated in Figures 5-5a and 5-5b. The axial linear elastic limit is -142.05 MPa (20,600 psi) with a hoop strain of 0.64% and an axial strain of -0.90%. The end of the hoop linear elastic range is 85.10 MPa (12,340 psi) with a hoop strain of 0.36% and an axial strain of -0.53%.

The 0H:-1A stress ratio had an axial stress loading rate of -68.25 kPa/sec (-9.89 psi/sec) and a constant internal pressure of 2.58 MPa (375psi). The corresponding applied stress to surface strain curve is illustrated in Figure 5-6. The end of the axial linear elastic range is -113.21 MPa (16,420 psi) with a hoop strain of 0.19% and an axial strain of -0.65%. Note the effect of bulging as seen by the positive hoop strain with the applied axial compression. Complete structural failure occurred at an axial stress of -271.40 MPa (39,360 psi), with corresponding hoop strain of 0.46% and an axial strain of -2.02%.

5.3.2 STRAIN-STRAIN / OIL VOLUME OBSERVATIONS

The surface strain-strain curve and the leakage curve for the 0H:1A stress ratio are illustrated in Figure 5-7. No fluid was visually seen weeping from the specimen wall before complete structural failure. However, an initiation point of leakage was noted by visual inspection at a hoop strain of -0.16% and an axial strain of 2.8%. Linear strain characteristics were exhibited to a hoop strain of -0.16% and an axial strain of 0.69%. The specimen under this stress ratio failed by abrupt fiber breakage after a small amount of fluid loss at a hoop strain of -0.32% and an axial strain of 1.64%.

The surface strain and leakage curve for the 1H:1A stress ratio are illustrated in Figure 5-8. An initiation point of leakage was noted at a hoop strain of 0.17% and an axial strain of 0.65%. The 1H:1A stress ratio exhibited linear strain characteristics up to a hoop strain of 0.10 % and an axial strain of 0.32%. Using the two slope leakage criteria (described in Chapter 4) the leakage failure was considered to occur at a hoop strain of

0.21% and an axial strain of 0.95%. This leakage plot is somewhat affected by the failure of the axial strain gauge during testing, therefore the best estimate of leakage failure was considered. After leakage failure, the test was continued until the intensifier reservoir was exhausted (Approximately 75-ml of oil volume). A considerable amount of non-linearity was observed prior to the leakage and final failure load.

The surface strain curve and the leakage curve for the 2H:1A stress ratio are illustrated in Figure 5-9. In this case the leakage curve indicated the onset of damage at 0.42% hoop strain and 0.39% axial strain. The linear strain characteristics were observed up to a hoop strain of 0.32 % and an axial strain of 0.26%. Leakage failure was observed at a hoop strain of 0.47% and an axial strain of 0.45%. Again, after leakage failure the test was allowed to run until the intensifier reservoir was exhausted. Similar to the stress ratio 1H:1A, the 2H:1A exhibited a considerable amount of non-linearly prior to the functional and final failure load.

The surface strain curve and the leakage curve for the 1H:0A stress ratio are illustrated in Figure 5-10. This stress ratio exhibited linear strain characteristics up to a hoop strain of 0.10% and an axial strain of 0.32%. For pure pressure loading, the pressure intensifier limited the test. The specimen was loaded to the maximum capacity of the pressure intensifier, 68.95 MPa (10,000 psi) with no indication of leakage. The final recorded strains were a hoop strain of 0.85 % and an axial strain of -0.32%. Leakage was not observed, but linear strain characteristics were noted, to about half the maximum applied internal pressure.

The surface strain curve and the leakage curve for the 1H:-1A stress ratio are illustrated in Figure 5-11. The leakage curve did not indicate the onset of any damage, which is similar to the pure hoop loading. However, this stress ratio exhibited linear strain characteristics up to a hoop strain of 0.32% and an axial strain of -0.48%. Like the pure pressure loading, the test was limited by the pressure intensifier capability. The final recorded values were a hoop strain of -1.42 % and an axial strain of -1.06%. Again the linear strain characteristic was observed to about half of the maximum applied axial stress, -214.96 MPa (-31200 psi).

The surface strain curve and the leakage curve for the 0H:1A stress ratio are illustrated in Figure 5-12. No fluid loss was observed prior to fiber failure. This test exhibited linear strain characteristics up to a hoop strain of 0.33% and an axial strain of -1.35%. The failure mode for this stress ratio is abrupt crushing of fibers at a hoop strain of 0.47 % and an axial strain of -2.02%. The positive hoop strain is an indication that the walls of the pipe were bulging out during compressive loading.

5.3.3 MONOTONIC BIAXIAL FAILURE ENVELOPES

Biaxial failure envelopes were constructed to present the data compiled from the tested stress ratios and to characterize the complex behavior of this multidirectional lay-up.

A monotonic failure envelope was constructed in stress space; applied axial stress verses the applied hoop stress, as illustrated in Figure 5-13. The monotonic failure envelope helps to visualize the results: the axial stress-strain linear limit is not attained under hoop loading, the hoop stress-strain linear limit under pure axial loading and the axial strain hoop strain linear limit was somewhere between the two stress-strain linear limits. As well, leakage occurred after the linear limits under axial tension. But, leakage was not observed prior to bursting under axial compression. This is an indication that axial tension is required to aid in crack development.

The monotonic failure envelope was also constructed in strain space, axial surface strain verses the hoop surface strain, as illustrated in Figure 5-14. Again the monotonic failure envelope in strain space helps to visualize that the hoop stiffness is almost double that of the axial stiffness as well as the proximity of the non-linear points to the leakage points in strain space.

5.3.4 MACRO FAILURE OBSERVATIONS

Only four stress ratios out of the six ratios tested had sustained a sufficient amount of observable damage. No damage was observed under the 1H:0A stress ratio and the 1H:-1A stress ratio. The complex ply interactions with different stress ratios can be deduced from the observed failure modes and accumulated damage.

The complexities of the failures for the multidirectional pipe can be seen in Figure 5-15 to 5-18. To visualize the macro damage through leakage, 5 ml of fluorescent penetrant was added to the fluid volume of the specimen. The fluorescent penetrant was a Magnaflux Zyglo ZL-56 that is highly visible under ultraviolet light. The macro failure observations of the filament wound pipe specimen are based on visual inspection during and after testing.

The final structural failure in the multidirectional pipe specimen with a 0H:1A applied stress ratio is illustrated in Figure 5-15. Matrix cracking developed parallel to the $\pm 66^0$ fibers, is observed on the outer surface. Acoustic emissions (unamplified) were also detected at approximately 70% of the structural failure stress 184.05 MPa (26700 psi), which continued for the duration of the test. Once structural failure occurred, the 0^0 fibers fractured, and then the specimen twisted fracturing remaining $\pm 66^0$ fibers. This twisting effect can be observed in Figure 5-15. Note the curvature of the fractured fibers. The twisting is due to the fact that the lay-up is neither balanced nor symmetric.

Figure 5-16 illustrates fluid leakage through uniform matrix cracking of the pipe for the 1H:1A stress ratio. The uniform matrix cracking parallel to the $\pm 66^0$ fibers eventually lead to functional leakage failure. Small oil droplets formed on the outer surface (weepage) as the test progressed, eventually wetting the entire surface. However, the specimen maintained structural integrity. The fluorescent penetrant provided a clear visualization of the damage as seen in Figure 5.16.

Leakage failure through matrix cracking and delamination of the pipe was observed for the 2H:1A stress ratio, as illustrated in Figure 5.17. Matrix cracking was not as uniform as the 1H:1A case. The formation of matrix cracking parallel to the ± 66^0 fibers is still evident. But extensive delamination is seen leading to leakage failure.

The structural crushing failure of the pipe with a 0H:-1A stress ratio is illustrated in Figure 5-18. The failure was seen in the specimen when the inner ± 66^0 plies buckled inwards fracturing the 0^0 plies.

5.3.5 MICRO DAMAGE OBSERVATIONS

To further investigate the damage mechanism, micrographs were made for each of the failed test specimens illustrated in Section 5.3.4.

The micro damage after structural failure of the pipe for the 0H:1A stress ratio is illustrated in Figure 5-19. A photograph was taken of the cross section of the specimen, near the end of damage zone observed in Figure 5-15. Extensive matrix damage can be observed in the 0^0 fibers as well as delamination of the 0^0 layer and the fiber failure of the ± 66^0 layers, which occurred after the initial failure of the 0^0 fibers.

The micro damage after uniform matrix cracking for the 1H:1A stress ratio is illustrated in Figure 5-20. The cracks extend through the 0^0 ply and into the ± 66^0 plies, resulting in the extensive cracking in the ± 66^0 plies. The damage accumulated as the test progressed ultimately leading to leakage failure. The delamination is seen in the thickest section of the wall thickness, where the resin build-up was the greatest.

Figure 5-21 illustrates the damage accumulated after matrix cracking in the pipe for the 2H:1A stress ratio. Note the cracking in the 0^0 layers and the crack, which extended through the first layer of ± 66^0 fiber. The amount of cracking in the ± 66^0 fiber is greatly reduced compared to the 1H:1A stress ratio. The reduction in cracking seen throughout the $\pm 66^0$ layers may be attributed to the high fiber loading in the hoop direction with this stress ratio.

The damage after structural failure by axial crushing of the specimen for the 0H:-1A stress ratio is illustrated in Figure 5-22. Note the separation of the inner $\pm 66^0$ plies at the 0^0 ply. The inner $\pm 66^0$ layer crushed inward and the outer layer crushed outward at the same time breaking the fibers.

5.4 INTERPRETATION OF DATA

5.4.1 LINEAR ELASTIC BEHAVIOR

The reduction in stiffness has long been used as an indication of the amount of accumulated damage. Studies have been conducted on flat specimens directly linking transverse cracking to the reduction in stiffness [38, 93]. The idea behind stiffness reduction, as explained by Talreja (1984), is that an increasing load applied to the laminates will eventually cause a crack in the laminates, which induces a displacement. This displacement introduces a non-uniform strain to the plies constraining the crack [93]. For the multidirectional fiber-wound pipe the linear elastic limit could be the onset of initiation of micro-cracking within the plies, which makes it an important threshold to correlate with other damage observations.

The linear elastic limit, in some cases, seemed to be independent of the stress ratio. The axial elastic limit for the 0H:1A, the 1H:1A and the 2H:1A stress ratios occurred around an axial stress of 57.00 MPa (8200 psi). This occurrence is also seen in the hoop linear elastic limit for the 2H:1A and the 1H:0A stress ratio and is somewhat comparable for the 1H:1A and the 1H:-1A stress ratios. The hoop linear elastic limit of the 2H:1A and the 1H:0A stress ratio and the 1H:1A and the 1H:-1A stress ratio are not comparable to each other. This seems to suggest that the hoop linear elastic limit is affected by the state of axial stress. However, the hoop stress does not seem to have any effect on the axial linear elastic limit.

The elastic moduli for the multidirectional tubes were determined from the tension and the pure pressure test illustrated in Figures 5-1 and 5-4, respectively. The slope of the linear portion of the stress-strain curve was examined to determine the elastic moduli. The axial elastic modulus, E_A, was estimated to be 18.2 GPa (2,639,000 psi) with a corresponding Poisson's ratio, ν_{AH}, of 0.24. The hoop elastic modulus, E_H, was found to be 37.7 GPa (5,468,000 psi) with a corresponding Poisson's ratio, ν_{HA}, of 0.33. The Poisson's ratios were determined from the surface strain curves, Figures 5-7 and 5-10, respectively.

These results are comparable to the values predicted by the classical laminate theory with an axial elastic modulus, E_A, of 21.6 GPa (3,142,000 psi) and a corresponding Poisson's ratio, ν_{AH}, of 0.24 and a hoop elastic modulus, E_H, of 37.7 GPa (5,473,000 psi) with a corresponding Poisson's ratio, ν_{HA}, of 0.33. The material properties used for the classical laminate calculations were obtained from Wang et al. (1997)[101]. The classical laminate code was obtained from Wolodko (1999) [104], based on Daniel (1994)[13].

The results show that despite defects and impurities (discussed in Chapter 2) the classical laminate theory is able to determine the characteristics of the linear response. However, the classical laminate theory cannot determine either the damage initiation or the linear elastic limit without recourse to the experimental values.

5.4.2 POISSON'S RATIO BEHAVIOR

A literature review revealed only a few papers discussing the Poisson's ratio of composite materials [12, 30, 35, 71, 80]. Only two focused on the Poisson's ratio as a damage parameter. Smith et al. (1990) and Harris et al. (1989) point out that a reduction in the Poisson's ratio was of considerable more interest for flat specimens then a stiffness reduction, because there was a larger change in Poisson's ratio for the same amount of damage [80, 30]. It thus amplifies the damage initiation point. Philippidis et al. (1994) concluded that little interest given to the reduction in the Poisson's ratio as a damage parameter, was because the experimental methods for determining the change in the transverse Poisson's ratio for flat specimens required either specialized equipment or a thicker specimen [71].

The advantage of the multidirectional pipe investigated here is its thick wall section, thus, making the reduction of the Poisson's ratio notable. The idea behind the reduction in the Poisson's ratio is the same as that of the reduction in stiffness as explained by Talreja (1984). An increasing load applied to the laminates eventually causes extensive microstructural cracking in the laminates, inducing an increased displacement. The displacement introduces a non-uniform strain to the plies constraining the cracking [93].

To observe a reduction in stiffness in a particular direction (i.e. hoop or axial direction) during biaxial loading, a certain stress level must be reached to develop damage in that particular direction. Since a sufficient amount of hoop stress is not obtained in the 0H:1A and 0H:-1A stress ratios, to cause damage in the hoop direction, and a sufficient amount of axial stress is not obtain in the 1H:0A stress ratio, to cause damage in the axial direction, it is difficult to make a comparison based on the reduction in stiffness. The initiation of non-linearity of the Poisson's ratio, on the other hand, removes the dependency on the wall stress. This then gives a damage indicator independent of the stress ratio.

5.4.3 LEAKAGE BEHAVIOR

The leakage curves, illustrated in Figure 5-7 to 5-12, were corrected for specimen movement and oil compression; thus, producing a characteristic leakage curve for the multidirectional lay-up under each particular stress ratio. Linking leakage to damage, the initiation point of leakage and initiation point of intense leakage provide a good indication of the extent of damage. However, leakage is time and damage dependent, which means that the point of detectable leakage is far beyond the point of initial cracking, this is seen by comparing the strain and leakage curves.

5.4.4 DISCUSSION OF THE FAILURE ENVELOPES

The biaxial envelope for the multidirectional pipe lay-up assuming an average stress through the wall thickness is illustrated in Figure 5-13. The biaxial envelope in terms of surface strain is illustrated in Figure 5-14. The biaxial envelopes summarize the stress-strain, strain-strain linear limits, the leakage initiation point and the initiation of intense leakage point, which help to visualize the complexity of this multidirectional lay-up.

The final data points obtained for each stress ratio was added to help visualize the other attainable points with the maximum attainable stresses and strains. For the axial dominated stress loading cases the final test points were obtained by structural failure. For the 1H:1A and 2H:1A stress ratios the final test points were obtained by depleting the fluid volume of the intensifier, where the 1H:0A and 1H:-1A stress ratios were limited by the capabilities of the testing machine.

A large variation in the stiffness between the hoop and axial directions can be noted in the biaxial envelopes, due to the amount of reinforcement contained in each direction. The hoop direction, with 15 layers of $\pm 66^0$ angle-ply, is about twice stiffer, than the axial direction with only 3 layers of 0^0 ply ($E_H / E_A = 37.7$ GPa/18.2 GPa).

The strength of this lay-up in both the hoop and axial directions is due to the fiber plies complementing these directions. However a weakness can be observed in the 1H:1A and 2H:1A stress ratios when the composite pipe is subjected to a high axial load and high internal pressure. A concave surface in the strain-strain linear limit curve can be noted as well as the proximity of the initiation point of leakage to the initiation point of intense leakage.

5.4.5 MACRO AND MICRO BEHAVIOR

Relating the stress ratio, failure mode and damage accumulation allow for some interesting observations to be made. The amount of axial tension in the specimen seems to govern the amount of matrix cracking. This is seen in the macro failure observations, as the axial tension is decreased so is the amount of matrix cracking to the point where no cracking is seen in the 1H:0A, 1H:-1A and the 0H:-1A stress ratios. Increasing the internal pressure seems to increase the amount of delamination as seen between the 1H:1A and the 2H:1A stress ratios. This shows that the worst combination occurs when the high internal pressure is combined with the high axial tension, as in the 1H:1A stress ratio.

For the 1H:1A stress ratio the combined axial tension and internal pressure cause a uniform matrix cracking parallel to the $\pm 66^0$ fibers. The micrograph (see Figure 5-20) indicates uniform matrix cracking through out the $\pm 66^0$ plies, which may be caused by the high transverse loading perpendicular to the $\pm 66^0$ fiber directions. The micrograph indicates longitudinal cracking in the 0^0 plies as well. In the case of the 2H:1A stress ratio the micrographs seem to indicate a decreased amount of cracking in the $\pm 66^0$ plies as compared to the 1H:1A stress ratio, which seems to provide evidence that axial tension is needed for matrix cracking in the $\pm 66^0$ angle-plies.

5.5 CONCLUDING REMARKS

A wealth of information was obtained from the monotonic biaxial testing of the commercially wound, multidirectional glass fiber reinforced epoxy pipes. The investigation revealed the response of the mechanical properties and the failure modes with monotonic biaxial loading. The results indicated that the lay-up was exceptionally strong in the principle pipe directions. In the hoop direction no damage was recorded under pure pressure loading.

A certain level of stress is needed in order to observed a stiffness reduction. Since a sufficient level of hoop stress was not obtained in the 1H:0A and 0H:-1A stress ratios and similarly the level of axial stress was negligible in the 1H:0A stress ratio, hence it is difficult to compare the damage sustained, based on a reduction in the stiffness. The initiation of non-linearity of the Poisson's ratio can be used as a damage indicator independent of the stresses and the stress ratio. The reduction in the Poisson's Ratio is notable because of the wall thickness of the specimen.

The corrected leakage curves proved to be valuable in determining a point of failure based on the onset of damage, as well as the development of the associated characteristics depending on the applied stress ratio.

Table 5-1 Loading Rate with Corresponding Reference Figures and Failure Modes

Stress Ratio	Loading Rate				Reference Figures				Failure Type
	Hoop (kPa/sec)	Axial (kPa/sec)	Pressure (kPa/sec)	Load (N/sec)	Stress-Strain (Figure #)	Strain-Strain (Figure #)	Macro-Damage (Figure #)	Micro-Damage (Figure #)	
0H:1A	0.000	68.255	0.000	80.0	5.1	5.7	5.15	5.19	Structural
1H:1A	68.255	68.255	16.871	83.0	5.2 (a-b)	5.8	5.16	5.20	Weepage
2H:1A	78.813	39.407	19.181	49.2	5.3 (a-b)	5.9	5.17	5.21	Weepage
1H:0A	68.255	0.000	16.969	0.0	5.4	5.10	n/a	n/a	n/a
1H:-1A	39.407	-39.407	9.741	-48.9	5.5 (a-b)	5.11	n/a	n/a	n/a
0H:-1A	0.000	-68.255	0.000	-84.6	5.6	5.12	5.18	5.22	Structural

Table 5-2 End of Linearly on the Hoop Stress/Strain Curve

Stress Ratio	Stress			Strain		Load	
	Hoop (MPa)	Axial (MPa)	Equivant (MPa)	Hoop (%)	Axial (%)	Load (kN)	Pressure (MPa)
0H:1A	n/a	n/a	n/a	n/a	n/a	n/a	n/a
1H:1A	115.469	11.437	113.053	0.22	0.73	138.990	28.182
2H:1A	159.358	79.433	137.699	0.34	0.33	99.157	38.783
1H:0A	154.794	0.490	154.549	0.42	-0.14	0.613	38.480
1H:-1A	85.095	-85.791	85.448	0.36	-0.53	-103.056	20.457
0H:-1A	n/a	n/a	n/a	n/a	n/a	n/a	n/a

Table 5-3 End of Linearly on the Axial Stress/Strain Curve

Stress Ratio	Stress			Strain		Load	
	Hoop (MPa)	Axial (MPa)	Equivant (MPa)	Hoop (%)	Axial (%)	Load (kN)	Pressure (MPa)
0H:1A	5.456	62.364	59.823	-0.06	0.31	77.517	3.289
1H:1A	60.849	59.300	60.090	0.07	0.24	73.963	14.851
2H:1A	103.132	52.379	89.323	0.22	0.19	65.389	25.097
1H:0A	n/a	n/a	n/a	n/a	n/a	n/a	n/a
1H:-1A	140.554	-142.051	141.309	0.64	-0.90	-170.635	33.788
0H:-1A	10.170	-113.207	118.621	0.19	-0.65	-142.115	2.472

Table 5-4 End of Linearly on the Hoop Strain/Axial Strain Curve

Stress Ratio	Stress			Strain		Load	
	Hoop (MPa)	Axial (MPa)	Equivant (MPa)	Hoop (%)	Axial (%)	Load (kN)	Pressure (MPa)
0H:1A	5.456	108.146	105.524	-0.16	0.69	134.424	3.289
1H:1A	67.671	66.568	67.127	0.07	0.26	83.027	16.516
2H:1A	140.703	70.108	121.852	0.30	0.28	87.518	34.243
1H:0A	168.398	-0.425	168.611	0.46	-0.15	-0.531	41.865
1H:-1A	78.559	-79.077	78.819	0.33	-0.48	-94.989	18.885
0H:-1A	10.386	-206.291	211.675	0.34	-1.35	-258.968	2.523

Table 5-5 Initiation Point of Leakage

Stress Ratio	Stress			Strain		Load	
	Hoop (MPa)	Axial (MPa)	Equivant (MPa)	Hoop (%)	Axial (%)	Load (kN)	Pressure (MPa)
0H:1A	5.456	102.134	99.518	-0.14	0.63	126.951	3.289
1H:1A	132.250	128.858	130.587	0.17	0.77	160.719	32.278
2H:1A	208.526	104.739	180.589	0.47	0.51	130.748	50.749
1H:0A	n/a	n/a	n/a	n/a	n/a	n/a	n/a
1H:-1A	n/a	n/a	n/a	n/a	n/a	n/a	n/a
0H:-1A	n/a	n/a	n/a	n/a	n/a	n/a	n/a

Table 5-6 Initiation Point of Intense Leakage

Stress Ratio	Stress			Strain		Load	
	Hoop (MPa)	Axial (MPa)	Equivant (MPa)	Hoop (%)	Axial (%)	Load (kN)	Pressure (MPa)
0H:1A	5.456	184.050	181.383	-0.33	1.57	228.771	3.289
1H:1A	142.970	139.329	141.185	0.19	0.95	173.778	34.894
2H:1A	213.115	106.458	184.563	0.49	0.55	132.894	51.866
1H:0A	n/a	n/a	n/a	n/a	n/a	n/a	n/a
1H:-1A	n/a	n/a	n/a	n/a	n/a	n/a	n/a
0H:-1A	9.960	-271.396	276.510	0.47	-2.03	-340.697	2.420

Table 5-7 Final Point

Stress Ratio	Stress			Strain		Load	
	Hoop (MPa)	Axial (MPa)	Equivant (MPa)	Hoop (%)	Axial (%)	Load (kN)	Pressure (MPa)
0H:1A	5.456	184.050	181.383	-0.33	1.57	228.771	3.289
1H:1A	164.708	164.186	164.448	0.24	1.23	204.782	40.200
2H:1A	235.510	117.334	203.958	0.55	0.66	146.470	57.316
1H:0A	287.832	-6.318	291.042	0.85	-0.33	-7.888	71.557
1H:-1A	221.221	-214.965	218.160	1.06	-1.49	-258.222	53.179
0H:-1A	9.956	-271.391	276.511	0.47	-2.03	-340.692	2.420

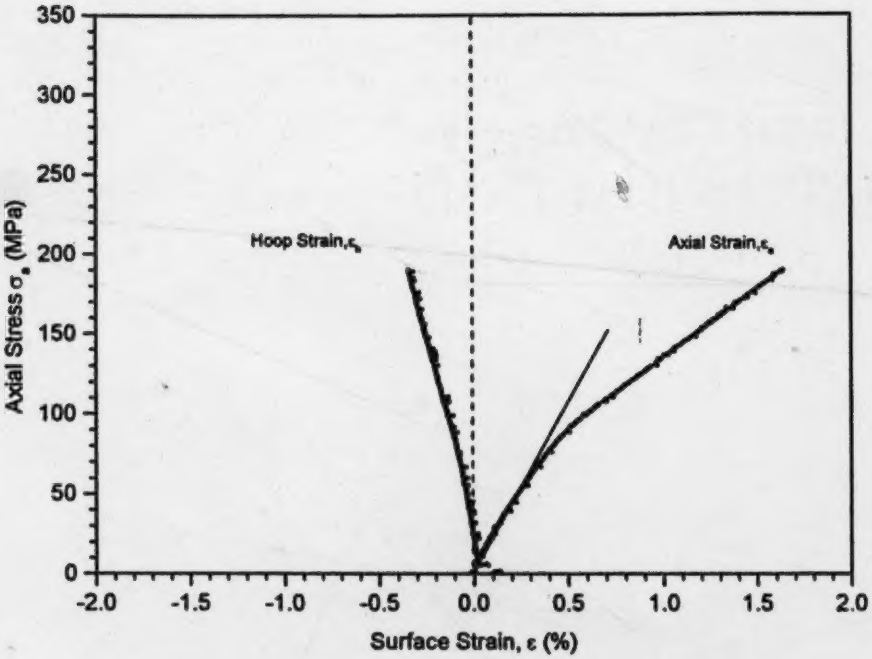

Figure 5-1: The applied axial stress with the corresponding surface strains for the 0H:1A stress ratio. The measured axial stiffness is 21.6 GPa.

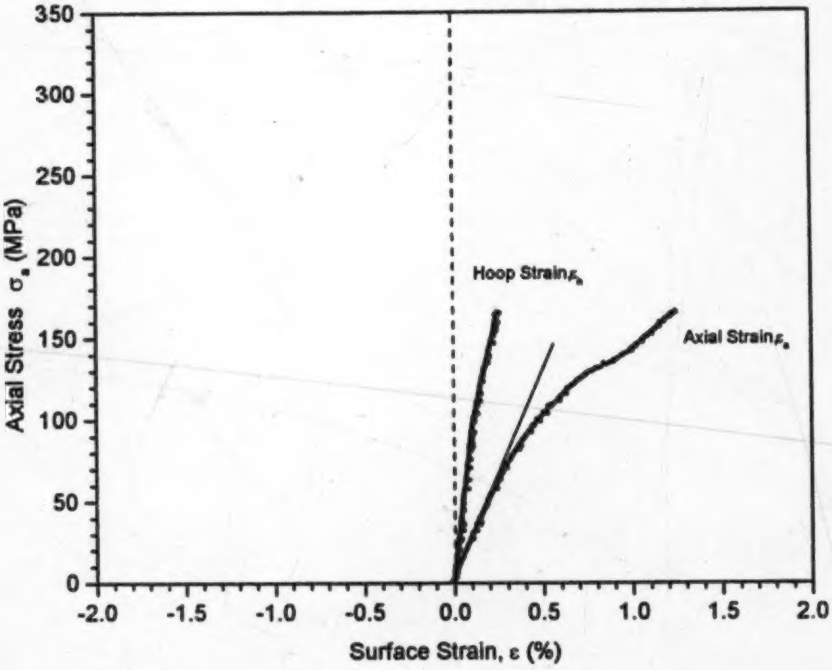

Figure 5-2a: The applied axial stress with the corresponding surface strains for the 1H:1A stress ratio.

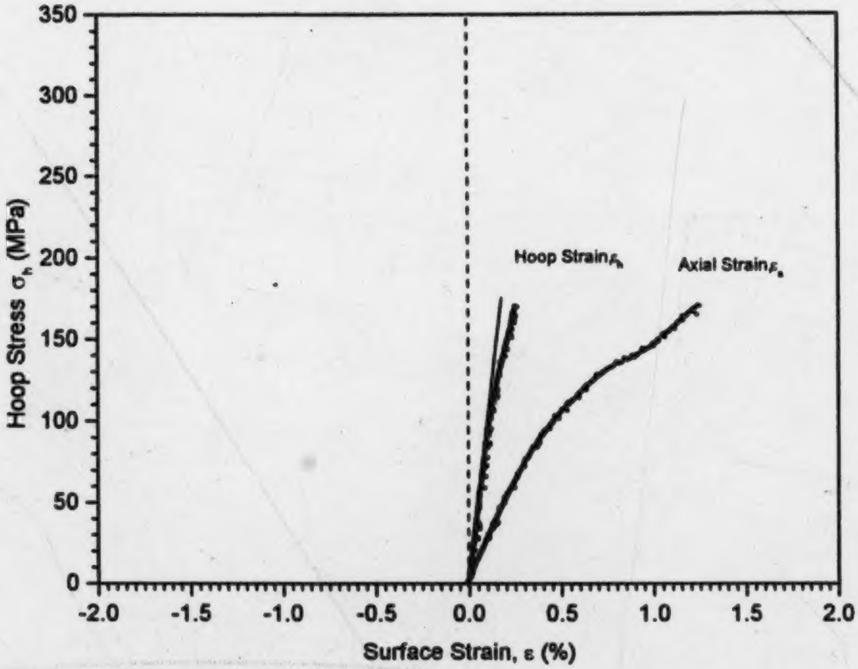

Figure 5-2b: The applied hoop stress with the corresponding surface strains for the 1H:1A stress ratio.

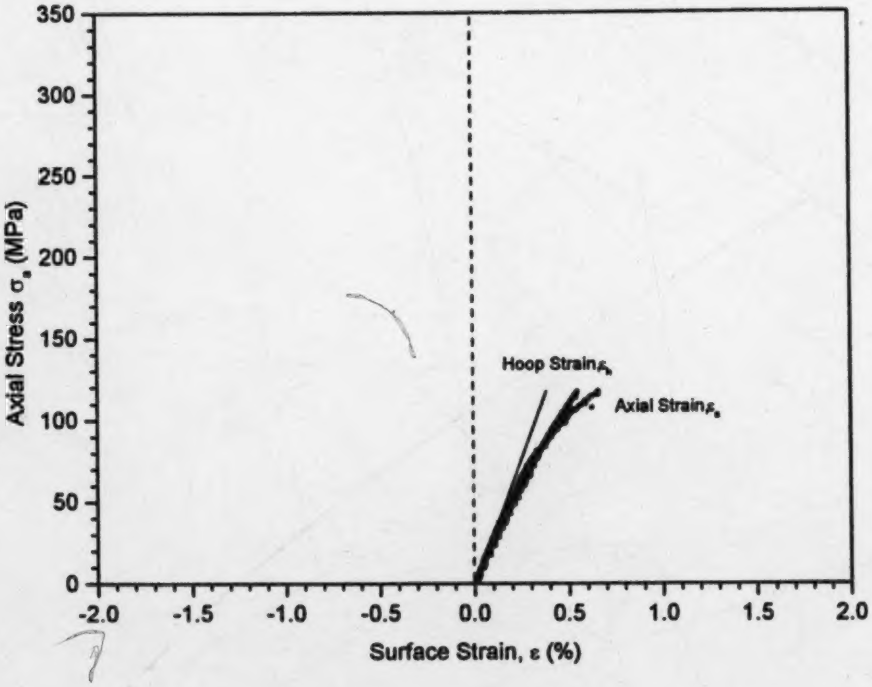

Figure 5-3a: The applied axial stress with the corresponding surface strain for the 2H:1A stress ratio.

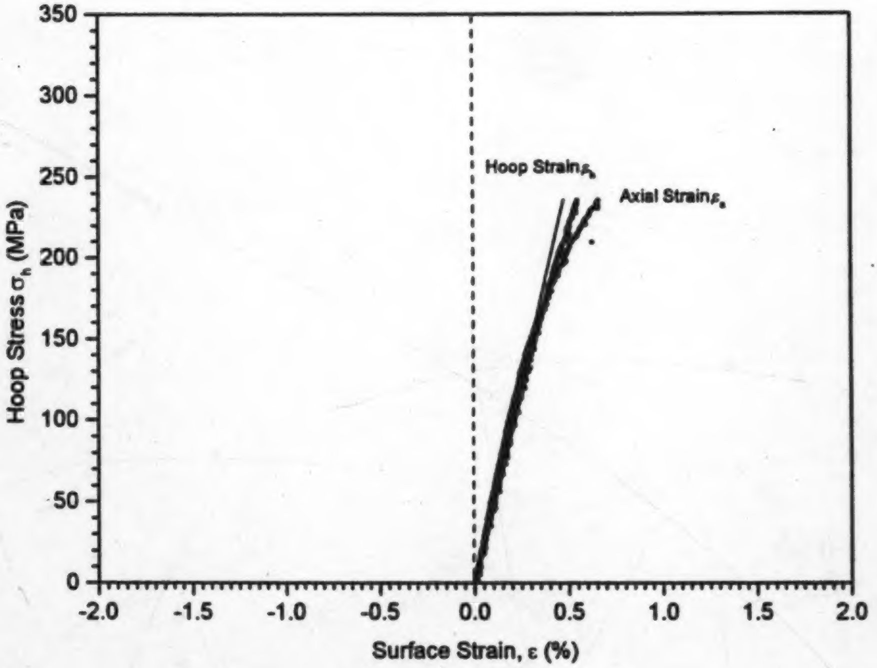

Figure 5-3b: The applied hoop stress with the corresponding surface strain for the 2H:1A stress ratio.

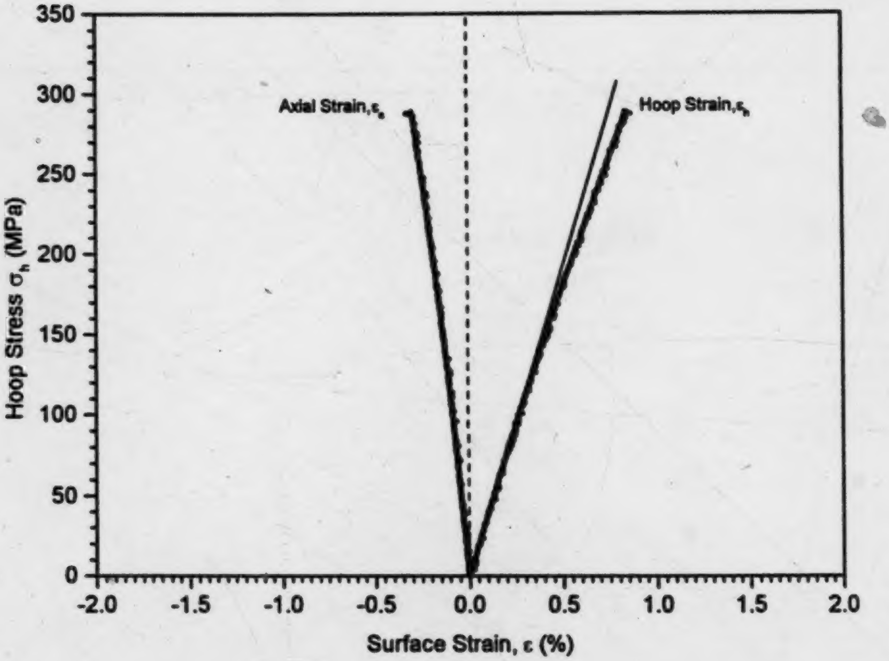

Figure 5-4: The applied axial stress with the corresponding surface strain for the 1H:0A stress ratio. The measured axial stiffness is 37.7 GPa.

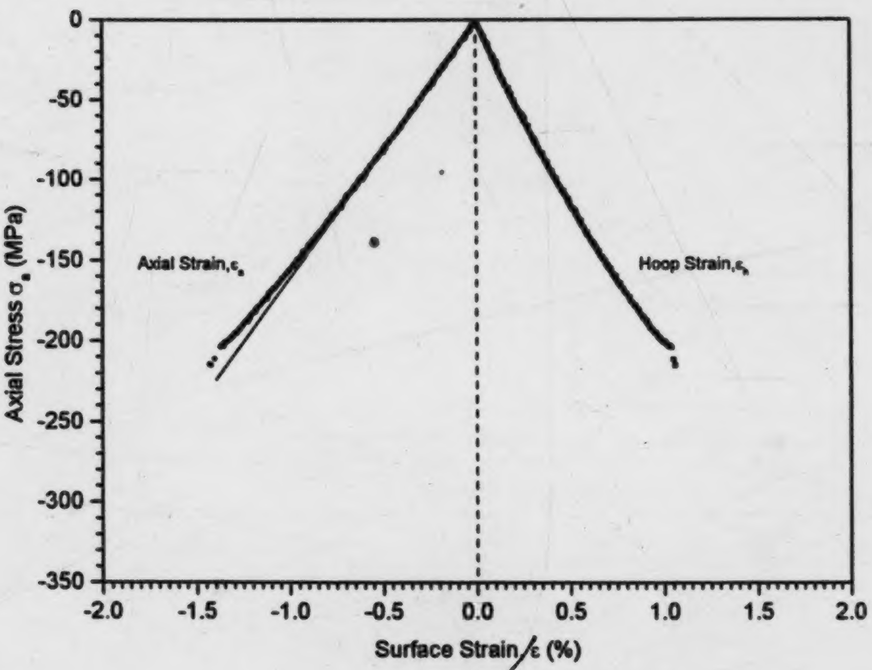

Figure 5-5a: The applied axial stress with the corresponding surface strains for the 1H:-1A stress ratio.

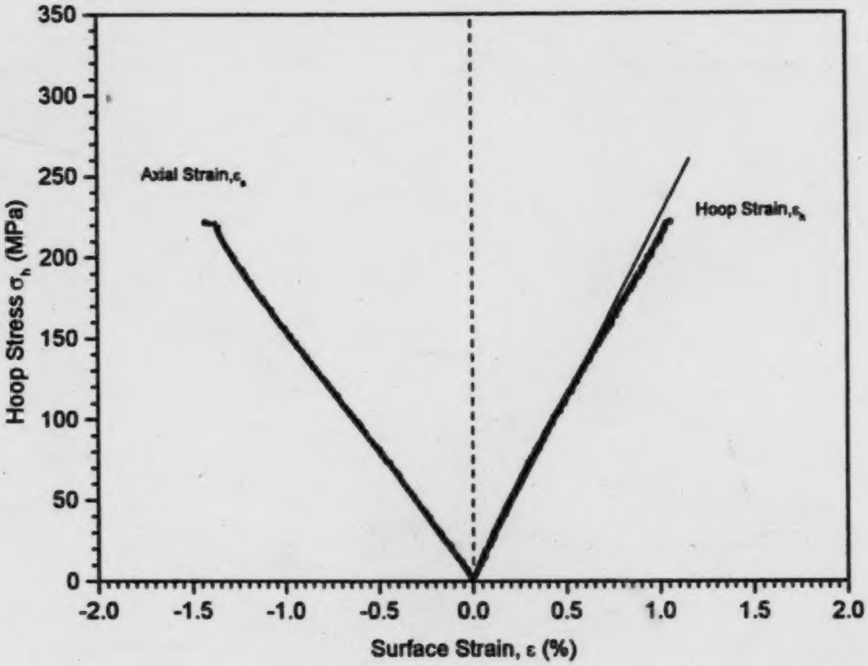

Figure 5-5b: The applied hoop stress with the corresponding surface strains for the 1H:-1A stress ratio.

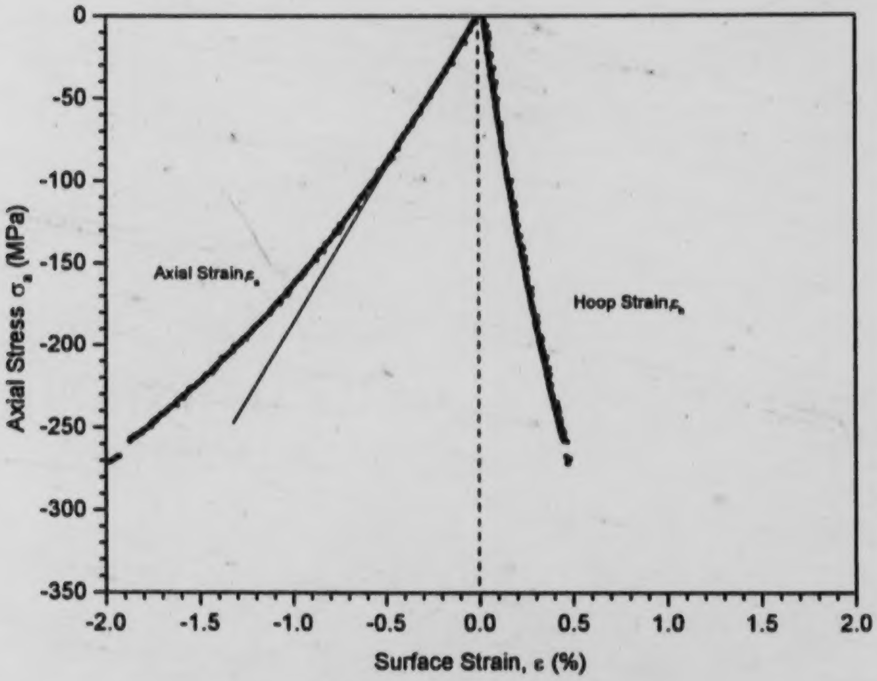

Figure 5-6: The applied axial stress with the corresponding surface strains for the 0H:-1A stress ratio.

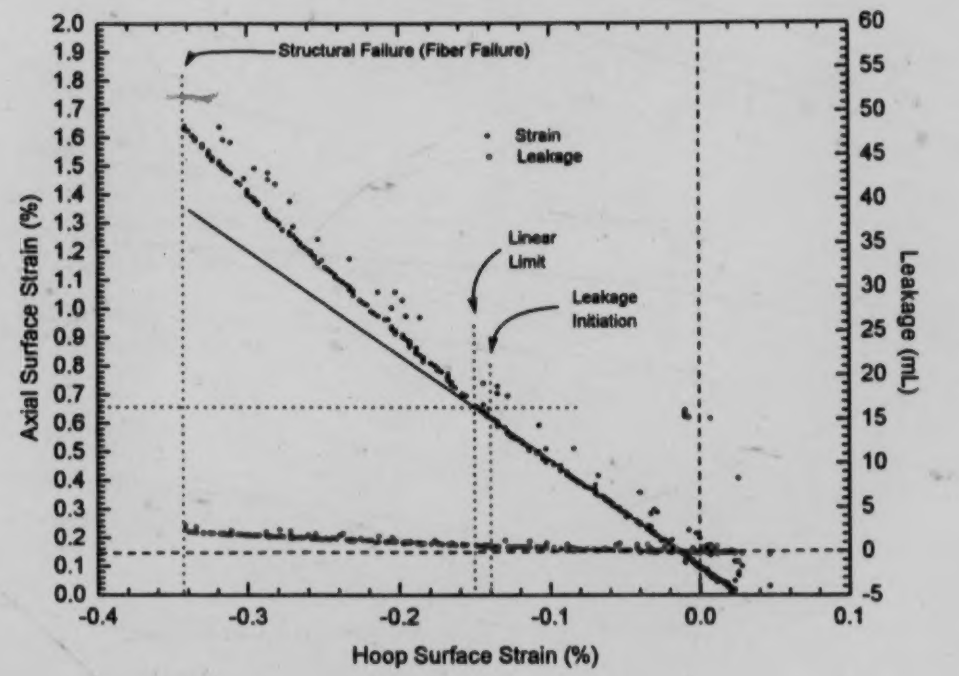

Figure 5-7: The axial surface strain with the corresponding hoop surface strain and corrected leakage curve for 0H:1A stress ratio. The measured axial to hoop Poisson's ratio is 0.244.

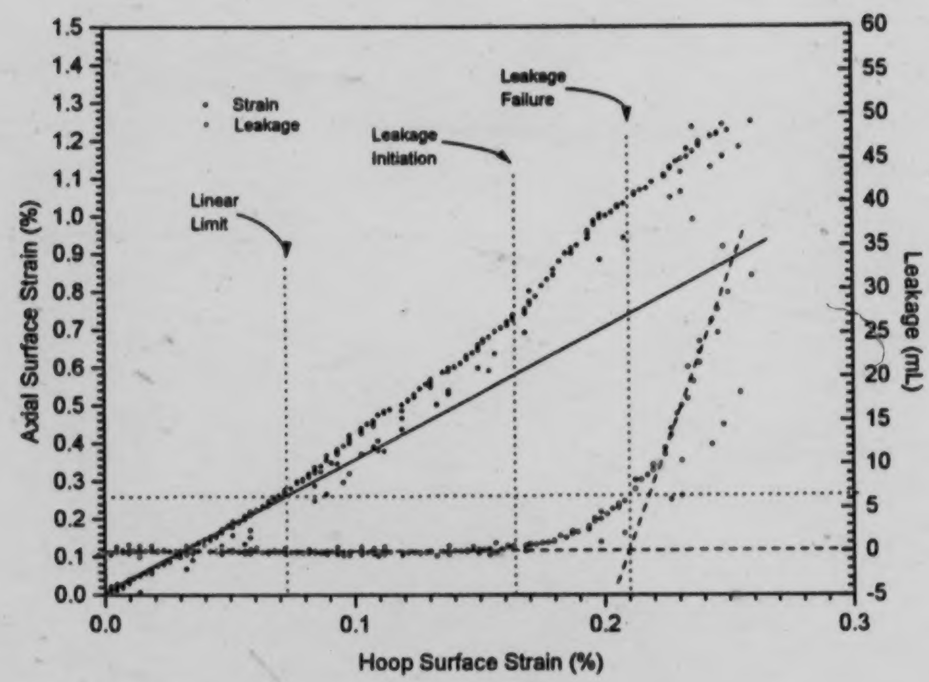

Figure 5-8: The axial surface strain with the corresponding hoop surface strain and corrected leakage curve for 1H:1A stress ratio.

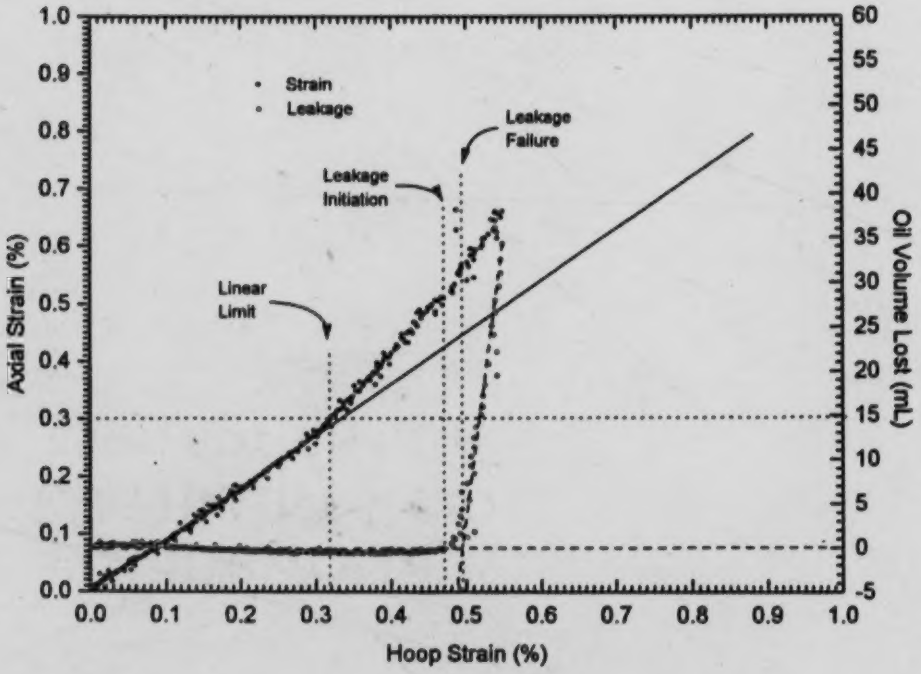

Figure 5-9: The axial surface strain with the corresponding hoop surface strain and corrected leakage curve for 2H:1A stress ratio.

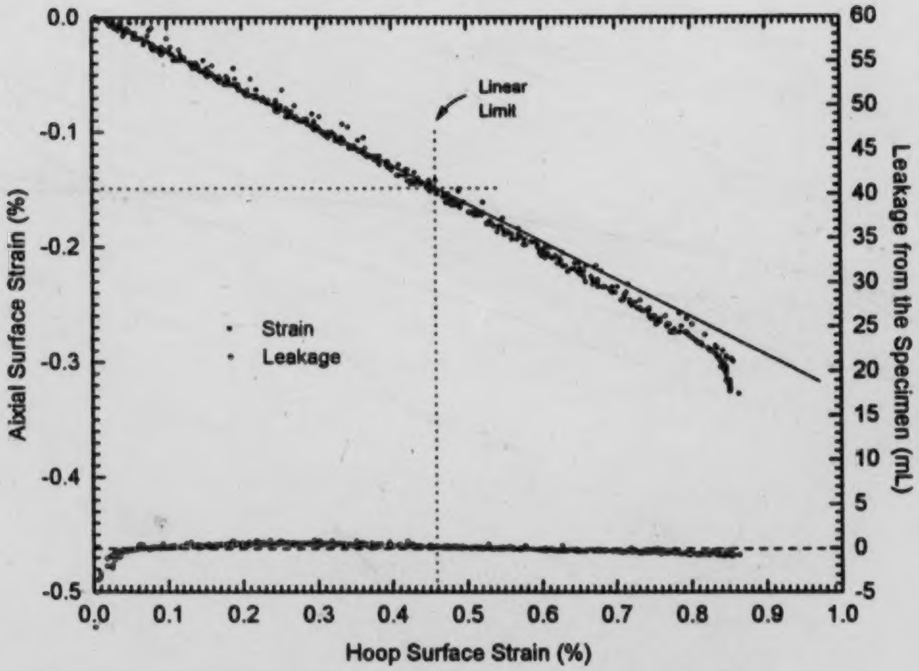

Figure 5-10: The axial surface strain with the corresponding hoop surface strain and corrected leakage curve for 1H:0A stress ratio. The measured hoop to axial Poisson's ratio is 0.326.

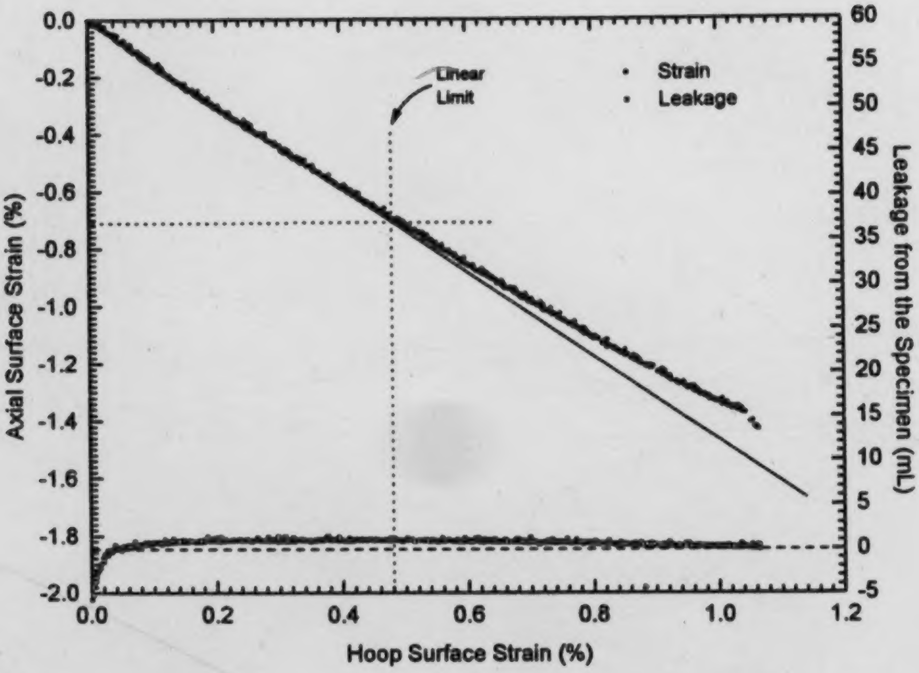

Figure 5-11: The axial surface strain with the corresponding hoop surface strain and corrected leakage curve for 1H:-1A

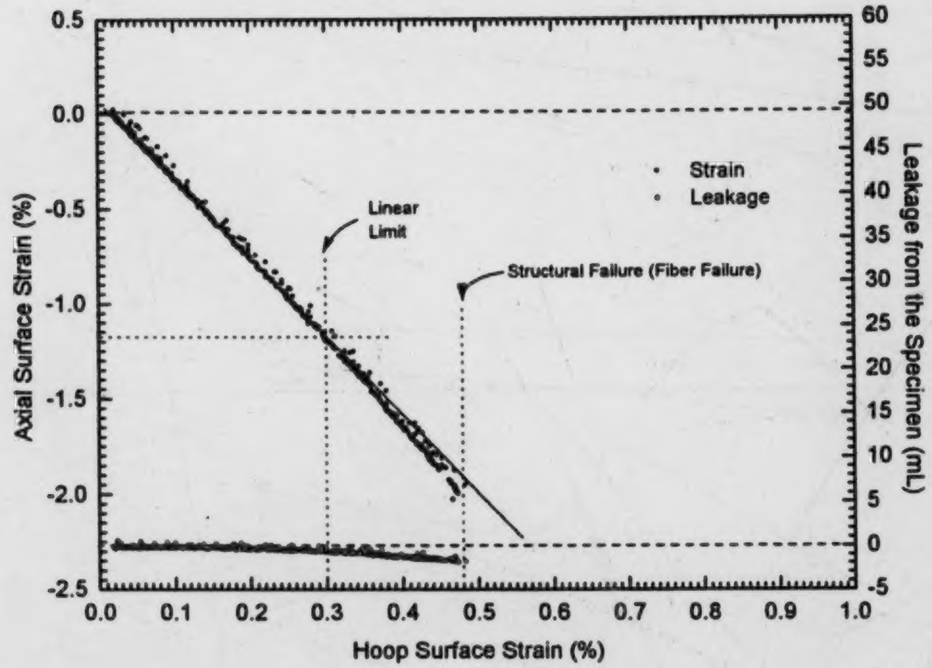

Figure 5-12: The axial surface strain with the corresponding hoop surface strain and corrected leakage curve for 0H:-1A

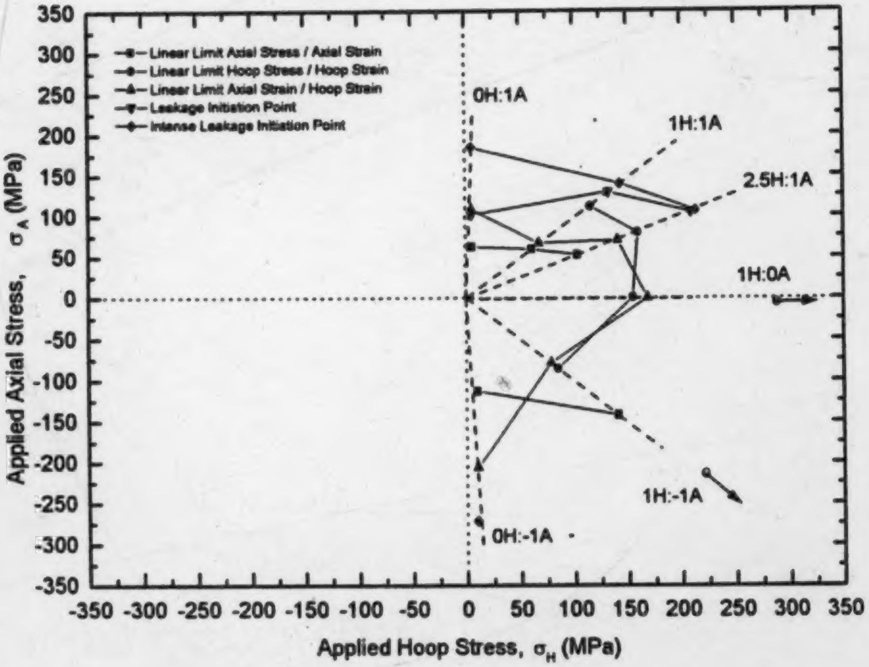

Figure 5-13: The monotonic biaxial failure envelopes illustrated in stress space. Observe the position of the linear limit points in comparison to the leakage.

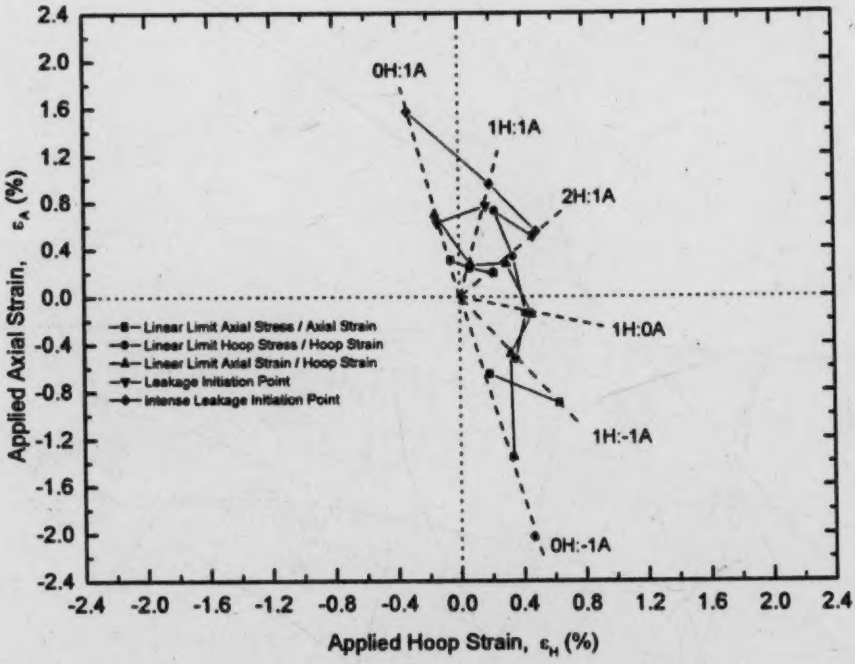

Figure 5-14: The monotonic biaxial failure envelopes illustrated in strain space. Observe the position of the linear limit points in comparison to the leakage.

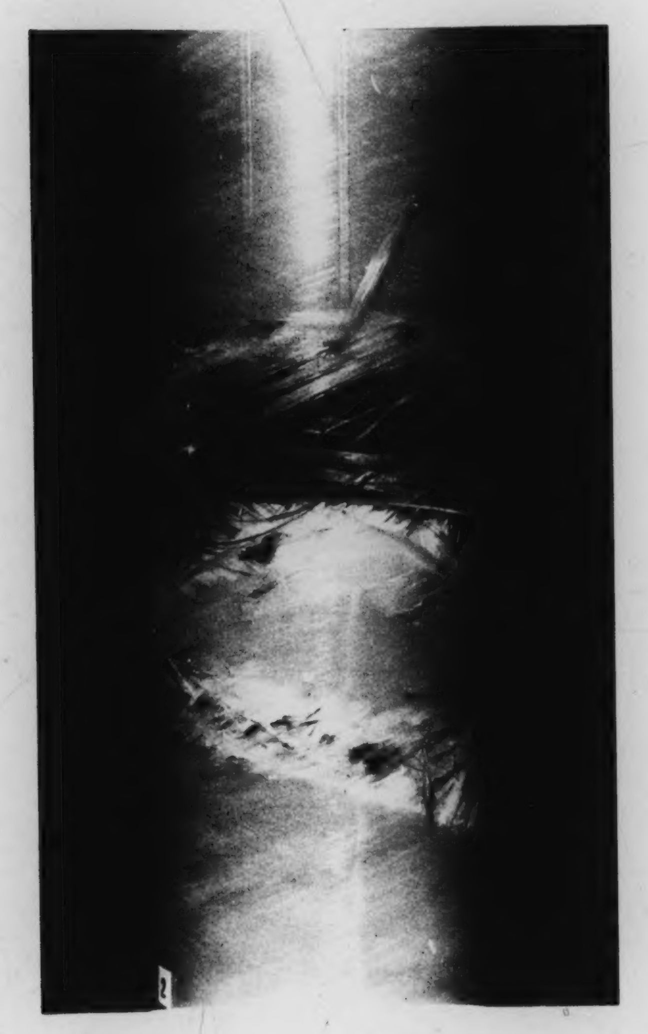

Figure 5-15: Structural failure observed for the 0H:1A applied stress ratio. Once structural failure occurred, the 0° plies fractured, the specimen twisted fracturing the ± 66° plies.

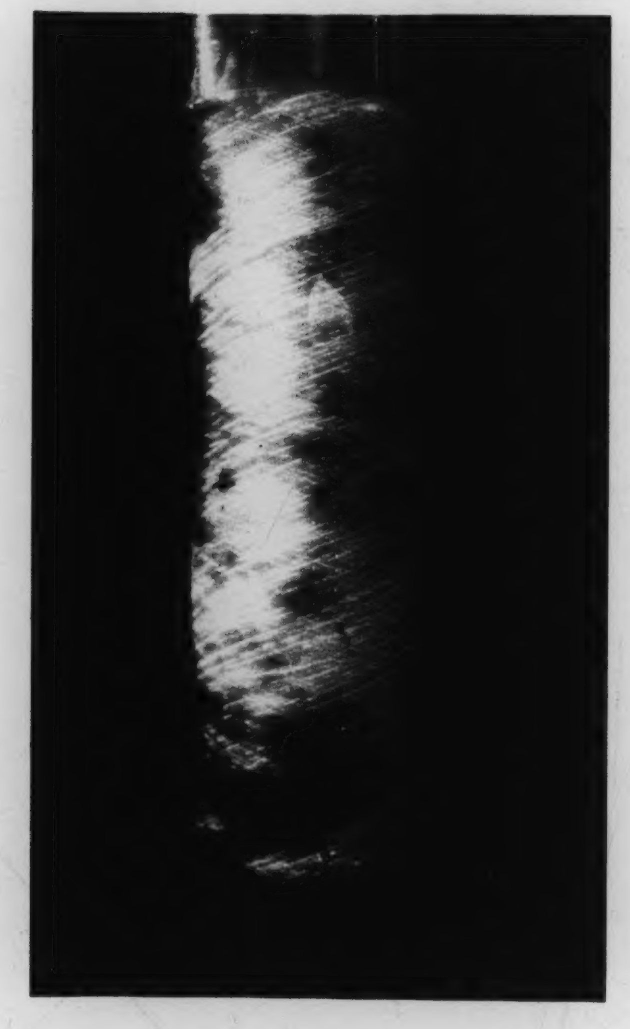

Figure 5-16: Uniform matrix cracking observed parallel to the ±66° plies for the 1H:1A applied stress ratio.

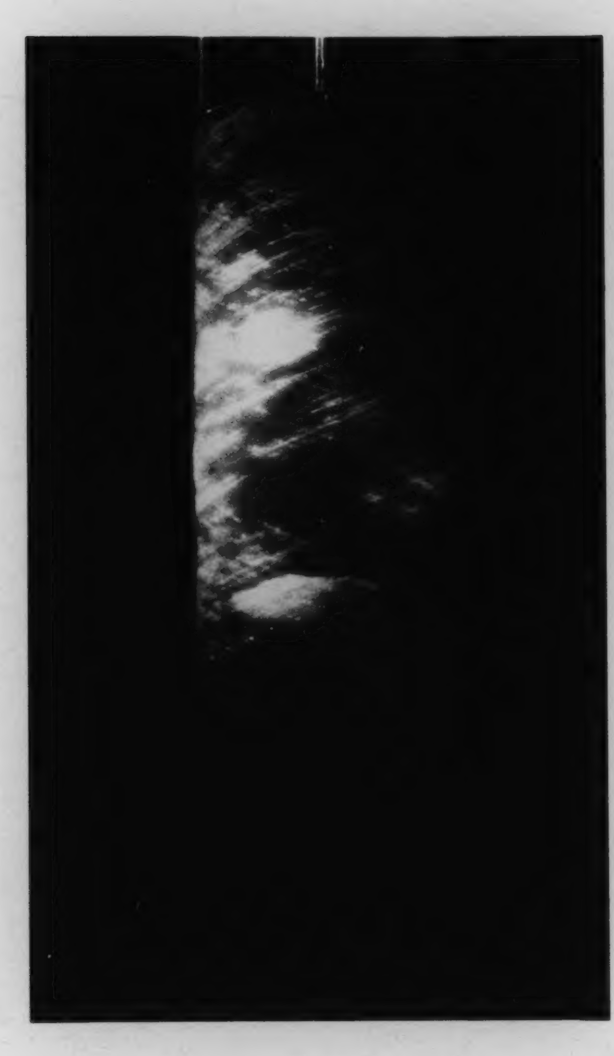

Figure 5-17: Matrix cracking and delamination observed for the 2H:1A stress ratio. The matrix cracking was not uniform.

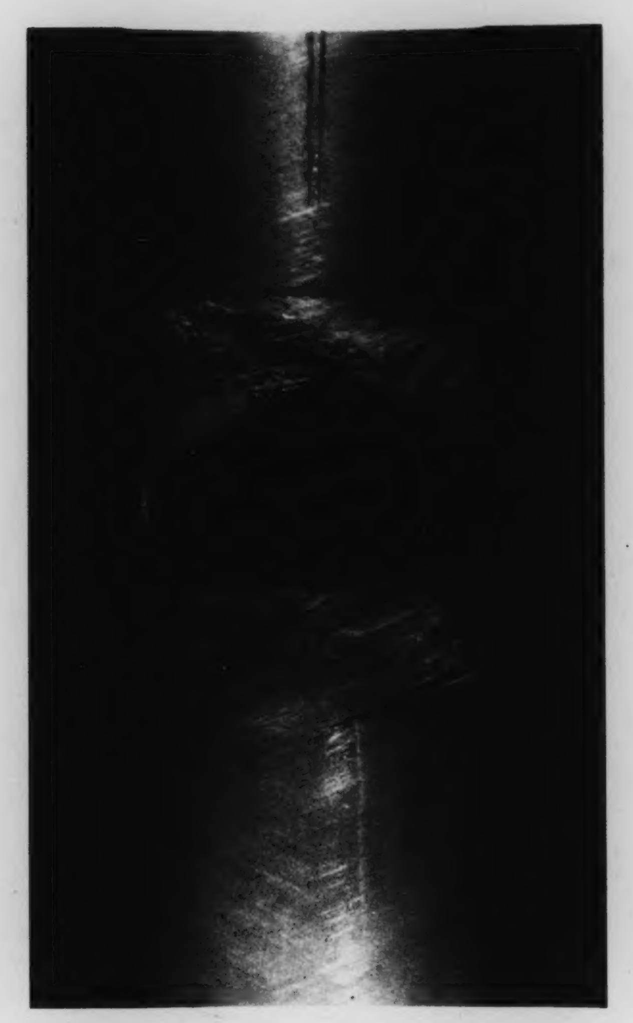

Figure 5-18: Structural crushing failure observed for the 0H:-1A stress ratio.

Figure 5-19: A photograph taken of the cross section of the observed structural failure for the 0H:1A stress ratio. Due to the visibility of the damage area a photograph was taken near the end of the damage zone.

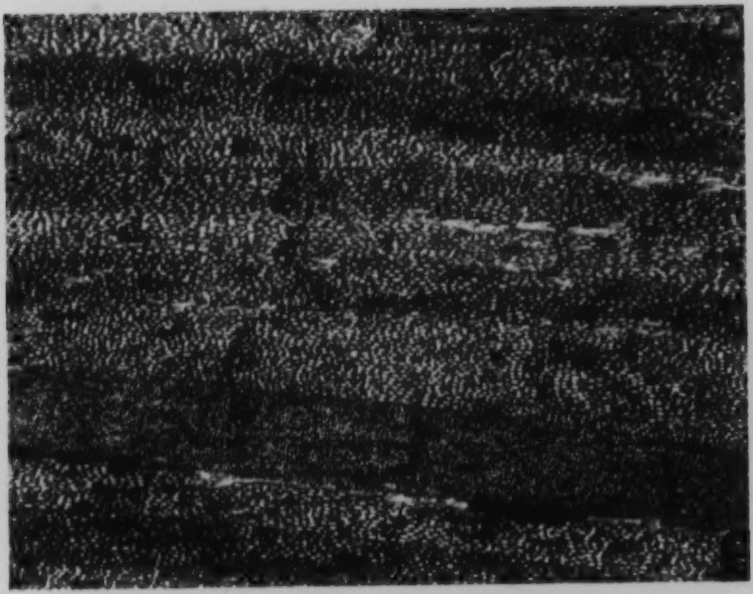

Figure 5-20: A micrograph taken of the observed uniform matrix cracking for the 1H:1A stress ratio magnified 40x. Observe the cracks, which extend through the 0^0 ply into the $\pm66^0$ plies.

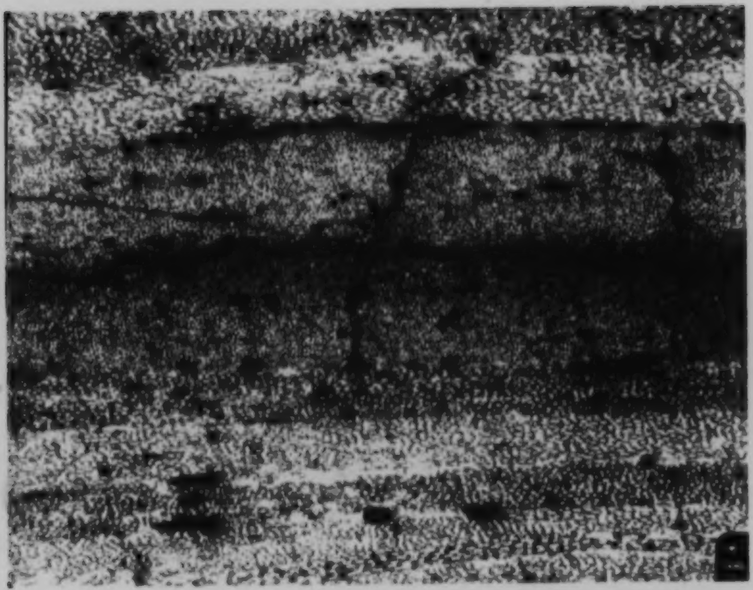

Figure 5-21: A micrograph taken of the observed matrix cracking and delamination for the 2H:1A stress ratio magnified 40x. Observe the inter-ply cracks, which extend through the 0° ply.

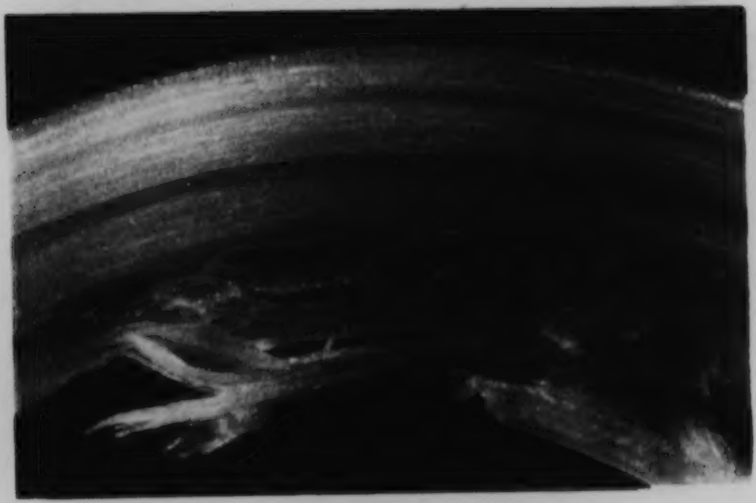

Figure 5-22: A photograph taken of the cross section of the observed structural failure for the 0H:-1A stress ratio. Due to the visibility of the damage area a photograph was taken near the end of the damage zone.

CHAPTER 6

FATIGUE TESTING

6.1 INTRODUCTION

The most important mechanical properties of a multidirectional composite pipe is the strength, the stiffness and the leakage life. These mechanical characteristics are imperative to determine integrity and reliability of the composite pipe. In Chapter 5, the leakage monotonic strength and stiffness were investigated. The lay-up was found to be exceptionally strong in the hoop direction, sustaining no damage under pure pressure loading to 68.95 MPa (10,000 psi).

This chapter is concerned with the development of a biaxial fatigue leakage life envelope to characterize the functional integrity of the multidirectional composite pipe under cyclic loading. The location of the observed imperfections (seen in Chapter 2) to the damaged area is also of considerable interest.

6.2 TESTING PROCEDURES

The biaxial fatigue leakage life envelope was developed under stress control, cycled over the full positive range of stress, to model the high cyclic loading conditions that a composite pipe might see in the field (i.e. worst possible service conditions). The following are the hoop to axial stress ratios applied to the specimen to define the leakage life envelope.

0H:1A The zero hoop to one axial stress ratio simulates a pipe receiving a small internal pressure (a small internal pressure to determine a leakage failure) and a cyclic axial load. This stress ratio is used to simulate cyclic axial tension. An internal pressure of 2.07 MPa

(300 psi) was applied to monitor leakage development. This small internal pressure translates into a 1H:9A stress ratio or greater. A smaller constant pressure is not attainable without triggering off the pressure interlock.

2.5H:1A The 2.5 hoop to one axial stress ratio simulates a pressure vessel type of loading. The pipe ends are capped and a cyclic internal pressure is applied.

1H:0A The one hoop to zero axial stress ratio simulates a pipeline with a cyclic internal pressure. The cyclic internal pressure determines the maximum functional capability of the pipe.

The slight difference in the pressure vessel loading stress ratio of 2H:1A for monotonic loading and 2.5H:1A for fatigue loading is due to the wall thickness of the pipe and the stress equation being defined by the mean radius rather than the inside radius. The 2.5H:1A stress ratio used in fatigue loading is obtained by applying an internal pressure without any axial correction required. (For a further description on this topic refer to Appendix D)

The hoop and axial stresses were cycled over their full stress range at 25 cycles per minute (0.42 Hz). The full stress range was determined by the R-ratio, which is the ratio of minimum to maximum stress, refer to by the Standard Practice for Obtaining Hydrostatic or Pressure Design Basis for "Fiberglass" (Glass-Fiber-Reinforced Thermosetting Resin) Pipe and Fittings, given the ASTM Designation: D2992-91 [81]. The ASTM D2992-91 Standard has a specified a R-ratio of zero (R-ratio = 0 ≈ 0.05) [81]. A R-ratio of zero represents the worst possible service condition scenario as discussed by Nova Pipelines (1990) [67].

The applied average stresses were calculated from the internal pressure and axial load according to the ASTM Standard D2992-91, thin cylinder theory [81]. Thin cylinder theory was assumed in order to simplify calculations (discussed in Chapter 2). (For a further description on the loading consideration required for fatigue testing see

Appendix B)

The data acquisition computer acquired 30 data points on every 100th cycle for the hoop (transverse) and axial strains, axial load, internal pressure, oil volume and axial stroke. The internal pressure and axial load were slowly increased simultaneously to the mean required loads before cyclic loading was initiated. The pressure and axial loads were applied until the test was halted. Stopping of the test occurred after the high-pressure reservoir in the intensifier was exhausted or after a significant amount of movement in the axial stroke was recorded. A significant amount of movement in the axial stroke during fatigue loading may occur by grip slippage, however, no such slippage was observed with the new grip design discussed in Chapter 3.

6.3 PROCEDURES FOR DETERMINING TEST RESULTS

6.3.1 STRESS-STRAIN RESPONSE

The fatigue life of a composite is limited by the ability of the matrix to resist damage (i.e. matrix cracking, fiber debonding, and delamination) during cyclic loading [10]. With the initiation of damage the stiffness properties degrade [68]. This degeneration of the stiffness properties can be monitored by the reduction in the secant modulus (some times referred to as the dynamic stiffness), which is the slope of the stress-strain hysteresis loop. The method of monitoring the reduction of the secant modulus has long been used to obtain an indication of the accumulated damage in composite materials [41, 42, 53, 68, 74]. For the multidirectional fiber-wound pipe the reduction in the secant modulus can be used to determine the level of micro-structural cracking.

The secant modulus was determined from linear regression calculated from the stress-strain hysteresis loop, along with the stress intercept, illustrated in Figure 6-1. This was developed in order to avoid the problem of the shifting of the maximum and minimum stress-strain data points collected. This shift is caused by the inability of the data acquisition system to obtain the true maximum and minimum points in the hysteresis loop. The purpose of linear regression is to obtain a secant modulus based on the entire hysteresis loop as well as obtain an indication of the global trends. This will help to observe the change in the shape of the hysteresis loops due to cracking as well as the variations of the reading due to noise and digital resolution.

6.3.2 LEAKAGE CURVES

An important aspect in the fatigue testing of composite pipe is damage detection, even though cracks can be observed by sectioning after testing. This does not give insight into the damage-state of the specimen during testing. To determine the state of damage, in which micro-cracks coalesce to form larger cracks through the wall thickness, the leakage was monitored. The corrected leakage curves can be correlated to the damage state.

The fatigue leakage curves were extracted from the change in the intensifier volume, accounting for the complexities of the system and the loading condition of the specimen (discussed in Chapter 4). For cyclic loading the volume changes as seen by the intensifier is due to fluid compression and specimen expansion. To ensure a stable reading of the oil volume, each leakage cyclic has been averaged, making the change in volume independent of the variances in the system (i.e. line noise, resolution, etc.). The C source code developed for data conversion of the fatigue tests is presented in Appendix E.

6.4 TEST RESULTS

The figures illustrated throughout this chapter are listed in Table 6-1 along with their corresponding fatigue test and stress ratio. The tests conducted along with the corresponding loading information and leakage life have been summarized in Tables 6-2, 6-3 and 6-4, for the 0H:1A, 2.5H:1A and 1H:0A stress ratios, respectively.

6.4.1 STRESS-STRAIN RESPONSE

A typical cyclic axial stress-strain diagram obtained for the 0H:1A stress ratio with a corresponding maximum axial stress level of 117.40 MPa (17,000 psi) is illustrated in Figure 6-2. The change in slope with the loading cycle is indication of the stiffness loss of the specimen with increasing number of cycles, which is illustrated in Figure 6-3. In this figure the secant modulus determined from linear regression of the stress-strain hysteresis loop, is plotted along with the stress intercept. An initial reduction in the axial secant modulus can be noted, which stabilizes after the first 2000 cycles. However, the stiffness change seen within the first 100th cycle is also due to a small amount of adjusting of the load required to obtain the maximum load. Initially there is a small increase in the axial stress intercept, which stabilizes. This indicates that there is a small amount of ratcheting strain in the lower half of the cycle.

The reduction in the axial secant modulus for the 0H:1A stress ratio with a maximum stress level of 78.01 MPa (11,300 psi) is illustrated in Figure 6-4. Note, the characteristic reduction in the axial secant modulus, which occurs within the first 20,000 cycles, until stabilizing. The small amount of rising and falling seen in the axial secant modulus and the initial decrease of the axial stress intercept is due to temperature fluctuations of the specimen. The topic of the temperature fluctuations and their effects are further discussed in Section 6.5.6.

A typical reduction in the secant modulus along with the corresponding stress intercept obtained from the 2.5H:1A stress ratio with a maximum hoop stress of 127.42 MPa (18,481 psi) and a maximum axial stress of 49.83 MPa (7,227 psi), are illustrated in Figure 6-5. An initial reduction in both the hoop and the axial secant modulus is noted, until debonding and slipping of the hoop (transverse) extensometer occurred.

Figure 6-6 illustrates the reduction in the secant modulus along with the corresponding stress intercept for the 2.5H:1A stress ratio, with a maximum hoop stress of 103.27 MPa (14,980 psi) and maximum axial stress of 41.30 MPa (5,990 psi). Note the greater initial reduction in the hoop secant modulus, followed by a gradual reduction. A gradual reduction is seen in both the hoop and axial secant which modulus stabilizes around 65,000 cycles. The phenomenon of the hoop (transverse) extensometer debonding and slipping occurred in the 2.5H1A stress ratio.

The slight reduction in the hoop secant modulus can be seen in Figure 6-7, for the 1H:0A stress ratio with the maximum hoop stress of 142.29 MPa (20,640 psi), until debonding and slipping of the hoop extensometer occurred.

The slight reduction in the hoop secant modulus can also be seen in Figure 6-8, for the 1H:0A stress ratio with the maximum hoop stress of 118.92 MPa (17,250 psi), until debonding and slipping of the hoop extensometer occurred. The phenomenon of the hoop extensometer debonding and slipping was only seen in the tests with high hoop loading. This phenomenon seems to show a dependence on the maximum applied hoop cyclic stress, suggesting that a certain level of damage must occur before debonding and slipping of the extensometer is seen.

6.4.2 LEAKAGE CURVES

The two points recorded from the corrected leakage curves by visual observations are the initiation point of leakage and the initiation point of intense leakage (discussed in Chapter 4). The leakage curves are presented in Figures 6-9, 6-10 and 6-11 for the 0H:1A, 2.5H:1A and 1H:0A stress ratios, respectively. Because of the varying total oil volume, which is the summed volume for the specimen and the pressurization system, the leakage curves have been made dimensionless, by dividing the average oil volume per cycle by the average initial oil volume and then subtracting one.

$$1-\frac{Vavg_{cycle}}{Vavg_{initial}} \qquad 6\text{-}1$$

The fatigue tests were allowed to run until the oil reservoir of the intensifier was exhausted (approximately 75 ml of oil volume), leakage curves were plotted to observe the change in the leakage rate. No change in the leakage rate was observed past the plotted range.

The leakage curves for the 0H:1A stress ratio are presented in Figure 6-9a to 6-9e in decreasing order from the highest axial cyclic stress of 117.40 MPa (17,000 psi) to the lowest of 78.01 MPa (11,000 psi). For the 0H:1A stress ratio a constant internal pressure was added for determining the leakage. The observed initiation point of leakage, which is not marked on the leakage plots, and the initiation point of intense leakage (N_L), are recorded in Table 6-2.

The characteristic leakage curves for the axial cyclic loading shows a slow initiation into leakage with a slow increase in the leakage rate until a constant rate (observe Figure 6-9a to 6-9e). However, the exception to this, is the lowest axial cyclic stress test of 78.01 MPa (11,000 psi). This leakage curve is illustrated in Figure 6-9e. The small amount of rising and falling noted in the leakage curve is also seen in the axial secant modulus in Figure 6-4. The observed rising and falling is due to the fluctuations in the temperature. The topic of the temperature fluctuations and their effects, are discussed in Section 6.5.6.

The leakage curves for the 2.5H:1A stress ratio are presented in Figure 6-10a to 6-10g in decreasing order from the highest hoop stress of 219.36 MPa (31,800 psi) to the lowest, 103.27 MPa (14,900 psi). The observed initiation point of leakage, which is not marked on the leakage plots, and the initiation point of intense leakage (N_L), are recorded in Table 6-3.

The characteristic leakage curves for the pressure vessel type of cyclic load shows a slow initiation into leakage followed by a rapid increase in the leakage rate. The difference in the characteristic leakage curve for the purely axial type of loading and the pressure vessel type of loading is noted in the transition zone.

The leakage curves for the 1H:0A stress ratio are presented in Figure 6-11a to 6-11e in decreasing order from the highest hoop stress of 219.11 MPa (31,700 psi) to the lowest of 71.09 MPa (10,300 psi). The observed initiation point of leakage, which is not marked on the leakage plots, and the initiation point of intense leakage (N_L), are recorded in Table 6-4.

The characteristic leakage curve for the pure pressure type of cyclic loading is very difficult to predict due to the changes in the mode of failure, as will be seen in Section 6.4.5. Figure 6-11a, with a hoop stress of 219.11 MPa (31,700 psi), shows a bursting failure with no initiation into leakage. Figure 6-11b, with a hoop stress of 166.77 MPa (24,190 psi), shows a slow initiation into leakage followed by a rapid increase in leakage rate, which is also seen in Figure 6-11c, with a hoop stress of 142.29 MPa (20,630 psi).

In Figure 6-11d, with a hoop stress of 118.92 MPa (17,250 psi) and Figure 6-11e, with a hoop stress of 71.09 MPa (10,300 psi), a slow leakage initiation is followed by a rapid increase in the leakage rate, appears to take place, however this may not the case. Due to the lengthy duration of these tests under high-pressure, leakage from the intensifier occurred. Figure 6-11d shows the effect of intensifier leakage along with temperature variations. Leakage was visually noted at 60,000 cycles, which corresponds with leakage curve. No leakage was visually seen in the specimen for Figure 6-11e, which may indicate intensifier leakage.

6.4.3 FATIGUE LIFE CURVES

The fatigue life curves, based on the visually observed initiation point of intense leakage found in Section 6.4.2, are presented in Figures 6-12, 6-13 and 6-14 for the 0H:1A, 2.5H:1A and 1H:0A stress ratios, respectively. The monotonic initiation point of intense leakage, developed in Chapter 5, has also been added to each figure. The maximum applied cyclic stress is plotted versus the number of cycles to leakage failure (N_L). Also depicted in the figures is the least square regression line (best fit) which corresponds to the data.

The fatigue life curve for the 0H:1A stress ratio is illustrated in Figure 6-12 with the maximum applied axial cyclic stress plotted verses the log of the cycles to failure. Note that the monotonic leakage failure point is only slightly higher in comparison to the short-term fatigue life.

The fatigue life curve for the 2.5H:1A stress ratio is illustrated in Figure 6-13 with the maximum applied equivalent cyclic stress plotted versus the log of the cycles to failure. The equivalent cyclic stress was calculated from Equation 5-1. In this case the short-term fatigue leakage failure points are slightly greater then the monotonic leakage failure point. This is in part due to the fact that the monotonic test was conducted at a 2H:1A stress ratio where fatigue testing was conducted at a 2.5H:1A stress ratio as well as the rate of loading effect.

The fatigue leakage life curve for the 1H:0A stress ratio is illustrated in Figure 6-14 with the maximum applied hoop cyclic stress plotted verses the log of the cycles to failure. The monotonic leakage failure point was marked as a continuation because leakage failure was not obtainable. A single long-term fatigue point has also been listed in which failure was not observed.

6.4.4 FATIGUE BIAXIAL FAILURE ENVELOPES

The biaxial fatigue leakage failure envelope was constructed to present the compiled data from the fatigue leakage life curves based on the initiation point of intense leakage. The biaxial fatigue leakage failure envelope illustrates the characteristic cyclic behavior of this multidirectional lay-up composite pipe. The very short-term leakage life 10^3 cycles through to the long-term leakage life, 10^6 cycles have been extracted from the fatigue life curves in Figure 6-12 to 6-14 and are illustrated in Figure 6-15. The monotonic leakage points were added for the sake of comparison. Note the concave shape of the envelope.

6.4.5 OBSERVATIONS OF MACRO DAMAGE

Only a few of the failed specimens from each of the stress ratios are illustrated because of the similarity in the observed macrostructural damage at the same load ratio. The complex ply interactions with different stress ratios are manifested in the failure mode and the accumulated damage.

The complexities of the failures for the multidirectional pipe are observed in Figure 6-16 to 6-25. To visualize the damage through leakage, 5 ml of fluorescent penetrant was added to the fluid volume of the specimen. The fluorescent penetrant was Magnaflux Zyglo ZL-56 that is highly visible under ultraviolet light. The failure observations of the filament wound pipe specimen are based on visual inspection during and after testing. Note that the highly visible area at the border of the epoxy end reinforcement and the specimen is due to the fluorescent penetrant, entering underneath a small area of the debonded epoxy, no damage was observed at this location.

Figures 6-16 and 6-17 illustrates the uniform matrix cracking of the multidirectional pipe at a 0H:1A stress ratio with a maximum cyclic axial stresses of 91.39 MPa (13,250 psi) and 79.04 MPa (11,460 psi), respectively. Uniform matrix cracking developed parallel to the $\pm 66^0$ angle-plies eventually leading to leakage failure, which can be noted on the outer surface. Small oil droplets formed on the outer surface (weepage) as the test progressed, eventually wetting the entire surface. The specimen maintained structural integrity throughout the test. The penetrant gives a clear visualization of the damage. A small amount of acoustic emission was detected during testing. Note that, even though uniform matrix cracking is the main type of damage, there is as greater concentration of cracking in the thinner section of the wall thickness as seen in Figure 6-17.

Leakage failure through combined matrix cracking and delamination of the pipe for the 2.5H:1A stress ratio with a maximum cyclic hoop stress of 127.42 MPa (18,480 psi) is illustrated in Figure 6-18. This shows a representative sample of the combined failure mode, which is typical of the 2.5H:1A stress ratio. Figure 6-19 illustrates the matrix cracking parallel to the ±66° angle-plies eventually leading to a leakage failure at the maximum cyclic hoop stress of 103.27 MPa (14,980 psi). Figure 6-20 illustrates the delamination leading to a pinhole bursting for the maximum cyclic hoop stress of 103.27 MPa (14,980 psi) in a different specimen. Figures 6-19 and 6-20 indicate the variation in the damage mechanism within the specimen at hoop stresses below 127.42 MPa (18,480 psi). Note the macro damage observed during fatigue loading in Figures 6-18 and 6-19 is similar to the damage mechanism observed under monotonic loading, Figure 5-17.

The changing macrodamage for the 1H:0A stress ratio is illustrated in Figure 6-21 to 6-25 in order of the descending maximum cyclic hoop stress. The uniform matrix cracking for the maximum cyclic hoop stress of 219.11 MPa (31,780 psi) is illustrated in Figure 6-21. Matrix cracking can be seen throughout the length of the specimen parallel to the ±66° angle-plies. This type of failure mode was initially seen in the 0H:1A stress ratio.

Delamination leading to a pinhole bursting, at a maximum cyclic hoop stress of 166.77 MPa (24,180 psi), is illustrated in Figure 6-22. Note the drastic change in the failure mode between Figures 6-21 and 6-22 with the difference in maximum cyclic hoop stress of 76.83 MPa (11,140 psi).

Decreasing the maximum cyclic hoop stress to 142.29 MPa (20,640 psi), delamination and matrix cracking lead to a pin hole bursting. A small amount of matrix cracking can be seen in the 0° fiber layer, as in Figure 6-23.

Decreasing the maximum cyclic hoop stress to 118.92 MPa (17,250 psi) the specimen encounters matrix cracking and delamination as illustrated in Figures 6-24 and 6-25. Only a spot (the size of a quarter) of delamination, which preceded pin hole bursting, is noted as in the Figure 6-24. This type of failure was first noted in the 2.5H:1A stress ratio with a maximum cyclic hoop stress of 71.09 MPa (14,980 psi), in

Figure 6-20. Figure 6-25 illustrates the matrix cracking, in the 0^0 and the $\pm 66^0$ angle-plies, as well as delamination occurring in the 0^0fiber layer.

6.4.6 OBSERVATIONS OF MICRO DAMAGE PART I

Due to the similarities in the observed micro and macro structural damage only a few of the failed specimens are illustrated for each of the stress ratios tested. The complex ply interactions at different stress ratios caused a change in the failure mode, and the accumulation of damage seen in the macro level is also observed in the micro structural damage.

A micrograph of the observed uniform matrix damage of the 0H:1A stress ratio is illustrated in Figure 6-26. Due to the uniformity of the matrix cracking the micrograph was taken of the cross section at the center of the gauge length in Figure 6-17. The majority of the cracking is seen as hairline cracking in the $\pm$ 66^0 angle-plies, with a few larger cracks running through the $\pm$ 66^0 plies. A small amount of interface cracking between the 0^0 and the $\pm$ 66^0 plies was also seen. However, most of the cracking took place in the thinner section of the wall thickness, as is noted in Figure 6-17. In the micrograph the lack of cracking in the 0^0 plies and an increase in the amount of cracking in the ± 66 plies is observed.

A micrograph of the delamination seen in Figure 6-18 of the 2.5H:1A stress ratio loading is illustrated in Figure 6-27. The micrograph was taken of the cross section through the center of the delaminated section. Once sectioned the delamination cracks could be seen visually without the aid of magnification. For the 2.5H:1A stress ratio, cracks were more notable in the thicker section of the wall thickness, in the resin rich regions of the 0^0 plies. The majority of the cracking did take place in the 0^0 plies branching out into the $\pm$ 66^0 plies. However, in a few locations cracks were seen in the $\pm$ 66^0 plies parallel to the cracks in the 0^0 fibers, this is illustrated in Figure 6-27. One observation is that, even though a crack existed in the 0^0 plies, some cracks were not reached by the fluorescent penetrant. This implies that a sufficient amount of cracking was not attained to allow the fluorescent penetrant to penetrate through the ±66° plies. In general to have a noticeable delamination revealed by the fluorescent penetrant, a sizable amount of micro cracking must taken place.

A micrograph of the observed delamination section seen in Figure 6-20 of the 2.5H:1A stress ratio is illustrated in Figures 6-28 and 6-29. The micrograph was taken of the cross section through the center of the delaminated section. Once sectioned the delamination cracks could be seen visually without the aid of magnification. The cracks were more noticeable in the thicker section of the wall thickness, in the resin rich regions of the 0° plies. Even though hairline cracks were seen throughout the 0° and ±66° plies, the majority of the delamination cracking took place in the 0° plies branching into the ±66° plies as shown in Figures 6-28 and 6-29.

A micrograph of the observed uniform matrix damage seen in Figure 6-21 of the 1H:0A stress ratio, is illustrated in Figure 6-30. Due to the uniformity of the matrix cracking a micrograph was taken of the cross section at the center of the gauge length. Extensive cracking can be seen in all three of the 0° plies as well as hairline cracks extending into the ±66° plies. This is illustrated in Figure 6-30, which shows the cracking in the inner most ±66° plies and extensive cracking in the inner most 0° ply.

A micrograph of the observed delamination damage and 0° fiber cracking for the 1H:0A stress ratio, as seen in Figures 6-23 and 6-25, is illustrated in Figures 6-31 and 6-32, respectively. The micrographs were taken of the cross section through the center of the delaminated section. Once sectioned the delamination cracks could be seen visually without the aid of magnification. Extensive cracking could be seen in all of the 0° plies extending into the ±66° plies.

The imperfections found in the composite pipe, (discussed in Chapter 2) were: The misalignment of fibers from the intended angle of lay-up, the existence of partial layers of fiber, fiber waviness from resin richness, resin rich regions in the 0° plies and voids (porosity). It is difficult to determine, from the micrographs, how much influence the misalignment of fibers from the intended angle of lay-up and the existence of partial layers have in the initiation of internal cracking and other forms of damage.

The micrographs were taken to give an indication of the proximity of the fiber waviness, regions in the 0^0 plies rich in resin and voids (porosity) to damaged area. Two observations made are:

1. Damage seen in the micrograph in the 0^0 plies appears to be confined to the regions in the resin rich plies. This is illustrated in Figure 6-33, which shows the over sized section in the 0^0 ply, the inter-ply and interface cracking.

2. Voids did not seem to have as much effect on crack placement as the resin richness in the 0^0 fibers and the size of the voids. The influence of void size on the location of cracking is illustrated in Figure 6-34, which shows a void comparably larger then the rest of the void population. In some cases the voids are seen as crack arrestors.

6.4.7 OBSERVATIONS OF MICRO DAMAGE PART II

In order to visualize the damage by fluorescent penetrant under ultraviolet light in the macro pictures the damage had to be near the surface. However, the use of micrographs to obtain a picture of the type and location of the damage based on a larger scale is difficult. In order to view the damage on a global scale, photographs of the cross-sections of the specimen, from which the micrographs were taken, are presented in Figure 6-35 to 6-40.

Fluorescent penetrant was added to the fluid volume of the specimen to visualize the complex failure modes of the multidirectional pipe, which is highly visible under ultraviolet light. The photographs of the cross-sections, taken under ultraviolet light and ambient light, make it easier to visualize the damage areas based on geometric irregularities.

A photograph of the observed uniform matrix cracking parallel to the ± 66° fibers of the 0H:1A stress ratio is illustrated in Figure 6-35. Damage in the ± 66° can be visualized as well as the absence of damage in the 0° plies. Note that there is a greater concentration of cracking in the thinner section of the wall thickness. Small oil droplets formed on the outer surface (weepage) as the test progressed, eventually wetting the entire surface, indicating that some cracking took place in the 0° plies.

Photographs of the observed delamination section seen in Figures 6-18 and 6-20 for the 2.5H:1A stress ratio are illustrated in Figure 6-36 and Figure 6-37, respectively. The decrease in the maximum cyclic hoop stress from 127.42 MPa (18,480 psi) to 103.27 MPa (14,980 psi) can be noted in the amount of internal damage. In Figure 6-36 the damage in the inner ± 66° plies and the cracking in the 0° plies is easily seen. The cracks are more notable in the thinner section of the wall thickness, but cracking can also be observed round the circumference in all the 0° plies. In Figure 6-37 damage can only be seen in the first few inner ±66° angle-plies. The delamination leading to pin hole bursting can be seen in the thinner section of the wall thickness.

Photographs of the observed delamination section seen in Figures 6-21, 6-23 and 6-25 of the 1H:0A stress ratio are illustrated in Figures 6-38, 6-39 and 6-40, respectively. The changing macro-damage can be seen in order of decreasing maximum cyclic hoop stress. The internal damage for the maximum cyclic hoop stress 219.11 MPa (31,780 psi) illustrated in Figure 6-38, shows less of a resemblance to the uniform matrix cracking seen of the 0H:1A stress ratio of loading, but more of resemblance to the delamination type of damage for the 2.5H:1A stress ratio as seen in Figure 6-36. Extensive cracking can be seen in both the 0° and ±66° plies. Greater damage can be seen in the thinner part of the wall thickness.

The damage in the inner ± 66° plies is easily visualized along with cracking in the 0° plies in Figure 6-39 for a maximum hoop stress of 142.29 MPa (20,640 psi) and Figure 6-40 for a maximum hoop stress of 118.92 MPa (17,250 psi). Note that there is a greater concentration of cracking in the thicker section of the wall thickness, where the 0^0 ply is the richest in resin.

6.5 INTERPRETATION OF DATA

6.5.1 STRESS-STRAIN BEHAVIOR

The secant modulus determined from linear regression of the stress-strain hysteresis loop, along with the stress intercept has been plotted versus the number of cycles. This provides a good indication of the initial stiffness and the amount of stiffness reduction. Visualizing the small change in slope from the stress-strain hysteresis loop would be very difficult, as seen in Figure 6-2. The secant modulus is based on the applied cyclic load and the measured strain. Since the tests are based on a constant cyclic load, the reduction in the stiffness is mainly due to an increase in the cyclic strain. This increase in the cyclic strain has been linked to the initiation of cracking, which induces a non-uniform strain in the plies constraining the crack [93]. For the multidirectional fiber-wound pipe, the stabilizing of the secant modulus can be interpreted as the saturation limit of micro cracking within the plies.

For the 0H:1A stress ratio (see Figures 6-3 and 6-4) there was an initial drop in the axial secant modulus and it reaches a stable value after a few thousand cycles. This indicates that a substantial amount of damage occurs in the initial few thousand cycles. Comparison of the rate of reduction of the secant modulus between the two stress levels presented for the 0H:1A stress ratio, in Figures 6-3 and 6-4, indicates that the drop in the secant modulus is dependent of the applied cyclic load.

For the 2.5H:1A stress ratio, depicted in Figures 6-5 and 6-6, there is a slight drop in both the axial and the hoop secant modulus before stabilization (Figure 6-6) with a more significant initial drop seen in the hoop secant modulus. This again indicates that most of the damage occurs in the first few thousand cycles. However, in Figure 6-5 this initial drop in the hoop secant modulus is not seen, which could mean that a significant drop took place within the first hundred cycles.

For the 1H:0A stress ratio, seen in Figures 6-7 and 6-8, there is only a slight drop in the hoop secant modulus before stabilizing. This slight drop is more noticeable at lower hoop stresses. It is possible that a more significant drop occurs within a few hundred cycles or a few cycles as compared to a few thousand. This is hard to determine due to load adjusting in the first hundred cycles. This relatively small reduction in the secant modulus as compared to the 0H:1A and 2.5H:1A stress ratio could be due to the high fiber content in the hoop direction.

In comparison, the largest initial reduction is seen in the axial secant modulus under pure axial loading and the hoop secant modulus under pressure vessel type loading. However, the axial secant modulus under pure axial loading and in the hoop secant modulus under pure pressure type loading stabilizing after an initial reduction, unlike hoop and axial secant modulus under pressure vessel type loading. In all cases there is a noticeable decrease in the secant modulus followed by stabilizing. The amount of reduction in the secant modulus seems to show a connection between the stress ratio and the applied stress.

The phenomenon of the transverse extensometer debonding and slipping occurred in the cyclic tests under a high hoop stress, which can be seen in Figure 6-5 to 6-8. The debonding and slipping is seen in the stiffness curves as a sudden rise and fall in the secant modulus and stress intercept. The slippage, in terms of movement, is in the order of the diameter of the human hair, 0.1 mm (0.004 in). Slippage takes place only after a sufficient amount of damage has occurred and leakage has been noted.

6.5.2 LEAKAGE BEHAVIOR

The characteristic leakage curves, corrected for movement in the specimen and oil compression, are presented in Figure 6-9 to 6-11 for the 0H:1A, 2.5H:1A and 1H:0A stress ratios, respectively.

The leakage curves for the 0H:1A stress ratio are presented in Figure 6-9a to 6-9e in descending order from the highest axial cyclic stress of 117.40 MPa (17,000 psi) to the lowest of 78.01 MPa (11,000 psi). The characteristic leakage curve for this stress ratio is a slow leakage initiation with a slow increase in the leakage rate until rapid leakage.

The leakage curves for the 2.5H:1A stress ratio are presented in Figure 6-10a to 6-10g in descending order from the highest hoop stress of 219.65 MPa (31,800 psi) to the lowest of 103.27 MPa (14,900 psi). The characteristic leakage curve for this stress ratio is a slow leakage initiation followed by a rapid increase in leakage rate.

The leakage curves for the 1H:0A stress ratio are presented in Figure 6-11a to 6.11e in descending order from the highest hoop stress of 219.11 MPa (31,700 psi) to the lowest of 71.09 MPa (10,300 psi). They do not indicate a distinct characteristic leakage curve, except that there are some similarities to the characteristic leakage curve for the pressure vessel type of loading. At a high hoop stress of 219.11 MPa (31,700 psi) the mode of failure is pinhole bursting, which is seen as abrupt leakage. As the hoop stress is lowered the leakage curves resemble the characteristic leakage curve for the pressure vessel type of loading. However, as the hoop stress is lowered even more to the point where life is greater then a few hundred thousand cycles, leakage also occurs in the intensifier.

The slow leakage initiation followed by a rapid increase in leakage rate is a characteristic of the leakage curve for stress ratios with a substantial hoop loading. This indicates that once micro-cracks have formed from cyclic loading, aided by the internal pressure coalescing of cracks intensifies, which leads to an increase in the leakage rate. Increasing the internal pressure allows the fluid to penetrate through the micro-cracks, thus causing the cracks to open and coalesce, causing a rapid increase in leakage rate after a slow leakage initiation.

The leakage initiation and the point of intense leakage, obtained by visual inspection, are noted as functional failure points. The initiation point on the corrected leakage curve indicates that the extent of micro cracking has become sufficient to develop fluid loss. The points of leakage initiation and intense leakage are listed in Table 6-1 to Table 6-3. The point of leakage initiation was not plotted on the fatigue life curves because the data points closely resembled the points of intense leakage. It was found that the leakage initiation curves were slightly lower then the initiation point of intense leakage curve with comparable slopes.

6.5.3 FATIGUE LEAKAGE LIFE

The fatigue life curves were based on the visually observed initiation point of intense leakage found in Section 6.4.3. The visually observed initiation point of intense leakage is a good indicator that the micro-cracks are sufficient enough to allow for an increase in the leakage rate. This point is less sensitive to external effects.

In comparing the leakage life curves depicted in Figure 6-12 to 6-14, the fatigue life curves for the 0H:1A and 2.5H:1A stress ratios were found to have comparable life. However the 0H:1A stress ratio had a slightly steeper slope. This seemed to be influenced by the short-term life, which indicates that the fatigue life for the 0H:1A and 2.5H:1A stress ratios is governed by the axial stress component. The 2.5H:1A and the 1H:0A stress ratio have comparable slopes, but the 1H:0A stress ratio has a longer life. This indicates that the leakage failure for the 1H:0A stress ratio is governed by the hoop component, and because the predominant fiber content is in the hoop direction, greater life is achieved, as seen in Figure 6-15.

The monotonic initiation points of intense leakage (refer to Chapter 5) were also added for comparison of the fatigue leakage life curve. For the 0H:1A and 2.5H:1A stress ratios the very short-term life (i.e. life less than 10^3 cycles) is only slightly higher in the applied stress than the monotonic limit. At high stresses, cracks initiate and propagate rapidly with unrestricted fluid flow, thus monotonic and fatigue strengths are in close proximity.

6.5.4 FATIGUE LEAKAGE LIFE ENVELOPE

The compiled data from the fatigue life curves, based in the initiation point of intense leakage, is represented by a biaxial fatigue failure envelope. The biaxial fatigue failure envelope illustrates the characteristic cyclic behavior of this multidirectional lay-up in composite pipe. The very short-term leakage life, 10^3 cycles, to the long-term leakage life, 10^6 cycles, extracted from the fatigue leakage life curves, Figure 6-12 to 6-14 are illustrated in Figure 6-15. The monotonic leakage points were added for the comparison.

The biaxial fatigue leakage life envelope represents the initiation of intense leakage line under the cyclic biaxial state of stress. The large change from the convex shape for the monotonic leakage envelope to the concave shape for the fatigue leakage envelope is to be noted. Clearly the monotonic leakage envelope does not predict the shape or position of the fatigue leakage life envelope.

Note that under axial tension loading the very short-term (10^3 cycles) fatigue leakage life falls on the monotonic leakage point. There is, however, a considerable distance between the very short-term (10^3 cycles) fatigue leakage life and the maximum applied monotonic pressure loading.

6.5.5 MACRO AND MICRO BEHAVIOR

Only a few samples of the failed specimens from each of the stress ratios are illustrated because of the similarity in the observed macrostructural damage under the same loading ratio. The complex ply interactions and the damage accumulated from the different applied stress ratios and maximum applied stress can be observed from the macro and micro behavior as seen in the photographs.

The characteristic type of damage observed in the multidirectional pipe for the 0H:1A stress ratio is uniform matrix cracking, which develops parallel to the $\pm 66^0$ fibers, as seen in Figures 6-16 and 6-17. A micrograph of the observed uniformed matrix damage, illustrated in Figure 6-26, shows cracking in the $\pm$ 66^0 plies and no observed cracks in the 0^0 plies. This is emphasized in the photograph of the cross section, Figure 6-35. The damage in the $\pm 66^0$ plies and the absence of damage in the 0^0 plies can easily be visualized. Note that there seems to be a greater concentration of cracking in the thinner section of the wall thickness, suggesting that there is a higher stress at the thinner wall section.

The characteristic type of damage observed for the 2.5H:1A stress ratio is a combination of matrix cracking and delamination, as seen in Figure 6.18 to 6.20. These figures show the matrix cracking parallel to the $\pm 66^0$ angle-plies as well as delamination leading to pin hole bursting. Unlike the 0H:1A stress ratio, where the damage mode is not dependent on the applied maximum stress, the 2.5H:1A stress ratio is. Once the maximum applied hoop stress is below 127.42 MPa (18,480 psi) the damage type changes from a combined matrix cracking and delamination to a delamination pinhole bursting. This is further observed in the photographs of the cross section illustrated in Figures 6-36 and 6-37. The damage in the inner $\pm 66^0$ plies and the cracking in the 0^0 plies can be easily visualized in Figure 6-36. In Figure 6-37 there are considerably fewer cracks in the first few inner $\pm 66^0$ plies and in the 0^0 plies. Again cracking is more notable in the thinner section of the wall thickness. The micrographs for the 2.5H:1A stress ratio failed to show any distinct difference between the damage types as seen in Figure 6-27 to 6-29.

The 1H:0A stress ratio did not seem to have a distinct type of damage characteristic as seen in Figure 6-21 to 6-25. The observed damage appears to depend on the maximum applied stress. Damage changed uniform matrix cracking to delamination with pin hole bursting to a combination of both, with a difference in the maximum cyclic hoop stress of only 76.83 MPa (11,140 psi). The micrographs fail to show a distinction between the damage types as seen in Figure 6-30 to 6-32. However, the photographs of the observed damaged cross sections, as seen in Figure 6-38 to 6-40, show a distinct change in the observed damage with a descending maximum cyclic hoop stress.

Imperfections are obviously a contributor to the initializing of internal cracking and other forms of damage. However some of the effects of imperfections noted in Chapter 2 are difficult to determine from the micrographs and photographs of the cross section, like the misalignment of fibers and partial layers. The micrographs and photographs of the cross-section do give an indication of the proximity of the fiber waviness, resin rich regions in the 0^0 plies and voids (porosity) to the areas of cracking.

The micro-scale imperfections (i.e. voids and dust) seem to have less of an effect on crack initiation then macro-scale imperfections. However, the influence of void size on cracking is illustrated in Figure 6-34, which shows that there is influence in void size relative to the rest of the population of voids. Voids have been seen as crack arrestors in some cases.

Macro-scale type of imperfection seems to have more influence on crack initiation, these include fiber waviness and resin rich regions in the 0^0 plies. This is reinforced by Figure 6-33, which shows the inter-ply and interface cracking in a resin rich section in a 0^0 ply. Photographs of the cross-section, seen in Figure 6-35 to 6-40, taken under ultraviolet light and ambient light, make it easier to visualize the damage areas based on geometric irregularities.

From the cross-section photographs a greater concentration of cracking in the thinner section of the wall thickness can be seen with the exception of Figures 6-39 and 6-40. These figures, which show an abnormal build up of resin, have a greater concentration of cracking in the thicker wall section. This can only be explained by the existence of higher stresses in these sections.

6.5.6 TEMPERATURE BEHAVIOR

The temperature of the specimen was monitored during fatigue testing by a type J thermo-couple placed on the surface of the specimen with Devcon 5-Minute Epoxy. The purpose for monitoring the temperature was to obtain an over all idea of the environmental effects on the specimen over the duration of fatigue testing. The problem with measuring the temperature increase of the specimen, due to any type of natural heating from cyclic loading, was influenced by three outside heat sources. The hydraulic power unit situated in the same room as the testing apparatus, the overall building temperature and the fluid from the intensifier pressurizing the specimen, all contributed to the rise in temperature of the specimen. In order to alleviate the problem of varying temperature, as seen in Figures 6-4 and 6-11d, the airflow over the hydraulic power unit was increased equalizing the room temperature to the building temperature. This did help to level out the data curves, which showed sensitivity to temperature fluctuation. However, this still left fluctuation in temperature from the building and the pressurizing fluid.

The temperature results gave an explanation of the fluctuations seen in the data. As mentioned in Chapter 4, the compressed oil volume is a function of temperature. This is noted in Figure 6-11d. Due to time constraints, lack of experimental equipment and unavailable information on the subject from the hydraulic fluid supplier, the compressed oil volume was not corrected for temperature. Temperature fluctuations will also have some effect on the expansion shape of the specimen causing a negative zero shift in the extensometers.

Temperature fluctuations with this experimental apparatus proved to be difficult to control. So, it is not possible to say if the slight changes in temperature had any significant effect on the fatigue life or damage development. However, measuring the temperature at the specimen to determine the temperature rise due to any cyclic heating was totally inconclusive, as expected.

6.6 FATIGUE AND MONOTONIC RESULTS

An important question which arises at this point is: can the data collected from monotonic testing be used to estimate the biaxial fatigue leakage life envelope? The monotonic data points collected for the multi-directional lay-up under study have been superimposed onto the biaxial fatigue leakage life envelope, as illustrated in Figure 6-41. The complexities of this multi-directional lay-up can be seen from the combined data points.

However, the monotonic data points seem to, exceed (overestimate) the fatigue leakage life envelopes. There is some correlation between the short-term leakage life, 10^4 cycles, and the linear limit on the strain-strain curve with the exception of a single data point, as illustrated in Figure 6-42. It is difficult at this point to determine if this relationship is coincidental or not. Since the nonlinear points on strain-strain curve were determined with human bias, the points thus determined would dependent on the plotted scale.

The monotonic test data fails to predict the concave shape of the fatigue leakage life, which is very important in evaluating a multidirectional lay-up. The long-term leakage life, 10^6 cycles or greater is needed to determine a maximum operating pressure for the composite pipe. This combined biaxial leakage life and strength envelope does give insight into the complex behavior of this multi-directional lay-up.

6.7 CONCLUDING REMARKS

Considerable insight was gained into the complex behavior of the commercially wound, multidirectional glass fiber reinforced epoxy pipe from biaxial fatigue testing. The cyclic investigation revealed mechanical characteristics, imperative to determine the functional integrity and reliability of the pipe. The results showed that this lay-up had a greater resistance to fatigue under 0H:1A and 1H:0A stress ratio then the 2.5H:1A stress ratio.

The secant modulus determined from linear regression calculated from the stress-strain hysteresis loop, along with the stress intercept, proved to be invaluable in obtaining an ideal of the global trends.

The corrected leakage curves proved to be exceptionally valuable in determining a point of failure based on the onset of damage, as well as the development of the associated characteristics depended on the applied stress ratio.

Table 6-1 - Summary of Test Results For The Applied 0H:1A Stress Ratio

Test	Stress Ratio	Reference Figures				
		Secant (Figure #)	Leakage (Figure #)	Macro-Damage (Figure #)	Micro-Damage (Figure #)	Cross-Section (Figure #)
1	0H:1A	6-3	6-9 a			
2	0H:1A		6-9 b			
3	0H:1A		6-9 c	6-16		
4	0H:1A		6-9 d	6-17	6-26	6-35 (a-b)
5	0H:1A	6-4	6-9 e			
1	2.5H:1A		6-10 a			
2	2.5H:1A		6-10 b			
3	2.5H:1A		6-10 c			
4	2.5H:1A		6-10 d			
5	2.5H:1A	6-5	6-10 e	6-18	6-27	6-36 (a-b)
6	2.5H:1A		6-10 f			
7	2.5H:1A	6-6	6-10 g	6-20	6-28, 6-29	6-37 (a-b)
1	1H:0A		6-11 a	6-21	6-3	6-38 (a-b)
2	1H:0A		6-11 b	6-22		
3	1H:0A	6-7	6-11 c	6-23	6-31, 6-33, 6-34	6-39 (a-b)
4	1H:0A	6-8	6-11 d	6-24, 6-25	6-35	6-40 (a-b)
5	1H:0A		6-11 e			

Table 6-2 - Summary of Test Results For The Applied 0H:1A Stress Ratio

Test	R-ratio	Cyclic Frequency (Hz)	Maximum Hoop Stress (MPa)	Minimum Hoop Stress (MPa)	Maximum Axial Stress (MPa)	Minimum Axial Stress (MPa)	Leakage (Initiation) Cycle	Leakage (Intense) Cycle	Last Recorded Cycle
1	0.05	0.417	8.493	8.493	117.396	5.870	6000	15000	39000
2	0.05	0.417	8.763	8.763	100.905	8.570	3000	10000	33000
3	0.05	0.417	8.449	8.449	91.376	4.569	35000	55000	182300
4	0.05	0.417	8.442	8.442	79.041	3.952	17000	72000	301200
5	0.05	0.417	11.523	11.523	78.013	3.901	220000	270000	275800

Table 6-3 - Summary of Test Results For The Applied 2.5H:1A Stress Ratio

Test	R-ratio	Cyclic Frequency (Hz)	Maximum Hoop Stress (MPa)	Minimum Hoop Stress (MPa)	Maximum Axial Stress (MPa)	Minimum Axial Stress (MPa)	Leakage (Initiation) Cycle	Leakage (Intense) Cycle	Last Recorded Cycle
1	0.05	0.417	219.653	13.723	83.441	4.536	100	160	450
2	0.05	0.417	218.816	13.305	83.432	4.808	60	170	350
3	0.05	0.417	164.426	10.459	62.423	3.294	500	1100	2600
4	0.05	0.417	137.730	8.786	52.293	2.631	2000	4000	9500
5	0.05	0.417	127.424	6.371	49.832	2.492	3500	6500	13500
6	0.05	0.417	110.537	7.113	42.029	2.611	25000	31000	50000
7	0.05	0.417	103.273	5.164	41.309	2.065	30000	70000	124560

Table 6-4 - Summary of Test Results For The Applied 1H:0A Stress Ratio

Test	R-ratio	Cyclic Frequency (Hz)	Maximum Hoop Stress (MPa)	Minimum Hoop Stress (MPa)	Maximum Axial Stress (MPa)	Minimum Axial Stress (MPa)	Leakage (Initiation) Cycle	Leakage (Intense) Cycle	Last Recorded Cycle
1	0.05	0.417	219.110	10.955	0	0	70	70	2300
2	0.05	0.417	166.772	8.339	0	0	6500	14600	28500
3	0.05	0.417	142.289	7.114	0	0	9500	52000	71300
4	0.05	0.417	118.924	5.946	0	0	15000	80000	226000
5	0.05	0.417	71.092	3.555	0	0	n/a	n/a	1200000

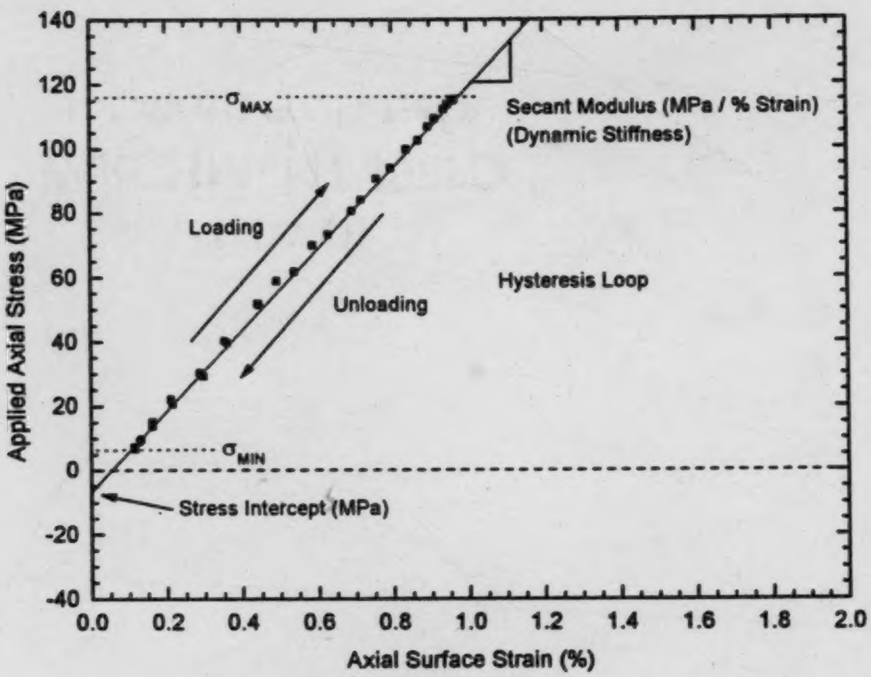

Figure 6-1: Illustration of the secant stress-strain behavior during a single fatigue cyclic. The secant stiffness was determined by linear regression fit through the stress-strain data.

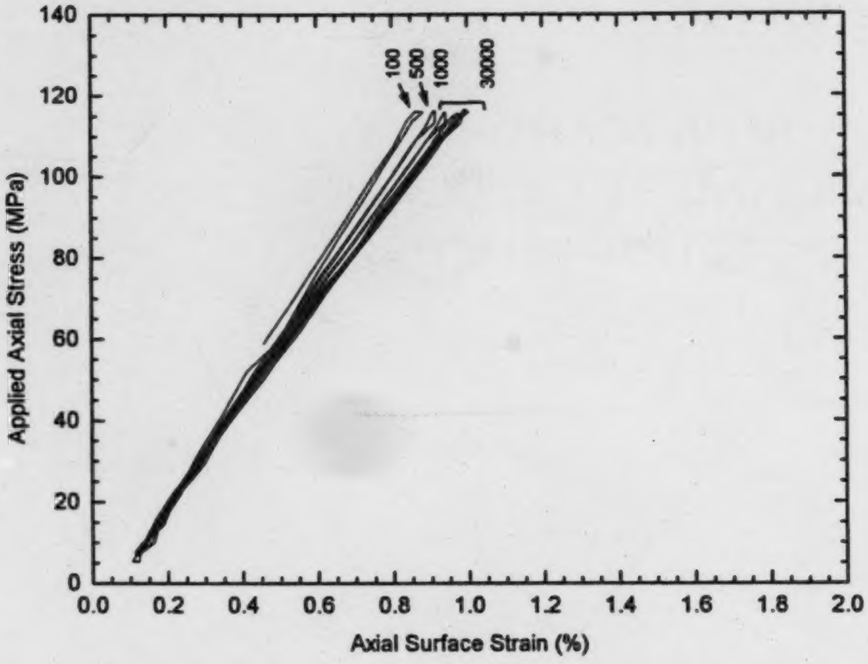

Figure 6-2: Recorded applied axial stress verses axial surface strain response of the composite pipe under investigation with a 0H:1A stress ratio, note the change in slope with loading cycle.

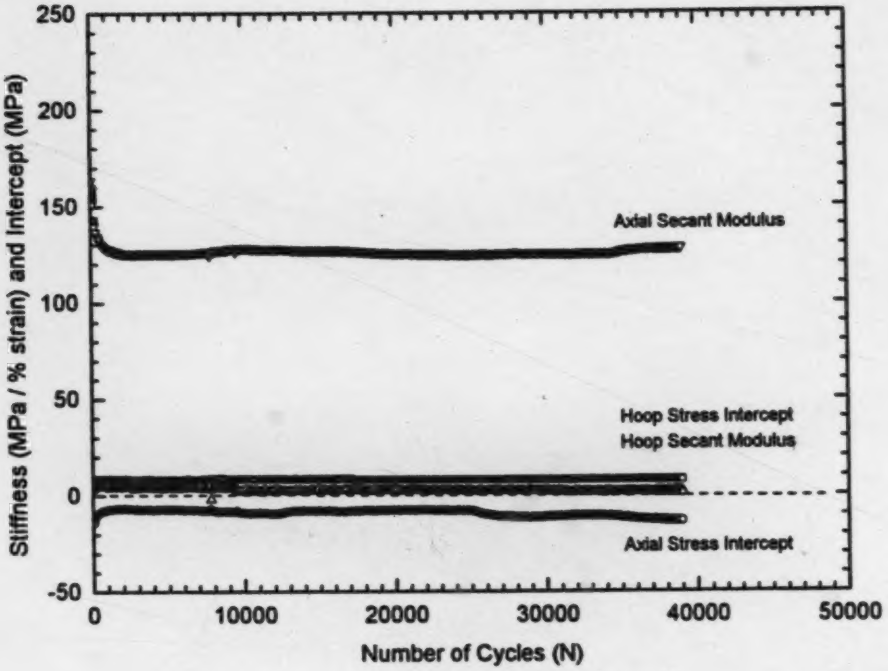

Figure 6-3: Secant modulus and stress intercept curves for the 0H:1A stress ratio the corresponding applied stress-strain response was presented in Figure 6-2. This test had a maximum axial stress level of 117.4 MPa (17000 psi).

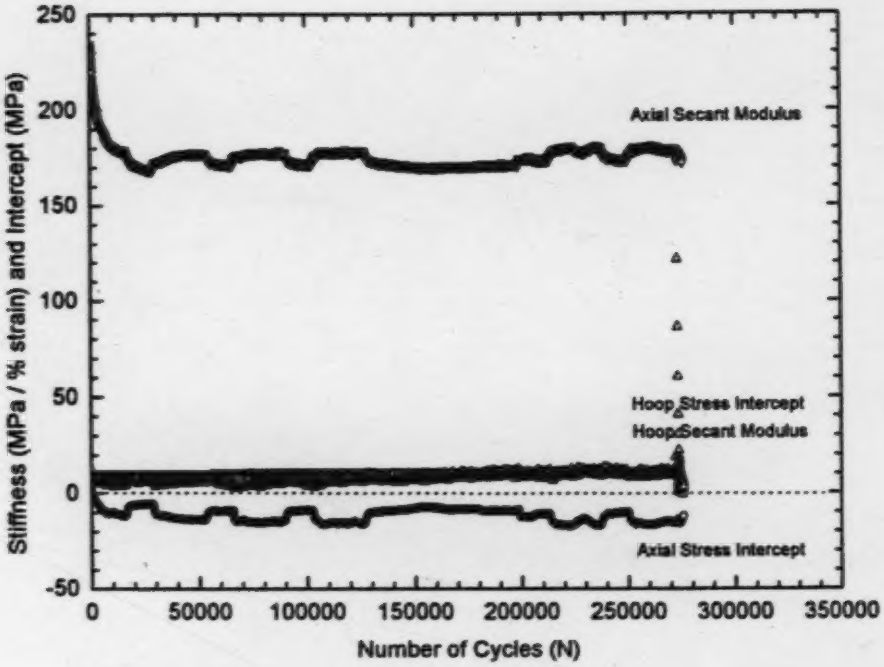

Figure 6-4: Secant modulus and stress intercept curves with a 0H:1A stress ratio. The corresponding maximum axial stress level is 78.01 MPa (11310 psi). Note the waviness in the axial secant modulus and stress intercept is due to temperature interference.

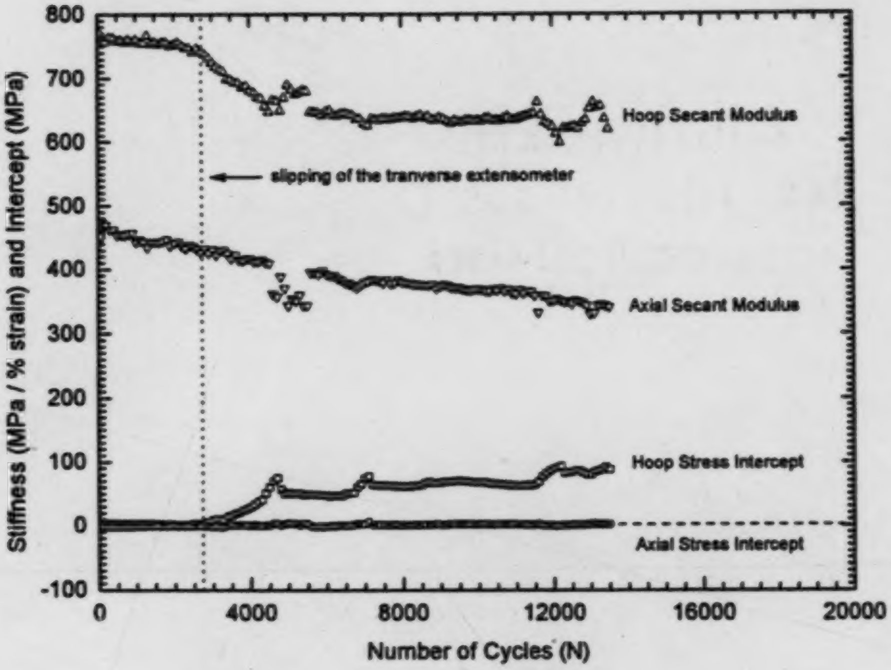

Figure 6-5: Secant modulus and stress intercept curves with a 2.5H:1A stress ratio. The corresponding maximum hoop stress level is 127.4 MPa (18481 psi) and the maximum axial stress level is 49.8 MPa (7227 psi). Note the debonding and slipping of the transverse extensometer occurred at approximately 2700 cycles.

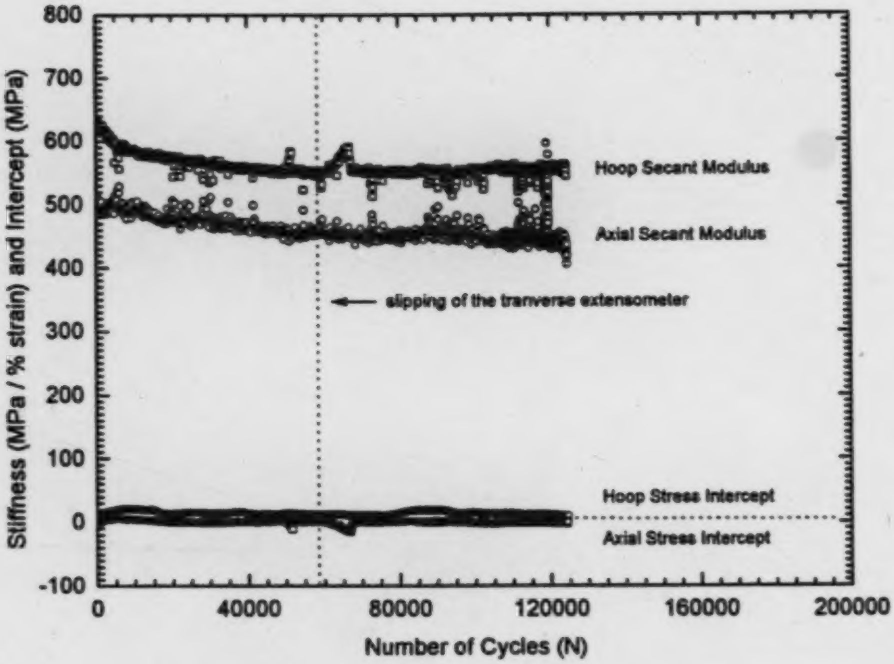

Figure 6-6: Secant modulus and stress intercept curves with a 2.5H:1A stress ratio. The corresponding maximum hoop stress level is 103.3 MPa (14978 psi) and maximum axial stress is 41.3 MPa (5991 psi). Note the debonding and slipping of the transverse extensometer occurred at approximately 58000 cycles.

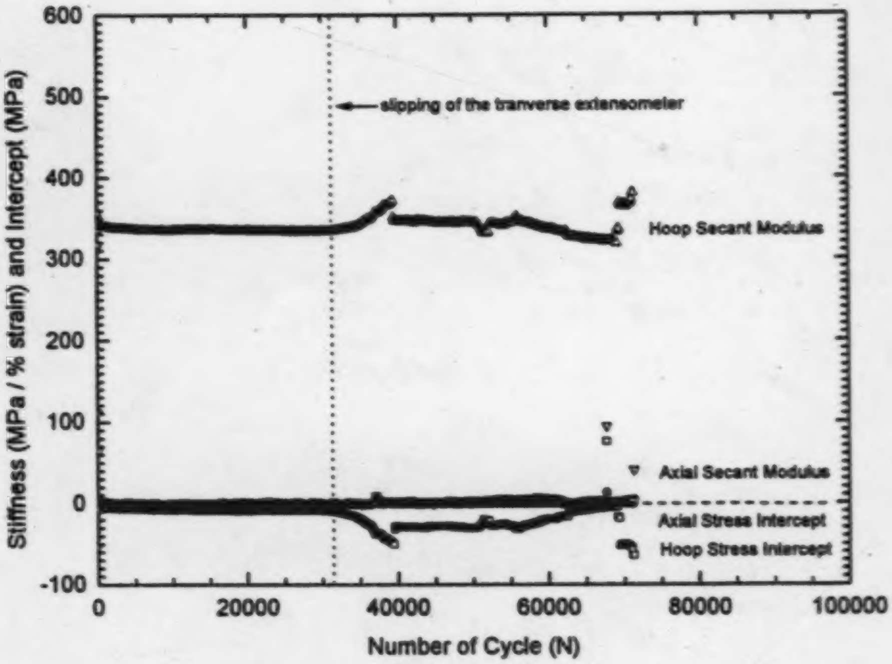

Figure 6-7: Secant modulus and stress intercept curves with a 1H:0A stress ratio. The corresponding maximum hoop stress level of 142.2 MPa (120637 psi). Note the debonding and slipping of the transverse extensometer occurred at approximately 32000 cycles.

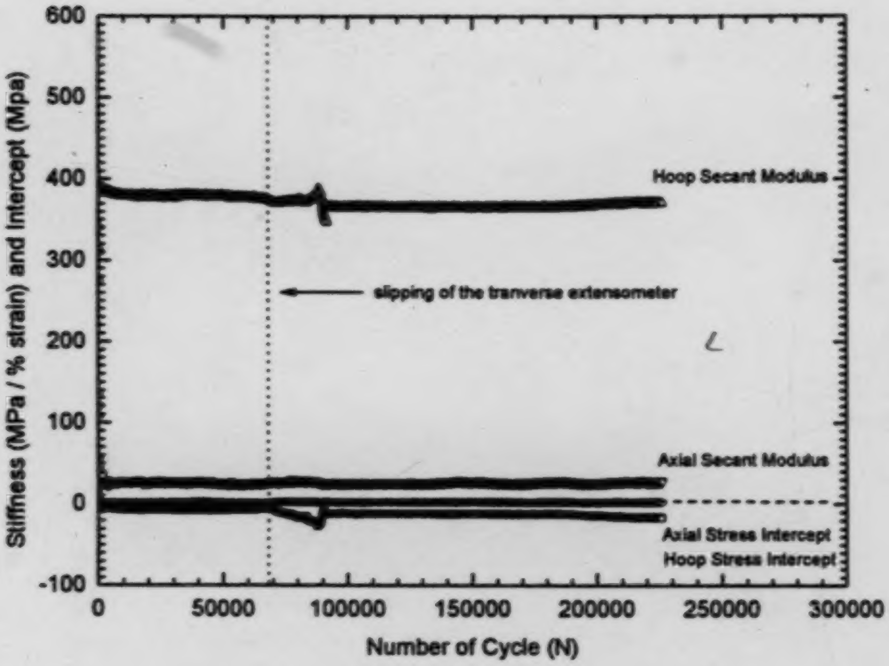

Figure 6-8: Secant modulus and stress intercept curves with a 1H:0A stress ratio. The corresponding maximum hoop stress level is 118.9 MPa (17248 psi). Note the debonding and slipping of the transverse extensometer occurred at approximately 70000 cycles.

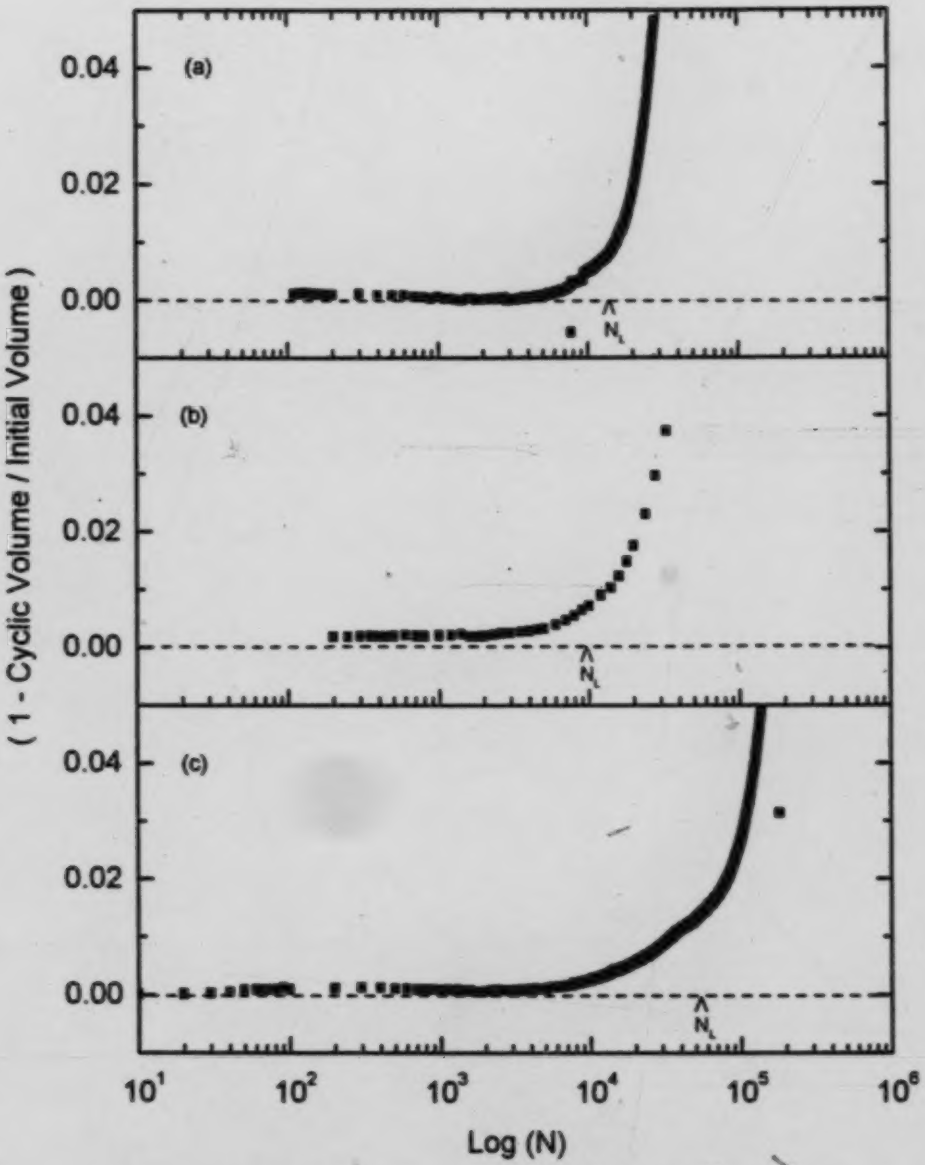

Figure 6-9 (a-e): Leakage verses the number of cycles for the 0H:1A stress ratio in descending order from the highest axial stress to the lowest.

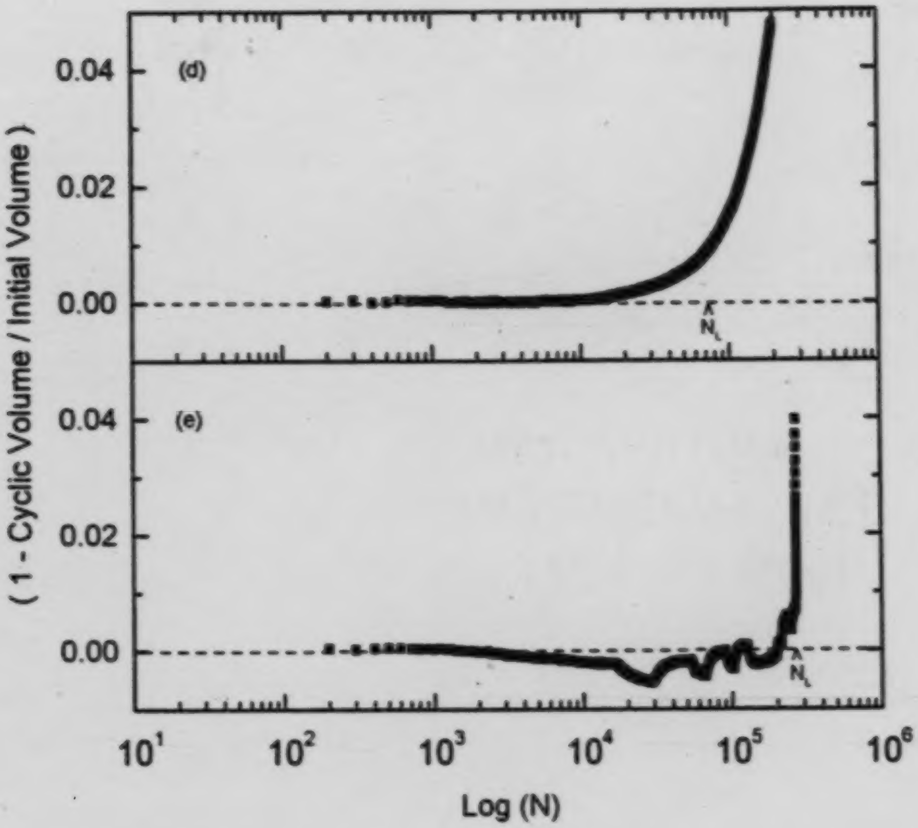

Figure 6-9 (a-e) (con't): Leakage verses the number of cycles for the 0H:1A stress ratio in descending order from the highest axial stress to the lowest.

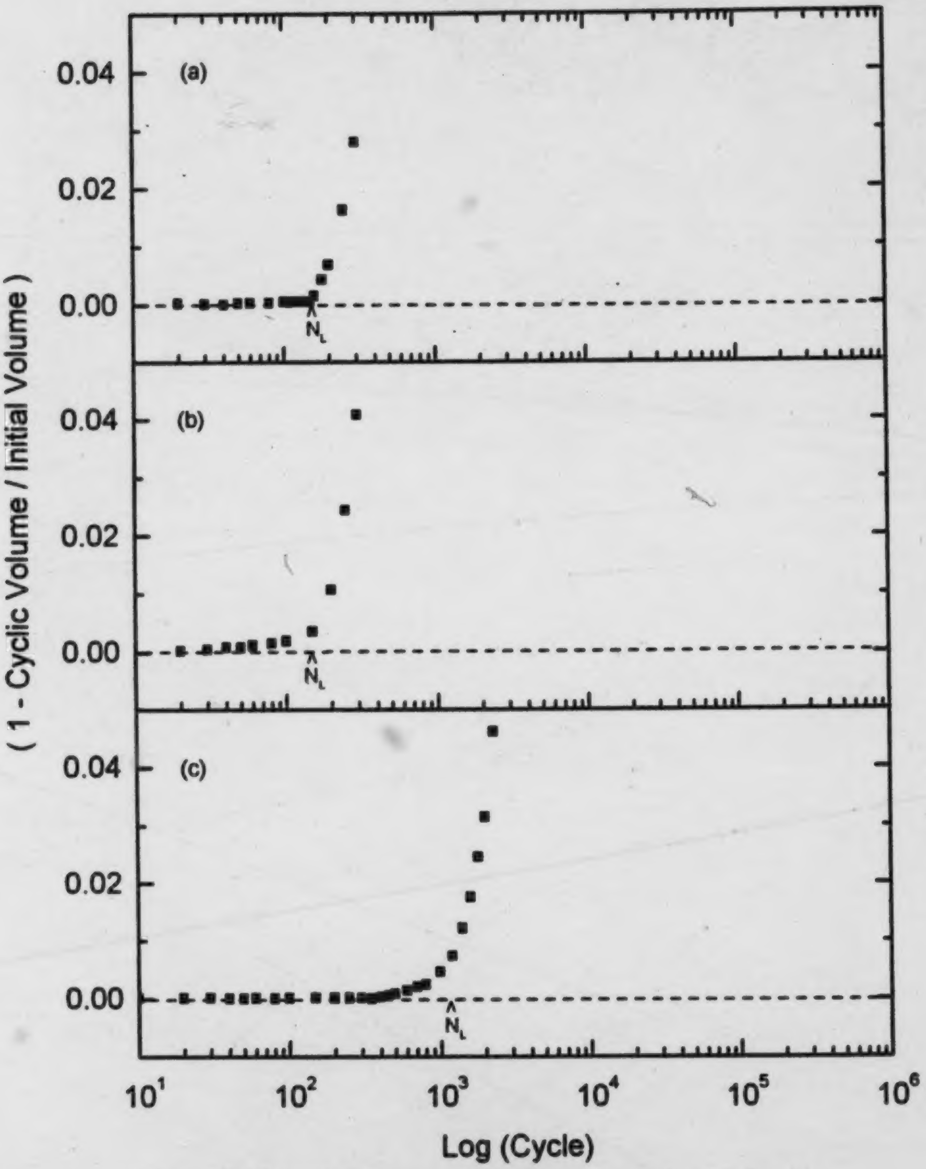

Figure 6-10 (a-g): Leakage verses the number of cycles for the 2.5H:1A stress ratio in descending order from the highest equivalent stress to the lowest.

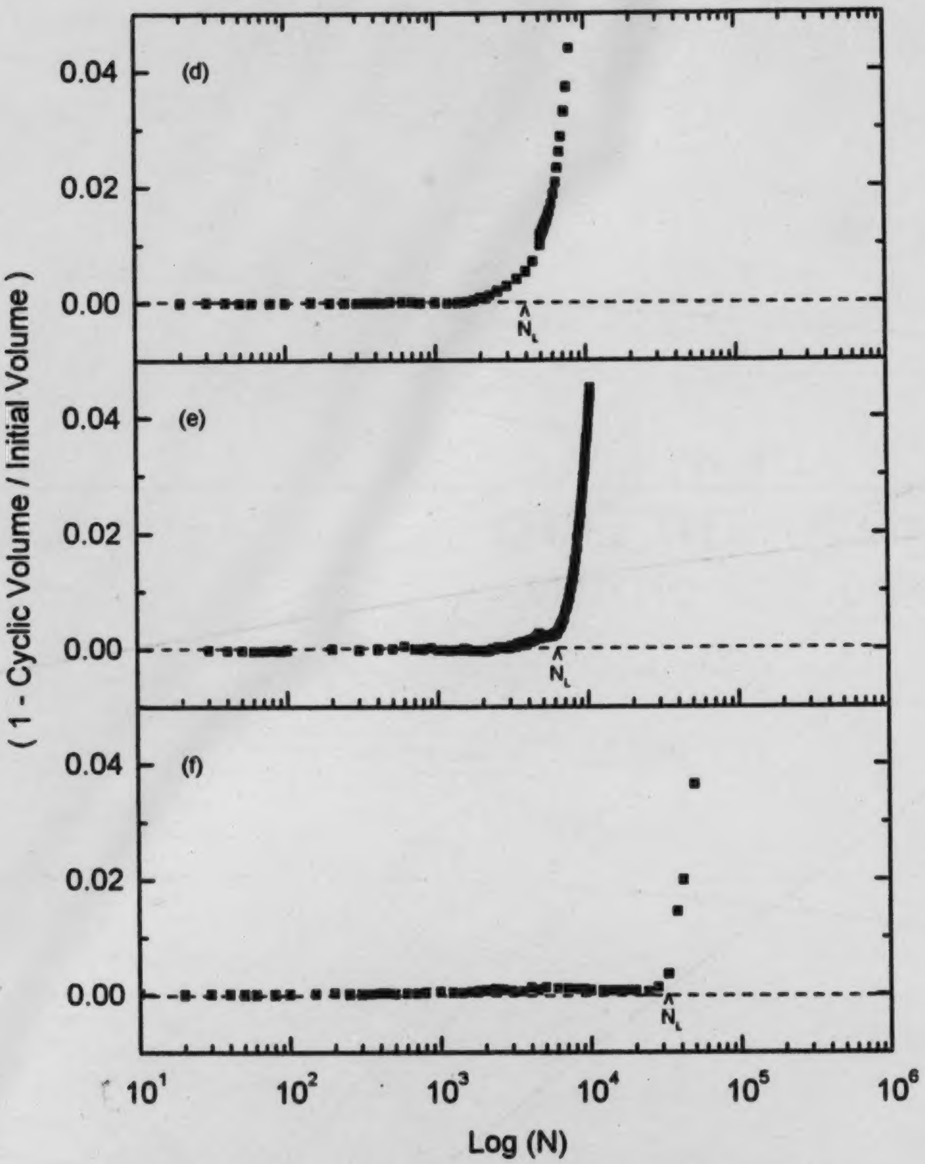

Figure 6-10 (a-g) (con't): Leakage verses the number of cycles for the 2.5H:1A stress ratio in descending order from the highest equivalent stress to the lowest.

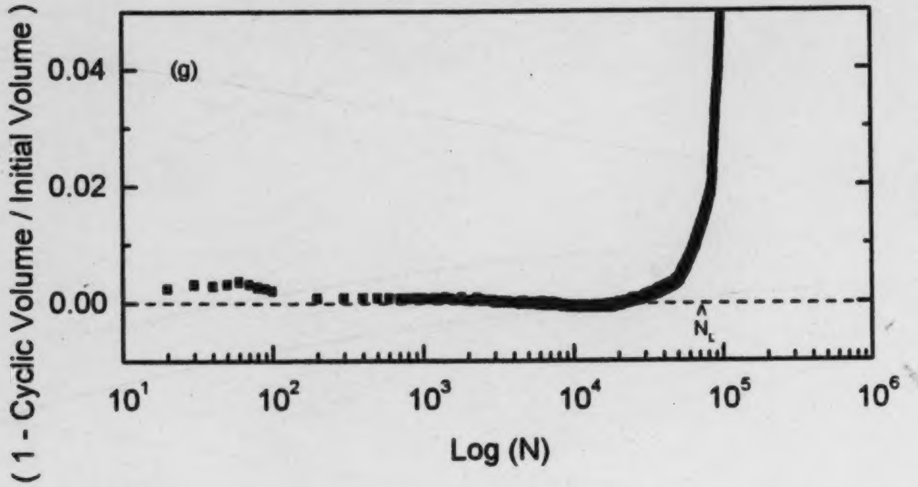

Figure 6-10 (a-g) (con't): Leakage verses the number of cycles for the 2.5H:1A stress ratio in descending order from the highest equivalent stress to the lowest.

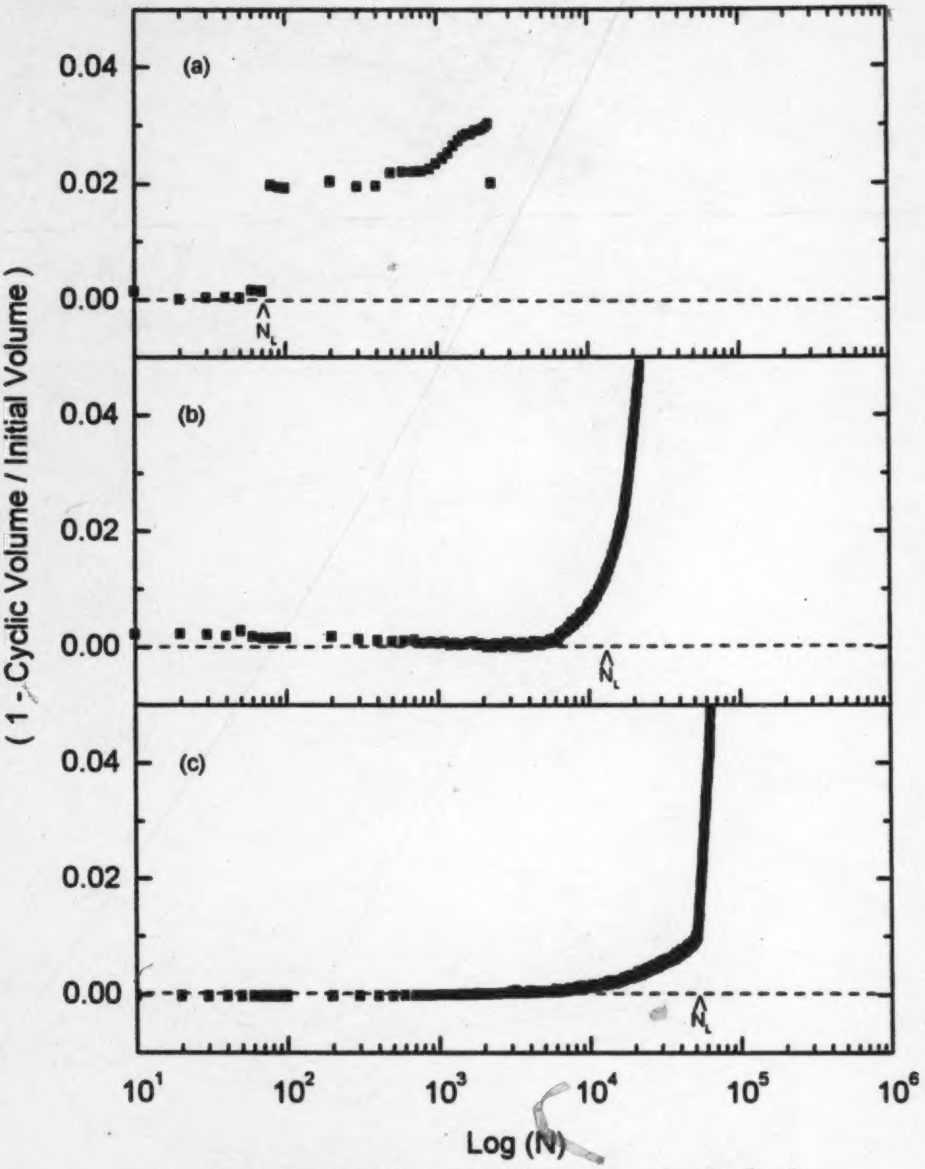

Figure 6-11 (a-e): Leakage verses the number of cycles for the 1H:0A stress ratio in descending order from the highest hoop stress to the lowest.

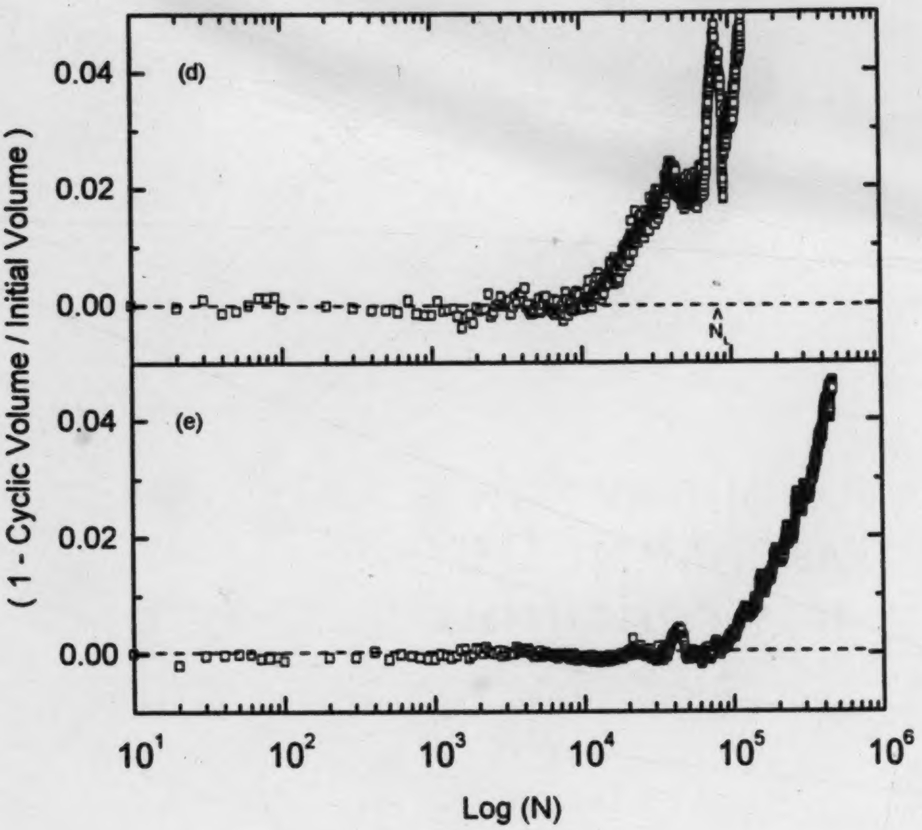

Figure 6-11 (a-e) (con't): Leakage verses the number of cycles for the 1H:0A stress ratio in descending order from the highest hoop stress to the lowest. Note intensifier leakage is suspected in Figure 6.11 (d-e)

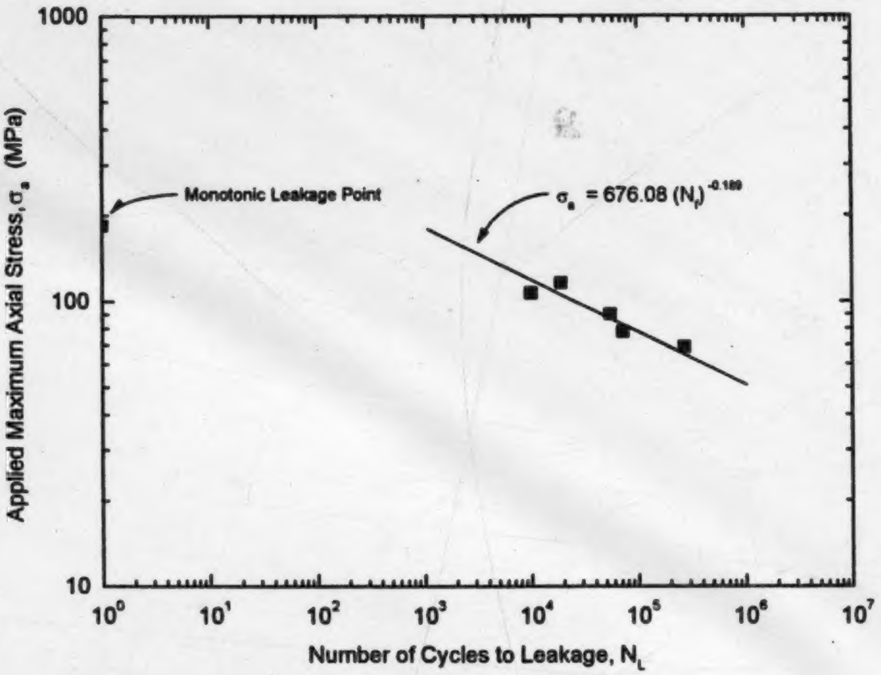

Figure 6-12: Applied maximum axial stress verses cycles to leakage in Log scale for the 0H:1A stress ratio

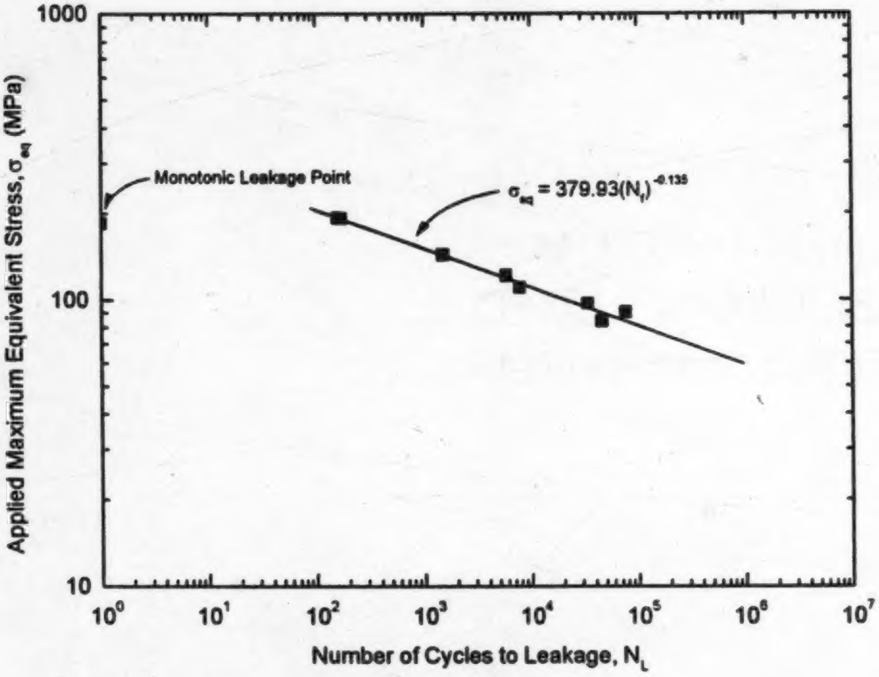

Figure 6-13: Applied maximum equivalent stress verses cycles to leakage in Log scale for the 2.5H:1A stress ratio

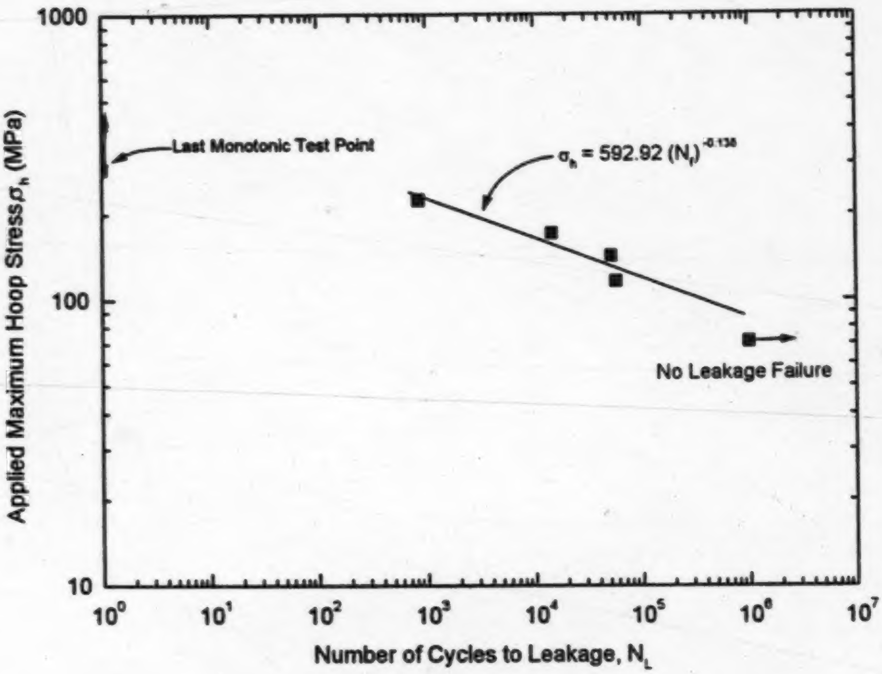

Figure 6-14: Applied maximum hoop stress verses cycles to leakage in Log scale for the 1H:0A stress ratio.

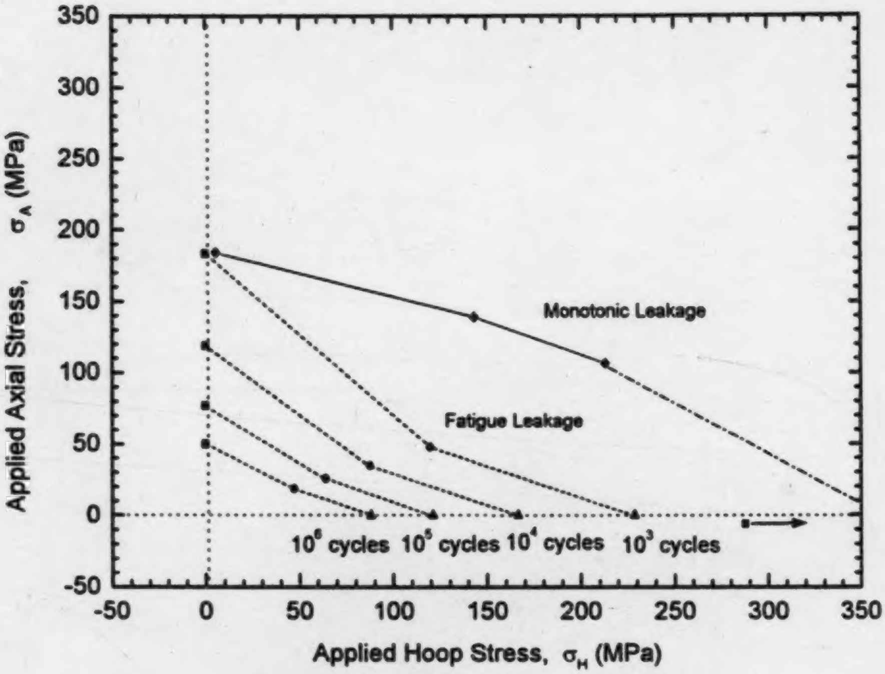

Figure 6-15: The biaxial fatigue leakage envelope illustrating the characteristic cyclic behavior of this multidirectional lay-up composite pipe for very short-term (10^3) to long-term (10^6) leakage. The monotonic leakage envelop is also included for comparison.

Figure 6-16: Photograph of the observed macro damage for the 0H:1A stress ratio with the corresponding maximum cyclic axial stress of 91.38 MPa (13250 psi). Note the uniform matrix cracking.

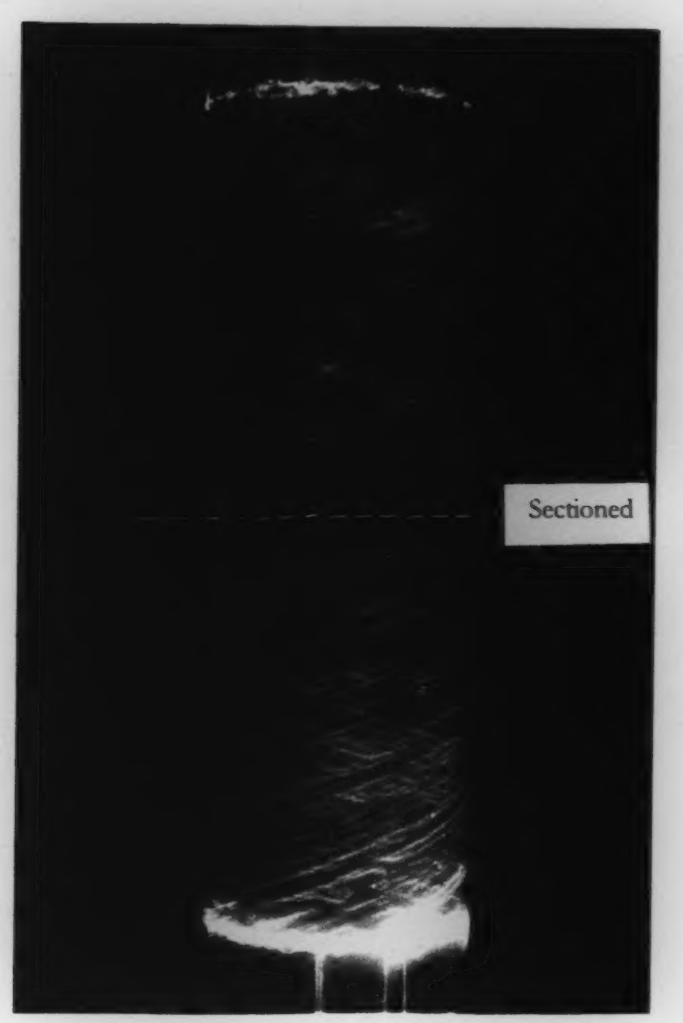

Figure 6-17: Photograph of the observed macro damage for the 0H:1A stress ratio with the corresponding maximum cyclic axial stress of 79.04 MPa (11460 psi). Note the uniform matrix cracking.

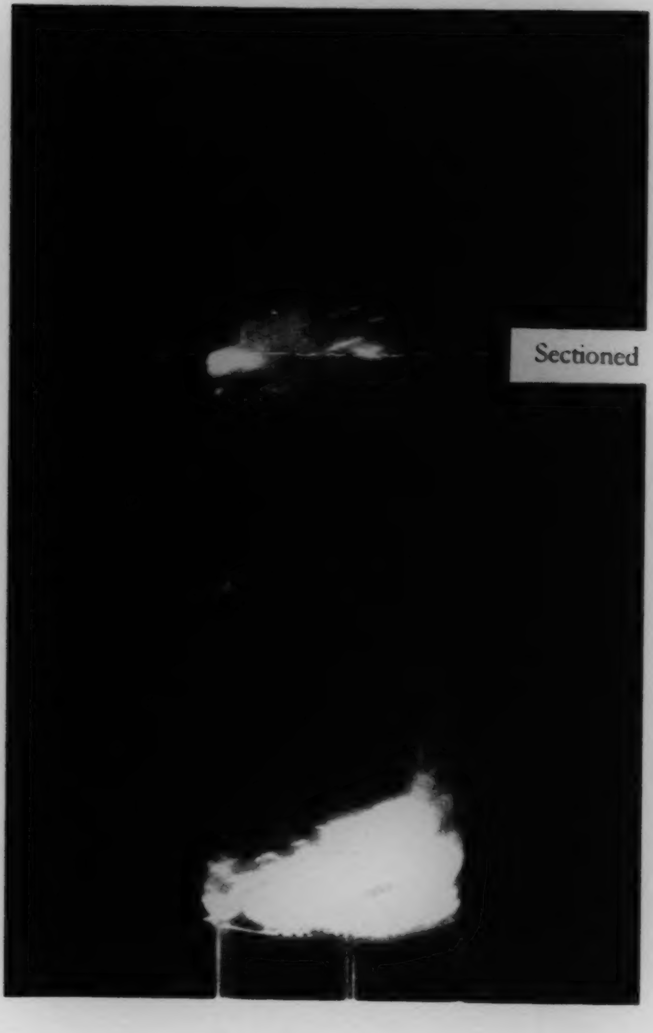

Figure 6-18: Photograph of the observed macro damage for the 2.5H:1A stress ratio with the corresponding maximum cyclic hoop stress of 127.42 MPa (18480 psi). Note the combined matrix cracking and delamination of the pipe.

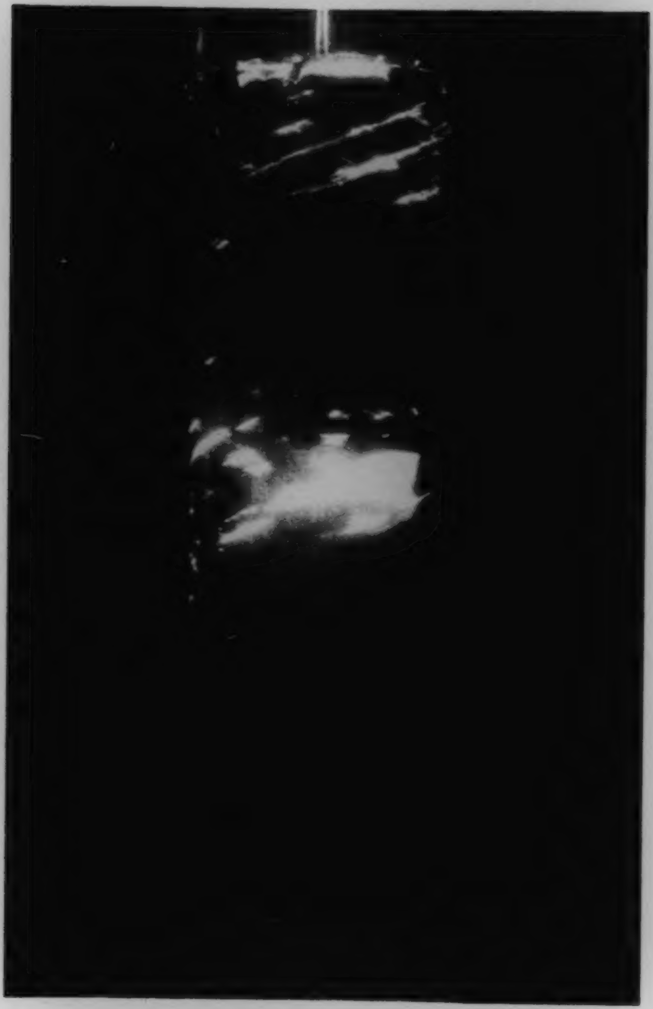

Figure 6-19: Photograph of the observed macro damage for the 2.5H:1A stress ratio with the corresponding maximum cyclic hoop stress of 103.27 MPa (14980 psi). Note the matrix cracking parallel to the ± 66^0 fibers.

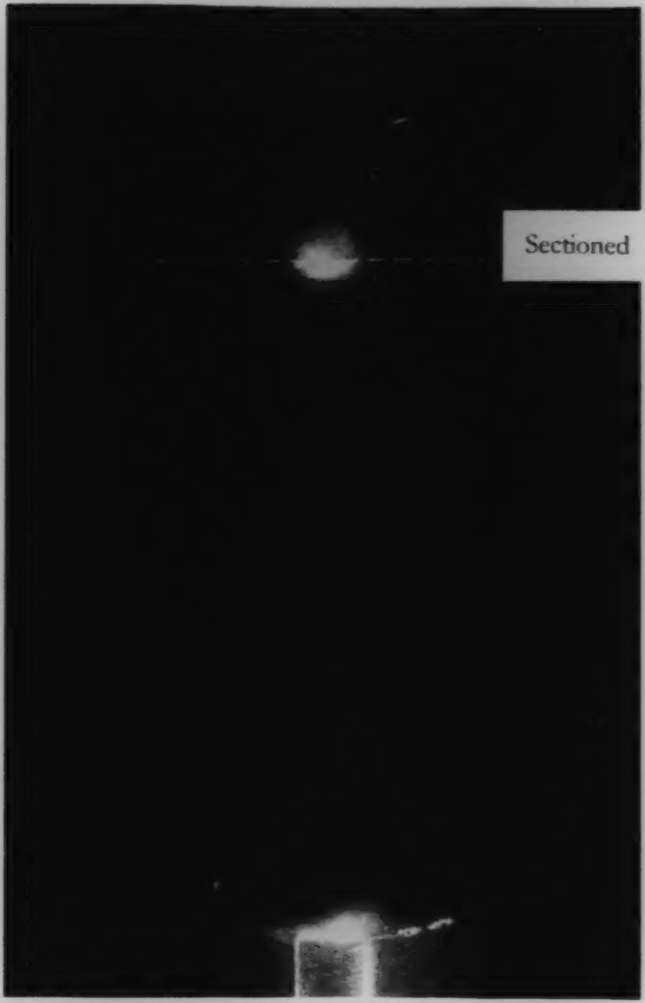

Figure 6-20: Photograph of the observed macro damage for the 2.5H:1A stress ratio with the corresponding maximum cyclic hoop stress of 103.27 MPa (14980 psi). This is a different specimen then the one presented in figure 6.19. Note the change in the failure mode to delamination leading to pin hole bursting.

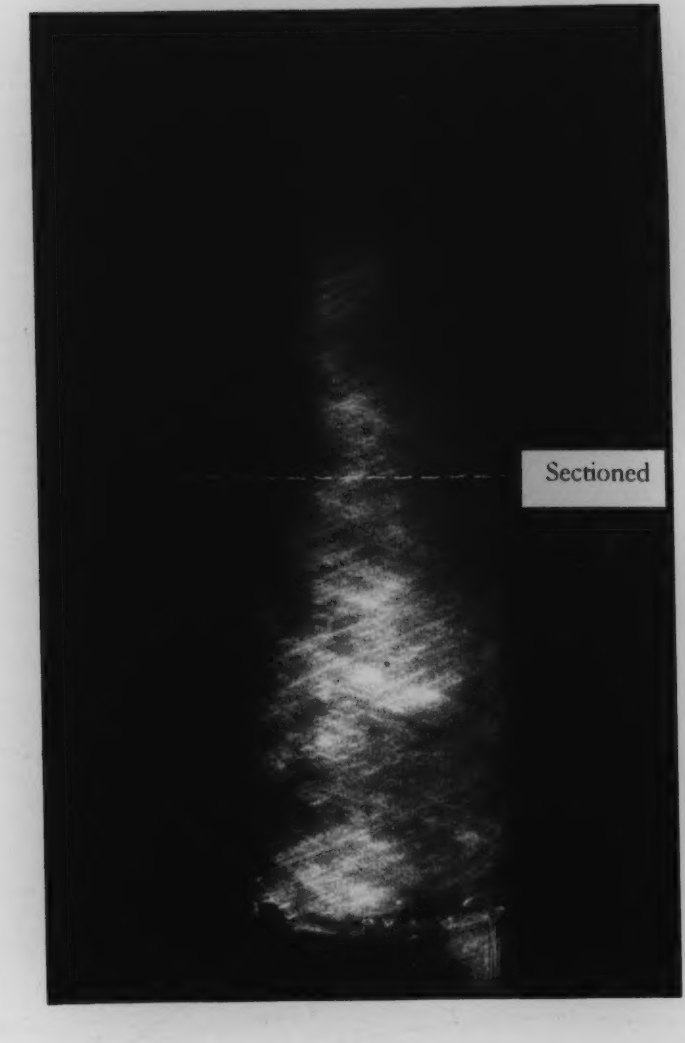

Figure 6-21: Photograph of the observed macro damage for the 1H:0A stress ratio with the corresponding maximum cyclic hoop stress of 219.11 MPa (31780 psi). Note uniform type of matrix cracking parallel to the ± 66° fibers, similar to the failure mode initially seen in the 0H:1A stress ratio.

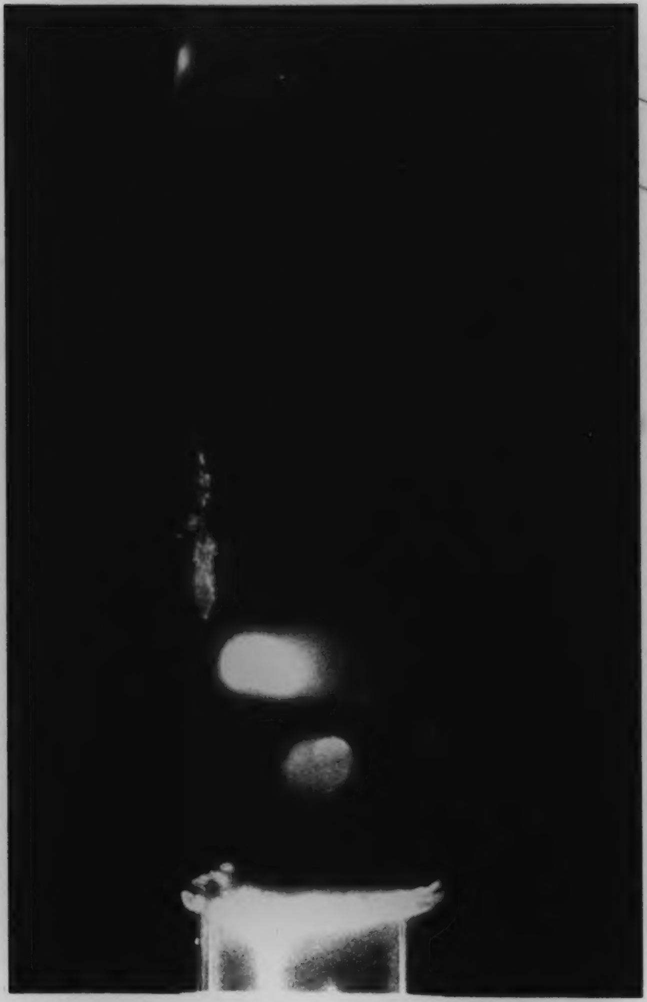

Figure 6-22: Photograph of the observed macro damage for the 1H:0A stress ratio with the corresponding maximum cyclic hoop stress of 166.7 MPa (24180 psi). Note delamination giving way to pin hole bursting.

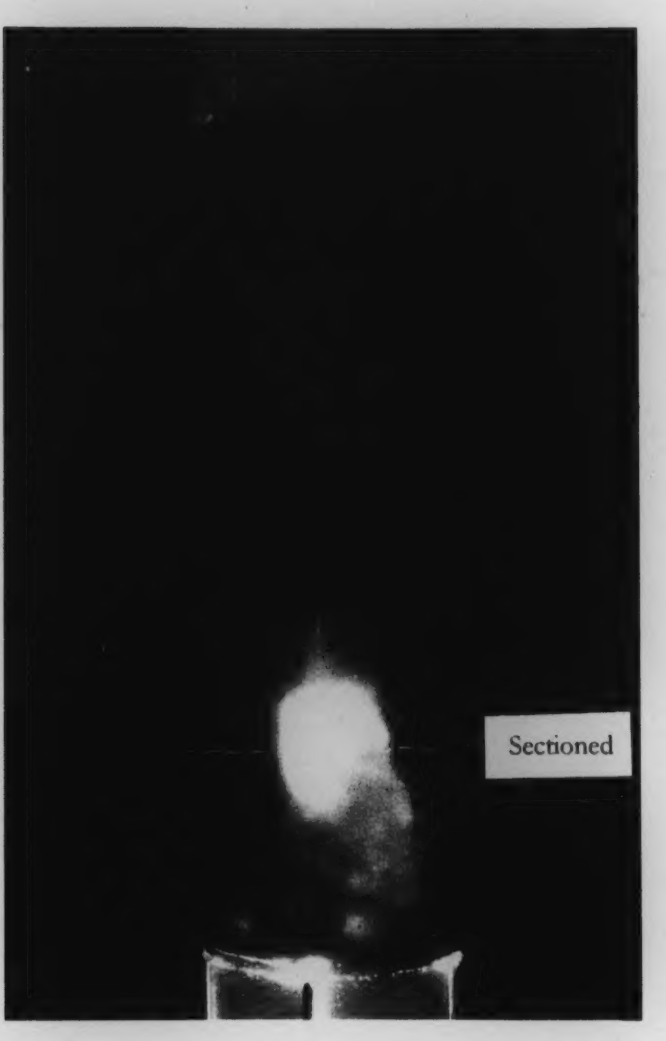

Figure 6-23: Photograph of the observed macro damage for the 1H:0A stress ratio with the corresponding maximum cyclic hoop stress of 142.28 MPa (20640 psi). Note delamination and matrix cracking can be seen giving way to pin hole bursting. As well a small amount of matrix cracking can also be seen in the 0^0fiber layer.

Figure 6-24: Photograph of the observed macro damage for the 1H:0A stress ratio with the corresponding maximum cyclic hoop stress of 118.92 MPa (17250 psi). Note only a spot of delamination giving way to pin hole bursting.

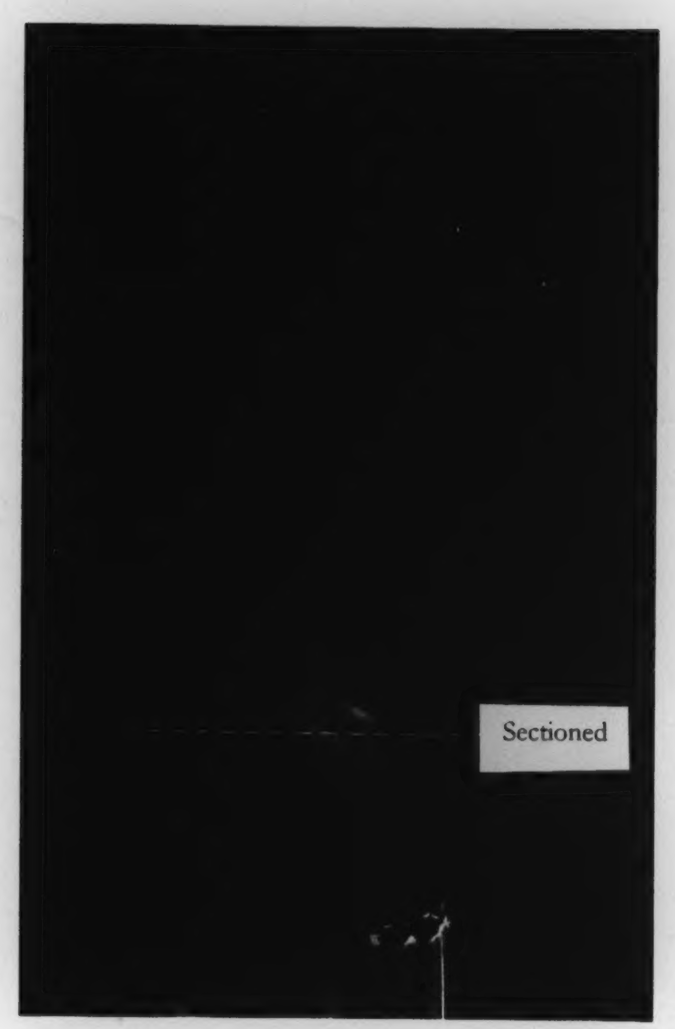

Figure 6-25: Photograph of the observed macro damage for the 1H:0A stress ratio with the corresponding maximum cyclic hoop stress of 118.92 MPa (17250 psi). This is the same specimen presented in figure 6.24, with a different orientation. Note the matrix cracking in, both the 0^0 and the $\pm 66^0$ fiber layer as well as delamination occurring in the 0^0fiber layer.

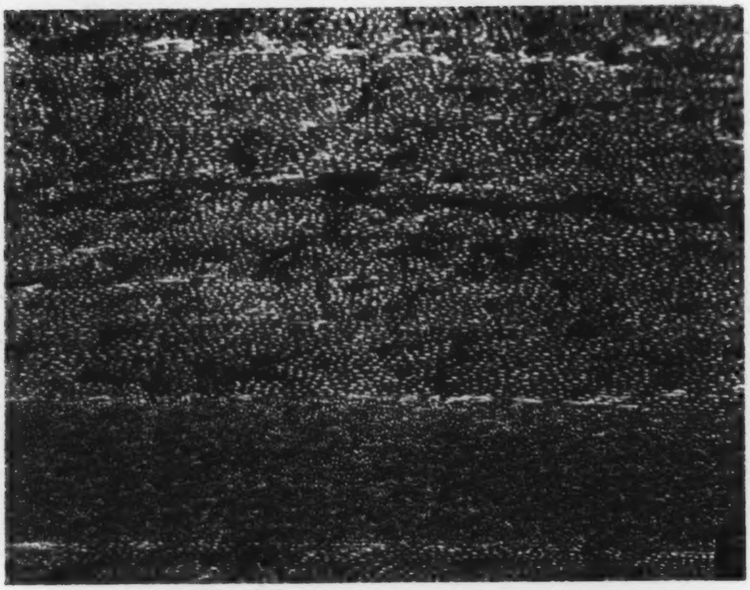

Figure 6-26: A micrograph taken of the observed uniform matrix cracking for the 0H:1A stress ratio magnified 40x. Observe the cracks in the ±66^0 plies.

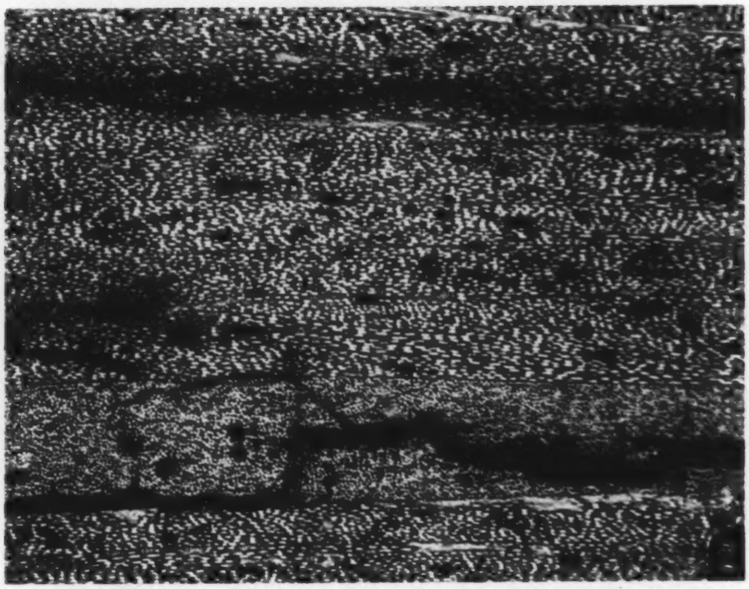

Figure 6-27: A micrograph taken of the observed matrix cracking and delamination section seen in Figure 6.18 for the 2.5H:1A stress ratio magnified 40x. Observe the cracks in the 0^0 ply.

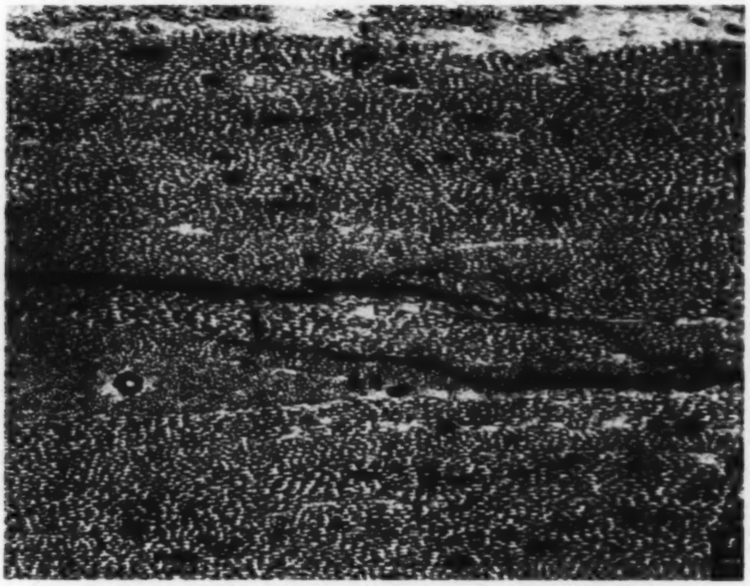

Figure 6-28: A micrograph taken of the observed matrix cracking and delamination section seen in Figure 6.20 for the 2.5H:1A stress ratio magnified 40x. Observe the cracks in the 0^0 ply extending into the $\pm 66^0$ plies.

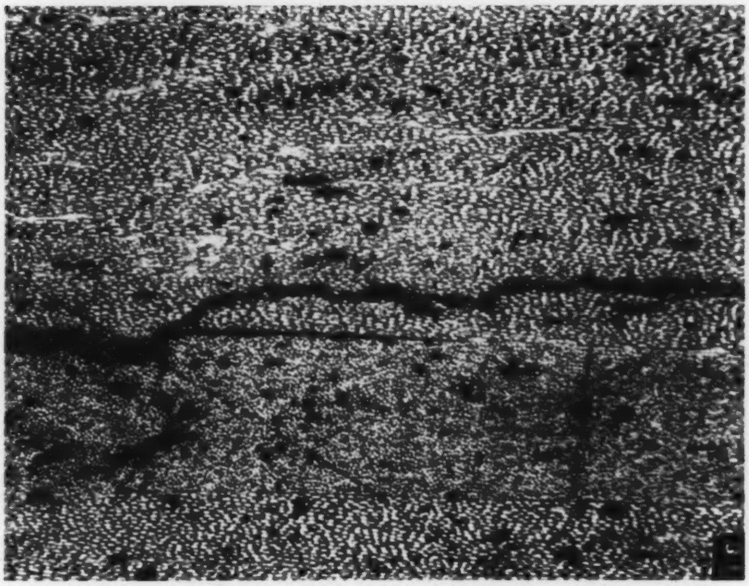

Figure 6-29: A micrograph taken of the observed matrix cracking and delamination section seen in Figure 6.20 for the 2.5H:1A stress ratio magnified 40x. Observe the cracks in the 0^0 ply extending into the $\pm 66^0$ plies.

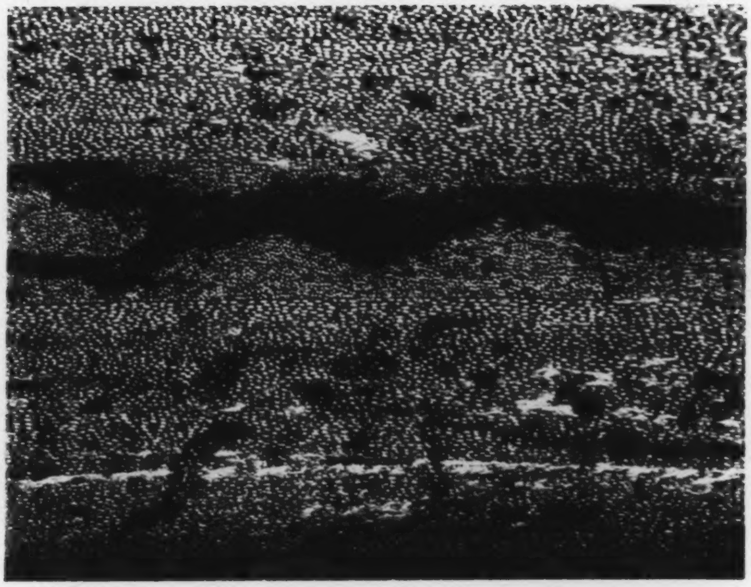

Figure 6-30: A micrograph taken of the observed uniform matrix cracking section seen in Figure 6.21 for the 1H:0A stress ratio magnified 40x. Observe the extensive cracking in both the 0^0 ply and the $\pm 66^0$ plies.

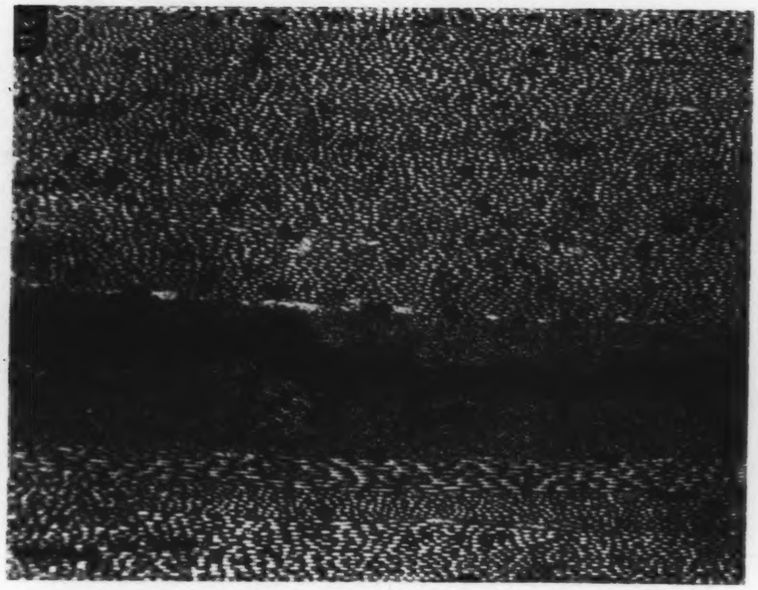

Figure 6-31: A micrograph taken of the observed matrix cracking and delamination section seen in Figure 6.23 for the 1H:0A stress ratio magnified 40x. Observe the extensive cracking in both the 0° ply and the ± 66° plies.

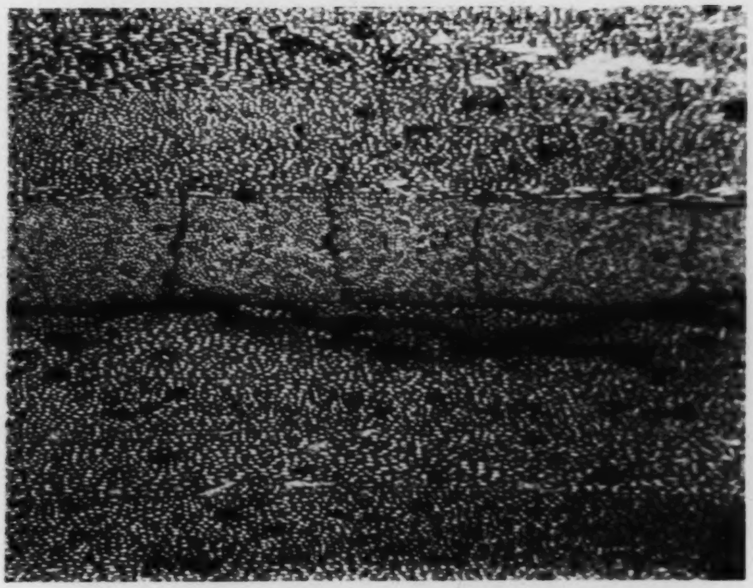

Figure 6-32: A micrograph taken of the observed matrix cracking and delamination section seen in Figure 6.25 for the 1H:0A stress ratio magnified 40x. Observe the extensive cracking in both the 0^{0} ply and the $\pm 66^{0}$ plies.

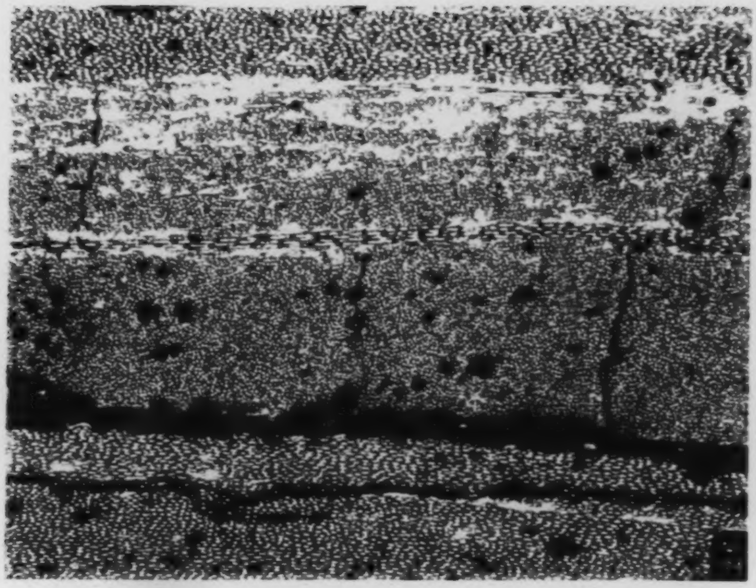

Figure 6-33: A micrograph taken of the observed cracking in a large resin rich area in the 0^{0} ply, magnified 40x, note how the inter-ply and interface cracking seams to be confined to this one area.

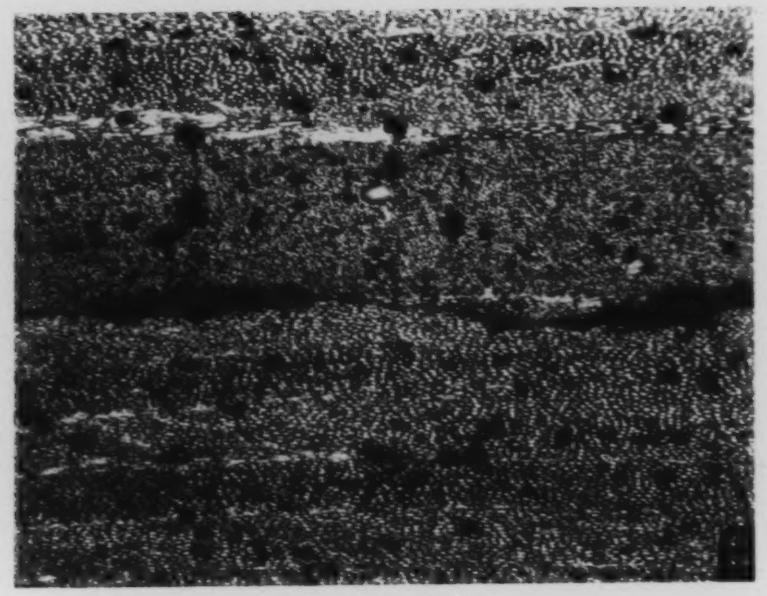

Figure 6-34: A micrograph, magnified 40x, taken of the observed cracking through two large voids in the 0^0 ply, note the over sized voids compared to the rest of the void population.

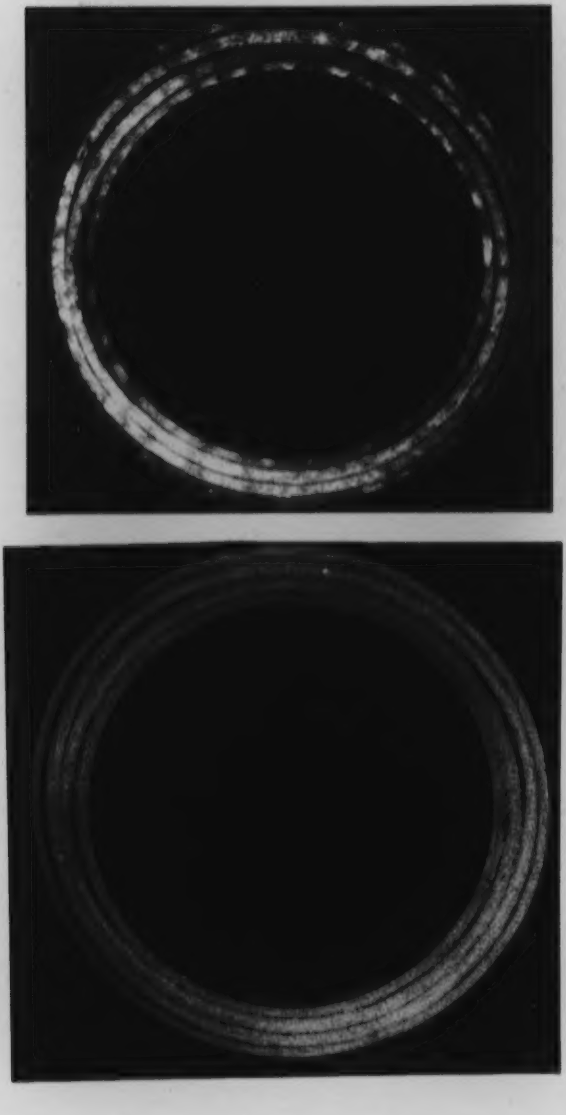

Figure 6-35: A photograph of the observed matrix cracking for the 0H:1A stress ratio, corresponding to Figure 6-17. The top photograph is taken under ultra violate light to observe cracking, the bottom is to compare damaged zones with imperfections.

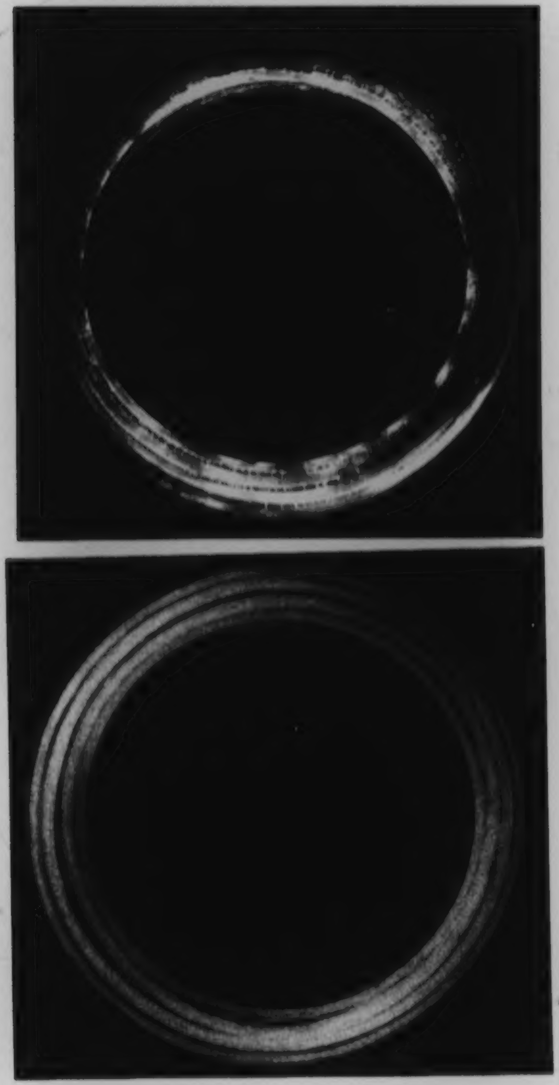

Figure 6-36: A photograph of the observed matrix cracking for the 2.5H:1A stress ratio, corresponding to Figure 6-18. The top photograph is taken under ultra violate light to observe cracking, the bottom is to compare damaged zones with imperfections.

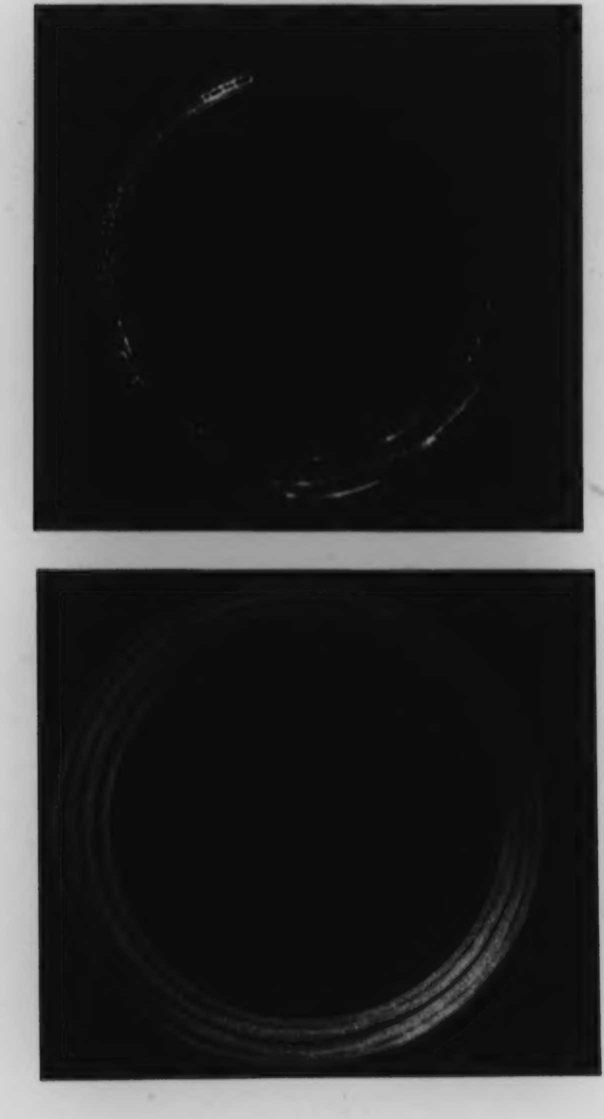

Figure 6-37: A photograph of the observed matrix cracking for the 1H:0A stress ratio, corresponding to Figure 6-20. The top photograph taken under ultra violate light to observe cracking, the bottom is to compare damaged zones with imperfections.

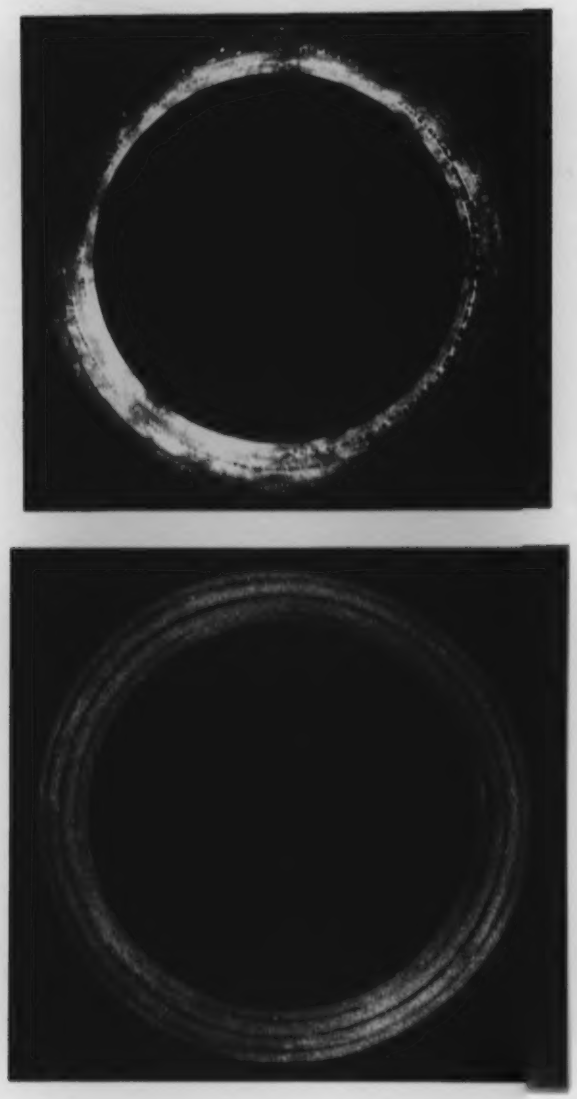

Figure 6-38: A photograph of the observed matrix cracking for the 1H:0A stress ratio, corresponding to Figure 6-21. The top photograph is taken under ultra violate light to observe cracking, the bottom is to compare damaged zones with imperfections.

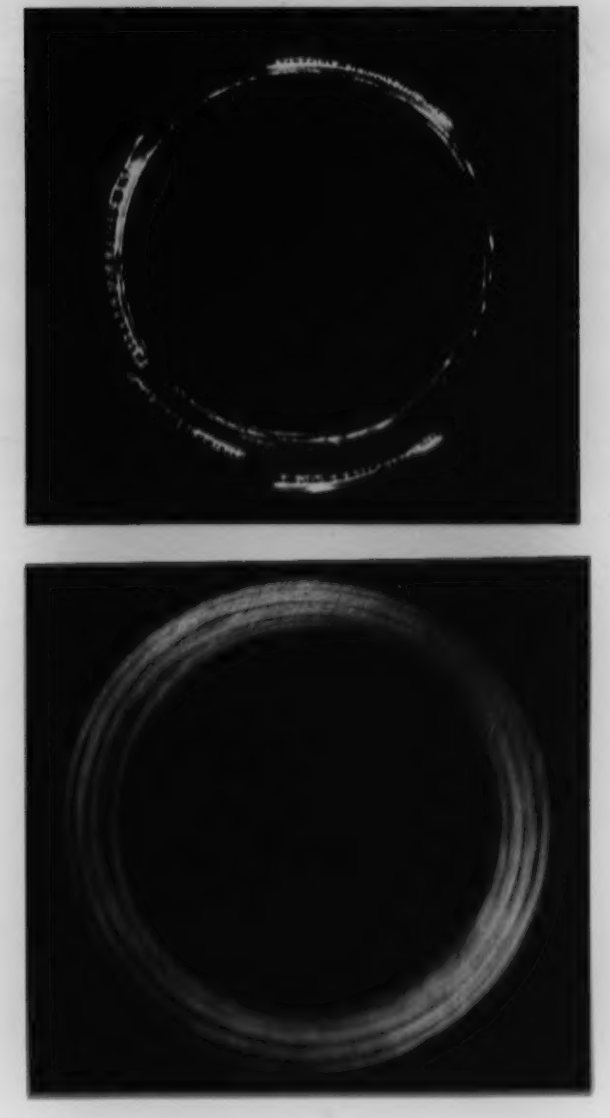

Figure 6-39: *A photograph of the observed matrix cracking for the 1H:1A stress ratio, corresponding to Figure 6-23. The top photograph is taken under ultra violate light to observe cracking, the bottom is to compare damaged zones with imperfections.*

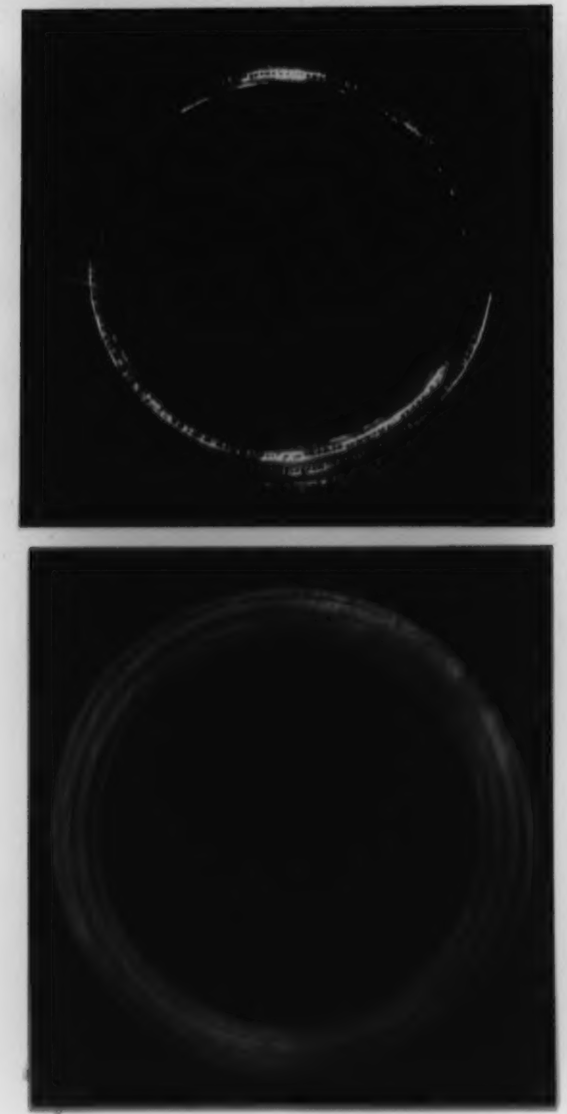

Figure 6-40: *A photograph of the observed matrix cracking for the III:1A stress ratio, corresponding to Figure 6-25. The top photograph is taken under ultra violate light to observe cracking, the bottom is to compare damaged zones with imperfections.*

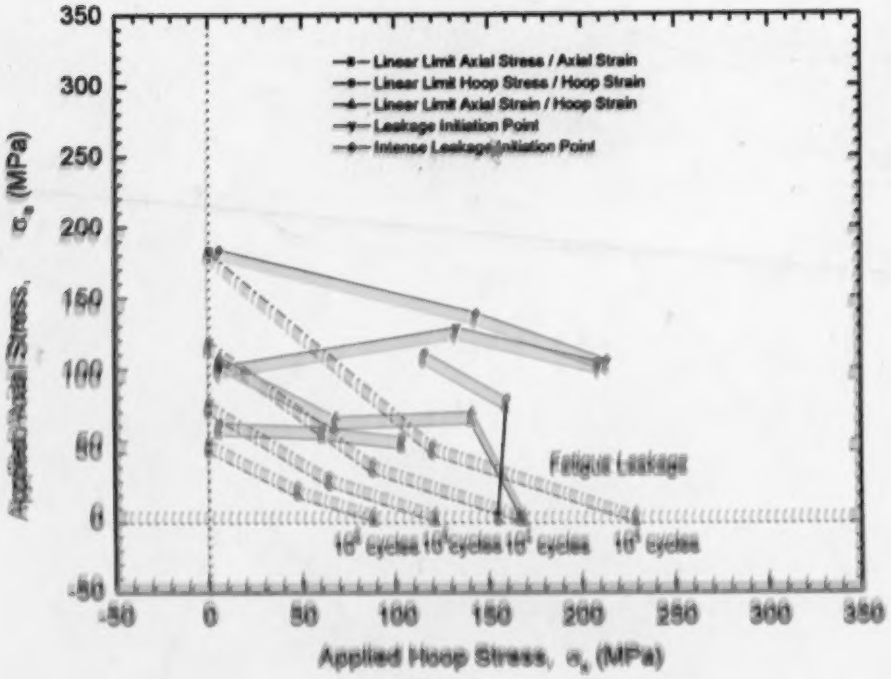

Figure 6-41: *The key monotonic data points superimposed on the biaxial fatigue life envelope.*

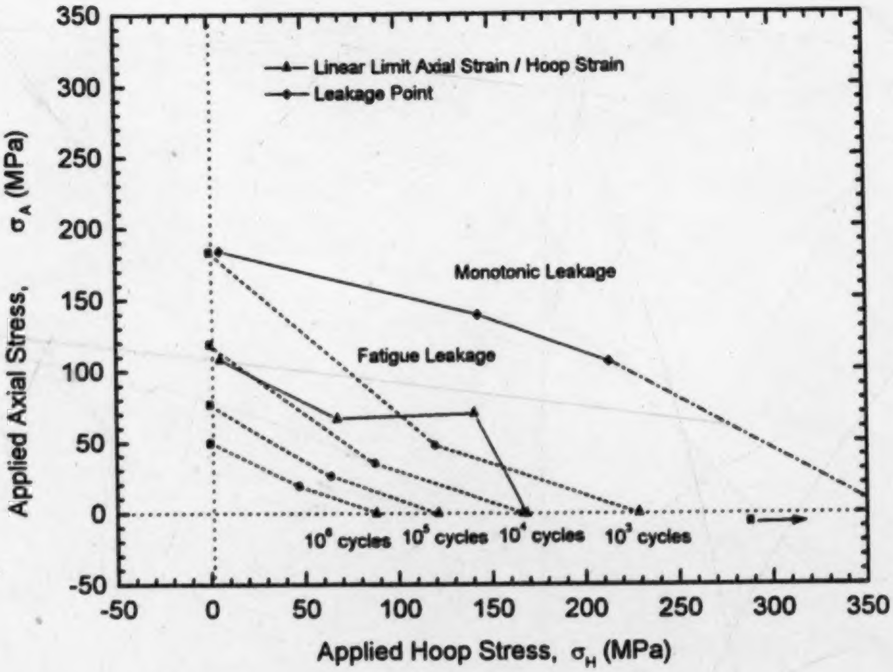

Figure 6-42: The linear limit strain-strain and the leakage failure points found from monotonic testing are superimposed on to biaxial fatigue life envelope. Note the relative position of the linear limit for strain-strain and the shot term fatigue leakage life (10^4 cycles).

CHAPTER 7

CONCLUSIONS

7.1 INTRODUCTION

One advantage of composite pipe is that it allows the fiber to be wound, in order to strengthen the most critical loading ratio. The development of the multidirectional lay-up will then allow for a strengthening of more than one critical loading ratio. This then gives an advantage to a composite pipe, when it is subject to several combinations of the loading ratios. The objective is to develop a composite pipe to withstand a high internal pressure and axial loading due to bending. In such a case one solution is to provide a dominant number of layers of glass fiber in the hoop direction, to resist the high internal pressure. In addition layers in the axial direction may be added to account for the axial loading.

The objective of this research project was to investigate the monotonic as well as the long-term behavior of a multidirectional fiberglass pipe. With a dominant number of layers of glass fiber in the hoop direction and added layers in the axial direction, to account for the high internal pressure, axial loads and combinations thereof. The importance of this effort was to obtain an understanding between the applied biaxial loading conditions and the leakage failures, in order to compile a leakage failure envelopes and a fatigue leakage life envelope.

The process of filament winding develops and introduces undesirable imperfection into the composite pipe. These imperfections are very difficult, if not impossible, to detect after the filament winding process by non-destructive means. A destructive investigation into the defects found in the pipe, revealed both macro-scale and micro-scale type of defects. The macro-scale type of defects included the misalignment of fibers from the intended angle of the lay-up, the existence of partial layers, the fiber waviness caused from the regions in the 0^0 plies rich in resin. The micro-scale type of defects included a small amount of impurities, voids (porosity) and waviness within the plies.

Detecting matrix cracking inside the composite specimen while *in-situ* is important for comparison. Cracks can be observed by sectioning after testing but this does not allow for *in-situ* determination of the damage-state. To determine the state of damage, in which micro-cracks coalesce to form larger cracks through the wall thickness, the leakage of fluid is monitored. Thus, leakage is correlated with other measured properties to determine a level of damage. To use leakage, as a measure of damage, the intensifier oil volume had to be corrected for the presence of air, the expansion of the specimen, and compression of the oil. Measuring leakage through the specimen, once the oil volume was corrected, was found to be sufficient in describing the state of damage. Leakage showed a dependency on the internal pressure of the specimen as well as time for the fluid to migrate into damaged areas.

Considerable information was obtained from the biaxial monotonic and biaxial fatigue testing of the commercially wound, multidirectional glass fiber reinforced epoxy pipe, the most important properties being strength, stiffness and leakage life. Monotonic testing showed that this lay-up was exceptionally strong in both the axial and hoop directions, especially in the hoop direction where no damage was recorded under pure pressure loading. The results from fatigue testing showed that the lay-up had a greater resistance to fatigue loading in both the axial and hoop directions. However, the fatigue leakage life was shorter under a pressure vessel type of loading (2.5H:1A load ratio).

7.2 MONOTONIC LOADING

The advantage of this multidirectional lay-up was the thickness of the wall section, which allowed for the reduction of the Poisson's ratio to be monitored during damage accumulation. Since a sufficient amount of stress was not obtainable under a certain stress ratios, it was difficult to compare the damage sustained based on the reduction in stiffness. The initiation of non-linearity of the Poisson's ratio as a damage indicator is independent of the stresses and the stress ratio.

The following are conclusions are drawn from the test results and micro-macro observations of failed pipes under monotonic biaxial testing:

- The mode of failure, the type of accumulated damage, the linearity limits on both the stress-strain and strain-strain curves and the leakage curves showed a dependence on the applied biaxial stress ratio.

- The elastic limit in the axial direction for 0H:1A, 1H:1A and the 2H:1A stress ratios, occurred approximately at the same axial stress valve. The linear elastic limit in the direction for the 2H:1A and the 1H:0A stress ratio also occurred at the same hoop stress valve.

- The elastic modulus and Poisson's ratio calculated from the classical laminate theory were very comparable to the experimentally determined valves, with the exception of the axial elastic modulus. These results indicate that even with the imperfection, discussed in Chapter 2, the classical laminate theory is able to predict the linear stiffness and Poisson's ratio.

- The initiation of non-linearity of the Poisson's ratio is a very useful indicator of the damage independent of the wall stresses and the stress ratio.

- A weakness was observed in the 1H:1A and 2H:1A stress ratios when the pipe was subjected to the high axial loads and high internal pressures. This produced a concave surface in the strain-strain linear limit curve. However the plot of the leakage initiation points did not show the same trends.

- The macro and micro damage seemed to indicate that the amount of axial tension in the specimen governs the uniformity of the matrix cracking. The increase in internal pressure increased the amount of delamination seen between the 1H:1A and the 2H:1A stress ratio.

7.3 FATIGUE LOADING

The small reduction in the stiffness of this multidirectional lay-up made it difficult to visualize the global trends found in the stress-strain hysteresis loop. To improve this the secant modulus was determined from linear regression calculated from the stress-strain hysteresis loop, along with the stress intercept.

The following conclusions are drawn from the test results and failure observations of biaxial fatigue tests:

- The type of accumulated damage, the decrease in secant modulus with cyclic loading and the leakage are shown to be dependent on the applied maximum biaxial stress and the applied biaxial stress ratio.

- In all cases there was a noticeable decrease in the secant modulus which stabilized after certain period. The level of reduction in the secant modulus and the rate of at which it stabilizes indicates that there is a connection between the stress ratio and the maximum applied stress. The largest initial reduction was seen in the axial secant modulus under pure axial loading and in the hoop secant modulus under pressure vessel type loading (2.5H:1A).

- Each stress ratio produced a characteristic leakage curve. The 0H:1A stress ratio had a slow leakage initiation with a slow increase in the leakage rate until rapid leakage. The 2.5H:1A stress ratio had a slow leakage initiation followed by a rapid increase in the leakage rate. However, the 1H:0A stress ratio had a change in the leakage curve, ranging from a burst type of leakage to slow leakage initiation with a slow increase in the leakage rate until rapid leakage, similar to the characteristic leakage curve for the 2.5H:1A stress ratio. Increasing the internal pressure allows the fluid to penetrate through the micro-cracks, causing the cracks to coalesce and a rapid increase in the leakage rate after a slow leakage initiation.

- The fatigue life curves for the 0H:1A and 2.5H:1A stress ratios were found to have comparable life. However the 0H:1A stress ratio had a slightly steeper slope. This seemed to be influenced by the short-term life, which indicates that the fatigue life for the 0H:1A and 2.5H:1A stress ratios is governed by the axial stress component. The 2.5H:1A and the 1H:0A stress ratio have comparable slopes, but the 1H:0A stress ratio has a longer life. This indicates that the leakage failure for the 1H:0A stress ratio is governed by the hoop component, and because the predominant fiber content is in the hoop direction, greater life is achieved.

- The compiled data from the fatigue life curves, based on the initiation point of intense leakage, clearly show a concave shape for the fatigue leakage envelope. This indicates that combining fiber in the axial direction to account for the large axial load and fiber in the hoop direction to account for the large transverse load leaves a significant weakness in the 2.5H:1A applied stress loading ratio. The monotonic leakage envelope neither predicted the shape nor the position of the fatigue leakage envelope.

- The characteristic type of damage observed in the multidirectional pipe for the 0H:1A stress ratio is uniform matrix cracking, which developed parallel to the $\pm 66^0$ fibers. The characteristic type of damage observed for the 2.5H:1A stress ratio was a combined matrix cracking and delamination, which was dependent on the applied load. The 1H:0A stress ratio did not seem to have a distinct characteristic type of damage. The observed damage, which ranged from a uniform matrix cracking to a delamination with pin hole bursting to a combination of both, appeared to be dependent on the maximum applied stress. The damage observed indicated that the amount of axial tension in the specimen governs the uniformity of the matrix cracking. The increase in internal pressure increased the amount of delamination.

- Imperfection obviously contributed to the initiation of internal cracking and other forms of damage. However the effect of some defects is difficult to determine from the micrographs and photographs of the cross-section. The imperfections include the misalignment of fibers from the intended angle of the lay-up and the existence of partial layers. The micrographs and photographs of the cross-section did give good indication of the proximity damage region to the fiber waviness caused by resin rich regions in the 0^0 plies, resin rich regions in the 0^0 plies, and voids (porosity) of a certain size.

- In general there appeared to be a greater concentration of cracking in the thinner section of the wall thickness, suggesting that there is a higher stress concentration through the wall thickness in the thinner wall section. However, when the resin rich regions in the 0^0 plies became abnormally thick, a shift in the cracking area is seen. This seems to indicate that the micro-scale type of defects seems to have a lesser effect on the cracking initiation than geometric irregularities.

- The amount of micro-scale type imperfections (i.e. voids and dust) does not appear to have as much effect on the crack initiation as the macro-scale imperfections (i.e. resin rich regions and fiber waviness). However, a void size larger than the relative average void size of the population seemed to influence cracking, but voids have been seen as crack arrestors in some cases, as well.

- Changes in the temperature appeared to have more influence on the fatigue testing than it was first thought. The purpose for monitoring the temperature was to obtain an over all indication of the surrounding temperature effects on the specimen during the fatigue testing. Most of the data show some sensitivity to the fluctuations in the temperature, which was caused by the hydraulic power unit, the overall building temperature and the fluid pressurizing the specimen.

- The key monotonic data points collected for the multidirectional lay-up under study have been superimposed on to the biaxial fatigue leakage life envelope, to see if the data collected through monotonic testing could be used to determine the biaxial fatigue leakage life envelope. In most cases the monotonic data are higher that the short term fatigue leakage life envelopes. However, some correlation between the short-term leakage life, 10^4 cycles, and the linear limit extracted from the strain and strain curves was observed except for a single data point. At this point it is difficult to ascertain whether this relationship is coincidental or not. The monotonic test data failed to predict the concave shape of the fatigue leakage life, which is very important in evaluating a multidirectional lay-up.

Bibliography

[1] Adams, D. O., & Hyer, M. W. (1994, August). Effect of layer waviness on the compression fatigue performance of thermoplastic composite laminates. Fatigue, 16, 385-390.

[2] Albright, F. J., & Annala, J. (1994, January). Practical aspects of dynamic verification of extensometers: Part I- the concepts. Journal of Testing and Evaluation, 22 (1), 53-56.

[3] Albright, F. J., & Annala, J. (1994, January). Practical aspects of dynamic verification of extensometers: Part II- actual examples. Journal of Testing and Evaluation, 22 (1), 56-62.

[4] Bai, J., Seeleuthner, P., & Bompard, P. (1997). Mechanical behavior of ± 55° filament-wound glass-fibre/epoxy-resin tubes: I. Microstructural analysis, mechanical behavior and damage mechanisms of composite tubes under pure tensile loading, pure internal pressure, and combined loading. Composite Science and Technology, 57, 141-153.

[5] Boyle, J. T., & Spence, J. (1981, June). A simple stress analysis for out-of-round pressurized pipe bends. International Journal Pressure Vessels Piping, 9 (4), 251-261.

[6] Bradford, S. A., (1992). Corrosion Control. New York: Van Nostrand Reinhold.

[7] Brown, T. L., & Hyer, M. W. (1992, October). Analysis of the influence of layer waviness in hydrostatically loaded thick cylinders. Proceeding of the American Society for Composites, (7th) Technical Conference. Pennsylvania.

[8] Carroll (1994). Lay-up and rate effects on fibreglass/epoxy laminates and tubulars. master's thesis, Department of Mechanical Engineering, University of Alberta, Edmonton, Alberta, Canada.

[9] Cantwell, W. J., & Morton, J. (1992). The significance of damage and defects and their detection in composite material: a review. Journal of Strain Analysis, 27 (1) 29-42.

[10] Chamis, C. C., & Smith, G. T. (1985, June). Resin selection criteria for "tough" composite structures. AIAA Journal, 23 (6), 902-911.

[11] Cohen. D., (1997). Influence of filament winding parameters on composite vessel quality and strength. Composites Parts A, 28A, 1035-1047.

[12] Craig. P. D., & Summerscales, J. (1988). Poisson's ratio in glass fiber reinforced plastic. Composite Structures, 9, 173-188.

[13] Daniel, I.M., & Ishai, O. (1994). Engineering mechanics of composite materials. New York, NY: Oxford University Press Inc..

[14] Dean, J.A., (Ed.). (1985). Lange's handbook of chemistry (13 th ed.,). New York: MaGraw Hill. 10-122-10-126.

[15] Dostal. C. A., (Ed.). (1987). Engineered materials handbook: Composites. (Vols. 1) Metals Park, Ohio: ASM International.

[16] Ellyin F., (1997). Fatigue damage crack growth and life prediction. New York: Chapman & Hall.

[17] Ellyin, F., Kujawski, D., & Culen, M. S. (1995, August). Fatigue behavior of pressurized filament wound fibreglass / epoxy tubes. Proceeding of ICCM-10, vol. I: Fatigue and Fracture, 641-648.

[18] Ellyin, F., Carrol, M., Kujawski, D., & Chiu, A. S. (1997). The behavior of multidirectional filament wound fibreglass/epoxy tubulars under biaxial loading. Composites Part A 28A, 781-790.

[19] Ellyin, F., Kujawski, D., & Culen, M.S. (1998). The fatigue behavior of filament-wound fiberglass/epoxy tubes under cyclic pressure. Journal of Reinforced Plastics and Composites, 17(3), 268-281.

[20] Ellyin, F., & Valaire, B. (1982, May). High-strain biaxial fatigue test facility. Proceedings of the 1982 Joint Conference on Experimental Mechanics, Oahu-Maui, Hawaii. Society for Experimental Stress Analysis. Brookfield Center, Connecticut, 136-143.

[21] Fiber Glass System, Inc. STAR® (1997). Product Information. [Catalog]. San Antonio, Texas: Author.

[22] Frost, S.R., (1995, August). Predicting the long-term fatigue behavior of filament wound glass-fibre/epoxy matrix pipes. Proceeding of ICCM-10, vol. I: Fatigue and Fracture, 649-656.

[23] Frost, S.R., The fatigue performance of glass fibre/epoxy matrix filament wound pipes, 684-691.

[24] Gent, A. N., & Meinecke, E. A. (1970, January). Compression, bending and shear of bonded rubber blocks. Polymer Engineering and Science, 10 (1), 48-53.

[25] Groves, S., Sanchez, R., Lyon, R., & Magness, F. (1992). Evaluation of cylindrical shear joints for composite materials. Journal of Composite Materials, 26 (8), 1134-1150.

[26] Gu, J., Lu, C., Mitchell, R., Thorp, K., & Crasto, A. (1997, March). Fungal Degradation of fiber-reinforced composite materials, Material Processing, 37-42.

[27] Haigh, B.P. (1936). An estimate of the bending stresses induced by pressure in a tube that is not initially quite circular. Second Report to the Welding Research Committee. Proceedings Internal Mechanical Engineering. 133, 96-98.

[28] Hamilton, J. D., and McCallum, J. (1961, November). Fluid-power circuit design. Conference Oil Hydraulic Power Transmission and Control, Institute Mechanical Engineers, London, 247-255.

[29] Hancox, N.L. (1981). The influence of voids on the hydrothermal response of carbon fiber reinforced plastic. Journal of Material Science. 16, 627-632.

[30] Harris, C. E., Allen, D. H., & Nottorf, E.W. (1989, Summer). Predictions of poisson's ratio in cross-ply laminates containing matrix cracks and delaminations. Journal of Composite Technology & Research. 11(2) 53-58.

[31] Hart-Smith L. J., & Peterson. D. A. (1990). A rational development of lamina-to-laminate analsys methods for fibrous composites. Composite Material Testing and Design (vol. 9) ASTM STP 1059, Garbo, S.P. (Ed.,). American Society for Testing and Material, Philadelphia, 121-164.

[32] Hart-Smith. L. J. (1992). A scientific approach to composite laminate strength prediction. Composite Material Testing and Design (vol. 10) ASTM STP 1120, Glenn C. G. (Ed.,). American Society for Testing and Material, Philadelphia, 142-169.

[33] Hart-Smith, L. J. (1996). A re-examination of the analysis of in-plane matrix failure in fibrous composite laminates. Composites Science and Technology, 56, 107-121.

[34] Hayward, A .T. J. (1961, November). Aeration in hydraulic system: Its assessment and control. Conference Oil Hydraulic Power Transmission and Control, Institute Mechanical Engineers, London, 216-224.

[35] Herakovich, C. T. (1984, September). Composite laminates with negative through-the-thickness poision's ratio. Journal of Composite Materials, 18, 447-455.

[36] Hewson, W. D. (personal communication, June 19, 1997) Imperial Oil Products and Chemicals Division.

[37] Houghton, C. J. (1997, October) Composites use on platform topsides: a recent case history and future prospects. Second International Conference on Composite Material for Offshore Operations. CMOO-2, University of Houston, Houston, TX

[38] Hoover, J. W., Kujawski, D., & Ellyin, F. (1997). Transverse cracking of symmetric and unsymmetric glass-fibre/epoxy-resin laminates. Composites Science and Technology, 57, 1513-1526.

[39] Hull, D., & Spencer, B. (1978, October). Effect of winding angle on the failure of filament wound pipe. Composites, 263-271.

[40] Hull, D., & Jones, M. L. C. (1979). Microscopy of failure mechanisms in filament-wound pipe. Journal of Materials Science, 14, 165-174.

[41] Hwang, W. & Han, K. S. (1986, March). Fatigue of composite-fatigue modulus concept and life prediction. Journal of Composite Materials, 20, 154-165.

[42] Hwang, W & Han, K. S. (1989). Fatigue of composite materials-damage model and life prediction. Composite material: Fatigue and Fracture, Second Volume, ASTM STP 1012, Paul A. Lagace (Vol. ed.), American Society for Testing and Material, Philadelphia, 87-102.

[43] Industrial Formulators of Canada LTD (1997) Product Information. [Catalog]. Burnaby, British Columbia: Author.

[44] International Organization for Standardization (1984, November), International Standard ISO/DIS 7500/1, Metallic materials – verification of static uniaxial testing machines – Part 1: tensile testing machines, 2.

[45] Jansen, J. (personal communication, January 13, 1998) Vice President of Operations, McClean Anderson, Division of Isamu, a manufacturer of fiber wounding machines. Schofield, Wisconsin.

[46] Joseph, E., & Perreux, D. (1994). The effect of frequency on the fatigue performance of filament-wound pipes under biaxial loading: experimental results and damage model. Composites Science and Technology, [illegible], [illegible].

[47] Keithley Metrabyte. (1996-1997). Data acquisition catalog and reference guide, Vol. 28 [Catalog]. Taunton, Massachusetts: Author.

[48] Karassik, I. J., Krutzsch, W. C., Fraser, W. H., & Messina, J.P. (1986). Pump handbook (2nd ed.). New York: McGraw-hill Book Company.

[49] Kitching, R., & Hose, D. R. (1992). The influence of the variation in wall thickness of glass fiber reinforced plastic pipe bends subjected to in-plane bending. Journal of Strain Analysis, 27, 113-121.

[49A] Knight, C. E. (1988). Residual stress and strength loss in filament-wound composites, Composite Materials: Testing and Design (Eighth Conference), ASTM STP 972, J. D. Whitcomb, Ed., American Society for Testing and Material, Philadelphia, 413-422.

[50] Kujawski, D., Chiu, A. S., & Ellyin, F. (July, 1996). An effective stress parameter for long-term fatigue strength of fiber-reinforced plastic pipes. Journal of Composite Technology & Research, 18(3), 215-220.

[51] Lee, S. M. (Ed.). (1989). International encyclopedia of composites. (Vols. 1-6). New York: VCH Publishers, Inc.

[52] Lea, R. H., & Schmit, K. (1995). Twenty-year history of successful applications of composite pipe in seawater service. National Institute of Standards Technology, 261-268.

[53] Lee, L. J., Yang, J. N., & Sheu, D. Y. (1993). Prediction of fatigue life for matrix-dominated composite laminates. Composites Science and Technology, 46, 21-28.

[54] Lehman, F. L. (1993, November). Automated data acquisition and load and strain measurement resolution. Journal of Testing and Evaluation, 21(6), 510-514

[55] Liao, K., George, E. R., & Reifsnider, K. L. (1997). Characterization of ceramic matrix composite tubes under uniaxial/biaxial monotonic and cyclic loading. Multiaxial Fatigue and Deformation Testing Techniques, ASTM STP 1280, S. Kalluri and P. J. Bonacuse, (Vol. Ed.). American Society for Testing and Materials, 224-246.

[56] Lockett, F. L. (1986, October). Effects of anisotropy and inhomogeneity on GRP pressure pipe. Composites, 209-216.

[57] Lucas Schaevitz. (1990). Linear and Angular displacement transducers. (Catalog). Pennsauken, New Jersey: Author.

[58] Lyon, R. E. (1989, June). Physical basis for a pressure-dependent yield criterion for polymers. Polymer Engineering and Science, 29(12), 765-772.

[59] Martini, L. J. (1984). Practical seal design. New York: Marcel Dekker, Inc.

[60] McCloy, D., & Martin, H.R. (1980). Control of fluid power: analysis and design. England: Ellis Horwood.

[61] Michener, R. A. (1980). Millwrights manual of instruction. Province of British Columbia, Ministry of Advanced Education and Job Training.

[62] Miller, D. M., (1987). Glass fibers. In Engineered Materials Handbook: Composite. (Vol.1 p.p. 45-48). Metals Park, OHIO: ASM International.

[63] Mok-Yeo, B. L. (1995, August). Sub-critical damage in glass-fibre/epoxy-resin laminates: use of laser diffraction and CLSM techniques. Proceeding of ICCM-10, vol. V: Fatigue and Fracture, 357-364.

[64] More House Roving (1967, November). Reference manual for proving ring S/N 495, York, Pennsylvania: Author.

[65] More House Roving Rings. Product Information. [Bulletin 260]. York, Pennsylvania: Author.

[66] MTS Systems Corporation. (1974, September). Reference manual for Model 831.32 resonant fatigue system, System Number 975.17-83, Minneapolis, Minn: Author.

[67] Nova Pipeline. (1990). Functional loads. Unpublished Manuscript from Nova Pipeline LTD.

[68] O'Brien, T. K., & Reifsnider, K. L. (1981) Fatigue damage evaluation through stiffness measurements in boron-epoxy laminates. Journal Composite Material, 15, 55-70

[69] Omega Engineering, Inc. (1995). OMEGA complete pressure, strain and force measurement handbook and encyclopedia. [Catalog]. Stamford, Connecticut: Author.

[70] Oswald, K.J. (1988, August). The effect of 25 years of oil field flowline service on epoxy fiberglass pipe. Material Processing, 81-85.

[71] Philippidis, T. P., & Theocaris, P. S. (1994). The transverse poisson's ratio in fiber reinforced laminae by means of a hybrid experimental approach. Journal of Composite Materials, 28(3) 252-261.

[72] Rajani, B. B. (1993, spring) Deformations of pipelines embedded in frozen soil. doctoral thesis, Department of Civil Engineering, University of Alberta, Edmonton, Alberta, Canada.

[73] Ramirez, G., & Engelhardt, M. D. (1997, fall). Experimental methods for large scale composite tubes. Second International Conference on Composite Material for Offshore Operations. CMOO-2, University of Houston, Houston, TX

[74] Reifsnider, K. L., Schulte, K. & Duke, J.C. (1983). Long-term fatigue behavior of composite materials. Long-Term Behavior of Composites, ASTM STP 813, T.K. O'Brien, (Vol. ed.). American Society for Testing and Material, Philadelphia, 136-159.

[75] Reinhart, T. J. (Chairman), (1987). Engineered Material Handbook: Composite (vol.1) ASM International, Metals Park, Ohio.

[76] Rinheart, K. (1995). Secondary stress in flexible composite pipe. master thesis, Department of Mechanical Engineering, University of Alberta, Edmonton, Alberta, Canada.

[77] Sauer, J. A., Mears, D. R., & Pae, K. D. (1969, October). Effects of Hydrostatic Pressure on the mechanical behavior of polyethylene and polypropylene. Journal of Applied Physics, 40 (11), 4229-4237

[78] Sauer, J. A. (1977, March). Deformation, yield and fracture of polymers at high pressure. Polymer Engineering and Science, 17(3), 150-163.

[79] Smith, L. H., Jr., Peeler, R. L., & Bernd, L. H. (1960). Hydraulic fluid bulk modulus: Its effect on system performance and techniques for physical measurement. (16th) National Conference on Industrial Hydraulics, 4, 179-197.

[80] Smith, P. A., & Wood, J. R. (1990). Posson's ratio as a damage parameter in the static tensile loading of simple crossply laminates. Composite Science and Technology, 38, 85-93.

[81] Soden, P. D., Leadbetter, D., Griggs, P. R. & Eckold, G. C. (1978, October). The strength of a filament wound composite under biaxial loading. Composites, 247-250.

[82] Soden, P. D. W. & Highton, J. (1982). End reinforcement and grips for anisotropic tubes. Journal of Strain Analysis, 17(1), 31-43.

[83] Soden, P. D., Highton, J., & Adeoye, A. B. (1985). Fracture stresses for 75 degree filament wound GRP tubes under biaxial loads. Journal of Strain Anlysis, 20 (3), 139-150.

[84] Soden, P. D., Kitching, R., & Tse, P.C. (1989, May). Experimental failure stresses for ± 55^0 filament wound glass fiber reinforced plastic tubes under biaxial loads. Composites, 20(2), 125-135.

[85] Soden, P. D., Lee, J., Kitching, R. & Tse, P.C. (1989, May). Strength of filament wound GRP tubes with axisymmetric steps. Composites, 20(3), 234-243.

[86] Soden, P. D., Kitching, R., Tse, P.C., Tsavalas, Y. & Hinton, M.J. (1993). Influence of winding angle on the strength and deformation of filament-wound composite tubes subjected to uniaxial and biaxial loads. Composites Science and Technology, 46, 363-378.

[87] Standard test method for cyclic pressure strength of reinforced thermosetting plastic pipe, ASTM Designation: D2105 reapproved 1987).

[88] Standard test method for cyclic pressure strength of reinforced thermosetting plastic pipe, ASTM Designation: D2143-69 (reapproved 1987).

[89] Standard Practice for obtaining hydrostatic or pressure design basis for "Fiberglass" (glass-Fiber-Reinforced thermosetting resin) pipe and fittings, ASTM Designation: D2992-91.

Bibliography

[90] Standard test methods for void content of reinforced plastic, ASTM Designation: D2734-70. (reapproved 1985).

[91] Starrett L.S. Company (1994, October). Precision Tool, Gauges and Sews. (3th ed. Vol. 2 No. 28) [Catalog]. Athol, Massachusetts: Author.

[92] Sullivan, T.L. & Chamis, C.C. (1973). Some important aspects in testing high-modulus fiber composite tubes in axial tension. Analysis of Test Methods for High Modulus Fibers and Composites, ASTM STP 521, American Society for Testing and Materials, 277-292

[93] Talreja, R. (1984, July). Transverse cracking and stiffness reduction in composite laminates. Journal of Composite Material, 19, 355-375.

[94] Tang, J. M., Lee, W. I., & Springer, G. S. (1987, May). Effects of pressure on resin flow, voids, and mechanical properties. Journal of Composite Material, 21, 421-439.

[95] Tarnopol'ski, Y. M., & Beil', A. I. (1983) Problems of the mechanics of composite winding. In Kelly, A. & Mileiko, S.T. (Series Ed.) Handbook of Composite: Fabrication of Composites (Vol. 4 pp. 45-108) New York: Elsevier Science Publishing Company, Inc.

[96] Timoshenko, S., & Woinowsky-Krieger, S. (1959). Theory of plates and shells (2nd ed.). New York: McGraw-Hill.

[97] Thompson, S.C., Kim, H. C. & Matthews, F. L. (1973, March). The effect of processing on the microstructure of CFRP. Composites, 86-87.

[98] Van Dreumel, W. H. M., & Kemp, J. L. M. (1977). Non hooken behaviour in the fiber direction of carbon-fiber composites and the influence of fiber waviness ion the tensile properties. Journal Composite Material, 11, 461-469.

[99] VanWylen, G. J., Sonntag, R. E., & Borgnakke, C. (1994). Fundamentals Classical Thermodynamics (4th ed.). New York: John Wiley & Sons, Inc.

[100] Vickers. (1992). Vickers Industrial Hydraulics Manual. Rochester Hills, Michigan: Author.

[101] Wang, S. S., Srinivasan. S., & Cole, B., (1997). Long-term leakage failure and life prediction of fiber composite laminate tubing under combined internal pressure and axial loading: Theory and Experiments. Second International Conference on Composite Material for Offshore Operations. CMOO-2, University of Houston, Houston, TX

[102] Wess, M., (personal commination, November 2, 1998) NOVA Research and Technology Corporation, Fluid Dynamic Group, Calgary, Alberta, Canada.

Bibliography

[103] Whiteman, V., (1994). Brief history of fibreglass pipelines. Unpublished Manuscript from Western Fiberglass Pipe Sales LTD.

[104] Wolodko, J. (1999, Spring) Biaxial fatigue and leakage characteristics of fiber reinforced composite tubes. doctoral thesis, Department of Mechanical Engineering, University of Alberta, Edmonton, Alberta, Canada.

[105] Xia, Z., & Ellyin, F. (1998). Time-dependent behavior and viscoelastic constitutive modeling of an epoxy polymer. Polymers & Polymer Composites, 6(2), 75-83.

APPENDIX A

NETTING ANALYSIS

A.0 NOMENCLATURE

N_ϕ	The membrane load in the axial (meridional) direction of the composite pipe
N_θ	The membrane load in the hoop (circumferential) direction of the composite pipe
N_f	The membrane load in the fiber
$t_{\alpha f}$	The thickness of the fiber in the fiber direction
t_{comp}	The thickness of the composite pipe
P	The internal pressure in the pipe
$\overline{R}$	The mean radius of the pipe
n	The number of layered pairs of fibers
L	Applied axial load
σ_h	Applied traction stress in the hoop direction
σ_a	Applied traction stress in the axial direction
$\sigma_{\alpha f}$	Design fiber stress in the direction of the fiber
M	Applied bending moment

A.1 INTRODUCTION

This section describes the preliminary design methodology using the netting theory, and composite degradation, first described by Tew (1995). Netting analysis is a preliminary design technique for designing with fiber-reinforced composite material for components such as pipes, pressure vessels, storage tanks and rocket motor casings. The theory of netting analysis is based on the assumptions that the wall structure acts as a membrane, does not carry any out-of-plane bending or shear loading, the fibers are unassisted by the resin and no interaction between the fiber layers exists [A1]. Netting analysis can be used as a quick calculation tool to determine design variables such as size, thickness, and to predict the hoop to axial stress ratio such that the fiber take the predominant amount of the load [A2].

The netting analysis enables the designer to select the appropriate winding angle based on the ratio of the applied axial stress to the hoop stress [A3]. However, a fully developed failure envelope is still needed to determine the strength under a variety of loading conditions.

A.2 NETTING ANALYSIS

The membrane forces N_θ and N_ϕ, which are applied to the composite pipe, in the hoop and axial (meridional) direction, respectively, are illustrated in Figure A-1. A free-body diagram of two filament-wound $[\pm\alpha]$ plies of fiber is shown in Figure A-2. Summing the membrane forces in the circumferential (θ) and longitudinal (ϕ) directions the following relationships are obtained:

$$2 \cdot N_f \cdot \sin^2(\alpha) - N_\theta = 0 \qquad \text{A-1}$$

and

$$2 \cdot N_f \cdot \cos^2(\alpha) - N_\phi = 0 \qquad \text{A-2}$$

where N_f is the membrane forces carrying capacity of a single ply, it is determined from the following relationship:

$$N_f = t_{\alpha f} \cdot \sigma_{\alpha f} \qquad \text{A-3}$$

where $t_{\alpha f}$ is the fiber thickness and $\sigma_{\alpha f}$ is the design fiber strength.

The total membrane forces N_θ and N_ϕ for a multi-layered filament-wound structure can be obtained by the superposition principal. Equation A-1 and Equation A-2 are expanded to obtain:

$$N_\theta = \sum_{j=1}^{i} 2 n_j N_{fj} \sin^2 \alpha_j \qquad \text{A-4}$$

and

$$N_\phi = \sum_{j=1}^{i} 2 n_j N_{fj} \cos^2 \alpha_j \qquad \text{A-5}$$

where n_j is the number of pairs of plies wound at the angle α_j. Note, that because n_j is set up for two plies in the $\pm\alpha_j$ directions, n_j must be set to 0.5 for a single ply.

The membrane forces can then be used to determine the applied internal pressure, axial load and bending moment, as follows:

$$N_\theta = P \cdot \overline{R} \qquad \text{A-6}$$

where P is the internal pressure of the pipe and $\overline{R}$ is the mean radius. Equation A-6 is independent of the end conditions.

Equation A-7 is setup for a closed end cylinder under pressure loading.

$$N_{\phi} = \frac{P \cdot \overline{R}}{2} \qquad \text{A-7}$$

Equation A-7 is expressed in terms of applied axial tension, L, as in Equation A-8.

$$N_{\phi} = \frac{L}{2 \cdot \pi \cdot \overline{R}} \qquad \text{A-8}$$

Equation A-8 can be expressed in determines the applied bending moment in the composite cylinder.

$$N_{\phi} = \frac{M}{\pi \cdot \overline{R}^2} \qquad \text{A-9}$$

The hoop to axial stress ratio for the maximum strength under the predominant load-carrying component for the winding angles is determined from Equation A-1 and Equation A-2 to obtain:

$$\frac{\sigma_h}{\sigma_a} = \frac{N_{\theta}}{N_{\phi}} = (\tan \alpha)^2 \qquad \text{A-10}$$

where σ_h is the hoop stress, σ_a is the axial stress, and $N_{\theta} = \sigma_h \cdot t_{comp}$, and $N_{\phi} = \sigma_a \cdot t_{comp}$ with t_{comp} being the thickness of the composite pipe.

A.3 FIBER STRENGTH

The composite fiber strength decreases from it virgin manufactured fiber strength due to cyclic loading, long-term static loading, thermal degradation, chemical degradation, ultraviolet degradation, fabrication processing, as well as structural geometry [A1]. The virgin manufactured fiber strength is adjusted with strength modifiers in order to obtain the design fiber strength, obtained for Tew (1995).

$$\sigma_{\alpha f} = \sigma_v \cdot V_f \cdot P_c \cdot P_s \cdot P_t \cdot P_{ch} \cdot P_u \cdot P_p \cdot P_{sc}$$

where

$\sigma_{\alpha f}$ = the design fiber strength
σ_v = the manufactures virgin fiber strength
V_f = fiber volume fraction
P_c = the modifier for cyclic loading
P_s = the modifier for static fatigue
P_t = the modifier for thermal degradation
P_{ch} = the modifier for chemical degradation
P_u = the modifier for ultraviolet degradation
P_p = the modifier for processing fabrication
P_{sc} = the modifier for structural geometry do to stress concentrations

The modifiers reduce the virgin strength of the fiber, such that the fiber can sustain the appropriate loading under the required conditions. For example for a filament wounded part the strength reduced by the fiber volume fraction and further reduced by 20% to 25% for stress concentrations and another 20% to 25% for fabrication processing [A1]. The other modifiers have been further described in Tew (1995).

A.4 FIBER FAILURE ENVELOPE

The lay-up sequence for the composite pipe investigated in this thesis is as follows:

$$\text{Inside } [\pm 66^{\circ}_{4}, 0^{\circ}, \pm 66^{\circ}_{3}, 0^{\circ}, \pm 66^{\circ}_{3}, 0^{\circ}, \pm 66^{\circ}_{5}] \text{ Outside}$$

This leaves 15 layers of $\pm 66^{\circ}$, and 3 layers of 0°, for a total of 33 fiber layers with an average wall thickness (t_{comp}) of 6.35 mm (0.25 in) and an average ply thickness (t_{α}) of 0.192 mm (0.007575 in). These values were determined neglecting fiber crossovers and resin built up with in the plies.

The virgin fiber strength (σ_v) for fiberglass listed by Reinhart (1987) was 3.447 GPa (500000 psi). The fiber volume fraction, founded experimentally in Chapter 2, was 58%. Factoring in a 40 % reduction for any excessive amount of stress concentrations (P_{sc}) and a 40 % reduction for fabrication processing (P_p), which were noted as the defects and impurities in Chapter 2 [A1, A2]. The fiber design strength ($\sigma_{\alpha f}$) then becomes 719.8 MPa (104400 psi), which gives a corresponding membrane force (N_ℓ) carrying capacity for a single ply of 138,201 N/m (psi).

The total membrane forces N_θ and N_ϕ for the filament-wound structure are then obtained from Equation A-4 and Equation A-5, to yield:

$$N_\theta = 2 \cdot (15) \cdot (138{,}201\,\mathrm{N/m}) \cdot \sin^2 66^{\circ} = \ 3460.1\ \mathrm{kN/m}\ (237{,}085\ \mathrm{lbf/ft})$$

$$N_\phi = 2 \cdot (15) \cdot (138{,}201\,\mathrm{N/m}) \cdot \cos^2 66^{\circ} + 2 \cdot (0.5 \cdot 3) \cdot (138{,}201\,\mathrm{N/m}) \cdot \cos^2 0^{\circ}$$

$$= \ 1100.5\ \mathrm{kN/m}\ (75{,}406\ \mathrm{lbf/ft})$$

This corresponds to the hoop and axial stress of:

$$\sigma_h = \frac{N_\theta}{t_{comp}} = 544.9\ \mathrm{MPa}\ (79{,}200\ \mathrm{psi})$$

$$\sigma_a = \frac{N_\phi}{t_{comp}} = 173.3 \text{ MPa} \ \ (25192 \text{ psi})$$

and the corresponding internal pressure and axial loads, with an average radius of

$\overline{R} = 27.94$ mm (1.1 in)

$$P = \frac{N_\theta}{\overline{R}} = 123.4 \text{ MPa} \ \ (18000 \text{ psi})$$

$$L = N_\phi \cdot 2 \cdot \pi \cdot \overline{R} = 193.0 \text{ kN} \ \ (43500 \text{ lbs.})$$

The maximum strength under the predominant load-carrying component for the winding angles is then obtained:

$$\sigma_\alpha = \frac{(30) \cdot N_f}{t_{comp}} = 652.9 \text{ MPa (94908 psi)}$$

$$\frac{\sigma_h}{\sigma_a} = \left(\tan 66^\circ\right)^2 = \frac{5}{1}$$

From the complied data, the fiber failure envelope based on the netting analysis for this pipe lay-up is illustrated in Figure A-3. From experimental testing complete structural failure for axial loading occurred at an axial stress of 184.049 MPa (26,694 psi), which is comparable to the predicted netting analysis valve of 173.7 MPa (25192 psi). Structural failure was not observed under pure pressure loading, therefore no comparison could be made.

A.5 BIBLIOGRAPHY

[A1] Tew, B.W. (1995, November). Preliminary design of tubular composite strucres using netting theory and composite degradation factors. Journal of Pressure Vessel Technology, Transations of the ASME, 117, 390-394.

[A2] Reinhart, T.J. (1987). Engineered Material Handbook: Composite (vol. 1) ASM International, Metals Park, Ohio. 508

[A3] Soden, P.D., Leadbetter, D., Griggs, P.R. & Eckold, G.C. (1978, October). The strength of a filament wound composite under biaxial loading. Composites, 247-250.

Appendix A: Netting Analysis

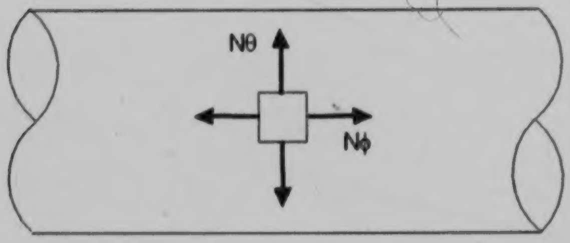

Figure A-1: Orientation of the membrane loads, N_θ and N_ϕ, for the composite pipe, figure adapted form Tew (1995).

Appendix A: Netting Analysis

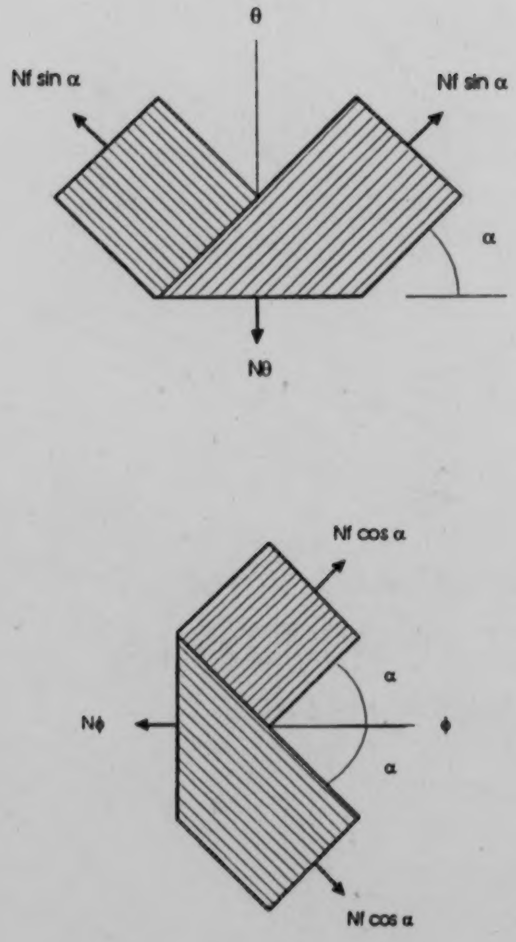

Figure A-2: Free-body diagrams of the fibers oriented in circumferential (θ) and longitudinal (ϕ) directions, figure adapted form Tew (1995).

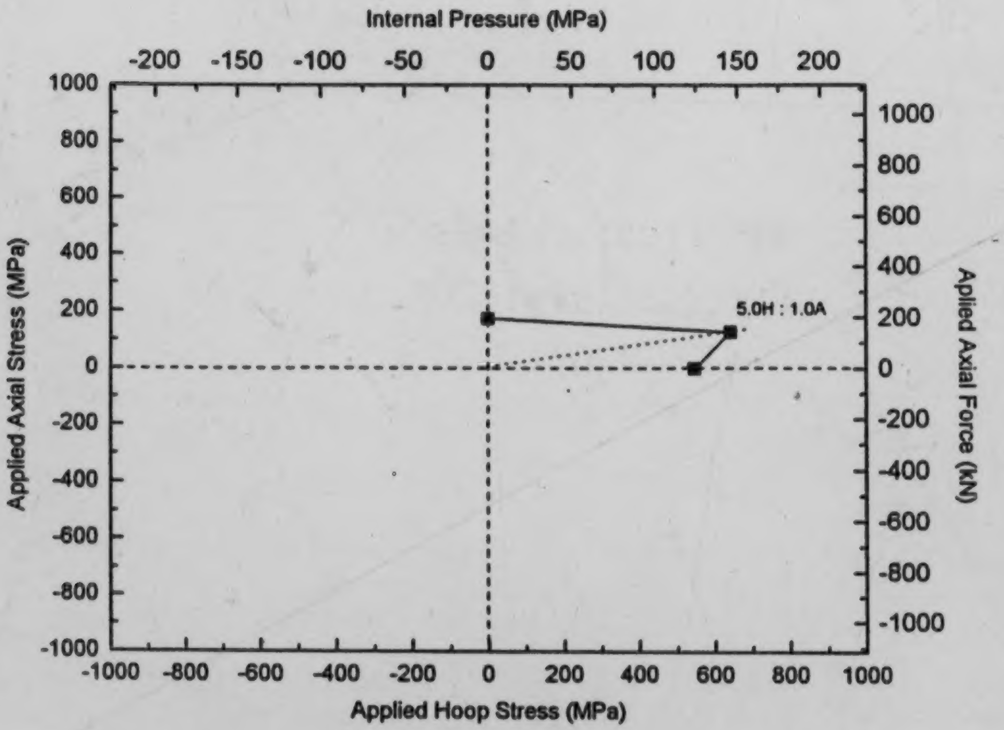

Figure A-3: The fiber failure envelope based on netting analysis for the pipe lay-up under investigation in this thesis. Note complete structural failure with an axial applied load occurred at an axial stress of 184.049 MPa. Failure in the hoop direction was not attainable under internal pressure loading.

APPENDIX B

STRESS AND LOAD CALCULATIONS

B.0 NOMENCLATURE

$Area_{internal}$	Internal area of the composite cylinder
$Area_{cross}$	Cross sectional area of the composite cylinder
A/H	The global applied axial stress to hoop stress ratio
D_{max}	Maximum measured outside diameter of the composite cylinder
D_{min}	Minimum measured outside diameter of the composite cylinder
D_{ave}	Average outside diameter calculated from D_{min} and D_{max}
D_{inside}	The measured inside diameter of the composite cylinder
$P_{internial}$	Internal pressure of the specimen
$L_{required}$	The required axial load on the composite cylinder
L_{actual}	The actual axial load in the cylinder directly related to $L_{required}$
$L_{applied}$	The axial load applied to the composite cylinder from testing machine
$L_{pressure}$	The axial component of the load which is produced from pressure
L_{cell}	The load seen by the load cell
σ_{axial}	Globally applied axial stress as seen by the tubular specimen
σ_{hoop}	Globally applied hoop stress as seen by the tubular specimen
R	The ratio of minimum to maximum stresses, loads or pressures
t_{mean}	Mean thickness of the specimen
r_{mean}	Mean radius of the tubular specimen

Appendix B: Stress and Load Calculations

B.1 INTRODUCTION

The commercially wound multidirectional pipes used in this investigation are under a complex state of stress. Residual stresses caused from curing as well as stresses caused during loading, which change upon the initiation of damage. With the addition of stress raisers covered in Chapter 2, the stress fields become even more complex. In order to avoid complications the globally applied traction stresses in the composite pipes was calculated using thin walled cylinder theory, as out lined by the ASTM Standard D2992-91 [B1].

B.2 CALCULATING GLOBALLY APPLIED STRESSES

The applied average stresses were calculated from the internal pressure and axial load according to the ASTM Standard D2992-91, which uses the thin-walled cylinder theory [B1]. The hoop stresses were calculated for the tubular specimen loaded by internal pressure with fixed end conditions according Equation B-1 and the axial stress according to Equation B-2.

$$\sigma_{hoop} = \frac{P \cdot r_{mean}}{t_{mean}} \qquad \text{B-1}$$

$$\sigma_{axial} = \frac{P \cdot r_{mean}}{2 \cdot t_{mean}} \qquad \text{B-2}$$

Where t_{mean} the mean thickness of the tube and r_{mean} the mean radius, calculated from Equation B-3 and Equation B-4 respectively.

$$t_{mean} = \frac{\sum_{i=1}^{m} t_i}{m} \qquad \text{B-3}$$

$$r_{mean} = r_{inside} + \frac{t_{mean}}{2} \qquad \text{B-4}$$

The mean values are used due to the variations around the external perimeter. The pipes were wound on a smooth ground mandrel, which leaves the internal surface consistently round with small variations in diameter, ± 0.254 mm (± 0.001 inch). The external surface, on the other hand, is somewhat irregular, thus causing large variations in the outer diameter, ± 1.2 mm (± 0.050 inch).

The average axial stress was calculated from the required axial load is calculated from Equation B-5.

$$\sigma_{axial} = \frac{L_{required}}{Area_{cross}} \qquad \text{B-5}$$

where cross-section area is based on the average external diameter and the internal diameter, given by Equation B-6.

$$Area_{cross} = \frac{\pi}{4} \cdot [D^2_{outside} - D^2_{inside}] \qquad \text{B-6}$$

The outer surface shape only dependent on the placement of the resin rich area between the $\pm 66°$ and the 0^0 layers. The most straightforward approach is to approximate the cross sectional area with the average diameter

B.3 EQUATIONS FOR TUBULAR TESTING

However, the most important aspect for building both monotonic and fatigue failure envelopes is developing the required stress ratios as in Equation B-7. The stress ratio can also be calculated from the required load and required internal pressure as in Equation B-8.

Appendix B: Stress and Load Calculations

$$A/H = \sigma_{axial} : \sigma_{hoop} \qquad \text{B-7}$$

$$A/H = \frac{L_{required}}{P} \cdot \frac{t_{mean}}{Area_{cross} \cdot r_{mean}} \qquad \text{B-8}$$

The internal pressure applied to the specimen produces an added axial load called a pressure load ($L_{pressure}$), as seen in Equation B-2. The pressure load ($L_{pressure}$) is calculated from Equation B-9. The required load ($L_{required}$), which is predetermined based on the stress ratio, is sought after to produce the correct stress ratio. In order to accounting for the internal pressure effect, the pressure load ($L_{pressure}$) is subtracted from the required load ($L_{required}$) as in Equation B-11. This leaves a machine-applied load called loaded applied ($L_{applied}$). Load applied ($L_{applied}$) is the axial load, which the testing machine applies to the specimen [B2]. The axial load is added or subtracted from the specimen to produce the correct stress ratio. This load applied ($L_{applied}$) is also the same load seen by the load cell (L_{cell}) thus developing a feed back loop as in Equation B-12.

The actual load (L_{actual}) in the specimen is now found by adding the pressure load to the load seen by the load cell, note Equation B-13. This actual load (L_{actual}) then the sought after required load ($L_{required}$), Equation B-14 [B2].

$$L_{pressure} = P \cdot Area_{internal} \qquad \text{B-9}$$

where

$$Area_{internal} = \frac{\pi \cdot D_{inside}^{2}}{4} \qquad \text{B-10}$$

Appendix B: Stress and Load Calculations

$$L_{applied} = L_{required} - L_{pressure} \tag{B-11}$$

$$L_{applied} = L_{cell} \tag{B-12}$$

$$L_{actual} = L_{cell} + L_{pressure} \tag{B-13}$$

$$L_{actual} = L_{required} \tag{B-14}$$

The R ratio is the ratio of minimum to maximum stress, load, or pressure, and is used to specify the lower limit of fatigue cyclic, Equation B-15. The R ratio represents the surging internal pressure with similar axial loading effects. For fatigue tests, the maximum stress is based on the failure point from the monotonic tests. The mean and amplitude can be calculated from the maximum stress, load, or pressure, as in Equation B-16 and Equation B-17 respectively.

$$R = \frac{\sigma_{min}}{\sigma_{max}} = \frac{L_{min}}{L_{max}} = \frac{P_{min}}{P_{max}} \tag{B-15}$$

$$\sigma_{mean} = \sigma_{max} \cdot \frac{(1+R)}{2} \tag{B-16}$$

$$\sigma_{amp} = \sigma_{max} \cdot \frac{(1-R)}{2} \tag{B-17}$$

The fatigue cycle, which is based on the sinusoidal curve, is calculated from the known maximum stresses, loads, or pressures. An example of pressure is given below:

$$P_{wave} = P_{max} \cdot \frac{(1+R)}{2} + P_{max} \cdot \left(\frac{(1-R)}{2}\right) \cdot \sin(2\pi ft) \tag{B-18}$$

Where t is time in seconds which runs from the initial point t = 0 through the full cycle to t = (1/f), for the given frequency (f).

The machine-applied load can be obtained from Equation B-19, by using Equation B-1 to obtain the hoop stress, Equation B-5 for axial stress, and Equation B-9 for the required load.

$$L_{applied} = \frac{P_{wave} \cdot (A/H) \cdot (Area_{cross}) \cdot r_{mean}}{t_{mean}} - P_{wave} \cdot Area_{interinal} \tag{B-19}$$

Taking into account the internal pressure, the globally applied axial stress can be calculated from Equation B-5, Equation B-10 and Equation B-13 as in Equation B-20.

$$\sigma_{axial} = \frac{L_{required}}{Area_{cross}} = \frac{L_{applied} + P \cdot Area_{internal}}{Area_{cross}} \tag{B-20}$$

B.4 CASE SCENARIOS FOR APPLYING STRESS RATIO

The machine-applied load calculations depend solely on the required stress ratios. With the different interactions of the pressure and the required load, three separate cases of stress ratio are required.

Case (1) $A \neq 0 \; H \neq 0$ Originates from Equation B-19

$$L_{applied} = \frac{P_{wave} \cdot (A/H) \cdot (Area_{cross}) \cdot r_{mean}}{t_{mean}} - P_{wave} \cdot Area_{interinal}$$

Case (2) $A = 0 \; H \neq 0$ Originates from Equations B-10 and Equation B-11

$$L_{applied} = -L_{pressure} = -P \cdot Area_{internal}$$

Case (3a) $A \neq 0 \; H = 0$ Originates from Equation B-10 and Equation B-11

$$L_{applied} = L_{required} - P_{constant} \cdot Area_{internal}$$

Case (3b) $A \geq 20 \; H = 1$ Originates from Equation B-9, Equation B-10 and Equation B-11

$$P_{wave} = \frac{(L_{required})_{wave} \cdot t_{mean}}{(A/H) \cdot Area_{cross} \cdot r_{mean}}$$

$$L_{applied} = (L_{required})_{wave} - P_{constant} \cdot Area_{internal}$$

B.5 BIBLIOGRAPHY

[B1] Standard Practice for obtaining hydrostatic or pressure design basis for "Fiberglass" (glass-Fiber-Reinforced thermosetting resin) pipe and fittings, ASTM Designation: D2992-91.

[B2] Wolodko, J. (1999, Spring) Biaxial fatigue and leakage characteristics of fiber reinforced composite tubes. doctoral thesis, Department of Mechanical Engineering, University of Alberta, Edmonton, Alberta, Canada.

APPENDIX C

SPECIMEN EXPANSION VOLUME

C.0 NOMENCLATURE

a	The inside radius of the pipe
d_i	The inside diameter of the pipe
D_θ	The flexural stiffness in the hoop direction
D_x	The flexural stiffness in the axial direction
ε_a	The axial strain measured by an extensometer.
ε_h	The hoop strain measured by an extensometer.
E_θ	The stiffness in the hoop direction determined from monotonic testing. 37735 MPa (5472999 psi)
E_x	The stiffness in the axial direction determined from monotonic testing. 18.235 MPa (2639000 psi)
h	The mean wall thickness
L	The wetted length of the specimen
$\nu_{x\theta}$	The Poisson's Ratio of the axial direction on the hoop direction determined from monotonic testing. 0.3261
$\nu_{\theta x}$	The Poisson's Ratio of the hoop direction on the axial direction determined from monotonic testing. 0.2439

C.1 INTRODUCTION

The expansion of the specimen under loading is a large consumer of the oil volume. An estimation of the expanded shape was developed based on thin cylinder theory from the associated measured surface strains of the specimen. The expansion volume was then determined from the estimated expansion shape.

C.2 MAXIMUM EXPANDED VOLUME

It is important to determine the maximum expanded volume in order to determine the validity of the estimated expanded volume when the specimen is loaded. The maximum expanded volume has been separated into two sections as illustrated in Figure C-1. The reason for this will become evident later on. The first expended volume (V1) is described from the axial extended length, measured from the axial strain at the mid-length of the specimen. Thus:

$$V1 = \frac{\pi}{4} \cdot d_{inside}^{2} \cdot L \cdot \varepsilon_a$$

Where, d_{inside} is the internal diameter, L is the wetted length and ε_a is the measured axial strain.

The second expended volume (V2) describes the deformation of the specimen in the radial direction as well as the corresponding axial extended length.

$$V2 = \frac{\pi}{4} \cdot \left[\left(d_{inside}^{2} \cdot (1+\varepsilon_h) \right)^{2} - d_{inside}^{2} \right] \bullet \left[L \cdot (1+\varepsilon_a) \right]$$

where ε_h is the mid-length measured hoop strain.

The summation of the first and second expended volumes gives the total maximum expanded volume of the specimen.

$$\Delta Volume = V1 + V2 = \frac{\pi}{4} \cdot d_{inside}^{2} \cdot L \bullet \left\{ \varepsilon_a + \varepsilon_h \cdot (1+\varepsilon_a) \cdot (\varepsilon_h + 2) \right\}$$

The above calculation will result in an upper bound, since a uniform radial expansion through the specimen length was assumed.

C.3 EXPANDED VOLUME

The boundary conditions introduced by grips cause the specimen to take on a barrel shape as illustrated in Figure C-2 [C1, C2]. The expanded volume can be estimated from the barrel shape by assuming a general pipe deflection shape. A general pipe deflected shape can be assumed based on the associated surface strains measured form the axial and hoop extensometers and the material properties.

The expanded volume is again separated into two sections because barreling does not affect the first expansion volume (V1).

The second expended volume is shape dependent as illustrated in Figure C-2. The barrel shape is estimated from the general solution in terms of the hyperbolic functions for pipe deformation given in Timoshenko & Woinowsky-Krieger (1959) [C3].

$$w(x) = f(x) + C_1 \sin(\beta x)\cdot\sinh(\beta x) + C_2 \sin(\beta x)\cdot\cosh(\beta x) + C_3 \cos(\beta x)\cdot\sinh(\beta x) + C_4 \cos(\beta x)\cdot\cosh(\beta x)$$

Where,

$$\beta^4 = \frac{3\cdot(1-\nu_{x\theta}\nu_{\theta x})}{h^2\cdot a^2}\cdot\frac{D_\theta}{D_x}$$

$$D_\theta = \frac{E_\theta\cdot h^3}{12\cdot(1-\nu_{x\theta}\nu_{\theta x})} \qquad D_x = \frac{E_x\cdot h^3}{12\cdot(1-\nu_{x\theta}\nu_{\theta x})}$$

The adaptation to orthotropic material is taken from Vinson et al. (1986) and Vinson et al. (1989) [C4, C5].

Appendix C: Specimen Expansion Volume

Taking the origin of the coordinate system at the mid-line between the ends, as illustrated in Figure C-3, the above expression must be in terms of an even function of x to satisfy the coordinate system. Thus:

$$C_2 = C_3 = 0$$

If the edges of the shell are built in, the deflection and the slope must vanish at these ends, i.e.:

$$(w(x))_{x=k} = 0 \qquad \left(\frac{dw(x)}{dx}\right)_{x=k} = 0$$

Where, for simplicity $k = \frac{L}{2} \cdot (1 + \varepsilon_a)$, which is the mid-length of the expanded specimen.

However, the general deflection solution does not allow the displacement to be defined at x=0, because of the prescribed boundary conditions. Therefore, for the particular case, let f (x) = -f, where f is a constant defining the displacement.

From the general deflection solution and boundary conditions, the following can be obtained:

$$(w(x))_{x=k} = -f + C_1 \sin(\alpha) \cdot \sinh(\alpha) + C_4 \cos(\alpha) \cdot \cosh(\alpha) = 0$$

$$\left(\frac{dw(x)}{dx}\right)_{x=k} = C_1 \cos(\alpha) \cdot \sinh(\alpha) + C_1 \sin(\alpha) \cdot \cosh(\alpha)$$
$$- C4 \sin(\alpha) \cdot \cosh(\alpha) + C_4 \cos(\alpha) \cdot \sinh(\alpha) = 0$$

Where, for simplicity $\alpha = \beta k$

Appendix C: Specimen Expansion Volume

The solution to the boundary conditions gives:

$$C_1 = -f \bullet \frac{\cos(\alpha)\cdot\sinh(\alpha) - \sin(\alpha)\cdot\cosh(\alpha)}{\sin(\alpha)\cdot\cos(\alpha) + \sinh(\alpha)\cdot\cosh(\alpha)}$$

$$C_4 = f \bullet \frac{\cos(\alpha)\cdot\sinh(\alpha) + \sin(\alpha)\cdot\cosh(\alpha)}{\sin(\alpha)\cdot\cos(\alpha) + \sinh(\alpha)\cdot\cosh(\alpha)}$$

However, the deflection δ is measured at $x = 0$. Therefore the constant describing the deflection f is given as:

$$f = \frac{\delta}{\left[1 - \dfrac{\cos\alpha\cdot\sinh\alpha + \sin\alpha\cdot\cosh\alpha}{\sin\alpha\cdot\cos\alpha + \sinh\alpha\cdot\cosh\alpha}\right]}$$

The finial shape is illustrated in Figure C-4.

Now the deflection shape can be used to determine the change in volume based on the associated deflection determined from the mid-length hoop strain. The change in volume is given in following equation:

$$\Delta V = 2\pi\int_0^k \left\{[F(x)]^2 - [G(x)]^2\right\}$$

Where,

$$F(x) = w(x) + a \qquad\qquad G(x) = a$$

Solving for the change in volume the following is obtained:

$$V2 = 2\pi \{ f^2 \bullet [x + \frac{A}{\beta}(\cosh(\beta x)\sin(\beta x) - \sinh(\beta x)\cos(\beta x))$$

$$- \frac{B}{\beta}(\cosh(\beta x)\sin(\beta x) - \sinh(\beta x)\cos(\beta x)) + \left[\frac{AB}{4} \cdot \frac{e^{2\beta x}}{4\beta}\right](-\sin(2\beta x) + \cos(2\beta x))$$

$$- \left[\frac{AB}{4} \cdot \frac{e^{-2\beta x}}{4\beta}\right](\sin(2\beta x) + \cos(2\beta x))$$

$$+ \left[\frac{A^2}{4}\frac{e^{2\beta x}}{4\beta}\right] - \left[\frac{A^2}{4}\frac{e^{2\beta x}}{8\beta}\right](\cos(2\beta x) + \sin(2\beta x))$$

$$- \left[\frac{A^2}{4}\frac{e^{-2\beta x}}{4\beta}\right] - \left[\frac{A^2}{4}\frac{e^{-2\beta x}}{8\beta}\right](-\cos(2\beta x) + \sin(2\beta x)) - \frac{A^2}{4}\beta x + \frac{A^2}{4}\frac{1}{2}\sin(2\beta x)$$

$$+ \left[\frac{B^2}{4}\frac{e^{2\beta x}}{4\beta}\right] - \left[\frac{B^2}{4}\frac{e^{2\beta x}}{8\beta}\right](\cos(2\beta x) + \sin(2\beta x))$$

$$- \left[\frac{B^2}{4}\frac{e^{-2\beta x}}{4\beta}\right] + \left[\frac{B^2}{4}\frac{e^{-2\beta x}}{8\beta}\right](-\cos(2\beta x) + \sin(2\beta x)) + \frac{B^2}{4}\beta x + \frac{B^2}{4}\frac{1}{2}\sin(2\beta x)]$$

$$+ f^2 \cdot a \bullet [x + \frac{A}{2\beta}(\cosh(\beta x)\sin(\beta x) - \sinh(\beta x)\cos(\beta x))$$

$$- \frac{B}{2\beta}(\cosh(\beta x)\sin(\beta x) - \sinh(\beta x)\cos(\beta x))]]\}$$

Where,

$$A = \frac{\cos(\alpha)\cdot\sinh(\alpha) - \sin(\alpha)\cdot\cosh(\alpha)}{\sin(\alpha)\cdot\cos(\alpha) + \sinh(\alpha)\cdot\cosh(\alpha)}$$

$$B = (-1)\frac{\cos(\alpha)\cdot\sinh(\alpha) + \sin(\alpha)\cdot\cosh(\alpha)}{\sin(\alpha)\cdot\cos(\alpha) + \sinh(\alpha)\cdot\cosh(\alpha)}$$

The summation of the first and second expanded volumes gives the total expanded volume of the specimen.

$$\Delta\text{Volume} = V1 + V2$$

C.4 ASSUMPTIONS

In order to approximate the expanded volume using the deflections measured from the hoop and axial extensometer the following assumptions were made:

First, the hoop deflection measured by the hoop extensometer at the mid-length on the exterior surface is the same as if it were measured on the interior surface. However, Sullivan (1973) has shown that there was a variation in strain between the inner and outer surface [C1]. The small radial component, which makes up a portion of the mid-length hoop strain, might be able to account for the variation [C6].

Second, the thickness around the circumference of the specimen is constant. Therefore, giving a constant radial expanded around the circumference.

Third, the axial extensometer does not see any effects of radial expansion [C2]. To overcome the effects of radial expansion on the axial strain the axial stroke might be considered. But, flexing in the grips may affect the axial stroke.

C.5 VALIDITY

To ensure that the assumed expansion shape can approximately determine the expanded volume, a fatigue cycle was plotted, as shown in Figure C-5. The intensifier oil volume expansion was corrected by adding the oil compression volume and the specimen expansion volume, to give the overall change in volume for the specimen and the intensifier.

However, in this case, compared to the oil compression volume the specimen expansion is almost negligible. Thus making it difficult to determine the validity of the assumed shape.

C.6 BIBLIOGRAPHY

[C1] Sullivan, T.L. & Chamis, C.C., (1973). Some important aspects in testing high-modulus fiber composite tubes in axial tension. ASTM STP 521 American Society for Testing and Materials, 277-292.

[C2] Ellyin, F. & Valaire, B., (1982, May). High-strain biaxial fatigue test facility. Proceedings of the 1982 Joint Conference on Experimental Mechanics, Oahu-Maui, Hawaii. Society for Experimental Stress Analysis. Brookfield Center, Connecticut.
136-143.

[C3] Timoshenko, S., & Woinowsky-Krieger, S. (1959). Theory of plates and shells (2^{nd} ed.). New York: McGraw-Hill.

[C4] Vinson, J. R., & Sierakowski, R.L., (1986). The behavior of structures composed of composite materials. Dordrech: Martinus Nijhoff Publishers.

[C5] Vinson, J. R., (1989). The behavior of thin walled structures: beams, plates, and shells. Dordrech: Klumer Academic Publishers.

[C6] Rinheart, K. (1995). Secondary stress in flexible composite pipe. master thesis, Department of Mechanical Engineering, University of Alberta, Edmonton, Alberta, Canada.

Appendix C: Specimen Expansion Volume

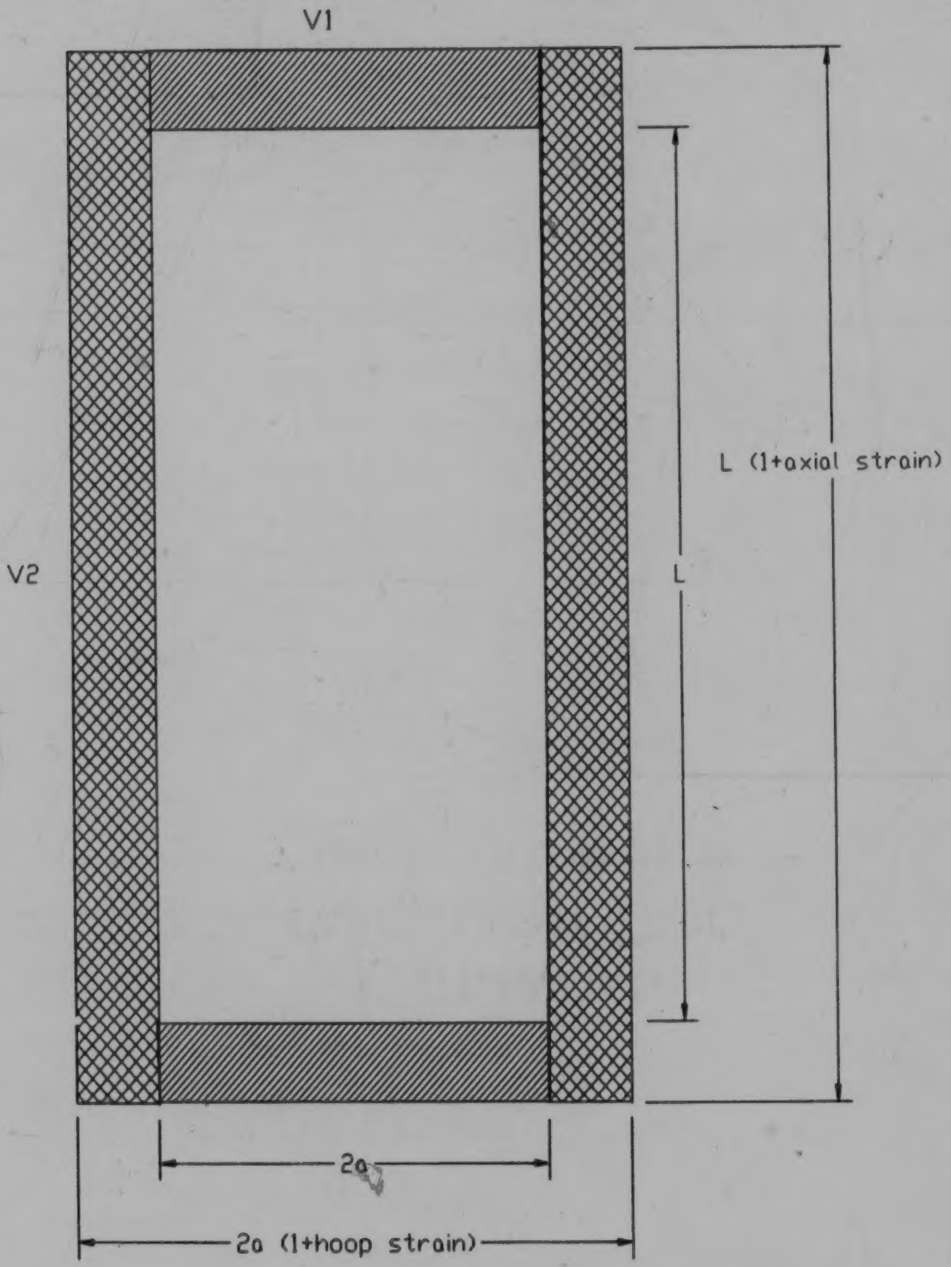

Figure C-1: Layout of the expanded specimen assuming a uniform radial expansion through the specimen length.

Appendix C: Specimen Expansion Volume

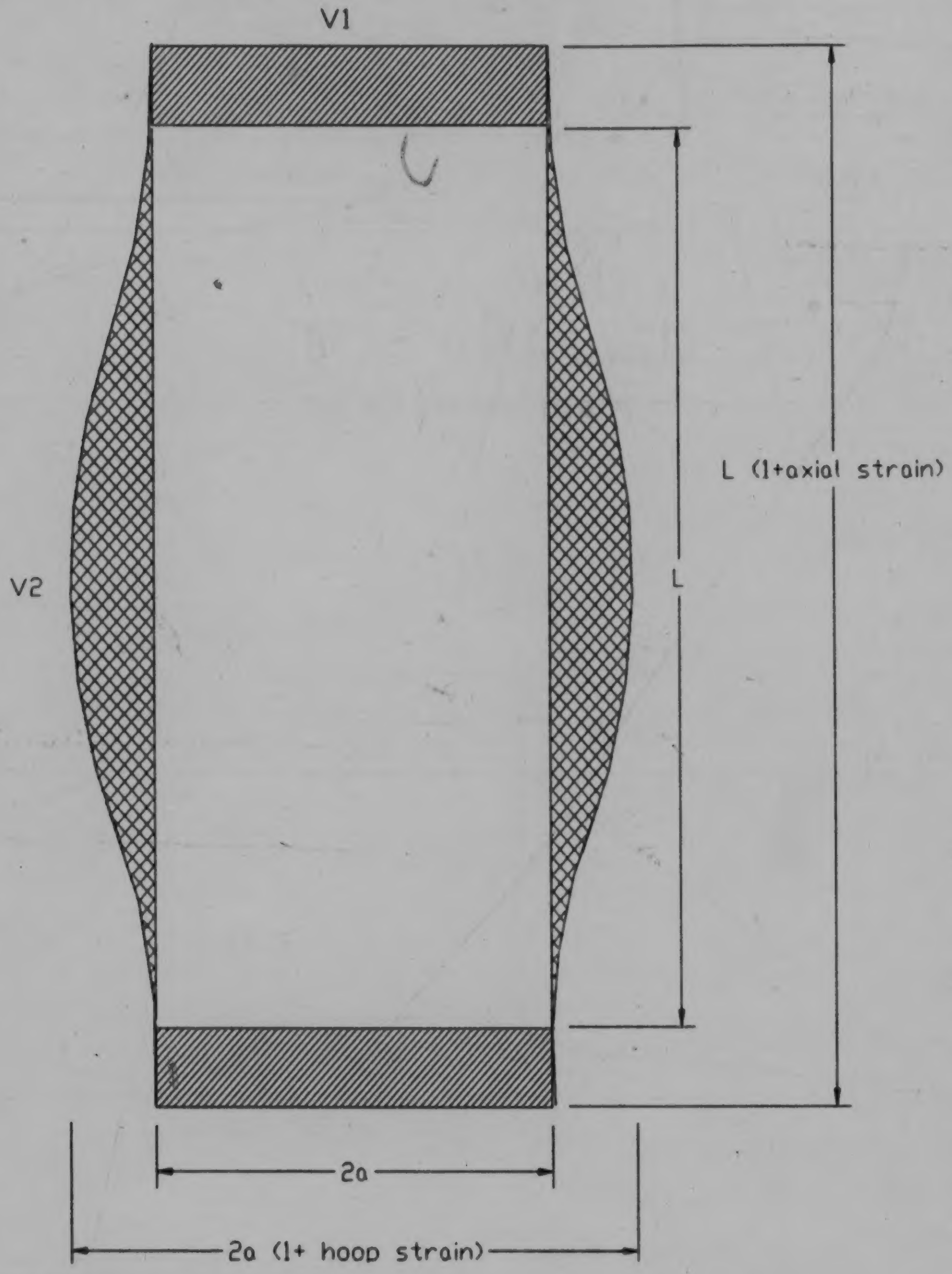

Figure C-2: Layout of the expanded specimen accounting for radial expansion through the specimen length.

Appendix C: Specimen Expansion Volume

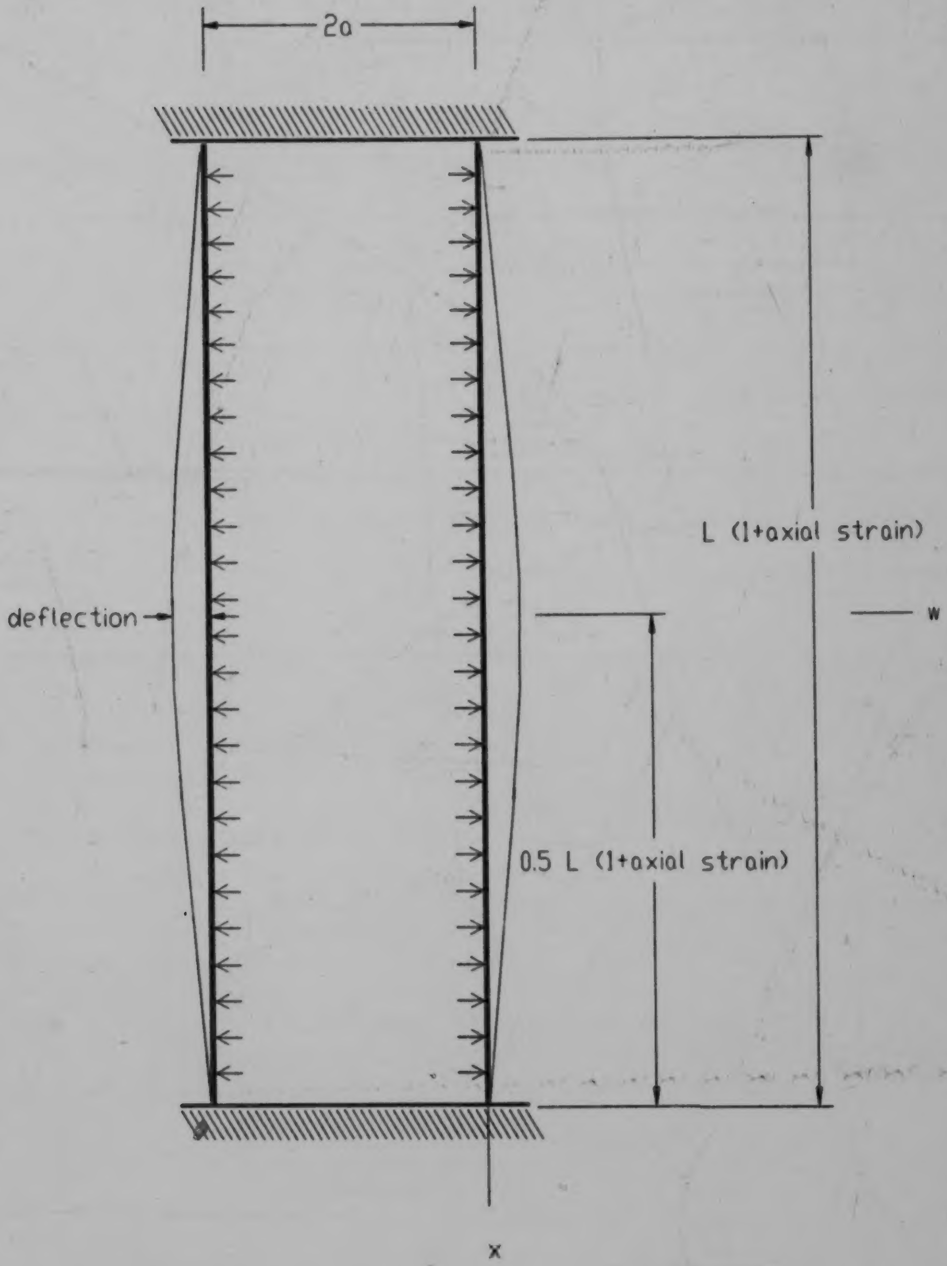

Figure C-3: An illustration of the loaded pipe specimen with fix end conditions.

Appendix C: Specimen Expansion Volume

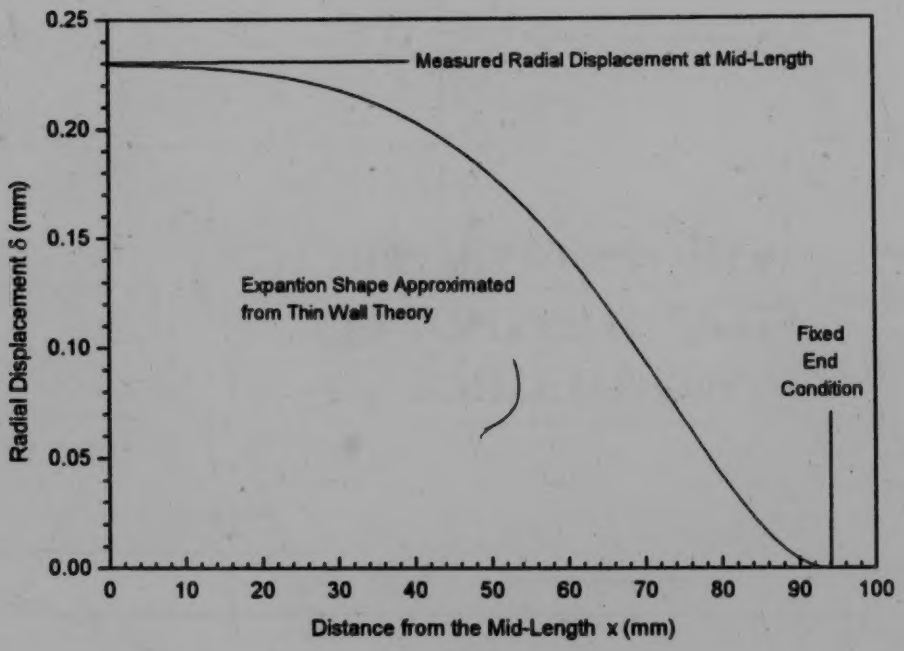

Figure C-4: A plot of the expanded shape, of the loaded pipe specimen with fix end conditions, approximated from Thin Wall Theory.

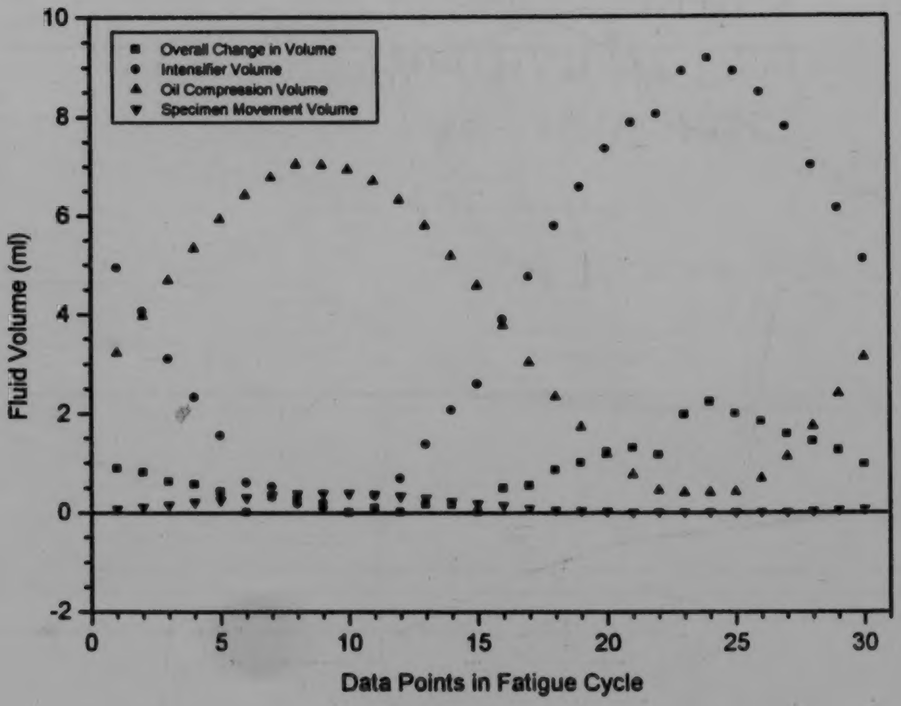

Figure C-5: A plot of the fluid volume for a fatigue cyclic. Shows the corrections applied to the volume change of the intensifier by specimen expansion and oil compression to obtain the overall volume expansion.

APPENDIX D

PRESSURE VESSEL LOADING STRESS RATIO

D.0 NOMENCLATURE

H / A	The global applied hoop to axial stress ratio
P	Internal pressure of the specimen
$L_{required}$	The required axial load on the composite cylinder
$L_{applied}$	The axial load applied to the composite cylinder from testing machine
$L_{pressure}$	The axial component of the load which is produced from pressure
σ_{axial}	Globally applied axial stress as seen by the tubular specimen
σ_{hoop}	Globally applied hoop stress as seen by the tubular specimen
t_{mean}	Mean thickness of the specimen
r_{mean}	Mean radius of the tubular specimen
r_o	Outside radius of the tubular specimen
r_i	Inside radius of the tubular specimen

D.1 INTRODUCTION

A free end condition is applied to the specimen in order to produce the required pressure vessel loading in which the axial load is developed by the internal pressure on the capped ends. There is some question regarding the hoop to axial stress ratio while internal pressure is applied to a pipe relatively small radius and large thickness, as the present specimen.

Appendix D: Pressure Vessel Loading Stress Ratio

Note the ASTM Standard D2992-91 has outlined the end conditions. (1) Free Ends – the specimen is stressed by internal pressure in both hoop and axial directions. (2) Restrained Ends - the specimen is stressed by internal pressure in the hoop direction.

D.2 DERIVATION OF STRESS RATIO

The applied traction stresses were calculated from the internal pressure and axial load according to the ASTM Standard D2992-91, which uses thin cylinder theory [D1]. The hoop stress was calculated for the tubular specimen loaded by internal pressure according Equation D-1 and the axial stress according to Equation D-2.

$$\sigma_{hoop} = \frac{P \cdot r_{mean}}{t_{mean}} \qquad \text{D-1}$$

$$\sigma_{axial} = \frac{P \cdot r_{mean}}{2 \cdot t_{mean}} \qquad \text{D-2}$$

The axial stress based on the axially applied load is calculated from Equation D-3.

$$\sigma_{axial} = \frac{L_{required}}{\pi \cdot (r_o^2 - r_i^2)} \qquad \text{D-3}$$

The hoop to axial stress ratio can be expressed as

$$H/A = \frac{\sigma_{hoop}}{\sigma_{axial}} = \frac{P \cdot r_{mean} \cdot \pi \cdot (r_o^2 - r_i^2)}{L_{required} \cdot t_{mean}} \qquad \text{D-4}$$

From Equation D-4 the required load based on the hoop to axial stress ratio can be expressed as:

Appendix D: Pressure Vessel Loading Stress Ratio

$$L_{required} = \frac{P \cdot r_{mean} \cdot \pi \cdot (r_o^2 - r_i^2)}{(H/A) \cdot t_{mean}} \qquad \text{D-5}$$

And the axial loading do to the pressure effect is expressed as:

$$L_{pressure} = P \cdot \pi \cdot r_i^2 \qquad \text{D-6}$$

The machine-applied axial load can then be expressed as:

$$L_{applied} = L_{required} - L_{pressure} = \frac{P \cdot r_{mean} \cdot \pi \cdot (r_o^2 - r_i^2)}{(H/A) \cdot t_{mean}} - P \cdot \pi \cdot r_i^2 \qquad \text{D-7}$$

For true pressure vessel type of loading the Equation D-7 is zero.

$$L_{applied} = 0 = \frac{P \cdot r_x \cdot \pi \cdot (r_o^2 - r_i^2)}{(H/A) \cdot t_{mean}} - P \cdot \pi \cdot r_i^2 \qquad \text{D-8}$$

where r_x is the radius for determining the hoop to axial stress ratio. Using the typical dimensions found for the specimen.

$r_i = 0.975$ $\quad r_o = 1.225$ $\quad r_{mean} = 1.1$ $\quad t_{mean} = 0.25$

The hoop to axial stress ratio can be determined from the r_x. Using the design radius where $r_x = r_i$ the hoop to axial stress ratio becomes 2.256 which is equivalent to 2. Using the mean radius for $r_x = r_m$ the hoop to axial stress ratio becomes 2.545. For pressure vessel loading case during fatigue the stress ratio of 2.5 was used.

To check the validity Equation E-8 the hoop to axial stress ratio should approach 2 as the radius approaches infinity and the thickness approaches zero. Manipulating Equation E-8 the following form can be obtained.

Appendix D: Pressure Vessel Loading Stress Ratio

$$(H/A) = \frac{r_i \cdot (r_o^2 - r_i^2)}{r_i^2 \cdot t_{mean}} \qquad \text{D-9}$$

Let $t_{mean} = (r_o - r_i)$ and let $r_o = r_i + \frac{1}{r_i}$ this defines the case of increasing radius with a decreasing thickness i.e. describes a thin cylinder. From this the following is obtained:

$$(H/A) = \frac{r_i \cdot \left(r_i^2 + 2 + \frac{1}{r_i^2} - r_i^2 \right)}{r_i^2 \cdot \left(r_i + \frac{1}{r_i} - r_i \right)} \qquad \text{D-10}$$

Simplifying the above equation the following is obtained:

$$(H/A) = 2 + \frac{1}{r_i} \qquad \text{D-11}$$

Taking the limit.

$$\lim_{r_i \to \infty+} (H/A) = \lim_{r_i \to \infty+} 2 + \frac{1}{r_i} = 2 \qquad \text{D-12}$$

So Equation E-8 checks, as the radius increases and the thickness decreases, i.e. thin cylinder theory, the hoop to axial stress ratio approaches two to one. This illustrates the effect of the radius and the wall thickness on the pure internal pressure loading case, as well as the design radius, which is the inside radius, and the mean radius.

D.3 BIBLIOGRAPHY

[D1] Standard Practice for obtaining hydrostatic or pressure design basis for "Fiberglass" (glass-Fiber-Reinforced thermosetting resin) pipe and fittings, ASTM Designation: D2992-91

APPENDIX E

FATIGUE CONVERSION SOURCE CODE

E.1 INTRODUCTION

The source code for converting the raw fatigue data file into a usable form is present in this section. Many complex interactions between the data sectors were required in order to determine the corrected leakage curves and the secant modulus based on the entire hysteresis loop.

E.2 C SOURCE CODE

```
/*
**********************************************************************
*  The following program was written to convert the raw data which ca          *
*  from the MTS testing machine.  Converting from that format will              *
*  required that this program by edited.                                        *
* THE CONVERTING PROGRAM WRITTEN BY MICHAEL G. MARTENS                          *
*              WRITTEN IN THE SUMMER OF 1997                          *
*                                                                               *
**********************************************************************
*/
#include <math.h>
#include <conio.h>
#include <string.h>
#include <stdio.h>
#include <alloc.h>
#include <ctype.h>
#include <dos.h>

#define PI 3.14159265359

int main(void)
{


// DEFINING LOCAL FUNCTIONS SETUP INSIDE THIS PROGRAM

void press_key(void);
void info_box(void);
float array_max(float vals[], int j);
float array_min(float vals[], int j);
float array_amp(float vals[], int j);
float array_mean(float vals[], int j);
float fita1(float val1[], float val2[], int j);
float fita0(float val1[], float val2[], int j);
float volume(float thickness, float radia, float inside_diameter, float L, float axial_strain, float hoop_strain);
```

Appendix E: Fatigue Conversion Source Code

```
// DEFINING LOCAL CHARS ARRAYS

char get_string[100];         // DATA LINE READER
char dummy[100];              // DO NOT CARE LINE READER
char str[30], ch;             // STR -> Y OR N HOLDER
char i_name[13];              // INPUT FILE NAME
char o_name_one[13];          // OUTPUT FILE NAME
char o_name_two[13];          // OUTPUT FILE NAME

// SPECIMEN PROPERTIES

float AREA_internal, AREA_cross;  // SPECIMEN AREA
float length_wet,dia_inside;      // WETTED LENGTH AND INSIDE .DIAMETER
float r_mean,t_mean;               // THE MEAN THIN WALL RADIUS AND WALL THICKNESS

// DEFINING LOCAL VARIABLE ARRAYS WHICH ARE FILLED FROM THE DATA FILE

long int loop_number[100];
float load_im[100],pressure_im[100];
float load_si[100],pressure_si[100];
float stress_axial_im[100],stress_hoop_im[100];
float stress_axial_si[100],stress_hoop_si[100];
float stress_hoop_axial_ratio[100];
float axial_strain[100], hoop_strain[100];
float stroke_mts_im[100];
float stroke_mts_si[100];
float tempature[100];
float oil_vol[100],oil_vol_intensifer[100];
float oil_compression[100], specimen_movement[100];
float oil_vol_lost[100];
float function_generater[100];
float specimen[100];
float true_oil_volume[100];

// DEFINING LOCAL VARIABLES FOR CALCULATION RUTINE INSIDE THE IMPORTER

float oil_volume_zeroed;
float intital_specimen_volume;

// DEFINING LOCAL VARIABLES WHICH RUN IMPORTER

int LINES_SKIPPED, i;
int first_string = 1, first_loop = 1, failure = 0, count = 0;
long int current_cycle, previous_cycle;

// DEFINING LOCAL MISC. VARIABLES

float temp1, temp2;
float tube_oil_volume=30.4;

// SETTING UP POINTERS FOR FILES NAMES

FILE *in_file;            // THE RAW DATA FILE
FILE *out_file_one;       // THE CONVERTED OUTPUT DATA FILE
FILE *out_file_two;       // THE CONVERTED OUTPUT MANULAPED DATA FILE

// THE START OF THE PROGRAM

do
{

clrscr();                         // CLEAR SCREEN
info_box();                       // ADD TITLE BOX

// PROMPTS FOR THE DATA FILE NAMES

printf("     Enter the name of data file to be converted      : ");
scanf ("%s",i_name);
printf("     Enter the name of the output file converted data : ");
scanf ("%s",o_name_one);
```

```
printf("     Enter the name of the output sum file data      : ");
scanf ("%s",o_name_two);

// PROMPS THE USER FOR RELAVANT DATA

printf("\n      PLEASE ENTER THE RELAVANT DATA.               ");
printf("\n      Pipe Intineral Area (inch^2)               : ");
scanf ("%f", &AREA_internal);
printf("     Pipe Cross-Sectional Area (inch^2)           : ");
scanf ("%f", &AREA_cross);
printf("     The mean Radius (inch)                     : ");
scanf ("%f", &r_mean);
printf("     The mean Thickness (inch)                   : ");
scanf ("%f", &t_mean);
printf("     The Wetted Length of the Specimen (inch)      : ");
scanf ("%f", &length_wet);
printf("     The Inside Diameter of Specimen (inch)        : ");
scanf ("%f", &dia_inside);
printf("     The oil volume at zero load (mL)            : ");
scanf ("%f", &oil_volume_zeroed);
printf("     IS THIS IN FORMATION CORRECT (y or n)         : ");
scanf ("%s", str);
ch = toupper(*str);

} while(ch != 'Y');

// OPENS UP THE RAW FILE READS IN A STRING WHICH INPUTS INTO ARRAYS

if ((in_file = fopen(i_name,"r")) ==NULL)
{
printf(" There is a ERROR in opening the file (%s)        \n", i_name);
printf(" make sure that this file is in the current       \n");
printf(" working directory.                              \n");
press_key();
}

// PROCESSING OF THE RAW DATA FILE

printf("\n      The file (%s) has been successfully opened.\n", i_name );
printf("\n      Data is being processed
                       \n"       );
// OPENS UP OUTPUT FILE AND WRITES IN THE INTRODUCTION INFORMATION

if ((out_file_one = fopen(o_name_one,"w")) ==NULL)
{
printf("\n      The file (%s) cannot be opened.", o_name_one);
press_key();
}

printf("\n      The file (%s) has been successfully opened.\n", o_name_one );

// PRINT TO FILE THE INPUTED DATA

fprintf(out_file_one,"   internal area =(%7.5f) "
"   cross-section area =(%7.5f)    wetted length =(%7.5f) "
"   inside diameter =(%7.5f)    mean radius =(%7.5f) "
"   mean thickness =(%7.5f)    oil volume at zero load =(%7.5f)",
AREA_internal, AREA_cross, length_wet, dia_inside, r_mean,t_mean,
oil_volume_zeroed);

// PRINT TO FILE THE COLUME HEADINGS

fprintf(out_file_one,"\n Number"
"     Fnmean(V)      Fnamp(V)       Fnmax(V)       Fnmin(V)"
"   TLmean(lbs)    TLamp(lbs)     Pmean(psi)      Pamp(psi)"
"     TLmean(N)       TLamp(N)     Pmean(MPa)       Pamp(MPa)"
"   SAmean(psi)    SAamp(psi)   SHmean(psi)     SHamp(psi)"
"   SAmean(MPa)     SAamp(MPa)    SHmean(MPa)     SHamp(Mpa)"
"      H/ARmean        H/ARamp        SAmean          SAamp"
"        SHmean          SHamp      FITA0Hoop       FITA1Hoop"
```

Appendix E: Fatigue Conversion Source Code

```
"   FITA0Axial    FITA1Axial   OVmean(mL)    OVamp(mL)"
"   SMmean(mL)    SMamp(mL)    Smean(mL)     Samp(mL)"
"   OCmean(mL)    OCamp(mL)    TVmean(mL)    TVamp(mL)"
"    Tmean(C)       Tamp(C)    STmean(in)    STamp(in)"
"   STmean(mm)    STamp(mm)");

// OPENS UP THE SECOND OUTPUT FILE AND WRITES IN THE INTRODUCTION INFORMATION

if ((out_file_two = fopen(o_name_two,"w")) ==NULL)
{
printf("\n      The file (%s) cannot be opened.", o_name_two);
press_key();
}

printf("\n      The file (%s) has been successfully opened.\n", o_name_two );

// PRINT TO FILE THE TYPED IN DATA

fprintf(out_file_two,"   internal area =(%7.5f) "
"   cross-section area =(%7.5f)    wetted length =(%7.5f) "
"   inside diameter =(%7.5f)    mean radius =(%7.5f) "
"   mean thickness =(%7.5f)    oil volume at zero load =(%7.5f)",
AREA_internal, AREA_cross, length_wet, dia_inside, r_mean,t_mean,
oil_volume_zeroed);

// PRINT TO FILE COLUME HEADINGS

fprintf(out_file_two,"\n Number"
"       Fun(V)       TL(lbs)       P(psi)       TL(N)"
"       P(MPa)       SA(psi)       SH(psi)      SA(MPa)"
"      SH(MPa)        H/AR          SA(T)        SH(T)"
"       OV(mL)       SM(mL)        S(mL)        OC(mL)"
"       TV(mL)         T(C)        ST(in)       ST(mm)");

// PROCESS TO CLEAR SCREEN AND PRINT TITLE BOX

clrscr();
info_box();

// SKIPS OVER THE FIRST FEW LINES OF THE DATA FILE

LINES_SKIPPED = 4;

for(i=0; i < LINES_SKIPPED; i++)
{
fgets(dummy,99,in_file);
}

// DO WHILE LOOP TO PROCESS THE DATA LOOP BY LOOP UNTIL "FAILURE" OR "   "

//   ********************************************************************************

do
{

fgets(get_string, 99,in_file);   // reads in the data line

// CHECK FOR FAILURE OR END OF FILE

if ( (strstr(get_string, "Failure")) || (feof(in_file)) )
{
failure = 1;
}

// READS IN THE CURRENT CYCLE LOOP NUMBER TO COMPARE LATER

else
{
sscanf(get_string,"%li", &current_cycle);
}
```

Appendix E: Fatigue Conversion Source Code

```
// ONLY FOR THE FIRST STRING READ IN FROM THE FILE

if (first_string == 1)
{
first_string = 0;
}

// THIS IS THE HEART OF THE PROGRAM WHERE EVER THING IS READ INTO ARRAYS

else
{
// NOTE: THIS CHECKS TO SEE IF WE HAVE A HOLE LOOP OR NOT. THIS IS DONE BY
// 1.) IF THE PREVIOUS STRING LOOP NUMBER IS DIFFERENT THEN THE CURRENT ONE
// 2.) IF THE CURRENT STRING LOOP NUMBER IS REPLACED BY THE WORD " FAILURE "

if (current_cycle != previous_cycle || failure == 1)
{
count–;
gotoxy(12,20);
printf("current cyclic: %6li",current_cycle);

for (i = 0; i <= count; i++)
{
// BITS ARE CHANGED INTO LOADINGS
function_generater[i] = function_generater[i] * 0.004884004884;

// LOAD ON THE COMPOSITE SPECIMEN

pressure_im[i] = pressure_im[i] * 1500.0 * 0.004884004884;
pressure_si[i] = pressure_im[i] * 0.00689475729317;
load_im[i] = load_im[i] * 8400.0 * 0.004884004884 + pressure_im[i] * AREA_internal;
load_si[i] = load_im[i] * 4.44822161526;

// STRESS ON THE SPECIMEN BASED ON THE INPUT DATA

stress_axial_im[i] = load_im[i] / AREA_cross;
stress_axial_si[i] = stress_axial_im[i] * 0.00689475729317;
stress_hoop_im[i] = pressure_im[i] * (r_mean / t_mean);
stress_hoop_si[i] = stress_hoop_im[i] * 0.00689475729317;

// THE STRESS RATIO A CHECK

if (stress_axial_im[i]==0)
{
stress_hoop_axial_ratio[i] = 0;
}
else
{
stress_hoop_axial_ratio[i] = stress_hoop_im[i] / stress_axial_im[i];
}

// THE STRAIN DATA FROM THE EXTENSOMETERS

axial_strain[i] = axial_strain[i] * 0.5 * 0.004884004884;
hoop_strain[i] = hoop_strain[i] * 0.5 * 0.004884004884;

// THE TEMPERATURE READ FROM A J TYPE THERMO COUPLE

tempature[i] = tempature[i] * 0.004884004884 * 10.0;

// THE STROKE READ FROM THE MTS LVDT

stroke_mts_im[i] = stroke_mts_im[i] * 0.004884004884 * 1.00787401575;
stroke_mts_si[i] = stroke_mts_im[i] * 25.4;

// OIL VOLUME READ FROM THE INTENSIFIER

oil_vol_intensifer[i] = ( 71.31 - ( oil_vol[i] * 0.004884004884 * 17.69 ) + oil_volume_zeroed );
```

Appendix E: Fatigue Conversion Source Code

```
// THE TOTAL OIL VOLUME OF THE SPECIMEN

intital_specimen_volume = 0.25 * PI * length_wet * dia_inside * dia_inside * 16.387064;

// THE OIL VOLUME DO TO MOVEMENT CALL IN THE VOLUME FUNCTION

temp1 = intital_specimen_volume * axial_strain[i];

temp2 = volume(t_mean,r_mean,dia_inside,length_wet,axial_strain[i],hoop_strain[i]) *;

specimen_movement[i] = ( temp1 * (temp2 * 16.387064));

specimen[i] = intital_specimen_volume + specimen_movement[i];

// THE TOTAL OIL VOLUME BEFORE COMPRESSION

true_oil_volume[i] = (oil_vol_intensifer[i] + specimen[i] + tube_oil_volume);

// OIL VOLUME COMPRESSION MEASURED ON THE INTENSIFIER

oil_compression[i] = ( true_oil_volume[i] * (0.0458561211611 / 10000) * pressure_im[i]);

// THE TRUE OIL VOLUME WITH LEAKAGE, COMPRESSION, MOVEMENT

true_oil_volume[i] = true_oil_volume[i] + oil_compression[i] ;

// THE CONVERTED DATA IS PRINTED TO OUTPUT FILE

fprintf(out_file_two,"\n %6li"
"  %12.5f  %12.5f  %12.5f  %12.5f"
"  %12.5f  %12.5f  %12.5f  %12.5f"
"  %12.5f  %12.5f  %12.5f  %12.5f"
"  %12.5f  %12.5f  %12.5f  %12.5f"
"  %12.5f  %12.5f  %12.5f  %12.5f",
loop_number[i], function_generater[i], load_im[i], pressure_im[i],
load_si[i], pressure_si[i], stress_axial_im[i], stress_hoop_im[i],
stress_axial_si[i], stress_hoop_si[i], stress_hoop_axial_ratio[i],
axial_strain[i], hoop_strain[i], oil_vol_intensifer[i], specimen_movement[i],
specimen[i], oil_compression[i], true_oil_volume[i], tempature[i],
stroke_mts_im[i], stroke_mts_si[i]);

}

// POINTS OUT END OF THE FIRST LOOP IN A FILE

if (first_loop == 1)
{
first_loop = 0;
}

// THE CONVERTED DATA IS PRINTED TO FILE

fprintf(out_file_one,"\n %6li"
"  %12.5f  %12.5f  %12.5f  %12.5f"
"  %12.5f  %12.5f  %12.5f  %12.5f"
"  %12.5f  %12.5f  %12.5f  %12.5f"
"  %12.5f  %12.5f  %12.5f  %12.5f"
"  %12.5f  %12.5f  %12.5f  %12.5f"
"  %12.5f  %12.5f  %12.5f  %12.5f"
"  %12.5f  %12.5f  %12.5f  %12.5f"
"  %12.5f  %12.5f  %12.5f  %12.5f"
"  %12.5f  %12.5f  %12.5f  %12.5f"
"  %12.5f  %12.5f  %12.5f  %12.5f"
"  %12.5f  %12.5f  %12.5f  %12.5f"
"  %12.5f  %12.5f ",
loop_number[0],
array_mean(function_generater,count),array_amp(function_generater,count),
array_max(function_generater,count),array_min(function_generater,count),
array_mean(load_im,count),array_amp(load_im,count),
array_mean(pressure_im,count),array_amp(pressure_im,count),
array_mean(load_si,count),array_amp(load_si,count),
array_mean(pressure_si,count),array_amp(pressure_si,count),
array_mean(stress_axial_im,count),array_amp(stress_axial_im,count),
array_mean(stress_hoop_im,count),array_amp(stress_hoop_im,count),
array_mean(stress_axial_si,count),array_amp(stress_axial_si,count),
array_mean(stress_hoop_si,count),array_amp(stress_hoop_si,count),
array_mean(stress_hoop_axial_ratio,count),array_amp(stress_hoop_axial_ratio,count),
array_mean(axial_strain,count),array_amp(axial_strain,count),
array_mean(hoop_strain,count),array_amp(hoop_strain,count),
fita0(hoop_strain,stress_hoop_si,count),fita1(hoop_strain,stress_hoop_si,count),
fita0(axial_strain,stress_axial_si,count),fita1(axial_strain,stress_axial_si,count),
array_mean(oil_vol_intensifer,count),array_amp(oil_vol_intensifer,count),
array_mean(specimen_movement,count),array_amp(specimen_movement,count),
array_mean(specimen,count),array_amp(specimen,count),
array_mean(oil_compression,count),array_amp(oil_compression,count),
array_mean(true_oil_volume,count),array_amp(true_oil_volume,count),
array_mean(tempature,count),array_amp(tempature,count),
array_mean(stroke_mts_im,count),array_amp(stroke_mts_im,count),
array_mean(stroke_mts_si,count),array_amp(stroke_mts_si,count));

// IF END OF THE DATA THEN KICK OUT OF THE WHILE LOOP IF FAILURE

if (failure == 1)
{
break;
}

// REZEROING THE COUNT FOR A NEW LOOP ALREADY STARTED

else
{
count = 0;
}
}
}

// GRABE THE DATA FROM THE STRING AND PUTS IT INTO ARRAYS

sscanf(get_string,"%li  %f  %f  %f  %f  %f  %f  %f  %f",
&loop_number[count],      &pressure_im[count],
&function_generater[count],&load_im[count],
&hoop_strain[count],      &axial_strain[count],
&tempature[count],        &oil_vol[count],
&stroke_mts_im[count] );

previous_cycle = current_cycle;

// INCREASE THE COUNT BY ONE

count++;

} while (!feof(in_file));

// ******************************************************************************************

fclose(in_file);        // closing the in coming data file
fclose(out_file_one);   // closing the out going data file
fclose(out_file_two);   // closing the out going data file

printf("\n      All files have been closed \n");

press_key();
return 0;
}

/*
***************************************************************************
* FUNCTION NAME: info_box
* PURPOSE      : print a box containing information
* INPUT        : none
* OUTPUT      : prints to the user screen
* AUTHOR      : MICHAEL G. MARTENS
* DATE       : Oct 5, 97
**********************************************************************
*/
void info_box(void)
{
printf("   ************************************************************\n");
printf("   * THIS CONVERTING PROGRAM WRITTEN BY MICHAEL G. MARTENS  *\n");
printf("   *          WRITTEN IN THE SUMMER OF 1997          *\n");
printf("   *                                      *\n");
printf("   * This software was designed to process the raw data    *\n");
printf("   * which was collected by the data acquisition using the  *\n");
printf("   * MTS Biaxial Testing Machine under cyclic loading     *\n");
printf("   * conditions.                              *\n");
printf("   *                                      *\n");
printf("   ************************************************************\n");
}

/*
**********************************************************************
* FUNCTION NAME: array_max
* PURPOSE     : Is to find the maximum value in an array
* INPUT      : The array and the lenth of the array
* OUTPUT      : the maximum value in the array
* AUTHOR      : MICHAEL G. MARTENS
* DATE       : June 8, 96
**********************************************************************
*/
float array_max(float vals[], int j)
{
int i;
float max = vals[0];

for (i = 1; i <= j; i++)
{
if (max < vals[i]) max = vals[i];
}
return (max);
}

/**********************************************************************
FUNCTION NAME: array_min
PURPOSE     : Is to find the minimum value in an array
INPUT      : The array and the lenth of the array
OUTPUT      : the minimum value in the array
AUTHOR      : MICHAEL G. MARTENS
DATE       : June 8, 96
**********************************************************************/
float array_min(float vals[], int j)
{
int i;
float min = vals[0];

for (i = 1; i <= j; i++)
{
if (min > vals[i]) min = vals[i];
}
return (min);
}

/**********************************************************************
FUNCTION NAME: array_mean
PURPOSE     : Is to find the mean value in an array
INPUT      : The array and the lenth of the array
OUTPUT      : the mean value in the array
AUTHOR      : MICHAEL G. MARTENS
DATE       : June 9, 96
**********************************************************************/
```

Appendix E: Fatigue Conversion Source Code

```
float array_mean(float vals[], int j)
{
int i;
float min, max, set;
min = array_min(vals,j);
max = array_max(vals,j);
set = (max + min) * 0.5;
return (set);
}

/************************************************************************
FUNCTION NAME: array_amp
PURPOSE      : Is to find the amp value in an array
INPUT       : The array and the lenth of the array
OUTPUT       : the amp value in the array
AUTHOR       : MICHAEL G. MARTENS
DATE        : June 9, 96
************************************************************************/

float array_amp(float vals[], int j)
{
int i;
float min, max, span;
min = array_min(vals,j);
max = array_max(vals,j);
span = (max - min) * 0.5;
return (span);
}

/************************************************************************
FUNCTION NAME: press_key
PURPOSE      : Is to stop the progam and can be used any where
INPUT       : none
OUTPUT       : none
AUTHOR       : MICHAEL G. MARTENS
DATE        : July 3, 96
************************************************************************/
void press_key(void)
{
printf(" PRESS ANY KEY TO EXIT THE PROGRAM ");
for(;;)
{
if (kbhit()) break;
}
exit(1);
}

/************************************************************************
FUNCTION NAME: fita1 the second part of a two part function
PURPOSE      : using the least-squares regression the slope of the line is found  ( y = a0 + a1 x )

a1 = [n(sum(xi.yi))-(sum(xi).sum(yi)] / [n(sum(xi^2)) - (sum(xi))^2]

INPUT       : two arrays of the same point and the number of points
OUTPUT       : the slope of the line.
AUTHOR       : MICHAEL G. MARTENS
DATE        : July 3, 96
************************************************************************/
float fita1(float val1[], float val2[], int j)
{
float sumxy = 0, sumx = 0, sumy = 0, sumx2 =  0;
float A1;
int i;

for (i=0; i<=j; i++)
{
sumxy = sumxy + val1[i] * val2[i];
sumx  = sumx  + val1[i];
sumy  = sumy  + val2[i];
sumx2 = sumx2 + val1[i] * val1[i];
}

A1 = ((j * sumxy) - (sumx * sumy)) / ((j * sumx2) - (sumx * sumx));

return(A1);
}

/**********************************************************************
FUNCTION NAME: fita1 the first part of a two part function
PURPOSE     : using the least-squares regression finds the intersection to the Y axis ( y = a0 + a1 x )

a0 = mean(y) - a1(mean(x))

INPUT       : two arrays of the same point and the number of points
OUTPUT      : the intersection to the Y axis
AUTHOR      : MICHAEL G. MARTENS
DATE        : July 3, 96
**********************************************************************/
float fita0(float val1[], float val2[], int j)
{
float sumy = 0, sumx = 0, A0;
int i;

for (i=0; i<=j; i++)
{
sumx = sumx + val1[i];
sumy = sumy + val2[i];
}
sumx = sumx / j;
sumy = sumy / j;

A0 = sumy - fita1(val1,val2,j) * sumx;

return(A0);
}

/**********************************************************************
FUNCTION NAME: volume
PURPOSE     : to calculate the volume of a specimen with fixed end conditions
 this was developed from Timoshenko thin wall theory
INPUT       : the pipo gemoity and measured displacements
OUTPUT      : the volume
AUTHOR      : MICHAEL G. MARTENS
DATE        : may 2, 96
**********************************************************************/
float volume(float thickness, float radia, float inside_diameter, float L, float axial_strain, float hoop_strain)
{

float volume,d,Eoo,Exx,vox,vxo,Do,Dx;
float L2,x,bata,gama;
float c1,c2,f1,f2,k,a[25];

/* Test numbers for the volume
The axial volume = 0.3681 ml or 0.225 in3
maximum volume = 1.2081 ml or 0.0513 in3
shape volume = 0.7907 ml or 0.0258 in3
thickness = 0.254;
radia = 1.111;
inside_diameter = 1.95;
L = 7.521;
axial_strain = 0.100;
hoop_strain = 0.100;
Eoo = 5472999.033;
Exx = 2636931.109;
vox = 0.3261;
vxo = 0.2439;
*/

 Eoo = 547299.033; //calculated from monotest
 Exx = 3142387.625;  //calculated from monotest
```

Appendix E: Fatigue Conversion Source Code

```
vox = 0.3261;  //calculated from monotest
vxo = 0.2439;  //calculated from monotest

Do = ((Eoo*thickness*thickness*thickness) / (12*(1-vxo*vox)));
Dx = ((Exx*thickness*thickness*thickness) / (12*(1-vxo*vox)));
bata = (3 * (1-vxo*vox) / (thickness * thickness * radia * radia))*(Do / Dx);
bata = pow(bata,0.25);

d = ( (hoop_strain / 100.00) * inside_diameter) * 0.5;
L2 = L * (1 + (axial_strain / 100.00)) * 0.5;
gama = bata * L2;

x = 0;
c1 =  ((cos(gama)*sinh(gama))-(sin(gama)*cosh(gama))) / ((sin(gama)*cos(gama))+(sinh(gama)*cosh(gama)));
c2 = -((cos(gama)*sinh(gama))+(sin(gama)*cosh(gama))) / ((sin(gama)*cos(gama))+(sinh(gama)*cosh(gama)));
k = ( d / ( 1 + c1*sin(bata*x)*sinh(bata*x) + c2*cos(bata*x)*cosh(bata*x)) );

x = L2;
a[1]  = x;
a[2]  =  2*c1*(1/2*bata)*(cosh(bata*x)*sin(bata*x)-sinh(bata*x)*cos(bata*x));
a[3]  = -2*c2*(1/2*bata)*(sinh(bata*x)*cos(bata*x)+cosh(bata*x)*sin(bata*x));
a[4]  = (exp(2*bata*x) /(8*bata*bata)) * (- 2 * sin(2*bata*x) + 2 * bata * cos(2*bata*x) );
a[5]  = (exp(-2*bata*x)/(8*bata*bata)) * (- 2 * sin(2*bata*x) - 2 * bata * cos(2*bata*x) );
a[6]  =  ((c1 * c2) / 4) * (a[4] + a[5]);
a[7]  =   exp(2*bata*x) * ( 1 / (4*bata) ) - ( 1 / 8 * bata )*( cos(2*bata*x) + sin(2*bata*x));
a[8]  = -exp(-2*bata*x) * ( 1 / (4*bata) ) + ( 1 / 8 * bata )*(-cos(2*bata*x) + sin(2*bata*x));
a[9]  =  2 * ( ( -bata * x ) / 2) + (1/4) * sin(2*bata*x);
a[10] =  ( ( c1*c1 ) / 4 ) *  (a[7] + a[8] +a[9] );
a[11] =   exp(2*bata*x) * ( 1 / (4*bata) ) + ( 1 / 8 * bata )*(cos(2*bata*x) + sin(2*bata*x));
a[12] = -exp(-2*bata*x) * ( 1 / (4*bata) ) - ( 1 / 8 * bata )*(-cos(2*bata*x) + sin(2*bata*x));
a[13] =  2 *  ( ( bata * x ) / 2) + (1/4) * sin(2*bata*x);
a[14] =  ( ( c2*c2 ) / 4 ) *  (a[11] + a[12] +a[13] );
a[15] = x;
a[16] =  c1 * (1/(2*bata)) * ( cosh(bata*x) * sin(bata*x) - sinh(bata*x) * cos(bata*x) );
a[17] = -c2 * (1/(2*bata)) * ( sinh(bata*x) * cos(bata*x) + cosh(bata*x) * sin(bata*x) );

f1 = ( k*k * ( a[1] + a[2] + a[3] + a[6] + a[10] + a[14] ) + k * radia * ( a[15] + a[16] +a[17] ) );

x = 0;
a[1]  = x;
a[2]  =  2*c1*(1/2*bata)*(cosh(bata*x)*sin(bata*x)-sinh(bata*x)*cos(bata*x));
a[3]  = -2*c2*(1/2*bata)*(sinh(bata*x)*cos(bata*x)+cosh(bata*x)*sin(bata*x));
a[4]  = (exp(2*bata*x) /(8*bata*bata)) * (- 2 * sin(2*bata*x) + 2 * bata * cos(2*bata*x) );
a[5]  = (exp(-2*bata*x)/(8*bata*bata)) * (- 2 * sin(2*bata*x) - 2 * bata * cos(2*bata*x) );
a[6]  =  ((c1 * c2) / 4) * (a[4] + a[5]);
a[7]  =   exp(2*bata*x) * ( 1 / (4*bata) ) - ( 1 / 8 * bata )*( cos(2*bata*x) + sin(2*bata*x));
a[8]  = -exp(-2*bata*x) * ( 1 / (4*bata) ) + ( 1 / 8 * bata )*(-cos(2*bata*x) + sin(2*bata*x));
a[9]  =  2 * ( ( -bata * x ) / 2) + (1/4) * sin(2*bata*x);
a[10] =  ( ( c1*c1 ) / 4 ) *  (a[7] + a[8] +a[9] );
a[11] =   exp(2*bata*x) * ( 1 / (4*bata) ) + ( 1 / 8 * bata )*(cos(2*bata*x) + sin(2*bata*x));
a[12] = -exp(-2*bata*x) * ( 1 / (4*bata) ) - ( 1 / 8 * bata )*(-cos(2*bata*x) + sin(2*bata*x));
a[13] =  2 *  ( ( bata * x ) / 2) + (1/4) * sin(2*bata*x);
a[14] =  ( ( c2*c2 ) / 4 ) *  (a[11] + a[12] +a[13] );
a[15] = x;
a[16] =  c1 * (1/(2*bata)) * ( cosh(bata*x) * sin(bata*x) - sinh(bata*x) * cos(bata*x) );
a[17] = -c2 * (1/(2*bata)) * ( sinh(bata*x) * cos(bata*x) + cosh(bata*x) * sin(bata*x) );

f2 = ( k*k * ( a[1] + a[2] + a[3] + a[6] + a[10] + a[14] ) + k * radia * ( a[15] + a[16] +a[17] ) );

volume = 2 * 3.14159565359 * ( f1 - f2 );

return(volume);
}
```